Nonlinear Mechanical and Actuation Characterization of Piezoceramic Fiber Composites

by

Robert Brett Williams

Dissertation submitted to the faculty of
Virginia Polytechnic Institute and State University
in partial fulfillment of the requirements for the degree of

Doctor of Philosophy

in

Mechanical Engineering

Dr. Daniel J. Inman, Chairman

Dr. Michael W. Hyer

Dr. Donald J. Leo

Dr. Liviu Librescu

Dr. Gyuhae Park

Dr. W. Keats Wilkie

March 22, 2004
Blacksburg, Virginia

Keywords: Macro Fiber Composite, material properties, nonlinear piezomechanical behavior, Preisach model

Nonlinear Mechanical and Actuation Characterization of Piezoceramic Fiber Composites

R. Brett Williams

Dr. Daniel J. Inman, Chairman
Virginia Polytechnic Institute and State University
Department of Mechanical Engineering

(Abstract)

The use of piezoelectric ceramic materials for structural actuation is a fairly well developed practice that has found use in a wide variety of applications. However, actuators with piezoceramic fibers and interdigitated electrodes have risen to the forefront of the intelligent structures community due to their increased actuation capability. However, their fiber-reinforced construction causes them to exhibit anisotropic piezomechanical properties, and the required larger driving voltages make the inherent piezoelectric nonlinearities more prevalent. In order to effectively utilize their increased performance, the more complicated behavior of these actuators must be sufficiently characterized.

The current work is intended to provide a detailed nonlinear characterization of the mechanical and piezoelectric behavior of the Macro Fiber Composite actuator, which was developed at the NASA Langley Research Center. The mechanical behavior of this planar actuation device, which is both flexible and robust, is investigated by first developing a classical lamination model to predict its short-circuit linear-elastic properties, which are then verified experimentally. The sensitivity of this model to variations in constituent material properties is also studied. Phenomenological models are then used to represent the measured nonlinear short-circuit stress-strain response to various in-plane mechanical loads. Piezoelectric characterization begins with a nonlinear actuation model whose material parameters are determined experimentally for monotonically increasing electric fields. Next, the response of the actuator to a sinusoidal electric field input is measured under various constant mechanical loads and field amplitudes. From this procedure, the common linear piezoelectric strain coefficients are presented as a function of electric field amplitude and applied stress. In addition, a Preisach model is developed that uses the collected data sets to predict the hysteretic piezoelectric behavior of the MFC. Lastly, other related topics, such as manufacturing, cure kinetics modeling and linear thermoelasticity of the Macro Fiber Composite, are covered in the appendices.

Acknowledgements

Thanks to **Dr. Daniel J. Inman**, for his endless support, e-mails, and flexibility on my location and research topics, without which, none of this work would have been possible.

Thanks also to **Dr. W. Keats Wilkie** for serving as my GSRP advisor, scheduling experiments for my many trips to NASA Langley Research Center, and inspiring me to work hard so that I can one day own a German sports car and an expensive mountain bike.

Thanks to **Dr. Michael W. Hyer** for offering ideas for theoretical, experimental, and finite element analyses. His composites expertise has been invaluable. Also, thanks to **Dr. Don Leo, Dr. Liviu Librescu,** and **Dr. Gyuhae Park** for serving on my committee, reviewing my dissertation, and offering technical insight upon request.

Thanks to **James High** for teaching me how to make MFC's and discussing golf, tennis, and our favorite Manhattan restaurants. Also, **Brian Grimsley** at NASA LaRC helped me a great deal in their Materials Processing Lab. Thanks also to **Bob Simonds** for helping me in the ESM "busting lab," along with **Dr. Marc Schultz, Danny Reed** and **Tim Eggborn.**

Thanks to **Dr. Marca Lam** at The Cooper Union for the Advancement of Science and Art in New York City for sharing her office, enduring the stories of my Manhattan adventures during Summer 2001, and providing a place for me to write this work during Summer/Fall 2003-Spring 2004.

Thanks goes out to my **CIMSS colleagues** who were forced to work alongside me, for listening to my endless barrage of sordid tales. Your companionship both in the office and at the bars has sustained me during my time at CIMSS.

Thanks to **Bob and Mary Williams** for their support and guidance from the beginning. They have taught me many valuable lessons, most importantly, to not settle for mediocrity; I should strive to be the best at everything I attempt. It turns out, however, that I can do so without eating vegetables and meatloaf. Thanks also to my "bigger" little brother **Brian Williams**, who has become a great friend over the past few years.

My undying gratitude and admiration goes out to **Rachel Bachman**, a woman with an infinite amount of love, patience, and tolerance for me. Her affection, companionship, home-cooked meals, and financial support in Manhattan have enriched my life in so many ways for many years. I also appreciate her insisting on adopting **Little Jerry Seinfeld**, an adorable Chihuahua who has brought us many more enjoyable moments together.

Acknowledgement of Funding

The Air Force Office of Scientific Research (AFOSR) supported this research effort under grant number F49620-99-1-0231. Also, the NASA Langley Research Center provided specific funding for the study of Macro Fiber Composites under grant number NASA LaRC 01-1103. Additionally, the NASA Graduate Student Researchers Program (GSRP) and the NASA Virginia Space Grant Consortium provided funding for R. Brett Williams while he completed his graduate education. The financial and technological support of these organizations is gratefully acknowledged.

Table of Contents

List of Figures

List of Tables

Chapter 1

Introduction to Piezoceramic Fiber Actuators

1.1 Motivation:

The past few decades have seen the development and integration of active materials into a variety of host structures as a superior means of measuring and controlling its behavior. While there exist many types of useful active materials, such as shape memory alloys, electrostrictives and magnetorheological fluids, piezoelectrics remain the most widely used "smart" material for a number of reasons. First, piezoceramics have a high structural stiffness, which affords them a strong, voltage-dependent actuation authority, while piezopolymers are less stiff but offer superior sensing capability. Additionally, piezoelectrics are capable of interacting with dynamic systems over a wide range of frequencies from zero into the megahertz range [Banks, Smith and Wang, 1996]. Piezoelectric materials have been used to enhance the performance of aerospace structures, automobiles and sporting equipment by performing shape control and vibration and acoustic noise reduction. Some notable aerospace applications of these materials are helicopter rotor blades [Flinn, 1999; and Cesnik and Shin, 2001],

inflatable satellite components [Jha, 2002], and airplane tail fins [Moses et al., 2001], while Chrysler [Malowicki, 2001] and Volkswagen [Manz and Schmidt, 2000] have tested piezoceramics in their cars to produce quieter, more comfortable rides. Some tennis rackets [Continuum Control, 2000], snow skis [Cymer, 1998], and baseball bats [Rotman, 1999] are now equipped with piezoelectric dampers to reduce vibrations, increase performance, and help prevent bodily injury. A review of other state of the art smart material technologies is given by Chopra [2002].

While a good deal of success was obtained in the field of intelligent structures, defined as those "possessing the ability to sense and actuate in a controlled manner in response to variable ambient stimuli" [Banks, Smith and Wang, 1996] using monolithic wafers of piezoceramic material in the past, there are several practical limitations to implementing this delicate type of material. First, the brittle nature of ceramics makes them vulnerable to accidental breakage during handling and bonding procedures, as well as their extremely limited ability to conform to curved surfaces. Also, there is a large add-on mass associated with using a typically lead-based piezoceramic.

1.2 Piezocomposite Actuators:

The idea of a composite material consisting of an active piezoceramic fibrous phase embedded in a polymeric matrix phase remedies many of the aforementioned restrictions and offers other benefits [Hagood and Bent, 1993]. Typically, crystalline materials have much higher strengths in fibrous form, where the decrease in volume fraction of flaws leads to an increase in specific strength. Since they will be encased in a polymer and laminated with other flexible layers, the fibers can be thinner, thus less stiff in bending than a monolithic stand-alone layer. Furthermore, in addition to protecting the fibers, the flexible nature of the polymer matrix allows the material to more easily conform to the curved surfaces found in realistic industrial and aerospace applications. These types of devices are also capable of being added to a lay-up as "active layers" along with conventional fiber-reinforced laminae. Most importantly, the

use of interdigitated electrodes causes these actuators to develop much higher forces or displacements by capitalizing on the stronger longitudinal (d_{33} constant) piezoelectric effect, in which the largest mechanical response occurs in the direction of applied electric field [Wilkie et al., 2000].

1.2.1 History of Piezoceramic Fiber Composites and Interdigitated Electrodes:

The current state of the art for piezoceramic fiber composite actuators with interdigitated electrodes has been arrived at by several smaller steps which advanced and combined pre-existing technologies. This section outlines the development of such devices through a chronological discussion of the cornerstone publications in this field.

1.2.1.1 Development of the Active Fiber Composite

Hagood et al. [1993] attempted to improve planar actuation by using interdigitated electrodes to apply in-plane fields to monolithic piezoceramic wafers. This technique succeeded in applying such an electric field, which was used to pole and then actuate that material through the stronger d_{33} piezoelectric effect. However, high electric field gradients near the edges of the electrodes caused stresses large enough to crack the brittle ceramic. Nevertheless, the electric field between the electrodes was shown to be relatively uniform and in the desired planar direction. Thus, the idea of interdigitated electrodes was a significant contribution and the critical component of today's high-strain actuators.

Around this same time, piezoceramic fiber composites (PFCs) with uniform electrodes were developed at MIT in an effort to achieve in-plane orthotropic actuation. This concept utilized round, extruded piezoceramic fibers embedded in an epoxy matrix. Electric fields were applied to the device through uniform electrode layers on the top and bottom of a single layer of fibers. Of course, this type of electroding poled the actuator through its thickness; therefore planar actuation was achieved through the weaker d_{31} piezoelectric effect. Nevertheless, the device showed much larger

deflections parallel to the fibers than in the transverse direction. This directional actuation offered a designer the ability to excite only specific deformation modes of a host structure. However, the large dielectric mismatch between the piezoceramic and epoxy greatly reduced the electric field available for the fibers. The result was an device with actuation capability comparable to the relatively weak piezopolymer, PVDF. Various electromechanical models were developed at the microstructural level using a uniform fields approach for a continuum containing both piezoelectric and polymer matrix phases [Hagood and Bent, 1993]. The uniform fields model is an extension of Mechanics of Materials that includes 3-D electromechanical coupling. These models were then applied to the specific geometry of round, unidirectional piezoceramic fibers embedded in epoxy. The result was a set of equations that predicted the effective elastic and piezoelectric properties of the PFC. The methodology for manufacturing experimental specimens was presented, and the effective properties were measured and seen to be in reasonable agreement with the discretized model and a finite element analysis. Also, a twist-extension bimorph structure was built to demonstrate the ability to induce twisting deformation in an isotropic host material using anisotropic actuation [Bent, 1994, and Bent, Hagood and Rodgers, 1995].

Soon after, the piezoceramic fiber composite and interdigitated electrode technologies were combined to form Interdigitated Electrode Piezoelectric Fiber Composites (IDEPFCs). This union exploited the directional actuation, increased flexibility, and improved durability of the PFC, along with the increased strain output obtained by using IDEs in lieu of uniform electrodes [Bent and Hagood, 1997]. Again, micromechanical models, namely uniform fields and finite elements, were developed in order to predict the effective piezomechanical properties of the IDEPFC. These models were compared over a range of piezoceramic fiber volume fractions and seen to agree closely. Material preparation and subsequent manufacturing procedures for the IDEPFC were also discussed. Likewise, the experimental procedure undertaken to measure the piezomechanical properties was covered, and the results were in

reasonable agreement with the analytical predictions. As expected, the values of the free-strain constants were five times higher than PFCs with uniform electrodes, indicating much improved actuation performance. Also, the maximum free-strain output in the fiber direction was approximately three times greater than in the transverse direction, under comparable fields of $\pm 6.6\ kV/m$.

In his doctoral dissertation, Bent [1997] coined the term "Active Fiber Composite (AFC)," to take the place of IDEPFC, and presented a detailed design analysis, including constituent material characterization and selection. Additionally, a thorough derivation of the linear uniform fields and finite element models was presented, and the results were used to examine design tradeoffs between various fiber and matrix combinations. Manufacturing of several selected AFC designs and the experimental measurement of their relevant eletromechanical properties was discussed. It was shown that the behavior of the AFC was well described by the linear uniform fields model, however, actuation under high fields led to more complex nonlinear material behavior. More on this nonlinear behavior is presented in Section 1.4.5, where nonlinear piezoelectricity is discussed. Also, two helicopter rotor blade applications of the AFC were discussed, although not in detail. A good summary of the material selection and processing, actuator characterization, and structural control applications of the AFC was given by Janos and Hagood [1998].

1.2.1.2 Development of the Macro Fiber Composite

A great deal of information was learned about interdigitated electrodes and piezoceramic fiber composites through the development of the AFC. However, its performance was ultimately limited by design and manufacturing issues. Most importantly, the round cross-section fibers, seen in Figure 1.1, tended to have minimal contact area with the copper electrodes. This limitation, combined with the epoxy beneath the electrodes but adjacent to the contact region, made for an inefficient transfer of the electric field into the PZT fibers. Additionally, the PZT fibers used in the AFC are

obtained individually from an extrusion process, which required the thin, brittle fibers to be handled and aligned by hand. This procedure oftentimes resulted in broken, poorly aligned fibers. Furthermore, the vacuum infiltration process that was used to apply the epoxy to the fibers can leave air bubbles (voids) and particulate inclusions, both of which greatly increased the chance of electrical failure.

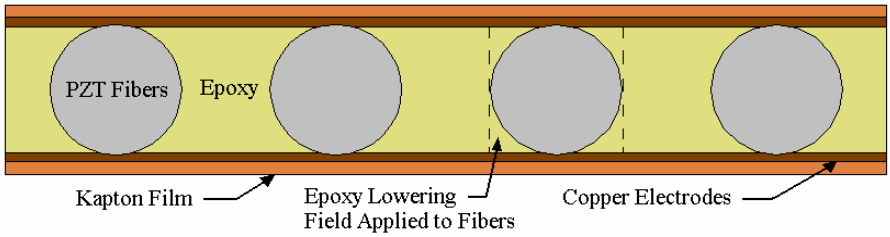

Figure 1.1: Schematic Illustrating Poor PZT-Electrode Contact for the AFC

In light of these limitations, the Macro Fiber Composite (MFC) was developed at NASA Langley [Wilkie et al., 2000]. The MFC is a layered, planar actuation device that employs rectangular cross-section, unidirectional piezoceramic fibers (PZT 5A – lead zirconate-titanate) embedded in a thermosetting polymer matrix. This active, fiber-reinforced layer is then sandwiched between copper-clad Kapton® film layers that have an etched interdigitated electrode pattern. Figure 1.2 shows the MFC, where the PZT fibers are aligned in the 3-direction and the copper electrode fingers are parallel to the 1-direction, according to standard piezoelectric notation.

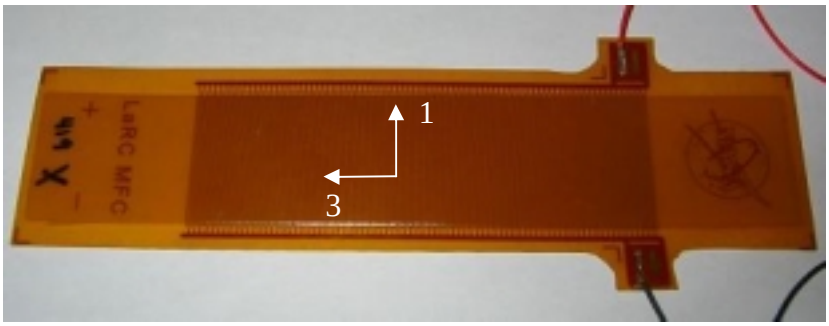

Figure 1.2: Macro Fiber Composite Actuator

Figure 1.3 demonstrates the flexibility of these piezoceramic fiber composite actuators.

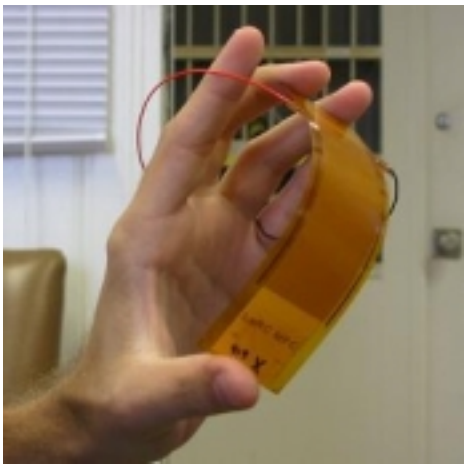

Figure 1.3: MFC – A Flexible Piezoceramic Actuator

During manufacturing, these layers are laid-up by hand and then cured in a vacuum hot-press. After the epoxy matrix that bonds the package together is fully cured, a high DC voltage is applied to the electrodes, thereby poling the piezoceramic material in the plane of the actuator and establishing the poling direction parallel to the PZT fibers. A more detailed outline of the MFC manufacturing process is given in Appendix B, while a comprehensive manual is found in High and Wilkie [2003]. The electric field distribution for an interdigitated electrode pattern is shown qualitatively in Figure 1.4.

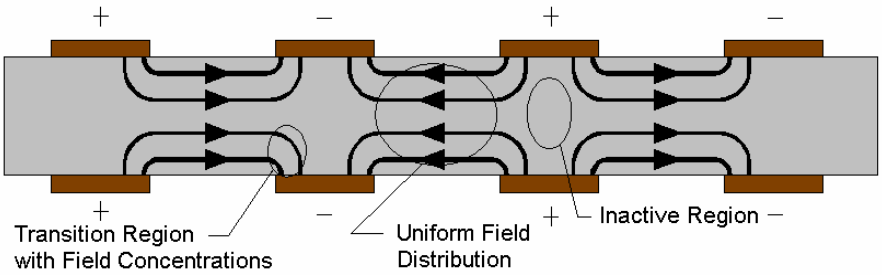

Figure 1.4: Electric Field Distribution for Interdigitated Electrode Pattern

This in-plane poling and subsequent voltage actuation allows the MFC to utilize the d_{33} piezoelectric effect, which is much stronger than the d_{31} effect used by traditional PZT actuators with through-the-thickness poling [Hagood et al., 1993]. As seen in Figure 1.5, the MFC had a uniform geometry, including PZT fiber and electrode spacing and continuity, as well as the absence of air voids or particulate inclusions. The use of

rectangular fibers also promoted maximum contact between the piezoceramic and the adjacent electrode finger, thus ensuring the most efficient transfer of electric field into the fibers. The photomicrograph in Figure 1.6 illustrates the exceptional contact between the copper electrode and the PZT fiber.

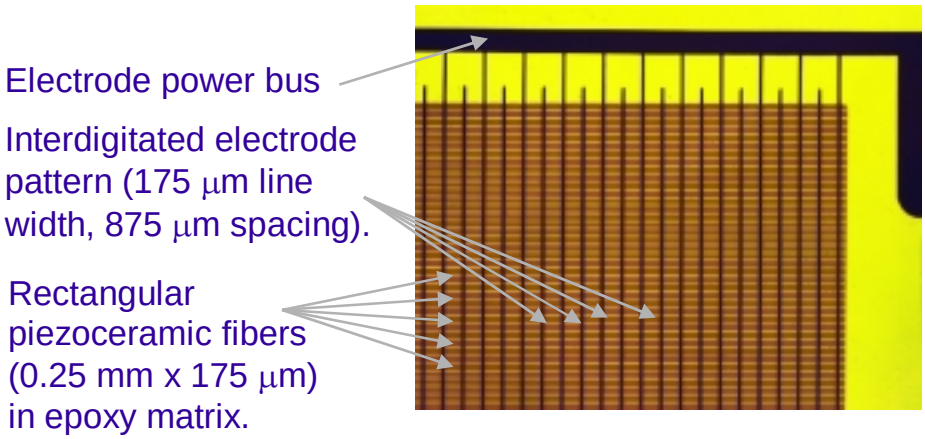

Figure 1.5: Photograph of the MFC - Uniform Geometry

With the benefits of interdigitated electrodes and PFCs clearly established and the insight of the research team at NASA Langley to utilize rectangular fibers, the design of the MFC required less iterative steps, material characterization and analytical investigation. Therefore, there exists much less literature pertaining to the MFC, particularly in the area or modeling or material characterization. However, the first

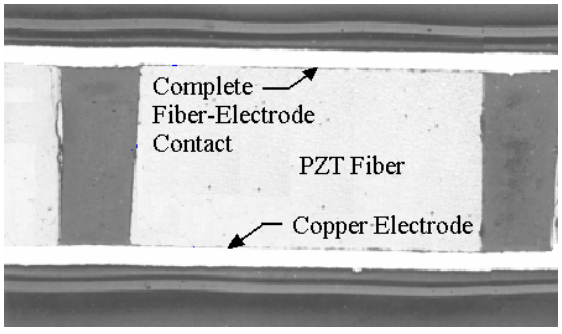

Figure 1.6: Photomicrograph of the MFC Showing Maximum Contact between Fiber and Electrode

paper published on the MFC generated a large amount of interest in the academic research community. This initial publication [Wilkie et al., 2000] discussed the design, manufacture and testing of the MFC actuator. A brief background of PFCs was presented, and the layer configuration of the MFC was illustrated along with the methodology required to prepare each of the various layers. The hand lay-up and cure procedures were outlined, and the critical structural components and their functions were clearly identified. Experimental results showed the free-strain-applied electric field relationship, peak strain outputs for several MFC specimens, and the lack of performance degradation after more than 90 million electrical cycles. The actuation performance of the MFC was also shown to be superior to many other commercially available piezoceramic actuators, both with and without interdigitated electrodes. Finally, preliminary studies were presented that indicate how the MFC was used to actively reduce vibration levels in inflatable, rigidizable struts and fighter jet tail fins, and representative electromechanical properties were given. One of the objectives of the current effort is to verify and update many of these preliminary properties.

At the conception of the current work, there existed very few publications dealing with characterization or modeling of the MFC actuator, as it was a relatively new invention. However, research stemming from this effort added a wealth of information to the written knowledge base in the areas of cure kinetics modeling of Loctite E-120 HP epoxy [Williams et al., 2003a], experimental determination of linear and nonlinear constitutive behavior under short-circuit conditions [Williams et al., 2003b], linear thermoelastic behavior [Williams, Inman, and Wilike, 2004], and measuring nonlinear actuation properties under various loads [Williams, Inman, and Wilkie, forthcoming]. These works are indeed the foundation for this dissertation.

1.2.1.3 AFC/MFC Applications

While the literature reviewed in the two previous sections deals primarily with actuator development, modeling, and characterization, there has been extensive analytical and

experimental research focused on utilizing the AFC or the MFC as an actuator (or sensor) for structural control. As structural applications are not at the focus of the present work, a detailed discussion is not warranted, however, a brief mention of some notable works serves to show the tremendous potential of IDEPFCs.

Researchers at The Massachusetts Institute of Technology [Cesnik and Shin, 2001] developed a 2-D linear model of a multi-cell composite helicopter rotor blade cross-section with active AFC plies, and performed a geometrically nonlinear 1-D (beam) analysis along the length of the blade. Closed-form expressions were presented for the cross-sectional stiffness constants, which were then used in the subsequent finite element beam model, which predicted displacements, rotations and strains of the reference line by accounting for external loads, actively induced strains and specific boundary conditions. The results of the model were compared to scaled models tested at MIT and found to agree closely. Later, Cesnik and Ortega-Morales extended these cross-sectional modeling efforts [2001] to include arbitrary geometries of either thin or thick sections with or without embedded active plies. The updated effort also included the effects of initial twist and curvature in the rotor blade, as well as the impact of foam core shear modulus. The model was verified against experimental results from a single cell NACA 0012 beam, a 1/6 Mach-scaled CH-47D blade section and an Active Twist Rotor (ATR) blade prototype, which included AFC actuation layers. At NASA Langley, Moses et al. [2001] used both the AFC and the MFC to actively reduce vibration levels in the tail fins of a wind-tunnel model of a fighter jet subjected to buffet loads. The model was tested at a Mach number of 0.105 and a 25 degree angle of attack, and one fin had five MFCs, while the other had five AFCs. Using a maximum closed-loop control signal input of 1000 volts to the lower actuators, the fin-tip peak acceleration was reduced by about 70% with the MFCs and about 85% for the AFCs at frequencies near the first bending mode. 30% and 40% reductions in torsional peak vibration levels were obtained by delivering a closed-loop control signal to the MFCs and AFCs respectively. Jha [2002] modeled the dynamics of a lightweight, inflatable toroidal shell commonly

used in telecommunications satellites and other space-based structures. After understanding the vibration characteristics of the torus, a genetic algorithm was used to determine optimal size and placement of sensors and actuators. Their passive impact on the dynamics of the torus was quantified along with the forces that they imparted to the structure. Lastly, an active control system for the torus was designed using a sliding mode controller/observer with both monolithic and MFC type actuators. Bevan [2001] and Azzouz et al. [2001] developed a fully-coupled shallow shell finite element formulation to investigate the effect of PZT fiber orientation on acoustic and structural vibration control of plate and shells using both AFCs and MFCs. The code was applicable to both integrated and surface mounted actuators. While not tremendously effective at attenuating acoustical noise from curved panels, the MFC was predicted to be very effective at reducing structural vibrations. However, the need for accurate electromechanical properties of the MFC was indicated repeatedly throughout these two works. Sodano, Park, and Inman [2003] experimentally investigated the suitability of using the MFC for structural vibration applications. Ground testing and active vibration control of an inflated Kapton torus was performed using Macro Fiber Composites. Also, by measuring changes in impedance, the MFC was able to accurately detect damage in a lap joint whose bolt preload was reduced, and a cantilevered beam whose clamped end was loosened. In addition, self-sensing technology was used with the MFC to reduce the vibration levels of a cantilevered aluminum beam. Ruggerio et al. [2002] used several MFCs as both actuators and sensors to measure the dynamic behavior of the same inflated Kapton torus and to control its vibration. Once again, the flexibility of the MFC made for convenient attachment to the doubly-curved surface and it was found to outperform other actuators and to have sensitivity comparable to other monolithic piezoelectric sensors. Schultz [2003] used the flexibility and high force output of the MFC to snap-through an unsymmetric composite laminate from one stable configuration to the other. Using the MFC with such anisotropic structures could open the door to large-deflection shape control such as morphing wing technology.

1.3 Objective:

The detailed objective of this research effort is to characterize the electromechanical behavior of the MFC actuator where material nonlinearities are considered. This task can be visualized as determining, either experimentally or analytically, the material properties required by the actuator form of the linear constitutive relationship that governs the behavior of piezoelectric devices, including the MFC:

$$S_{ij} = s^{E}_{ijkl} T_{kl} + d_{kij} E_{k} \qquad i, j, k, l = 1,2,3 \tag{1.1}$$

Here, using standard piezoelectric notation, S is the total strain, T is the mechanical stress, E is the applied electric field, s^E is the mechanical compliance tensor under short-circuit electrical boundary conditions, and d is the piezoelectric strain tensor. Thus, the material properties to be determined are s^E and d, and nonlinearities can arise when these parameters are not constant, but rather, vary with physical quantities such as stress, strain, voltage, or temperature. First, well-known composite techniques, such as the rule-of-mixtures and classical lamination theory, are applied to the various plies of the hybrid MFC laminate, which have either copper or piezoceramic fiber reinforcement with volume fractions as low as ~0.20 and as high as ~0.85. The suitability of these traditional models could be in jeopardy since they were developed for laminae reinforced with multiple rows of round cross-section graphite, boron or glass fibers, with volume fractions between 0.60 and 0.70. Therefore, this research effort endeavors to experimentally verify these well-established models by comparing measured values of the orthotropic short-circuit stiffness properties (as required in Equation 1.1) in the linear-elastic region to those predicted for the MFC laminate by the models. Also, under a large applied voltage (~1000 V), the MFC develops strains large enough to violate a linear relationship between electric field, stress, and strain. Therefore, the nonlinear mechanical behavior under short-circuit conditions is measured and the data represented using various well-known elastic-plastic deformation models. Lastly,

piezoelectrics are known to produce strain outputs that decreases with applied mechanical stress level, and this relationship must be characterized quantitatively. Initial experimentation has shown that the effective piezoelectric strain tensor, d_{ij}^{eff}, is not a constant, but rather can vary by a factor of two with large changes in the magnitude of applied voltage. In order to develop high fidelity structural actuation models, material nonlinearities such as changes in piezoelastic material properties under reasonable operating conditions must be considered.

1.4 Modeling of Piezoceramic Fiber Composites and Interdigitated Electrodes

There have been some efforts made to model the piezoelectric behavior of generic actuators consisting of piezoceramic fibers embedded in epoxy matrices. Poizat and Sester [1999] isolated unit cells for composites with both fibrous and particulate piezoceramic fibers with various geometries in passive epoxy matrices. Finite element models were then developed to determine the effective stress and strain coefficients, e_{ij} and d_{ij}, respectively, of these active composites. The finite element results were in close agreement to an effective-fields model as well as previously published experimental data.

Tan and Tong published a set of papers dealing with various types of piezoceramic fiber composites. In [2001], they predicted the piezoelastic and dielectric properties of PFCs with both rectangular and round fibers using micromechanical models with linear piezoelectric theory and iso-field assumptions. Basically, the iso-field assumptions lead to a set of boundary conditions, which were then applied to the piezoelectric constitutive relationship where some of the loads (strains or electric fields) were considered to be zero or nonzero. The properties were then determined as a function of piezoceramic fiber volume fraction, fiber and unit cell cross-section shapes, and constituent material properties. While some of the properties were independent of the loading conditions, a few were noted as depending on the type (single or multiple) of loads. Here, a single load referred to only one strain or electric field being nonzero,

while multiple loads meant that all of the strains and electric fields were constants, either zero or nonzero. Even though the notion of rectangular fibers is dismissed in this paper, its models are of significant interest to MFC designers. In a follow-up paper [2002a], the derivations in the previous work were reviewed and the influence of loading assumptions was investigated. The results showed the variation in electromechanical properties with piezoceramic fiber volume fraction and various loading conditions. It was found that all but one of the properties depends on the loading situation. For the fiber-direction properties derived using a single load scenario tended to agree with rule-of-mixture predictions, while properties calculated under multiple loads tended to agree with FEA and experimental results. In a work of critical importance to the current effort [2002b], a one-dimensional model for nonlinear electromechanical behavior was developed for round cross-section piezoceramic fiber-reinforced composites based on experimental results. The effects of stress applied in the fiber direction on the strain-field loops was investigated for several types of piezoelectric materials and composites. The stress-field behavior was also investigated as a function of piezoelectric fiber volume fraction, and applied strain level in the fiber direction.

Kim and Koo [2002] analytically investigated the use of different matrix materials to improve the actuation performance of PFCIDEs. A linear piezoelectric model was developed from 3D elasticity and dielectric theories to represent such structures and found to be in close agreement with both experimental data and previously published analytical results. Using this model, a 3D finite element model was constructed of a graphite epoxy laminate with integrated PFCIDEs, and the shape of the structure was found to be controllable based on PZT fiber angles, choice of matrix material, and elastic tailoring of the host structure.

The effective constants for linear piezoelastic behavior of a PFC device with rectangular fibers and uniform electrodes were predicted using micromechanical analyses based on

the method of cells and the strength of materials approach [Mallik and Ray, 2003]. The two methods were found go be in close agreement, and predicted that the effective piezoelectric stress constants, e_{ij}, reach maximum values in excess of that of the bulk piezoceramic around a critical fiber volume fraction around 0.85 for PZT-5H.

Lenglet, Hladky-Hennion, and Debus [2003] applied a numerical homogenization technique using the ATILA finite element code to model general PFCIDEs using representative volume elements and wave propagation theories. The model was then utilized to predict the piezomechanical properties of the AFC. The results were found to be in close agreement with analytical predictions available previously in the literature. The model was easily adaptable to any PFCIDE by changing only the mesh structure and material properties, which could be useful for future MFC designers.

Otter [2002] predicted the electrostatic potential and capacitance of interdigitated electrode structures using the potential function of two conducting semi-infinite plates. The resulting equations were much simpler to use than the results from previously published solutions, while still in close agreement with the exact solution for interdigitated electrodes.

Beckert and Kreher [2003] used detailed finite element analyses to model interdigitated electrodes with piezoelectric actuators. They investigated the impact of various geometrical and material parameters on actuation behavior for both monolithic sheets and round piezoceramic fibers. While the work with monolithics was not of particular interest to the current work, the understanding of the electric field developed within the piezoceramic material was essential. A phenomenological model of the effective deformation based on electrode geometry, applied voltage, and piezoelectric strain constants, as well as empirical parameters indicating elastic constraint of passive layers, loss of potential due to indirect contact, and the shape of the applied electric field was proposed. Additionally, the electric field distribution between the electrode fingers was

investigated in detail for various electrode widths, while the induced deformation was predicted for different levels of indirect contact between the electrode and fibers for epoxy matrices with various dielectric constants. The results of this work gave valuable insight into correctly approximating the average electric field in the PFCs for a given applied voltage.

Bowen et al. [1999] investigated the nonuniform electric field distribution, strain distribution and localized stresses developed between interdigitated electrodes on a monolithic piezoceramic substrate using finite elements. The experimentally measured strain output of the actuator, and the electric field distribution results agreed closely with the finite element predictions.

1.5 Contributions:

The work contained in this dissertation represents several significant contributions to advancing the state of the art for piezoceramic fiber composites, the MFC in particular. The list below highlights these contributions.

- Experimentally verified the suitability of rule-of-mixture and classical lamination theories for predicting the short-circuit, linear-elastic mechanical properties of the MFC actuator, namely E_x, E_y, G_{xy}, and υ_{xy}.
- Modeled the nonlinear short-circuit mechanical behavior of the MFC actuator subjected to longitudinal, transverse, and in-plane shear loading.
- Developed a model for the nonlinear response of a piezoelectric material to an initial monotonic increasing voltage input under both free-strain and constant nonzero mechanical stresses, and measured the nonlinear material properties required by this model for the MFC.
- Measured the linear piezoelectric strain parameters of the MFC using a peak-to-peak actuation approach under various voltage amplitudes and constant mechanical stress levels.

- Modified the classical Preisach model for use with MFC actuation hysteresis loops resulting from voltage profiles with or without equal but opposite maxima and minima.

1.6 Overview of Dissertation:

This first chapter discusses the concept of using piezoelectric materials for structural control, and more specifically, outlines the development of actuators that utilize piezoceramic fibers and interdigitated electrodes in order to outperform traditional monolithic piezoceramics. The Macro Fiber Composite actuator is introduced and its benefits are outlined. The objectives of this dissertation are presented, and then publications that shed insight on the modeling techniques available for such piezoelectric fiber composite actuators are discussed. The contributions of this work to the written literature are outlined, and the remainder of this section outlines the topics to be covered in subsequent chapters, as well as the appendices.

Chapter 2 uses classical lamination theory to model the MFC as a hybrid laminate and predict the four independent linear-elastic stiffness properties, E_x, E_y, ν_{xy}, and G_{xy} of the MFC under short-circuit boundary conditions. Elastic properties for the isotropic constituent materials are taken from material suppliers and rule-of-mixtures micromechanical formulas are used to formulate the reduced stiffness matrices for the orthotropic fiber-reinforced PZT/epoxy and copper/epoxy layers. While rule-of-mixture-type formulations are often inaccurate for advanced composites with round cross-section fibers, they work quite well for a single row of rectangular cross-section fibers used in the construction of the MFC. The layers of the MFC are then combined using standard techniques for composite laminates, and the in-plane extensional stiffness matrix, $[A]$, is found. The predicted values for E_x, E_y, ν_{xy}, and G_{xy} of the MFC are calculated from the inverse of $[A]$.

Chapter 3 describes experiments that measure the nonlinear mechanical behavior of the MFC under short-circuit boundary conditions. For this chapter, a total of three sets of tests were performed. The first two sets determined the tensile stress-strain behavior both parallel and perpendicular to the PZT fibers, while the third set measured the in-plane shear stress-shear strain relationship for the MFC. The effective E_x, E_y, ν_{xy}, and G_{xy} of the MFC were measured from the linear-elastic region of these curves and compared to those predicted in Chapter 2. Since there is significant nonlinear material behavior at strain levels that the MFC would see in a realistic aerospace application, nonlinear constitutive models, such as linear-elastic hardening and Ramberg-Osgood, are developed. The resulting equations are used to relate stresses and strains over a wide strain region, and also depict how the various stiffness parameters change with strain level.

Chapter 4 uses the linear model developed in Chapter 2 to analytically investigate the sensitivity of E_x, E_y, υ_{xy} and G_{xy}, of the MFC under short-circuit conditions to variations in the constituent material properties. While every reasonable effort is made to obtain the most recent and accurate required material properties for the Kapton, acrylic, copper, epoxy, and PZT, sometimes "typical" or "handbook" values are used instead of numbers provided by the material supplier. This overall goal of Chapter 4 is to determine which of these material properties has the largest impact on the desired effective MFC properties, and identify which material properties need to be measured independently by future researchers in order to develop higher fidelity models. In addition, the impact of certain geometric design parameters, namely fiber volume fractions and layer thicknesses, is investigated to establish design envelopes for the effective, short-circuit engineering properties of the MFC.

Chapter 5 moves onto characterizing the actuation capability of the MFC. Through Chapter 4, the modeling and experimental characterization of the MFC deals with only the mechanical behavior under constant, i.e. zero, electric field boundary conditions,

thus disregarding the actuation capability of the device. Thus, Chapter 5 begins by developing a reversible nonlinear model for the response of a poled piezoceramic continuum to a monotonic increase in electric field under a mechanical load. Then, an experimental procedure is designed to determine the material parameters for the MFC required for this model. This procedure involves loading the specimen to predetermined levels, which are then held constant by the hydraulic machine while the MFC is actuated under various amplitude, constant, low-frequency sinusoidal voltage profiles. The actuation voltages applied at each constant-load level consist of three different sets corresponding to 0, 250, and 500 volt DC biasing voltages. From the resulting experimental data, the desired nonlinear, monotonic actuation properties are obtained for the various electromechanical loading conditions.

Chapter 6 uses the same experimental data from Chapter 5 to first determine the effective linear piezoelectric strain coefficients for the MFC from the peak-to-peak actuation strain and electric field data. These parameters are found from a linear regression of the measured strain-electric field hysteresis loops under both free-strain and constant nonzero mechanical load conditions. While the former values are typically used for modeling efforts in the literature, knowing the effective actuation capability under nonzero loads is also quite useful. Next, the classical Preisach model is modified so that it can be used with the experimental procedure contained herein to predict strain outputs of the MFC in response to a general case of harmonic electrical excitation. The Preisach model, which is commonly used to represent irreversible nonlinearities (i.e. hysteresis), requires a dataset of reversal curves, some of which can be extracted from the experimental data already collected. A simple example is presented to illustrate the accuracy of this model.

Chapter 7 provides a brief summary of the results from the current research effort, including the limits of traditional linear piezoelectric models. Also, the contributions of this work to the written body of literature are discussed. Journal and conference

publications stemming from this dissertation research are listed, and then recommendations for improvements and future work are presented.

In addition to the seven chapters outlined above, this work includes an extensive set of appendices that present either detailed derivations and processes used throughout this work, *Mathematica* computer programs that are used in the development of these chapters, or additional work that was performed on the MFC actuator not pertaining to its nonlinear characterization. Appendix A applies a mechanics-of-materials approach to derive the rule-of-mixtures formulae for the apparent orthotropic moduli of a fiber-reinforced lamina from a representative volume element, based on the approach found in Jones [1999]. Appendix B presents a classical lamination code developed in *Mathematica* Version 4.0, while Appendix C gives the detailed procedure required to manufacture MFCs using a hand lay-up procedure, which is similar in many ways to the steps required to produce traditional fiber-reinforced laminates. Building on the manufacturing and processing steps outlined in Appendix C, Appendix D is devoted to developing a cure kinetics model that is based on heat flow measurements from dynamic and isothermal scans in a differential scanning calorimeter (DSC). Such a model can be used to help optimize the MFC manufacturing procedure in terms of significantly reducing the cycle time required to manufacture MFC actuators. Appendix E investigates nonlinear behavior resulting from changes in the linear-elastic compliance tensor under variations magnitude constant electric fields. This investigation involves performing tensile tests within the linear-elastic region under various applied DC voltages to determine how E_x changes with the DC electric field. The effect is found to be small compared to other nonlinear effects (~5%), and is neglected from further investigation. Also in Appendix E, analytical and finite element models are developed to predict the stiffness parameters and coefficients of thermal expansion of the MFC as a function of temperature from 0 to 250°C. While this range is well beyond that of current generation MFCs, important effects are noted for future actuators employing high temperature epoxy matrix systems. Appendix F presents the

Mathematica code developed for the sensitivity analysis contained in Chapter 4. For the case of nonzero constant mechanical loads, Appendix G has tabulated piezoelectric coefficients and peak-to-peak actuation strain values, while Appendix H gives the measured f_M and f_{Mm} values for the reference MFC for use in the classical Preisach model.

Chapter 2

Linear Constitutive Behavior of the Macro Fiber Composite under Short-Circuit Boundary Conditions

2.1 Introduction:

Chapter 1 discusses the concept of composite actuators that employ piezoceramic fibers and interdigitated electrodes. The history of these devices is discussed so that advancements in the technology are clear and naturally lead into the development of the Macro Fiber Composite actuator. With its benefits over other available devices established, this chapter focuses on the next step in the performance characterization: to determine the mechanical properties of the MFC under short-circuit conditions, as required by the compliance tensor, s^E, in Equation 1.1. While such short-circuit properties are a good baseline for model development and comparison with other types of actuators, the inherent assumption is that they do not vary with electric field. As will be discussed in more detail in Appendix E, voltage-independent properties are a reasonable presumption for the current characterization effort. This chapter considers the MFC as a sandwich of various isotropic and orthotropic layers, and then uses micromechanical equations for fiber-reinforced composites, derived in Appendix A, to

represent these laminae. Classical lamination theory is then used to combine these layers mathematically, from which, the effective engineering stiffness properties of the MFC are extracted.

2.2 The MFC – A Hybrid Laminate:

Since the MFC is composed of both isotropic and orthotropic layers, it is most adequately represented as a symmetric, hybrid, cross-ply laminate, or $[Iso_{Kapton}/Iso_{acrylic}/90°_{copper}/\overline{0}°_{PZT}]_S$. Using standard *x-y* notation for the geometric coordinate system of a laminated plate [Hyer, 1998], the overall mechanical behavior of this orthotropic laminate is fully described by four independent short-circuit stiffness quantities, E_x, E_y, ν_{xy}, and G_{xy}, where ν_{xy} represents the major Poisson's ratio. The first step in this modeling approach is to obtain expressions for the engineering constants for the various layers. Figure 2.1 shows the symmetric lamination scheme for the MFC, consisting of isotropic Kapton® and acrylic layers as well as orthotropic copper/epoxy and PZT/epoxy layers. It should be noted that all of the fibers are rectangular in cross section, perfectly aligned and uniformly spaced with the PZT fibers perpendicular to the copper electrodes.

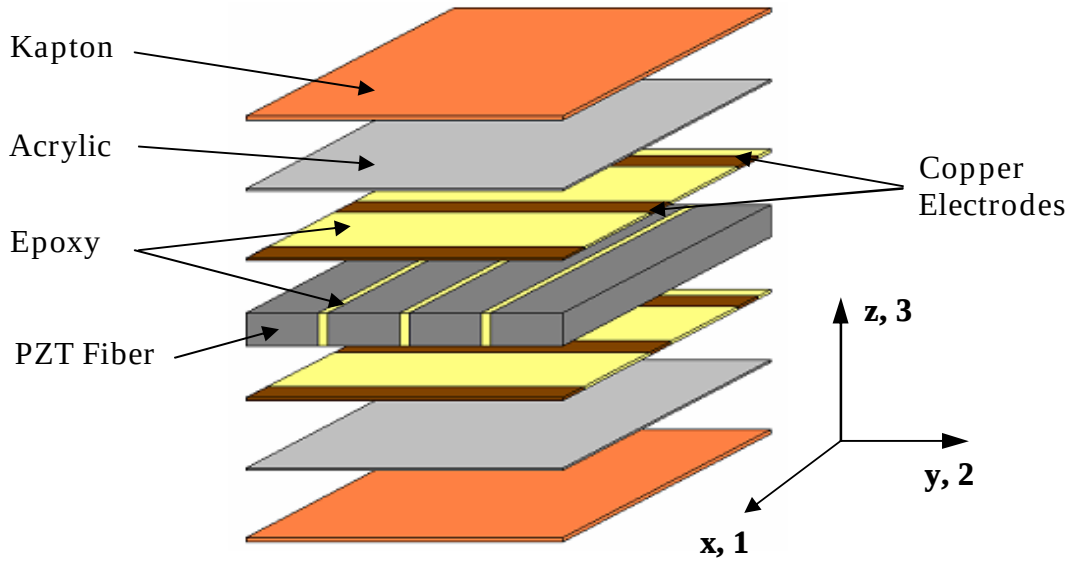

Figure 2.1: Exploded View of MFC Layers with Geometric (*x-y-z*) and Principal Material (1-2-3) Coordinate Systems

It should be noted at this point, that the epoxy and copper material is considered to be isotropic. However, the poling of the PZT material establishes a directional-dependence within the piezoceramic, thus these fibers are transversely isotropic, with the properties along the fiber differing from those in the transverse plane.

2.2.1 Isotropic Layers:

For isotropic materials, there are only two independent material properties, the elastic modulus E and Poisson's ratio ν. A third useful, yet non-independent stiffness, G (shear modulus), can be found using Equation 2.1.

$$G = \frac{E}{2(1+\nu)} \tag{2.1}$$

Since the MFC is a thin, planar actuation device, it will be considered to be in a state of plane stress, that is, out-of-plane normal and transverse shear stresses are all considered to be zero. In this case, for an isotropic layer in an orthogonal 1-2 coordinate system, the strains are simply the compliance matrix, *[S]*, times the stress vector, or

$$\begin{bmatrix} \varepsilon_1 \\ \varepsilon_2 \\ \gamma_{12} \end{bmatrix} = \begin{bmatrix} S_{11} & S_{12} & 0 \\ S_{12} & S_{11} & 0 \\ 0 & 0 & 2(S_{11} - S_{12}) \end{bmatrix} \begin{bmatrix} \sigma_1 \\ \sigma_2 \\ \tau_{12} \end{bmatrix} \tag{2.2}$$

Here, the normal strains are ε, normal stresses σ, shear strain γ, and shear stress τ, while

$$S_{11} = \frac{1}{E} \quad and \quad S_{12} = -\frac{\nu}{E} \tag{2.3}$$

2.2.2 Orthotropic Layers:

For the MFC, there are two types of orthotropic layers, copper/epoxy and PZT/epoxy. While each of these three materials is considered to be isotropic by itself (or transversely

isotropic in the case of the poled PZT), when fabricated into a fiber-reinforced lamina, the resulting composite behaves in an orthotropic manner, that is, having three mutually orthogonal planes of material property symmetry. Such materials are fully described by four independent material properties, E_1, E_2, G_{12}, and ν_{12} where the 1-2 coordinate system corresponds to the principal material axes as seen in Figure 2.2.

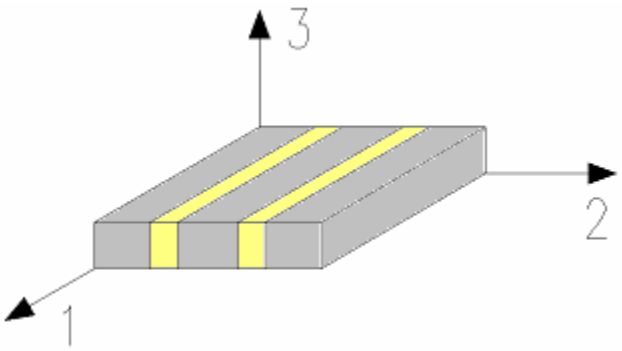

Figure 2.2: Principal Material Coordinate System of an Orthotropic Lamina

When such an orthogonal material is subjected to a state of plane stress, the in-plane strains are again equal to the compliance matrix, *[S]*, times the stress vector, or

$$\begin{bmatrix} \varepsilon_1 \\ \varepsilon_2 \\ \gamma_{12} \end{bmatrix} = \begin{bmatrix} S_{11} & S_{12} & 0 \\ S_{12} & S_{22} & 0 \\ 0 & 0 & S_{66} \end{bmatrix} \begin{bmatrix} \sigma_1 \\ \sigma_2 \\ \tau_{12} \end{bmatrix} \tag{2.4}$$

where the compliance terms can be written in terms of the engineering constants as

$$S_{11} = \frac{1}{E_1} \quad S_{12} = -\frac{\nu_{12}}{E_1} = -\frac{\nu_{21}}{E_2} \quad S_{22} = \frac{1}{E_2} \quad \textit{and} \quad S_{66} = \frac{1}{G_{12}} \tag{2.5}$$

2.2.2.1 Volume Fractions:

In order to utilize this macromechanical strain-stress relationship for the orthotropic layers, one must obtain the required engineering constants prescribed in Equation 2.5.

These properties for each lamina are formulated from a micromechanics approach based on the properties and relative amounts of each constituent material. The first step in a micromechanical analysis is to determine the volume fraction of each material. It is assumed that each orthotropic layer consists of either fibrous or matrix material, so that the sum of their volume fractions is equal to unity, or

$$V_f + V_m = 1 \tag{2.6}$$

where V is the volume fraction and the subscripts *f* and *m* refer to fiber and matrix material properties, respectively. The fiber volume fractions are easily calculated by considering an end view of the fibers, as seen in Figure 2.3, and applying Equation 2.7:

$$V_f = \frac{Fiber\ Area}{Fiber\ Area + Adjacent\ Matrix\ Area} \tag{2.7}$$

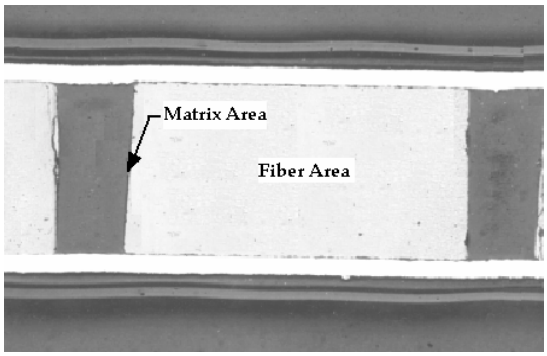

Figure 2.3: End View of PZT Fibers

The same approach is applied to the copper/epoxy layer, which also has rectangular cross-section fibers.

2.2.2.2 Rule-of-Mixtures Formulae for Orthotropic Layers:

Once the volume fractions of the fiber and matrix for an orthotropic layer are known, micromechanical equations are used to calculate the four engineering properties

required for Equation 2.5. While the micromechanics of predicting these properties for fiber-reinforced laminae is a science in and of itself, the current effort uses the simple, well-known rule-of-mixtures formulae. These formulae are straightforward to derive, as shown in Appendix A, using a mechanics-of-materials approach along with a set of simplifying assumptions. They are also widely available in all composites texts, such as Jones [1999] and Hyer [1998]. They are widely accepted to produce highly accurate predictions for E_1 and ν_{12} regardless of the fiber geometry or packing arrangement. However, these rule-of-mixtures formulations give a lower bound for values of E_2 and G_{12} [Jones, 1999] As a result, a great deal of the literature pertaining to composite materials focuses on more accurate models to predict these two properties, including exact elasticity solutions, numerical elasticity solutions, and finite element analyses [Hyer, 1998]. While these methods produce more accurate predictions of material properties in some cases, they are much more complicated to derive and implement, and oftentimes are only applicable to certain fiber packing arrangements (i.e. rectangular or hexagonal), certain ranges of volume fractions, limited by other specific simplifying assumptions or semi-empirical requiring experimental data collection for parameters such as stress-partitioning factors for a specific geometry.

For the current effort, the use of more complex formulae for E_2 and G_{12} was investigated initially. However, the rule-of-mixtures formulae were found to predict these properties with reasonable accuracy for a single row of uniformly spaced, rectangular cross-section fibers, as this geometry is physically a close representation of the lower bound predicted by such equations.

Having justified the use of the rule-of-mixture formulae, all four desired engineering properties can now be calculated using Equations (2.8) through (2.11). Note that these expressions are written to accommodate the transversely isotropic nature of the PZT fibers. However, the equations are fully applicable to the laminae containing isotropic copper fibers by simply omitting the directional superscript on the fiber properties.

The fiber-direction modulus, E_1, of the orthotropic PZT/epoxy and copper/epoxy layers of the MFC, is calculated as

$$E_1 = \mathrm{V}_f E_f^1 + \mathrm{V}_m E_m \tag{2.8}$$

where E_m is the elastic modulus of the matrix and E_f^1 is the elastic modulus of the fiber in the 1-direction. Next, the modulus of the lamina transverse to the fibers, E_2, is

$$E_2 = \frac{E_f^2 E_m}{V_m E_f^2 + V_f E_m} \tag{2.9}$$

where E_f^2 is the modulus of the fiber in the 2-direction. Now the major Poisson's ratio for each orthotropic layer, ν_{12}, is calculated as

$$\nu_{12} = \mathrm{V}_f \nu_f^{12} + \mathrm{V}_m \nu_m \tag{2.10}$$

where ν_f^{12} is the Poisson's ratio of the transversely isotropic PZT fiber relating strains induced in the 2-directions to those applied in the 1-direction of the fiber. Lastly, the in-plane shear modulus, G_{12}, is

$$G_{12} = \frac{G_f^{12} G_m}{V_m G_f^{12} + V_f G_m} \tag{2.11}$$

where G_f^{12} is the shear modulus in the 1-2 plane of the of the fiber.

At this point, it is possible to obtain all of the engineering properties required to fully populate the compliance matrices for both the isotropic and orthotropic laminae, as

specified in Equations (2.2-2.3) and (2.4-2.5). With these compliance matrices in hand, it is possible to use classical lamination theory to combine the mechanical effects of these layers when they are laminated together in the order specified in Figure 2.1.

2.3 Classical Lamination Theory

Now that apparent engineering constants are known for each lamina, the thickness geometry of the laminate must be quantified, as illustrated in Figure 2.4.

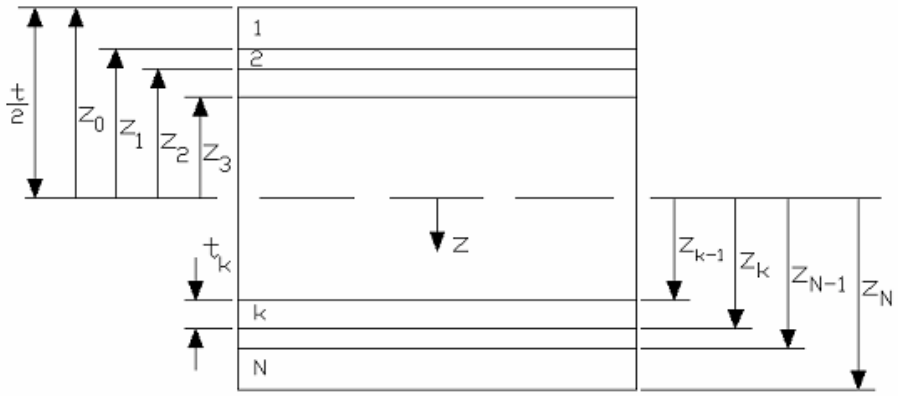

Figure 2.4: Thickness Geometry of an *N*-Layered Laminate

Numerical *z*-values can be obtained using the layer thicknesses corresponding to the lay-up seen in Figure 2.4. To simplify the current analysis, the central PZT/epoxy layer is considered as two individual laminae, with each having a thickness equal to half of the original lamina. Also, as seen in Figure 2.1, the 1-2 principal materials of the PZT/epoxy layer are coincident with the *x*-*y* geometric coordinates, while the copper/epoxy layer is rotated 90° in-plane. However, as will be investigated in Chapter 3, these coordinate systems are not necessarily always aligned. That is, the PZT fibers may be aligned at some intermediate angle, θ, as defined in Figure 2.5. However, no matter the orientation of the PZT fibers, the copper electrodes must always remain perpendicular to the piezoceramic in order to apply the most effective, in-plane electrical field when the MFC is used as an active device.

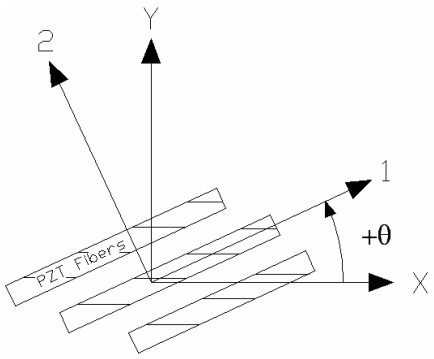

Figure 2.5: Positive Rotation of Principal Material Coordinate System

With the thickness and lamination angle geometry now quantified, and values of the required engineering constants in hand, the compliance and reduced stiffness matrices for each layer, [*S*] and [*Q*], respectively, are calculated. The form of the compliance matrix for an isotropic layer is found in Equation 2.2, while the individual compliance terms are specified in Equation 2.3 in terms of the engineering material properties. Likewise, the terms for the compliance matrix for the orthotropic layers given in Equation 2.4 are defined in Equation 2.5. The transformed reduced stiffness matrix for any k^{th} lamina under plane stress conditions is the inverse of the compliance matrix, or

$$[Q]_k = [S]_k^{-1} \tag{2.12}$$

The use of the *k* subscript is used to not only denote a layer number, but also to allow each layer to have a uniquely determined compliance matrix.

At this point, the compliance ([*S*]) and reduced stiffness ([*Q*]) matrices for each lamina are known. Next, each reduced stiffness matrix must be rotated to account for an arbitrary PZT lamination angle. For the isotropic layers, θ is always zero, and when the 1-2 principal material coordinate system of the PZT fiber layer is aligned with the *x*-*y* geometric coordinate system as depicted in Figure 2.1, θ_{PZT} is zero, while θ_{copper} is 90°. This rotation results in transformed reduced stiffness matrices, $\overline{Q}_{ij}$:

$$\left[\overline{Q}\right]_k = \left[T\right]_k^{-1}\left[Q\right]_k \left[T\right]_k^{-T} \tag{2.13}$$

where the transformation matrix is given as

$$\left[T\right]_k = \begin{bmatrix} \cos^2\theta & \sin^2\theta & 2\sin\theta\cos\theta \\ \sin^2\theta & \cos^2\theta & -2\sin\theta\cos\theta \\ -\sin\theta\cos\theta & \sin\theta\cos\theta & \cos^2\theta - \sin^2\theta \end{bmatrix} \tag{2.14}$$

In order to ensure that this model is applicable to any PZT lamination angle, Equation 2.8 should be used to calculate a transformed reduced stiffness matrix for all layers, regardless of the material or lamination angle. This transformation will ensure that the layer-wise material properties are aligned with the *x*-*y* geometric material coordinates system.

Next, the constitutive relationship for the k^{th} lamina in a state of plane stress in the *x*-*y* planar coordinate system is given as

$$\begin{bmatrix} \sigma_x \\ \sigma_y \\ \tau_{xy} \end{bmatrix}_k = \begin{bmatrix} \overline{Q}_{11} & \overline{Q}_{12} & \overline{Q}_{16} \\ \overline{Q}_{12} & \overline{Q}_{22} & \overline{Q}_{26} \\ \overline{Q}_{16} & \overline{Q}_{26} & \overline{Q}_{66} \end{bmatrix}_k \begin{bmatrix} \varepsilon_x \\ \varepsilon_y \\ \gamma_{xy} \end{bmatrix}_k \tag{2.15}$$

Up until this point, the mechanics of each lamina has been considered separately from the other laminae. From this point forward, all of the layers shall be considered as a laminate consisting of many laminae perfectly bonded together, where the bonds are infinitely thin and non-shear-deformable so that the displacements are continuous across lamina boundaries so that the laminae cannot move relative to one another [Jones, 1999]. For a thin laminate such as the MFC actuator, a group of appropriate

simplifying assumptions, known as the Kirchhoff hypothesis, is adopted. That is, a line that is initially straight and perpendicular to the midplane of the laminate, i.e. a "normal," remains straight and perpendicular throughout the deformation of the laminate, and does not change length. Mathematically, these restrictions render the transverse shear strains, γ_{xz} and γ_{yz}, and the out-of plane normal strain, ε_z, zero. Additionally, for linear-elastic behavior, the Kirchhoff hypothesis can be shown to require the strain of the laminate to vary linearly through the thickness (z-direction) [Jones, 1999]. That is,

$$\begin{bmatrix} \varepsilon_x \\ \varepsilon_y \\ \gamma_{xy} \end{bmatrix} = \begin{bmatrix} \varepsilon_x^\circ \\ \varepsilon_y^\circ \\ \gamma_{xy}^\circ \end{bmatrix} + z \begin{bmatrix} \kappa_x \\ \kappa_y \\ \kappa_{xy} \end{bmatrix} \tag{2.16}$$

where the naught superscript indicate mid-plane strains of the laminate, κ represents the mid-plane curvatures, and z is the thickness coordinate defined in Figure 2.4. Now, the stress-strain relationship for each layer, Equation 2.15, is rewritten in terms of the laminate mid-plane strains and curvatures through substitution of Equation 2.16:

$$\begin{bmatrix} \sigma_x \\ \sigma_y \\ \tau_{xy} \end{bmatrix}_k = \begin{bmatrix} \overline{Q}_{11} & \overline{Q}_{12} & \overline{Q}_{16} \\ \overline{Q}_{12} & \overline{Q}_{22} & \overline{Q}_{26} \\ \overline{Q}_{16} & \overline{Q}_{26} & \overline{Q}_{66} \end{bmatrix}_k \left[\begin{bmatrix} \varepsilon_x^\circ \\ \varepsilon_y^\circ \\ \gamma_{xy}^\circ \end{bmatrix} + z \begin{bmatrix} \kappa_x \\ \kappa_y \\ \kappa_{xy} \end{bmatrix} \right] \tag{2.17}$$

This equation represents a 3D loading system consisting of N bonded layers having a stress-strain relationship that varies with the thickness coordinate, z. An equivalent 2D representation of this loading scenario consists of resultant force per unit lengths ([N]) and moments per unit length ([M]), which are obtained by integrating the stresses in each layer through the laminate thickness.

$$\begin{bmatrix} N_x \\ N_y \\ N_{xy} \end{bmatrix} = \int_{-t/2}^{t/2} \begin{bmatrix} \sigma_x \\ \sigma_y \\ \tau_{xy} \end{bmatrix} dz \quad and \quad \begin{bmatrix} M_x \\ M_y \\ M_{xy} \end{bmatrix} = \int_{-t/2}^{t/2} \begin{bmatrix} \sigma_x \\ \sigma_y \\ \tau_{xy} \end{bmatrix} z\, dz \tag{2.18}$$

Here, the stresses are those for the entire laminate. However, from Equation 2.17, since each layer can have a different transformed reduced stiffness matrix, the stresses can vary from layer to layer. Thus, the stresses must be integrated over the thickness of each individual lamina, and then added together. Hence,

$$\begin{bmatrix} N_x \\ N_y \\ N_{xy} \end{bmatrix} = \sum_{k=1}^{N} \int_{z_{k-1}}^{z_k} \begin{bmatrix} \sigma_x \\ \sigma_y \\ \tau_{xy} \end{bmatrix}_k dz \quad and \quad \begin{bmatrix} M_x \\ M_y \\ M_{xy} \end{bmatrix} = \sum_{k=1}^{N} \int_{z_{k-1}}^{z_k} \begin{bmatrix} \sigma_x \\ \sigma_y \\ \tau_{xy} \end{bmatrix}_k z\, dz \tag{2.19}$$

Now, the stress-strain relationship for each k^{th} layer from Equation 2.17 can be substituted into Equation 2.19. For the case when the transformed reduced stiffness matrix is constant throughout the thickness of each respective laminae, the resultant force and moments per unit length from Equation 2.19 become

$$\begin{bmatrix} N_x \\ N_y \\ N_{xy} \end{bmatrix} = \sum_{k=1}^{N} \begin{bmatrix} \overline{Q}_{11} & \overline{Q}_{12} & \overline{Q}_{16} \\ \overline{Q}_{12} & \overline{Q}_{22} & \overline{Q}_{26} \\ \overline{Q}_{16} & \overline{Q}_{26} & \overline{Q}_{66} \end{bmatrix}_k \int_{z_{k-1}}^{z_k} \begin{bmatrix} \varepsilon_x^\circ \\ \varepsilon_y^\circ \\ \gamma_{xy}^\circ \end{bmatrix} dz + \begin{bmatrix} \kappa_x \\ \kappa_y \\ \kappa_{xy} \end{bmatrix} z dz \tag{2.20}$$

and

$$\begin{bmatrix} M_x \\ M_y \\ M_{xy} \end{bmatrix} = \sum_{k=1}^{N} \begin{bmatrix} \overline{Q}_{11} & \overline{Q}_{12} & \overline{Q}_{16} \\ \overline{Q}_{12} & \overline{Q}_{22} & \overline{Q}_{26} \\ \overline{Q}_{16} & \overline{Q}_{26} & \overline{Q}_{66} \end{bmatrix}_k \int_{z_{k-1}}^{z_k} \begin{bmatrix} \varepsilon_x^\circ \\ \varepsilon_y^\circ \\ \gamma_{xy}^\circ \end{bmatrix} z dz + \begin{bmatrix} \kappa_x \\ \kappa_y \\ \kappa_{xy} \end{bmatrix} z^2 dz \tag{2.21}$$

Now, noting that the mid-plane strains and curvatures can be removed from the summations as they are not functions of the thickness coordinate *z*, the integrations can be easily performed, which results in

$$\begin{bmatrix} N_x \\ N_y \\ N_{xy} \end{bmatrix} = \begin{bmatrix} A_{11} & A_{12} & A_{16} \\ A_{12} & A_{22} & A_{26} \\ A_{16} & A_{26} & A_{66} \end{bmatrix} \begin{bmatrix} \varepsilon_x^\circ \\ \varepsilon_y^\circ \\ \gamma_{xy}^\circ \end{bmatrix} + \begin{bmatrix} B_{11} & B_{12} & B_{16} \\ B_{12} & B_{22} & B_{26} \\ B_{16} & B_{26} & B_{66} \end{bmatrix} \begin{bmatrix} \kappa_x \\ \kappa_y \\ \kappa_{xy} \end{bmatrix} \tag{2.22}$$

and

$$\begin{bmatrix} M_x \\ M_y \\ M_{xy} \end{bmatrix} = \begin{bmatrix} B_{11} & B_{12} & B_{16} \\ B_{12} & B_{22} & B_{26} \\ B_{16} & B_{26} & B_{66} \end{bmatrix} \begin{bmatrix} \varepsilon_x^\circ \\ \varepsilon_y^\circ \\ \gamma_{xy}^\circ \end{bmatrix} + \begin{bmatrix} D_{11} & D_{12} & D_{16} \\ D_{12} & D_{22} & D_{26} \\ D_{16} & D_{26} & D_{66} \end{bmatrix} \begin{bmatrix} \kappa_x \\ \kappa_y \\ \kappa_{xy} \end{bmatrix} \tag{2.23}$$

where the integration of the transformed reduced stiffnesses gives the following extensional, bending-extension coupling and bending stiffness matrices, respectively:

$$\begin{aligned} A_{ij} &= \sum_{k=1}^{N} \left(\overline{Q}_{ij}\right)_k \left(z_k - z_{k-1}\right) \\ B_{ij} &= \frac{1}{2} \sum_{k=1}^{N} \left(\overline{Q}_{ij}\right)_k \left(z_k^2 - z_{k-1}^2\right) \\ D_{ij} &= \frac{1}{3} \sum_{k=1}^{N} \left(\overline{Q}_{ij}\right)_k \left(z_k^3 - z_{k-1}^3\right) \end{aligned} \tag{2.24}$$

In Equation 2.24, A_{ij} is thein-plane extensional stiffness matrix, B_{ij} is the bending-extension coupling stiffness matrix, and D_{ij} is the bending stiffness matrix. While Equations 2.23 and 2.24 contain many terms, the specific geometry of the MFC render many of these terms zero. Specifically, since the MFC actuator is a symmetric laminate, the bending-extension coupling matrix is equal to zero. Furthermore, when the PZT fibers are aligned with the *x*-*y* geometric coordinates (the most common configuration),

the MFC is a cross-ply laminate, which exhibits neither shear-extension coupling nor bend-twist coupling. Thus, A_{16}, A_{26}, D_{16}, and D_{26} are also identically zero for such a cross-ply laminate. However, the principal material coordinates of the PZT layer are not necessarily aligned with the geometric coordinates, as will be seen in Chapter 3.

Such a thorough derivation of these stiffness matrices has been presented as they all could be important depending on the type of problem to be solved. For example, the bending stiffness matrix is critical if the MFC is to be included as an active layer in a laminate or used in a standard piezoceramic "bender" application. However, at this point, it is desired to use A_{ij} to obtain the apparent engineering constants for the MFC laminate in the case where the PZT fibers are aligned with the *x*-*y* geometric coordinates. For this case, the in-plane stiffness matrix has the form

$$A_{ij} = \begin{bmatrix} A_{11} & A_{12} & 0 \\ A_{12} & A_{22} & 0 \\ 0 & 0 & A_{66} \end{bmatrix} \tag{2.25}$$

The inverse of A_{ij} is the 2D analogy of the compliance matrix S_{ij} from Equation 2.4; that is, A_{ij} has had the thickness of the laminate removed by way of the integration performed in Equations 2.20 and 2.21. This so called in-plane compliance matrix, a_{ij}, has the form

$$a_{ij} = \begin{bmatrix} \dfrac{A_{22}}{A_{11}A_{22} - A_{12}^2} & \dfrac{-A_{12}}{A_{11}A_{22} - A_{12}^2} & 0 \\ \dfrac{-A_{12}}{A_{11}A_{22} - A_{12}^2} & \dfrac{A_{11}}{A_{11}A_{22} - A_{12}^2} & 0 \\ 0 & 0 & \dfrac{1}{A_{66}} \end{bmatrix} \tag{2.26}$$

Using the definitions for the components of the compliance matrix in Equation 2.5, and multiplying through Equation 2.26 by the total thickness of the laminate yields

$$\begin{bmatrix} \dfrac{t_{LAM}A_{22}}{A_{11}A_{22}-A_{12}^2} & \dfrac{-t_{LAM}A_{12}}{A_{11}A_{22}-A_{12}^2} & 0 \\ \dfrac{-t_{LAM}A_{12}}{A_{11}A_{22}-A_{12}^2} & \dfrac{t_{LAM}A_{11}}{A_{11}A_{22}-A_{12}^2} & 0 \\ 0 & 0 & \dfrac{t_{LAM}}{A_{66}} \end{bmatrix} = \begin{bmatrix} \dfrac{1}{E_x^{LAM}} & -\dfrac{\nu_{12}}{E_x^{LAM}} & 0 \\ -\dfrac{\nu_{12}}{E_x^{LAM}} & \dfrac{1}{E_y^{LAM}} & 0 \\ 0 & 0 & \dfrac{1}{G_{xy}^{LAM}} \end{bmatrix} \tag{2.27}$$

The four independent apparent engineering stiffness properties of the laminate are now readily calculated from Equation 2.27. Thus, for the MFC

$$E_x^{MFC} = \frac{A_{11}A_{22}-A_{12}^2}{t_{MFC}A_{22}} \qquad \nu_{xy}^{MFC} = \frac{A_{12}}{A_{22}}$$

$$E_y^{MFC} = \frac{A_{11}A_{22}-A_{12}^2}{t_{MFC}A_{11}} \qquad G_{xy}^{MFC} = \frac{A_{66}}{t_{MFC}} \tag{2.28}$$

2.4 Material and Geometric Properties:

In order to obtain numerical results for the models developed in this chapter, a set of material and geometric properties is required. The properties for the various constituent materials are obtained from the material suppliers and handbooks as indicated in Tables 2.1 and 2.2. It should be noted that for the PZT fiber material, the short-circuit values for the material properties are given. However, these models are applicable for predicting the effective stiffness properties under any electrical boundary conditions, depending on which set of material properties are used. Furthermore, the coordinate system for the PZT fibers is given in Figure 2.2, where the fibers are poled in the 1-direction, which is in contrast to standard piezoelectric notation but consistent with the standard notation for composite materials.

Table 2.1: Material Properties for MFC Constituent Materials

Property	Kapton[1]	Acrylic[2]	Copper[3]	Epoxy[4]
E, GPa	2.5	2.7	117.2	3.378
ν	0.34	0.35	0.31	0.27
G, GPa	0.93	1.0	44.7	1.33

[1][DuPont, 1996]
[2][Dowling, 1999]
[3][Callister, 1994]
[4][MatWeb, 2003]

Table 2.2: Short-Circuit Material Properties for Transversely Isotropic Poled PZT Fibers

Property[1]	Poled CTS 3195 HD PZT
$E_{1,}$ GPa	53
E_2, GPa	61
ν_{12}	0.384
ν_{23}	0.35
G_{12}, GPa	21
G_{23}, GPa	22.6

[1][Morgan Matroc, 1997]

Poling of the fibers makes them transversely isotropic, which means that the properties in the fiber direction are not necessarily the same as in the plane perpendicular to the poling direction. Thus, the elastic behavior of the fibers requires five independent material properties. In the table above, G_{23} and υ_{23} are not both independent, but rather related through

$$G_{23} = \frac{E_2}{2(1+\nu_{23})} \tag{2.29}$$

Despite the presence of these five independent properties, the MFC and PZT fibers are assumed to be in a state of plane stress, which considers the out-of-plane normal (σ_3)

and shear stresses (τ_{23} and τ_{13}) to be zero, thus υ_{23} and G_{23} are not required for a two-dimensional analysis.

The geometric parameters required for the model developed in this chapter are specified in Table 2.3 and 2.4 for the reference and standard MFC configurations.

Table 2.3: Geometric Properties for Reference MFC Configuration

Property	Kapton	Acrylic	Copper	PZT
Thickness, mm (in)	0.0254 (0.001)	0.0127 (0.0005)	0.01778 (0.0007)	0.1905 (0.0075)
Fiber Width, mm (in)	N / A	N / A	0.127 (0.005)	0.381 (0.015)
Fiber Spacing, mm (in)	N / A	N / A	0.5334 (0.021)	0.4318 (0.017)
Kerf Width, mm (in)	N / A	N / A	0.4064 (0.016)	0.0508 (0.002)

Table 2.4: Geometric Properties for Standard MFC Configuration

Property	Kapton	Acrylic	Copper	PZT
Thickness, mm (in)	0.0254 (0.001)	0.0127 (0.0005)	0.01778 (0.0007)	0.1778 (0.007)
Fiber Width, mm (in)	N / A	N / A	0.1016 (0.004)	0.3556 (0.014)
Fiber Spacing, mm (in)	N / A	N / A	0.5334 (0.021)	0.4318 (0.017)
Kerf Width, mm (in)	N / A	N / A	0.4318 (0.017)	0.0762 (0.003)

As will be seen in Chapter 3 and beyond, the "reference" configuration, also referred to as the "tensile test" geometry, is the one fabricated for the experimental work contained herein and shown in Figures 1.2 and 1.3. Its purpose was strictly for measurement of material properties and model verification. However, the "standard" configuration is the one commonly available commercially and from NASA Langley, and is intended for actual intelligent structure applications.

2.5 Results of Classical Lamination Theory Model:

Due to the involved nature of the classical lamination model developed in this chapter for use with the MFC, a *Mathematica* code was written to perform the required calculations. This code is included as Appendix B. The output of this code, amongst other parameters, are the four desired effective, independent, short-circuit linear-elastic engineering constants for the MFC. The model was applied to both the reference and standard geometric configurations, and the predicted results are presented below in Table 2.5.

Table 2.5: Effective Linear-Elastic Engineering Constants for Reference and Standard MFC Configurations

Effective Property	Geometric Configuration	
	Reference	Standard
$E_{x,}$ GPa	31.2	28.6
E_y, GPa	17.05	13.14
ν_{xy}	0.303	0.29
G_{xy}, GPa	5.27	4.02

2.6 Summary:

This chapter develops a model for fiber-reinforced composite laminates to predict the effective engineering properties of the MFC actuator under short-circuit (constant field) electrical boundary conditions. The required properties for the constituent materials that comprise the MFC are presented, as obtained from material suppliers and handbooks. Also, the geometric properties of the standard and reference MFC configurations are specified. The aforementioned models are then used with the material and geometric properties to predict the desired effective engineering properties for each configuration of the MFC. Chapter 3 uses an experimental approach to verify the models developed in this chapter.

Chapter 3

Nonlinear Constitutive Behavior of the Macro Fiber Composite under Short-Circuit Boundary Conditions

3.1 Introduction:

Chapter 2 uses rule-of-mixtures formulae to represent the orthotropic laminae of the MFC actuator. These layers, along with the isotropic ones are combined using a classical lamination approach, and the effective orthotropic engineering properties, E_x, E_y, υ_{xy}, and G_{xy}, of the MFC under short-circuit conditions are predicted for linear-elastic behavior. The focus of this chapter is twofold: to verify the model and predicted linear-elastic constants developed in Chapter 2 and to measure and quantify the nonlinear mechanical behavior of the MFC. Since the MFC is an actuator that is capable of inducing high free-strains (~2000 με, free-strain, peak-to-peak) and is often incorporated into structures that operate under large strains (i.e. helicopter rotor blades) [Cesnik and Shin, 2001], nonlinear behavior can become significant and must be somehow incorporated into high fidelity structural actuation model. While the goals of the experimental work in this chapter are twofold, all of the desired measurements are extracted from the same set of experimental procedures discussed herein.

3.2 Background on Mechanical Testing of Composites:

This chapter deals with the tensile testing of the MFC under short-circuit boundary conditions; therefore, it is important to discuss the relevant literature devoted to the mechanical testing of composites. This field is governed in general by two ASTM standards. D 3039/D 3039M-00 specified testing and data analysis methodology required to accurately obtain tensile moduli and Poisson's ratios. Testing details included specimen and tab geometry, strain gage placement, and failure modes. In addition, data analysis schemes were specified for adjusting strains as to remove noisy data near the beginning of the test, calculating stresses, and slopes required for the desired material properties. ASTM Standard D 3518/D 3518M-94 dealt specifically with measuring the in-plane shear behavior of a fiber-reinforced composite lamina, as this topic was omitted from D 3039/D 3039M-00. The theory behind testing a ±45° laminate to measure shear behavior was presented, along with the preferred ply stacking sequence ($[45°/-45°]_{nS}$, where *n=4, 5* or *6* for unidirectional laminae), and specimen and tab geometry. Formulas for calculating stresses, various in-plane shear moduli and maximum stress/strain values were provided. However, this testing procedure under-predicted the shear strength, as the gage section was not in a state of pure shear, as an in-plane normal stress was present and an even more complex stress was present at the specimen edges the specimen. This ASTM Standard arose from the work on ±45° laminates presented in [Petit, 1969], and which proposed the use of such a stacking sequence, and was later examined experimentally by Rosen [1972]. The notion of measuring shear strain in an isotropic material using a specific arrangement of strain gages and circuitry was proposed by Perry [1969].

While the ASTM standard D 3518/D 3518M-94 is the industry standard for measuring shear behavior of unidirectional laminae, it is not always practical to test a laminate consisting of 16 to 20 plies, particularly with piezoelectric devices like the AFC or MFC, which are not readily available in mass quantities. Therefore, other researchers have developed tensile testing procedures that offer an accurate indication of shear behavior

for a single ply. Chamis and Sinclair [1977] proposed the off-axis tensile test, where the load was applied to the specimen at some intermediate angle to the fiber direction. The exact test angle was determined to maximize the shear strain in the principal material coordinate system and varied based on the elastic properties of the specimen. Inherent to this calculation was having a good estimate of the stiffness properties, including the shear modulus that was the desired quantity to be measured. However, the developed shear strain was not highly sensitive to the chosen test angle, so estimates of properties from micromechanics formulations were typically sufficient. The resulting presumed state of stress for a unidirectional lamina was biaxial with in-plane shear. Using the laws of elasticity, and either a rectangular strain rosette (three gages oriented at 0°-45°-90°) or a 60° delta rosette, a shear stress-shear strain curve was measured using a standard tensile test procedure on the off-axis specimen. However, subjecting an off-axis specimen to a uniaxial load causes it to take on an S-shape. Since this type of deformation is restricted by the rigid mechanical grips used in the testing machine, some argued that this approach was inaccurate due to a non-uniform state of stress developed across the gage section.

Several solutions were offered to prevent restriction of end-rotation within the mechanical grips. First, Sun and Berreth [1988] demonstrated that using end-tabs consisting of a fiberglass knit in a silicon rubber matrix allowed the specimen to undergo shear while in the hydraulic grips, thus producing a uniform state of stress across the width of the specimen. Additionally, this method removed stress concentrations, thereby allowing the shear strength to be accurately measured. However, these tabs required special manufacturing steps, and could not apply the large loads often required at elevated temperatures. Therefore, Sun and Chung [1993] proposed a new oblique end-tab design that still produces a nearly uniform state of stress throughout the gage section. The aluminum tabs, which were considered rigid for analytical purposes and shown in Figure 3.1, were cut at an angle ϕ determined by

using constitutive and strain displacement relationships to ensure uniform displacement along the load-direction, X.

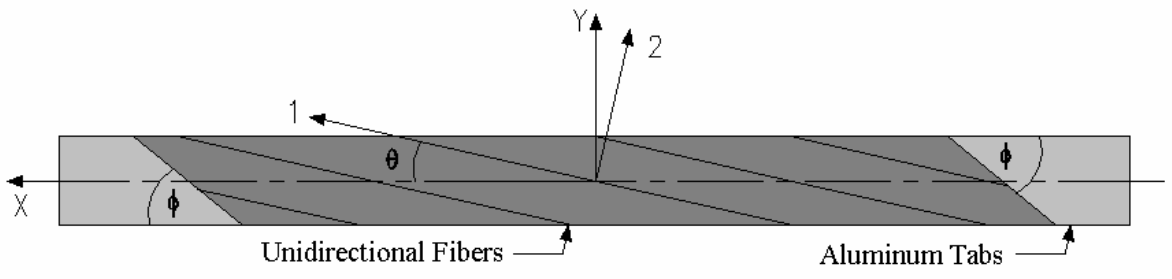

Figure 3.1: Off-Axis Test Specimens with Oblique Tabs

While each of the above approaches produced a roughly uniform state of stress across the specimen width, the method chosen for the current work was proposed by Pindera and Herakovich [1986]. He fabricated special grips, shown in Figure 3.2, with jaws that held the specimen firmly, but which were free to rotate about pivoted ends.

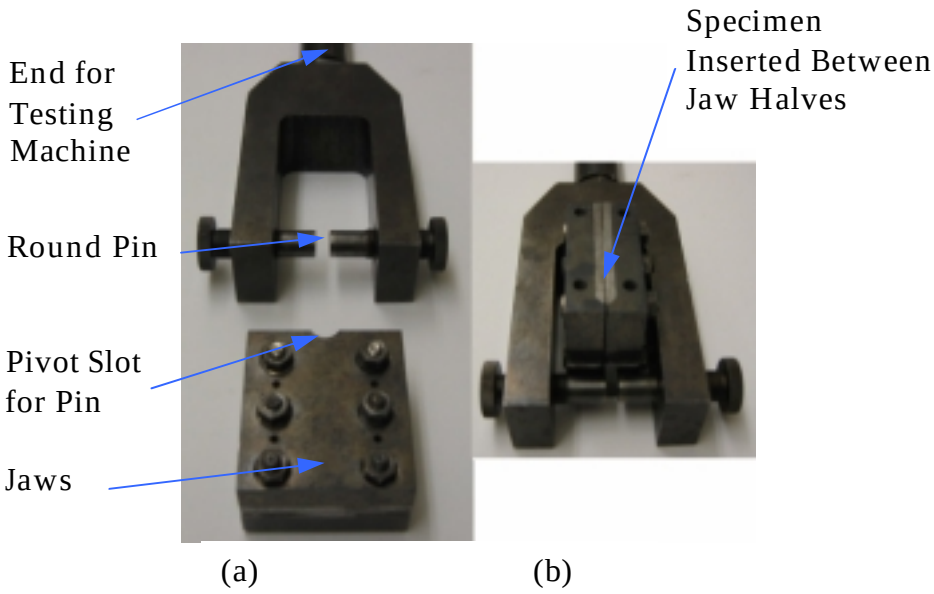

Figure 3.2: Pivoting Grips (a) Unassembled and (b) Assembled

When the off-axis specimen began to take on its deformed S-shape, the gripped ends were free to rotate about the round, lubricated pin. Thus, a uniform state of stress is promoted throughout the gage section, which allowed for accurate shear stress-shear strain behavior and shear strength values to be measured.

In addition to the aforementioned publications, a comprehensive handbook detailing the relevant mechanics of composites theory and lab procedures was given by Jenkins [1998]. The background on strain gage technology as it related to the testing of composites was of particular use to this effort.

A nonlinear investigation of the elastic-plastic behavior of unidirectional composites loaded in the fiber direction was performed by Lin, Salinas, and Ito [1971]. The analysis was based on special generalized plane strain conditions using finite elements and the Prandtl-Reuss incremental plasticity model. Boron fibers embedded in both aluminum and epoxy were modeled to illustrate how the behavior of the composite is related to that of the matrix. It was found that the ductile aluminum matrix allowed the composite to carry a slightly higher load up until the failure of the boron fibers, where as the boron/epoxy failed at a lower stress level. However, the ultimate tensile strength of the aluminum was about ten times greater than the epoxy; however, the boron/epoxy and boron/aluminum composite failed at roughly the same stress level (about 10% lower for the epoxy matrix). Therefore, it was noted that the ultimate tensile strength of a composite depended not only on the ultimate tensile strengths of the constituent materials, but also on their yield strength, elastic moduli, Poisson's ratio, and ductility.

A continuation of this work was presented by Zhong, Lin, and Lin [1998] where the nonlinear macroscopic stress-strain behavior of a cross-ply laminate subjected to non-proportional tensile and shear loads was predicted from a micromechanics approach. The composite material was represented as a homogeneous solid using Eshelby's

equivalent-inclusion method. The microstresses and strains were then investigated using Lin's method for elastically homogenous polycrystals, based on Green's functions of an infinite solid. The results were also useful in predicting the onset of global yielding of the composite, which was not caused by localized yielding, but rather, an average plastic strain sufficient to cause a global failure.

3.3 Experimental Procedure:

In order to characterize their tensile and shear constitutive behavior and mechanical properties, three sets of tensile test experiments were performed on MFC actuators. The first set was designed to measure the stress-strain behavior in the PZT fiber direction, while the second set captured such behavior transverse to these fibers. The third set measured the in-plane shear stress-shear strain performance. This section describes the design issues for the various types of specimens, briefly covers the manufacturing of these specimens, strain gage instrumentation, and finally Instron tensile-testing machine set-up and data acquisition.

3.3.1 Specimen Preparation:

While NASA Langley had manufactured a few different MFC geometries, most specimens were designed to be integrated into an intelligent structure. For the current effort, new specimen geometry is needed so that tensile-tests could be readily performed using standard universal testing machines. In addition, measuring the stress-strain in the PZT fiber direction, perpendicular to these fibers, and in-plane shear behavior required different specimens to be created. This section serves to address the issues involved with the design of all three types of specimens.

3.3.1.1 Design of PZT Fiber Direction (E_x) Specimens:

This specimen is intended to measure the mechanical behavior in the direction of the PZT fibers when they are aligned with the global *x*-*y* coordinates, as well as the major Poisson's ratio. The main issue with the design of these specimens was selecting a long,

slender active area (area containing copper electrodes)/gage section to minimize end effects associated with the mechanical grips. The selected active area dimensions are given in Table 3.1.

Table 3.1: MFC Experimental Specimen Dimensions

Specimen Type	Length, mm (in.)	Width, mm (in.)	Thickness, mm (in.)	Cross-Section Area, mm^2 ($in.^2$)
x-Direction Specimen	88.9 (3.5)	25.4 (1.0)	0.302 (0.0119)	7.67 (0.0119)
y-Direction Specimen	15.9 (0.625)	38.1 (1.5)	0.302 (0.0119)	11.5 (0.01785)
Shear Specimen	88.9 (3.5)	25.4 (1.0)	0.302 (0.0119)	7.67 (0.0119)

Furthermore, end-tabs are needed for loading into the grips. However, these tabs should contain the piezoelectric fibers, but not the interdigitated electrode pattern. These passive end-tabs are used to transfer the load uniformly through the gage section, while preventing the grips from damaging the "active area" and causing electrical failures of the specimen. Also, the power leads for the MFC must be out of the way of the tab and the gage sections, so that they can be connected to each other, thus ensuring the desired short-circuit electrical boundary condition. The selected "E_x Specimen" footprint is shown in Figure 3.3, where the PZT fibers are aligned in the *x*-direction and extend 25.4 mm (1.0 in.) past the active region in each direction.

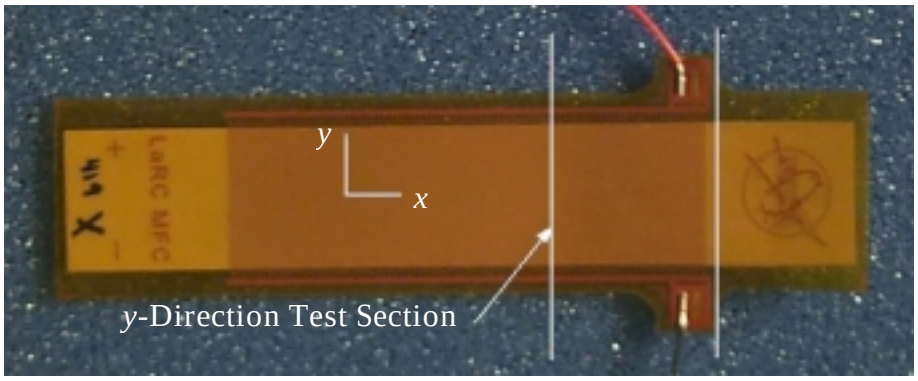

Figure 3.3: E_x – Specimen Footprint

3.3.1.2 Design of Electrode Direction (E_y) Specimens:

This specimen is intended to measure the mechanical behavior in the direction perpendicular to the PZT fibers when they are aligned with the global *x*-*y* coordinates. Since it is difficult and expensive to alter the orientation of the MFC electrode pattern, these "E_y-Specimens" are simply cut from the same type of specimens used to measure E_x, as illustrated in Figure 3.3. This particular region is selected because it contained only an active portion of the MFC, along with the solder tabs and leads which preserved the electrical connectivity of the device. Again, it is important to short-circuit the leads together so that the desired short-circuit properties are measured. Clearly, the E_y -specimen was much shorter than those used for the PZT fiber direction tests, and having enough area to fit into the grips while uniformly distributing the clamping pressure is an issue that was resolved by bonding fiberglass tabs onto the specimen using strain gage epoxy. The final E_y -specimen is shown in Figure 3.4.

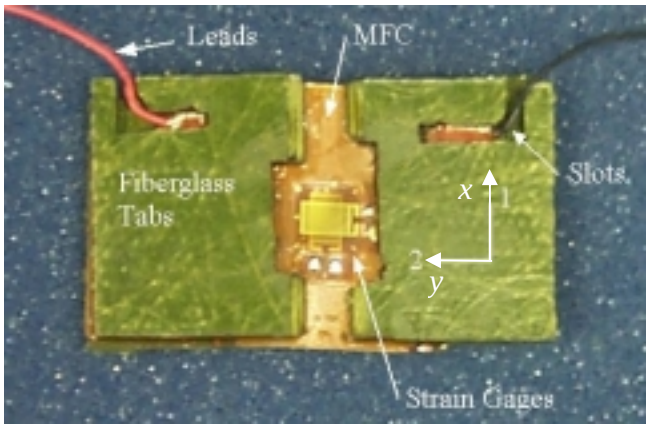

Figure 3.4: E_y -Specimen with Green Fiberglass Tabs

Fiberglass is chosen as its stiffness closely resembled the stiffness of the MFC in the *y*-direction, according to the values predicted in Chapter 2. The slots seen in Figure 3.4 are cut in order to allow the MFC leads to escape from the grips and be twisted together without damage so that the desired short-circuit properties were measured. However, the increased thickness of the specimen due to the tabs ultimately requires the use of

mechanical instead of pneumatic grips. The mechanical properties of the fiberglass tabs are given in Table 3.2.

Another implication of such a short gage length is the influence of end-effects associated with the rigid mechanical grips. It is decided that this length is sufficient for an *initial* measurement of E_y, although the grips are known to severely restrict the transverse deformation. The implications of this limitation are discussed in more detail in Section 3.5.1.4.

Table 3.2: Fiberglass Tab Mechanical Properties

Elastic Modulus, GPa	Poisson's Ratio	Shear Modulus, GPa
16	0.25	6.4

3.3.1.3 Design of Off-Axis (G_{xy}) Specimens:

As seen in the literature review above, there exist a variety of ways to measure the in-plane shear response of fiber-reinforced laminates. However, since MFCs are only available in limited quantities, the off-axis testing of a single layer proposed by Chamis and Sinclair [1977] was selected. They suggested that the load be applied at an angle between 0° and 90° to the fibers such that the in-plane shear strain is maximized. Chamis and Sinclair found that this optimum angle depends on the material properties of the laminate. Therefore, the predicted values for the orthotropic properties of the MFC from Chapter 2 are used in the subsequent analysis, where the MFC is considered to be a single orthotropic lamina where the 1-2 material coordinate system of the PZT fibers is to be rotated.

Consider an MFC having the *x*-*y* geometric coordinates and 1-2 principal material coordinates of the PZT fibers as seen in Figure 3.1 to be subjected to a unidirectional load in the *x*-direction. For the uniaxial stress, σ_x, developed in the geometric

coordinate system, the state of stress in the material coordinate system rotated by angle θ, is given as

$$\begin{bmatrix} \sigma_1 \\ \sigma_2 \\ \tau_{12} \end{bmatrix} = [T] \begin{bmatrix} \sigma_x \\ 0 \\ 0 \end{bmatrix} \tag{3.1}$$

where the transformation matrix, *[T]* is given by

$$[T] = \begin{bmatrix} \cos^2\theta & \sin^2\theta & 2\sin\theta\cos\theta \\ \sin^2\theta & \cos^2\theta & -2\sin\theta\cos\theta \\ -\sin\theta\cos\theta & \sin\theta\cos\theta & \cos^2\theta - \sin^2\theta \end{bmatrix} \tag{3.2}$$

The stresses calculated from Equation 3.1, normalized by σ_x, are plotted in Figure 3.5 for values of θ from 0° to 90°.

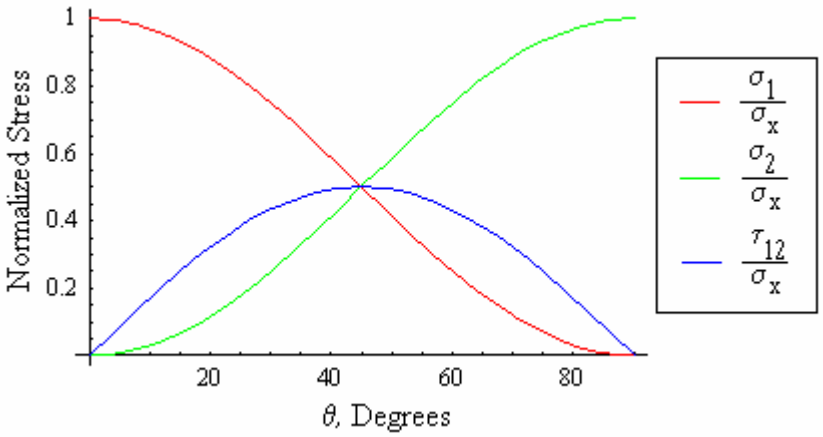

Figure 3.5: Normalized Stresses in the Material Coordinate System Caused by σ_x

Clearly, the maximum shear stress occurs at 45°, and is independent of material properties. Next, the strains in the material coordinate system are calculated from the material coordinate system stresses from Equation 3.1 as

$$\begin{bmatrix} \varepsilon_1 \\ \varepsilon_2 \\ \gamma_{12} \end{bmatrix} = [S] \begin{bmatrix} \sigma_1 \\ \sigma_2 \\ \tau_{12} \end{bmatrix} \tag{3.3}$$

where the compliance matrix *[S]* is

$$[S] = \begin{bmatrix} \frac{1}{E_1} & -\frac{\nu_{12}}{E_1} & 0 \\ -\frac{\nu_{12}}{E_1} & \frac{1}{E_2} & 0 \\ 0 & 0 & \frac{1}{G_{12}} \end{bmatrix} \tag{3.4}$$

Next, these material coordinate system stresses are normalized by the strain in the *x*-direction, ε_x, caused by the applied load, σ_x, which is calculated from

$$\begin{bmatrix} \varepsilon_x \\ \varepsilon_y \\ \gamma_{xy} \end{bmatrix} = [T]^T [S][T] \begin{bmatrix} \sigma_x \\ 0 \\ 0 \end{bmatrix} \tag{3.5}$$

Now, these strains in the material coordinate system, having been normalized by ε_x, are plotted as a function of the PZT fiber rotation angle, θ, in Figure 3.6.

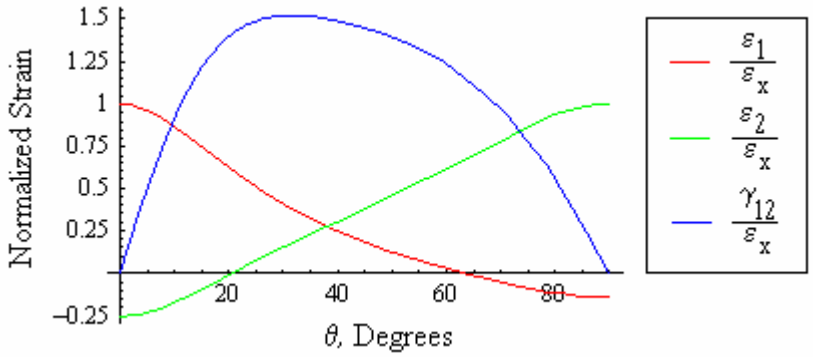

Figure 3.6: Normalized Strains in Material Coordinates Caused by σ_x

The local maxima of the blue shear strain curve can be found by setting its first derivative equal to zero and solving for θ. Performing this procedure reveals that the PZT fiber orientation angle that optimizes the in-plane shear strain is

$$\theta_{optimum} = 31.5^{\circ} \tag{3.6}$$

However, tensile-test coupons were manufactured with the PZT fibers oriented at 45° because the etched interdigitated electrodes and PZT fibers cut at 45° were readily available from NASA Langley. Examination of the plot in Figure 3.4 shows that using 45° test specimens instead of 31.5° samples results in only a 5% reduction in in-plane shear strain. The fabricated 45° off-axis specimens are pictured in Figure 3.7.

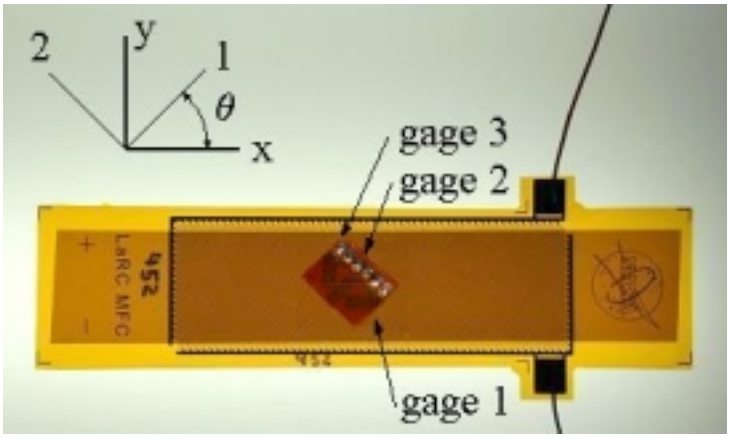

Figure 3.7 Off-Axis Tensile Specimen with PZT Fibers at 45°

Again, the end-tabs were used for loading into the grips; however, off-axis tensile specimens exhibit shear-extension coupling. This problem is solved in several ways as documented above in the literature review. For the current effort, the pivoting grips [Pindera and Herakovich, 1986] shown in Figure 3.2 are used to allow the ends of the specimen to rotate freely, thus promoting a uniform state of stress across the specimen width.

3.3.2 Specimen Manufacturing:

A detailed description of the manufacturing procedure used to assemble the Macro Fiber Composite is given in Appendix C, and a comprehensive production guide is presented in High and Wilkie [2003]. However, at this point it is important to outline the assembly steps for the various layers of the MFC tensile test specimens, which were designed specifically for the current research effort.

The MFC is assembled by hand and consists of three main layers: the bottom electrode, top electrode and the PZT fibers. These layers components are pictured in Figure 3.8, and are for the E_x – type specimens, but the off-axis specimen are assembled in the same manner, only the PZT fibers are cut at 45°, and the electrode fingers are at -45°.

Figure 3.8 a) Top and Bottom Electrode Layers and b) PZT Fibers on Blue Carrier Film

Each electrode layer consists of interdigitated copper electrode fingers that have been etched into the desired geometry. The top electrode has solder tabs with slots so that after assembly, the power leads can be soldered through these slots onto the bottom electrode's solder tab, thus establishing electrical connectivity between the two layers. With these three layers in hand, assembly of the MFC is as follows:

- Apply a thin layer of epoxy to the bottom electrode and to the PZT fibers.

- Stack PZT fibers on top, ensuring the fibers are in contact with and perpendicular to the electrodes.
- Precure these two layers in a vacuum hot press at 46 °C (115 °F) for fifteen minutes to adhere fibers to the bottom electrode.
- Apply a thin layer of epoxy to the top electrode and to the top of the PZT fibers.
- Stack the top electrode on top of the PZT fibers, ensuring that the electrodes are in contact with and perpendicular to the piezoceramic. The top and bottom electrode patterns should also be aligned.
- Cure the assembly in a vacuum hot press at 120 °C (250 °F) for two hours.
- Trim the fully cured part to the desired tensile-test specimen shape (Figure 3.3) and then remove Kapton from the slots in the top electrode's solder tabs. Attach power leads with solder.
- Measure and record the electrical properties of the device, and then pole the piezoceramic by applying 1500 volts DC for 5 minutes. Remeasure and record poled electrical properties.

Assembly of the MFC is now complete.

3.3.3 Strain Gage Instrumentation:

For the *x* and *y*-direction tests, strain gages capable of measuring both longitudinal and transverse strains simultaneously, type CEA-13-250WQ-350 from Vishay Measurements Group, are aligned with the *x*-*y* coordinate system seen in Figure 3.4, and then bonded to the center of the top and bottom of each MFC tests specimen. For the off-axis tests, 0°-45°-90° strain gage rosettes, type CEA-13-250UR-350 from Vishay Measurements Group, are aligned with the *x*-*y* coordinate system, and bonded to the top and bottom of the specimens as shown in Figure 3.7. All strain gages are bonded using M-Bond AE-15 strain gage epoxy, which is cured at 150°F for two hours as suggested by the manufacturer, and strain gage leads are attached using solder.

3.3.4 Tensile Testing Procedure:

Each MFC specimen was tensile tested using an Instron 4468 universal testing machine with a self-calibrating 1000 kN load cell and the appropriate grips. A fine mesh screen was inserted between the specimen and the grips to prevent slipping of the specimen during the test. All specimens were loaded at a crosshead speed of 0.2 mm/min until failure occurred in the specimen or near the grips. During the tensile tests, a ten channel stand-alone strain conditioner-amplifier and an analog to digital converter were connected to a PC, on which a Labview Virtual Instrument was used to collect numerous sets of data simultaneously, namely load from the testing machine and four (or six, for off-axis test) channels of voltage from the four (or six) strain gages.

Four E_x, four E_y, and five off-axis specimens were tested. The strain gages on the E_x and E_y specimens recorded in-plane strains in the direction of and transverse to the loading direction. The off-axis specimens recorded strains in three directions, which were later used to determine the in-plane shear strain, as discussed below in Section 3.4.4.

3.4 Experimental Results:

This section graphically presents the desired stress-strain behavior data collected from the three sets of tests to measure the behavior in the direction of the PZT fibers (E_x), transverse to the PZT fibers (E_y), and in-plane shear (G_{xy}). The value and behavior of the major Poisson's ratio, υ_{xy}, is also determined from the test in the direction of the PZT fibers.

3.4.1 Comments on Data Analysis:

For an engineering analysis, stress and strain values must be computed from the acquired load and voltage data. The actual strains are easily calculated from the recorded voltages, as the strain gage amplifier is calibrated such that one output volt equals 1000 microstrain ($\mu\varepsilon$). The strain values are then averaged from the top and bottom gages to remove any bending strain effects. The stress developed from the

applied load is calculated by dividing the load data by the cross-sectional area, specified in Table 3.1, of the active region / gage section of the MFC. Due to the manner in which the thickness of the actuator actually varied and iss measured, the cross-sectional area of the active region used in the calculations is slightly larger than what might be considered the average cross-sectional area. Referring to Figure 2.1, which shows the layers of the MFC, the micrometer used to measure the thickness contacted the outer surfaces of the upper and lower Kapton layers. The pressure used during the cure process causes some of the epoxy between the copper electrodes to be squeezed out, leaving a slight depression in the outer surfaces of the Kapton, between the electrodes. As the spacing between electrodes was 0.533 mm (0.021 in.), the micrometer head bridged the depressions, leading to a thickness measurement that is slightly larger than the average thickness. The photomicrograph in Figure 2.3 of the MFC cross-section indicates that using this maximum thickness is a reasonable approach. Lastly, the stress-strain curves are shifted horizontally so that the linear region extrapolates exactly through the origin in accordance with ASTM Standard D3039 / D3039M-00.

3.4.2 PZT Fiber Direction (E_x and ν_{xy}) Results:

As seen in Figure 3.9, there is an initially linear region of stress-strain behavior in the *x*-direction. The slope of a straight line passing through this data represents the effective elastic modulus in the PZT fiber direction, E_x. Accordingly, a least-squares linear regression analysis was performed on the data in this linear-elastic region for each of the four samples individually. This analysis provided a measured, numerical value of E_x for each data set. The average and sample standard deviation of these four values, are presented in Table 3.3 below.

Next, as depicted in Figure 3.10, the slope of the initially linear transverse-longitudinal strain data represents the major Poisson's ratio, ν_{xy}. Again, a linear regression analysis was used to determine a numerical value for this slope for each set of data, and the mean and sample standard deviation are also tabulated in Table 3.3.

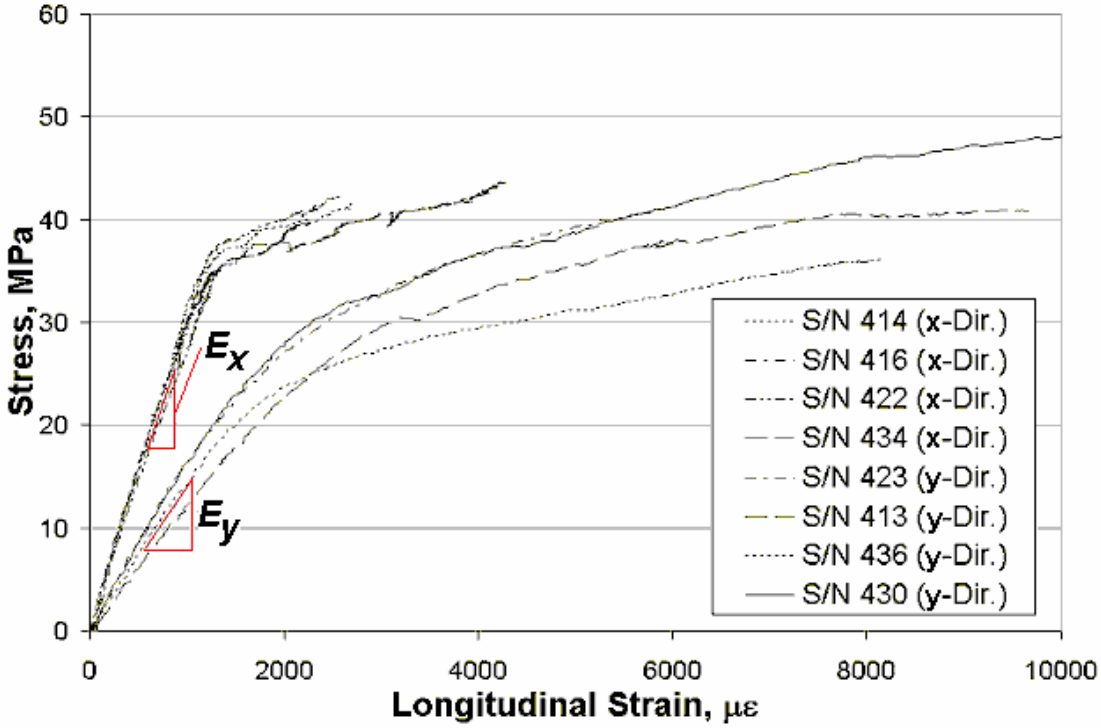

Figure 3.9: Stress-Strain Behavior in PZT Fiber and Electrode Directions

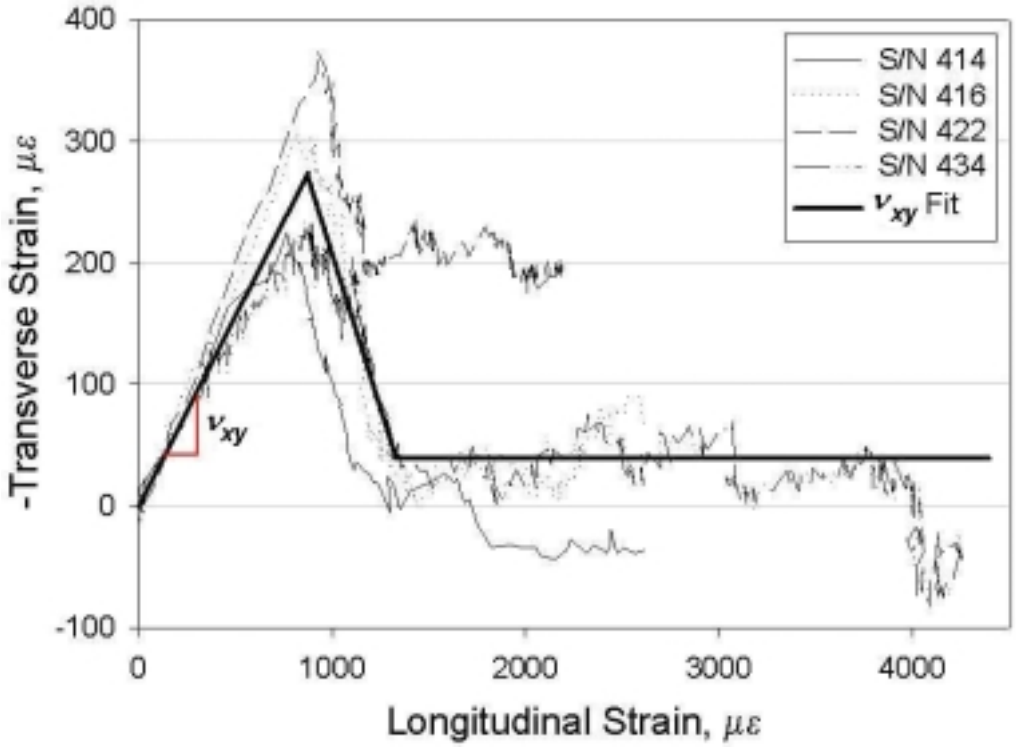

Figure 3.10: Transverse versus Longitudinal Strain for PZT Fiber Direction Tests

3.4.3 Electrode Direction (E_y) Results:

The elastic modulus perpendicular to the PZT fibers, E_y is found in the same manner as E_x above in Section 3.4.1, except the data from *y*-direction test is used instead. The desired slope is seen in Figure 3.9, and the average and sample standard deviation of the four test specimens are presented in Table 3.3 below.

3.4.4 Off-Axis (G_{xy}) Results:

In order to obtain a shear stress-shear strain curve, the collected stress-strain data from an off-axis specimen must be manipulated in the following manner. First, stress transformations give the shear stress in the material coordinates as

$$\tau_{12} = \frac{\sigma_x \sin 2\theta}{2} \tag{3.7}$$

Next, the shear strain in the material coordinate system is

$$\gamma_{12} = \left(\varepsilon_y - \varepsilon_x\right)\sin 2\theta + \gamma_{xy}\cos 2\theta\,. \tag{3.8}$$

Here, for 0°-45°-90° rosettes, ε_x and ε_y are equal to the strains from gages 1 and 3 (ε_{g1} and ε_{g3}), respectively, while the shear strain in the global geometric coordinates, γ_{xy}, is

$$\gamma_{xy} = -\varepsilon_{g1} + 2\varepsilon_{g2} - \varepsilon_{g3}\,. \tag{3.9}$$

However, since $\theta = 45°$ for these MFC coupons, Equation 3.7 simplifies to

$$\tau_{12} = \frac{\sigma_x}{2} \tag{3.10}$$

and γ_{xy} is not required as the last term in Equation 3.8 vanishes. Now, the desired relationship is found by plotting the shear stress from Equation 3.10 versus the shear strain calculated in Equation 3.8 at each load level. The resulting plot for the five specimens is depicted in Figure 3.11, where the effective in-plane shear modulus of the MFC, G_{xy}, is shown as the slope of the initial tangent to this curve.

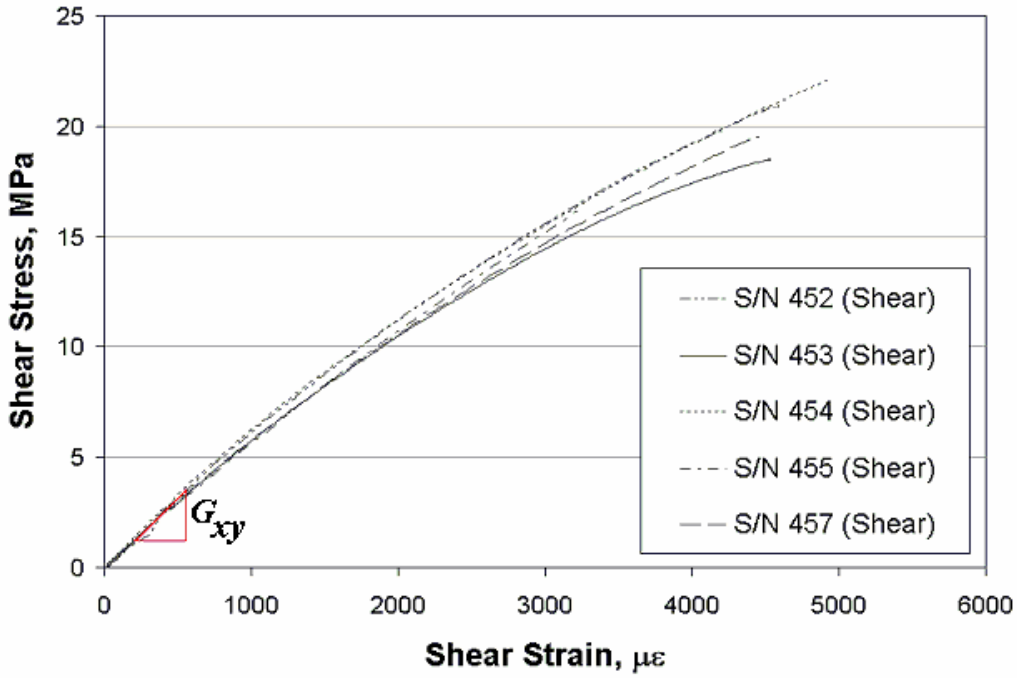

Figure 3.11: In-Plane Shear Stress-Shear Strain Behavior for the MFC Actuator

3.4.5 Measured Linear-Elastic Orthotropic Constants

Section 3.4 presented the experimental data from the three sets of tensile tests designed, in part, to measure the effective elastic orthotropic parameters of the MFC actuator under short-circuit electrical boundary conditions. In Figures 3.9 through 3.11, these values are depicted as slopes through the various sets of linear data, which were then statistically analyzed as discussed above. Table 3.3 presents the mean values and sample standard deviations for these experimentally measured properties.

Table 3.3: Measured Engineering Constants for Linear-elastic Behavior of the MFC

Property	Experimental Value	Standard Deviation
E_x, GPa	29.4	1.572
E_y, GPa	15.2	2.33
ν_{xy}	0.312	0.0640
G_{xy}, GPa	6.06	0.357

3.4.6 Comparison with Theoretical Linear Values:

In Chapter 2, classical lamination theory was used to predict effective laminate stiffness properties of the MFC, which are found in Table 2.5. These values are presented in Table 3.4, along with the percent error when compared to the experimental values obtained from the current effort in Table 3.3.

Table 3.4 Comparison of the Experimental and Predicted Engineering Properties of the MFC Actuator

Property	Experimental Value	Predicted Value	Percent Error
E_x, GPa	29.4	31.2	5.8%
E_y, GPa	15.2	17.05	10.85%
ν_{xy}	0.312	0.303	-2.97%
G_{xy}, GPa	6.06	5.27	-14.99%

Clearly, the traditional mechanics of composite materials theories predict, with reasonable accuracy, the four independent engineering properties in the linear-elastic region. This experimental verification of these well-known equations is significant because in Chapter 4, such techniques form the basis for a sensitivity analysis of the four effective stiffness parameters of the MFC for alternate lamination configurations, including various PZT fiber orientations, geometries and constituent material properties.

3.5 Elastic-Plastic Deformation Models:

This section develops various nonlinear models from Dowling [1999], and then uses the experimental data acquired from the procedure above to determine the required material parameters.

3.5.1 Models for *x* and *y*-Direction Behavior:

A quick examination of the stress-strain data from the *x* and *y*-direction tests in Figure 3.9 shows distinct elastic and plastic strain regions. Behavior of this type is commonly represented using two plastic deformation models, namely the elastic-linear hardening and Ramberg-Osgood relationships.

3.5.1.1 Elastic-Linear Hardening Relationship:

The elastic-linear hardening relationship describes the stress-strain behavior as linear at a slope of E_i ($i = x, y$) up to the onset of plastic deformation, and then linear again at a slope of $\delta_i E_i$ through the plastic region, where δ_i is the slope reduction factor for the *i*-direction test [Dowling, 1999]. For materials displaying hardening type plastic deformation, i.e., the MFC when tested in the *x* and *y*-directions, δ_i has a value between zero and one. Mathematically, this type of constitutive behavior is given as

$$\sigma_i = \begin{cases} E_i \varepsilon_i & (\sigma_i \le \sigma_{0i}) \\ (1-\delta_i)\sigma_{0i} + \delta_i E_i \varepsilon_i & (\sigma_i \ge \sigma_{0i}) \end{cases} \tag{3.11}$$

where σ_i is the normal stress, ε_i is the normal strain, and σ_{0i} is the stress at which plastic deformation begins. Application of this model to the data from the *x* and *y*-direction tests requires a linear regression of both the elastic and plastic regions, which provides values for E_i and $\delta_i E_i$ for each specimen, respectively. The onset of yielding is determined graphically as the point where the stress-strain curve begins to exhibit plastic deformation, in contrast to an offset yield point typically used with engineering

metals. These characteristic values are averaged from the four specimens for each of the two directions and appear in Table 3.5.

Table 3.5: Elastic-Linear Hardening and Ramberg-Osgood Parameters for *x* and *y*-Direction Behavior of the MFC Actuator

Test Type	E_i, GPa	$\delta_i E_i$, GPa	δ_i	σ_{oi}, GPa	n_i	H_i, GPa	ν_{xy}	Plastic ν_{xy}	ν_{yx}
x-Direction Test	29.4	3.53	0.1201	0.0350	0.0450	0.0545	0.312	-0.506	N / A
y-Direction Test	15.17	1.953	0.1287	0.0285	0.1715	0.1023	N / A	N / A	0.1607

Figure 3.12 shows a plot of Equation 3.7 using these parameters, along with the experimental data.

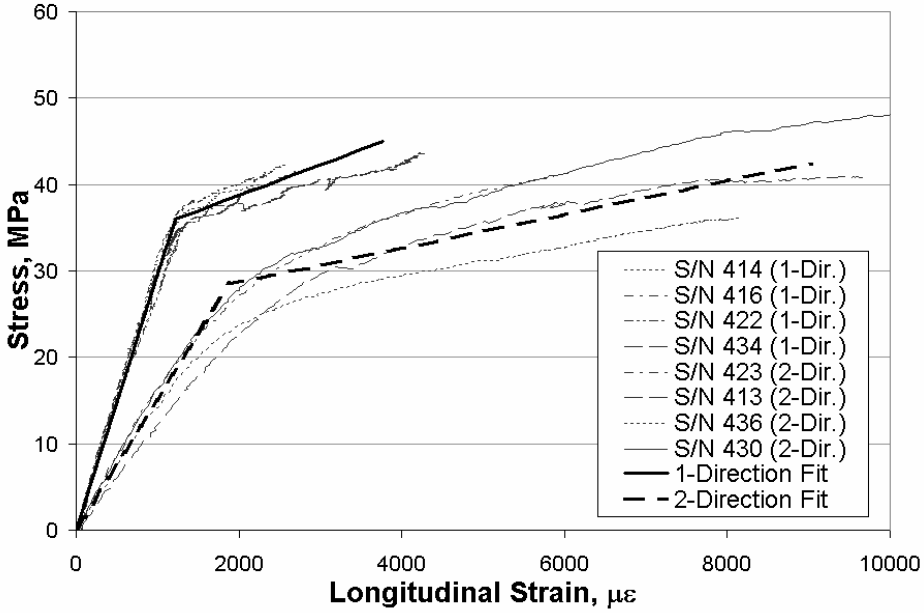

Figure 3.12 Elastic, Linear-Hardening Model and Experimental *x* and *y*-Direction Stress-Strain Relationships

Clearly, the models adequately represent the experimental data from the *x* and *y*-direction tests.

3.5.1.2 Ramberg-Osgood Relationship:

The Ramberg-Osgood plastic deformation model represents the total strain as the sum of the elastic and plastic strains components [Dowling, 1999]. Again, the elastic strain component is proportional to stress, however, the relationship between the plastic strain component and stress is exponential and given by

$$\sigma_i = H_i \varepsilon_{Pi}^{\,n_i} \tag{3.12}$$

where H_i is a material constant, n_i is a strain hardening exponent, and ε_{Pi} is the plastic strain component. Solving Equation 3.8 for ε_{Pi} and adding to the elastic strain gives the total strain as

$$\varepsilon_i = \frac{\sigma_i}{E_i} + \left(\frac{\sigma_i}{H_i}\right)^{\frac{1}{n_i}} \tag{3.13}$$

From the exponential nature of Equation 3.12, a plot of stress versus plastic strain is a straight line on a log-log plot. Values of H_i and n_i for a particular tensile test are found either graphically from this plot (where H_i is equal to σ_i at a ε_{Pi} equal to one, and n_i is the slope of the line if the logarithmic decades in the two directions are of equal lengths) or using a linear regression analysis of logarithmic data. The current effort uses the more precise latter approach to find H_i and n_i for each of the experimental stress-strain relationships. The averaged results for both the *x* and the *y*-direction tests are presented in Table 3.5. Figure 3.13 plots Equation 3.13 with these values, one curve for each direction, along with the corresponding experimental data. Again, the curves closely match the data.

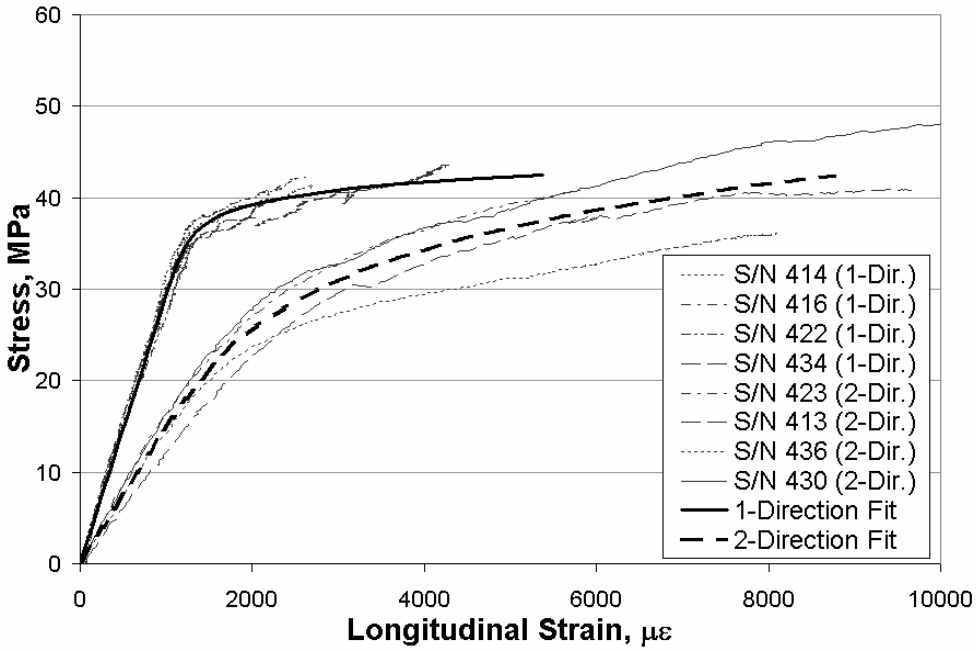

Figure 3.13 Ramberg-Osgood Model and Experimental Data: *x* and *y*-Direction Stress-Strain Relationships

3.5.1.3 Nonlinear Behavior of the Major Poisson's Ratio, ν_{xy}:

The experimental transverse strain data is used to determine Poisson's ratio, ν_{xy}. As seen in Figure 3.10, the slope of the linear fit, ν_{xy}, is constant in the linear-elastic region; however, at the onset of plastic behavior, it changes sign and magnitude. These changes are indicative of broken fibers returning to a lower or stress-free state, at which time the transverse strain is recovered. Beyond this strain level, ν_{xy} is essentially zero. Poisson's ratio values for the elastic and plastic regions are given in Table 3.5. It should be noted that the tension tests from this research effort are monotonic, and fiber breakage is a one-time event. Thus, Poisson's ratio could change for subsequent tensile loading and unloading scenarios, as would be the case for actuating the MFC under large harmonic voltage (above ~1250 volts peak-to-peak).

3.5.1.4 Comments on the Minor Poisson's Ratio, ν_{yx}:

Since the minor Poisson's ratio, ν_{yx}, is not an independent material property, it is not essential to verify its value experimentally. However, if one wishes to do so, it is

determined in the same manner as ν_{xy}, except that data from the *y*-direction test is substituted for the *x*-direction data. In the current experiments, transverse strain data was collected for the *y*-direction tests, however, since these test specimens are so short, the fiberglass tabs *severely* restrict the transverse contraction, thus resulting in experimental values of ν_{yx} that are much too low. The result presented in Table 3.5 are from calculated from the reciprocity relationship

$$\nu_{yx} = \nu_{xy} \frac{E_y}{E_x} \tag{3.14}$$

where the quantities on the right-hand side of Equation 3.14 are experimental values.

3.5.2 Models for In-Plane Shear Behavior:

Examination of the measured shear stress-shear strain behavior of the MFC depicted in Figure 3.11 shows a small amount of nonlinear behavior that should be represented as accurately as possible. Now, as discussed above, the active region / gage section of the test specimens is not in a state of pure shear, but rather a biaxial state of stress with in-plane shear loading. However, from Figure 3.6, the shear strain response is clearly the dominant response at a PZT fiber angle of 45°, as the normalized shear strain at this angle is many times larger than the normal strains. So, although the nonlinear behavior is not caused exclusively by shear deformation, this test method is believed to provide reliable initial material response and can establish shear stress-shear strain response well into the nonlinear region [ASTM D 3518 / D 3518M-94].

Having established the validity of the off-axis test, the next step is to represent the observed behavior. The next two sections modify the Ramberg-Osgood model used for the *x* and *y*-direction response and propose a second-order regression curve fit model. While the latter is strictly mathematically based, it provides a second equation, which is explicit in stress and can readily be used in more detailed structural models.

3.5.2.1 Ramberg-Osgood Relationship:

The Ramberg-Osgood model developed above easily adapts for use with nonlinear in-plane shear deformation by substituting shear stress and strain parameters for their normal stress and strain counterparts. The resulting expression for the intralaminar shear stress, τ_{xy}, is

$$\tau_{xy} = H_{xy}\gamma_{Pxy}^{\ n_{xy}} \tag{3.15}$$

where H_{xy} is a material constant, n_{xy} is a strain-hardening exponent, and γ_{Pxy} is the plastic component of shear strain. Solving Equation 3.15 for γ_{Pxy} and adding it to the elastic strain component gives the total strain as

$$\gamma_{xy} = \frac{\tau_{xy}}{G_{xy}} + \left(\frac{\tau_{xy}}{H_{xy}}\right)^{\frac{1}{n_{xy}}} \tag{3.16}$$

Following the regression analysis described above, average values for H_{xy} and n_{xy} are found from five test specimens and the corresponding shear stress-shear strain relationship from Equation 3.16 is plotted along with the experimental data in Figure 3.14.

3.5.2.2 Quadratic Least-Squares Fit:

Clearly, the Ramberg-Osgood model accurately represents the shear stress-shear strain data. However, it is preferable to have two expressions for all stress-strain curves, at least one of which can be solved explicitly for stress. Examination of the data shows only a small amount of plastic strain, so a power hardening type of relationship will not fit the data well. However, the shear stress-shear strain data does appear to possess a quadratic relationship of the form

$$\tau_{xy} = C_1\gamma_{xy} + C_2\gamma_{xy}^2 \tag{3.17}$$

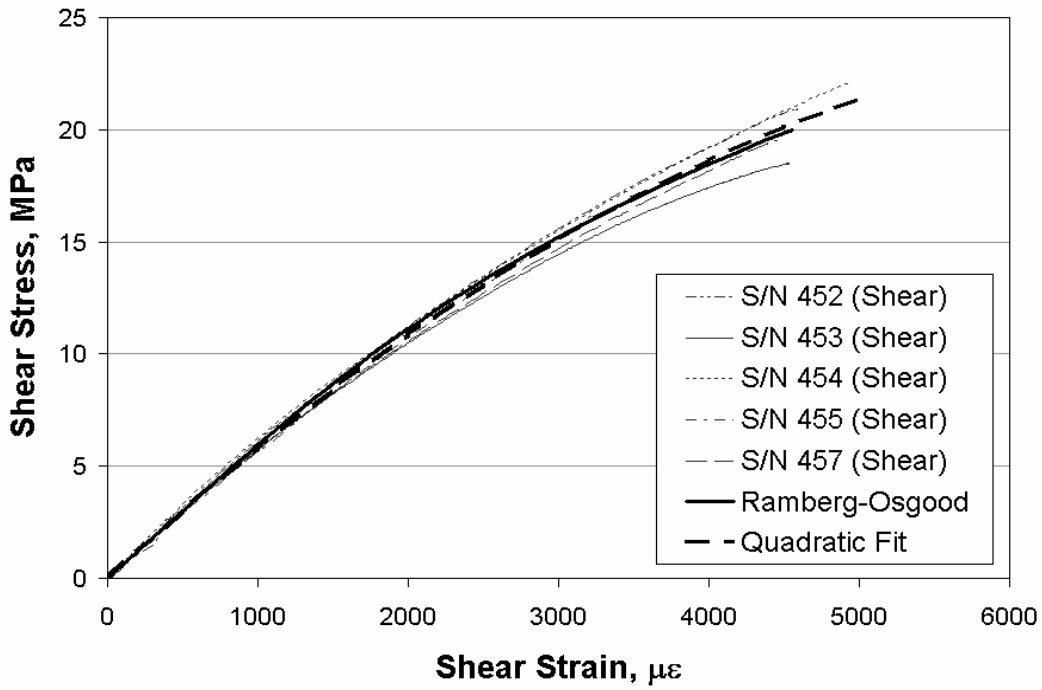

Figure 3.14 Ramberg-Osgood Model, Quadratic Least-Squares Fit and Experimental Data for Shear Stress-Shear Strain Relationships

where the constants C_1 and C_2 are found using a quadratic regression procedure for each specimen. The average values from five tests are presented in Table 3.6 and are used to plot Equation 3.17 along with the experimental data in Figure 3.14.

Table 3.6: Ramberg-Osgood and Quadratic Regression Parameters for Shear Behavior

G_{xy}, GPa	n_{xy}	H_{xy}, GPa	C_1, GPa	C_2, GPa
6.06	0.289	0.1383	6.20	-384

Unlike the elastic-linear hardening and Ramberg-Osgood models, this quadratic regression is purely mathematical and not based on any physical behavior. However, Equation 3.17 provides a good fit to the data and gives a simple shear stress prediction that can be readily applied for dynamic simulation and control models.

3.6 Summary:

This chapter experimentally determines the four independent orthotropic engineering properties in the linear-elastic region as well as characterizes the nonlinear constitutive behavior of the MFC actuator under short-circuit conditions. The experimental values of E_x, E_y, ν_{xy}, and G_{xy} agree with those predicted by the classical lamination model developed in Chapter 2 to within a few percent in most cases. Therefore, a researcher can use traditional mechanics of laminated composites models to develop new types of MFC actuators with various piezoelectric materials and geometries. Also, the models in Figures 3.12 and 3.13 depict high fidelity quantitative relationships for the nonlinear stress-strain behavior in the *x* and *y*-directions, while the off-axis test specimens provide accurate representation of the in-plane shear behavior of the MFC, as shown in Figure 3.14. However, these models all have both advantages and disadvantages. For the *x* and *y*-direction tests, one could argue that the Ramberg-Osgood is a better fit overall, particularly in the elastic-plastic transition region, yet it involves increased complexity, cannot be solved explicitly for stress, and exhibits no distinct yield point. While in general, either model is acceptable for design use, one concerned with overall stress-strain behavior would likely prefer the simpler elastic-linear hardening model, but if a failure and durability study of the MFC is performed, the Ramberg-Osgood model would be preferable due to its fidelity in the critical yielding region. As for the shear stress-shear strain behavior, both the Ramberg-Osgood model and the quadratic regression fit the data extremely well. While the former approach has the aforementioned drawbacks, it is derived from observed mechanical behavior, while the latter is simply a mathematical formula with no physical basis. Also, the fit-lines in Figure 3.10, the slopes of which represent the major Poisson's ratio, match the data well over the entire applicable strain range. Overall, this chapter gives researchers in the field of intelligent structures an in-depth view of the short-circuit mechanical behavior of the MFC actuator, including both values for essential elastic engineering constants as well as equations designed to handle complex plastic deformation.

Chapter 4

Sensitivity of Elastic Properties to Uncertainty in Constituent Material Properties and Geometric Design Parameters

4.1 Introduction:

In Chapter 2, a classical lamination model is developed to predict the effective orthotropic engineering properties, E_x, E_y, υ_{xy}, and G_{xy}, of the MFC under short-circuit conditions for linear-elastic behavior. While Chapter 3 discusses the experimental verification of these models and then characterizes the associated nonlinear mechanical behavior at higher strain levels, this chapter goes back and investigates the sensitivity of the linear model from Chapter 2 to uncertainty in constituent material properties. While every reasonable effort was made to obtain the most recent and accurate required material properties for the Kapton, acrylic, copper, epoxy and PZT, sometimes "typical" or "handbook" values were used instead of numbers provided by the material supplier. This chapter determines which of these material properties has the largest impact on the desired effective MFC properties, and identifies which material properties need to be measured independently by future researchers in order to develop higher fidelity models. In addition, the impact of certain geometric design parameters, namely fiber

volume fractions and layer thicknesses, is investigated to establish design envelopes for the effective, short-circuit engineering properties of the MFC. The plots in this chapter are all non-dimensionalized by the nominal reference MFC values presented in Table 2.5. Changes in these properties due to temperature and electric field are investigated in Appendix E.

4.2 Variations in Fiber Volume Fractions:

One of the fundamental concepts in the micromechanics of fiber-reinforced composites is predicting how the properties of a lamina change depending on the ratio of fiber to matrix material. For the MFC, there are two kinds of fiber-reinforced laminae, a PZT/epoxy layer and two copper/epoxy electrode layers. In this section, the rule-of-mixtures and classical lamination model developed in Chapter 2 is again utilized, only here the fiber volume fraction of PZT or copper is considered an independent variable while the other material and thickness properties retain their nominal values as specified in Tables 2.1, 2.2, and 2.3. The *Mathematica* code for the current sensitivity analysis is presented in Appendix F. Since the PZT and copper fibers are rectangular in cross-section, they have their own geometric properties such as width, fiber spacing and kerf (slot between fibers). However, it is accepted practice in the composites community to ignore the specific geometry of the fibers at this level and investigate parameters as a function of the fiber volume fraction. For the PZT/epoxy layer, the fiber volume fraction can be easily altered by programming the computer-controlled silicon dicing saw to cut various fiber widths and spacings, and the use of different width diamond encrusted saw blades results in different kerf widths. The fiber volume fraction of the copper electrode layer is altered by etching the copper-clad Kapton film into the desired pattern, including electrode line width and spacing. For rectangular fibers, the fiber volume fractions are

$$V_f = \frac{fiber\ width}{fiber\ width + kerf} \qquad \text{or} \qquad V_f = \frac{fiber\ spacing - kerf}{fiber\ spacing} \tag{4.1}$$

Using the linear model from Chapter 2, the four apparent mechanical properties of the MFC are plotted in Figure 4.1 with the PZT fiber volume fraction as the independent variable.

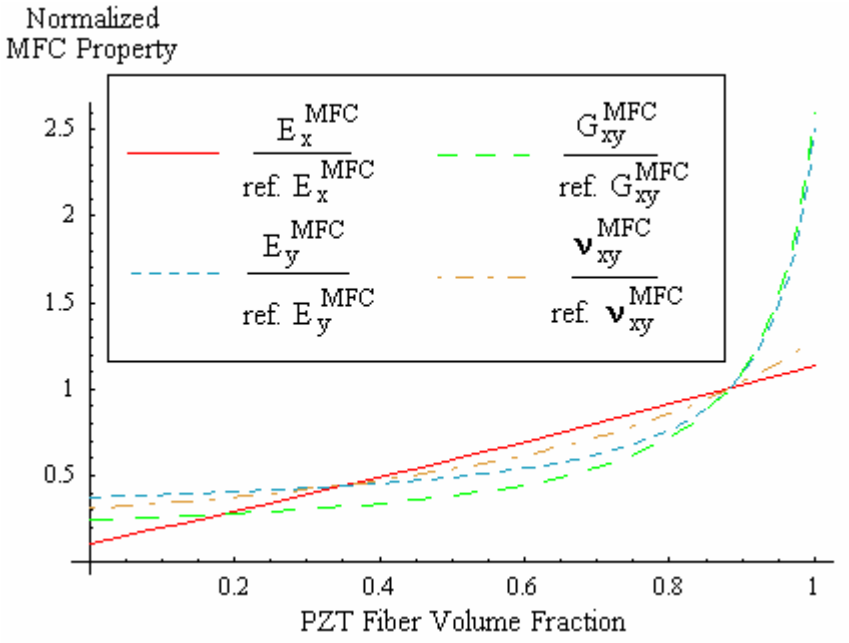

Figure 4.1: Elastic Properties of the MFC as a Function of PZT Fiber Volume Fraction

From this figure, the nominal reference PZT layer design is depicted as the intersection of the four curves at a PZT fiber volume fraction of about 0.88. The figure shows a linear relationship between PZT fiber volume fraction and E_x of the MFC that allows simple control of this apparent stiffness, and a reduction of about 90% is possible with low PZT fiber volume fractions. The other three apparent MFC properties have a more complex nonlinear relationship. E_y and G_{xy} of the MFC increase rapidly as the PZT fiber volume fraction approaches unity. Since these are matrix dominated quantities, the less epoxy, the closer the PZT layer behaves as a bulk rather than fibrous layer. As the PZT fiber volume fraction decreases from the nominal value, a rapid decrease in these two properties is noted initially, but then they begin to level of as the epoxy begins to dominate the behavior. The in-plane Poisson's ratio exhibits behavior similar to the transverse and in-plane shear moduli, except the variations are less severe.

Next, the apparent MFC properties are plotted in Figure 4.2, only this time the copper fiber volume fraction is the independent variable.

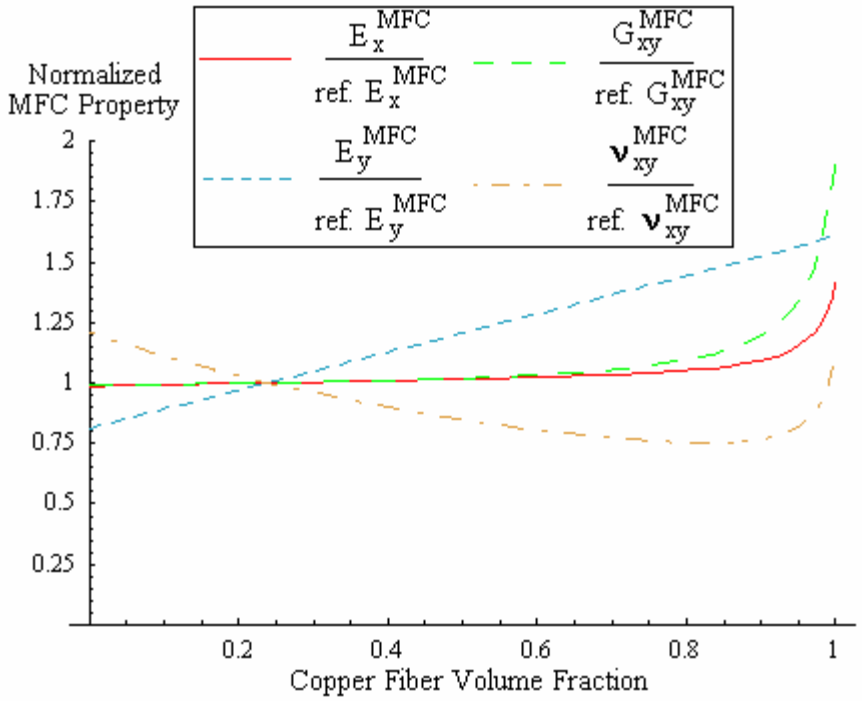

Figure 4.2: Elastic Properties of the MFC as a Function of Copper Fiber Volume Fraction

Again, the nominal design fiber volume fraction of electrode finger copper occurs where the four curves intersect, at a value of about 0.24. This figure serves primarily to illustrate how the copper electrode layers have a much smaller impact on the overall behavior of the MFC. At fiber volume fractions near the nominal value, E_x and G_{xy} are practically constant. Only at unreasonably high values do these properties begin to change radically, but such a copper electrode pattern is not feasible because it would be conducive to electrical failure of the device. However, the transverse modulus of the MFC is the most highly dependent property on the amount of copper, which stands to reason since the electrodes are stiff and aligned in the *y*-direction. In addition, the in-plane Poisson's ratio depends a fair bit on the copper fiber volume fraction because these fibers resist contraction in the *y*-direction when the MFC is loaded in the *x*-direction.

4.3 Variations in Layer Thicknesses:

In addition to altering the fiber volume fractions of the PZT/epoxy and copper/epoxy electrode layers during fabrication of those plies, the other geometric design variable is the thickness of each layer. Since the Kapton-acrylic-copper film is purchased from DuPont (Pyralux high-performance film), the thicknesses of these layers are predetermined. However, different product codes have different thicknesses for each layer [DuPont Films, Bulletin H-73244]. For example, the Kapton layer is available in certain thicknesses from 13 μm (0.0005 in.) up to 127 μm (0.005 in.), while the acrylic comes in various thicknesses between 13 μm (0.0005 in.) and 51μm (0.002 in.). The copper layer can be selected to have thicknesses between 17 μm (0.0007 in.) and 68μm (0.0028 in.). The nominal thicknesses for the MFC "reference" configuration are specified in Table 2.3. Figure 4.3 shows the effective properties of the MFC as a function of the Kapton thickness. Clearly, the Poisson's ratio of the MFC is not sensitive to these layers thicknesses. However, the other three properties vary in a nearly linear fashion, and are somewhat sensitive to changes in the Kapton thickness. For example, a 20% variation in Kapton thickness results in ~3% change in the three effective MFC moduli.

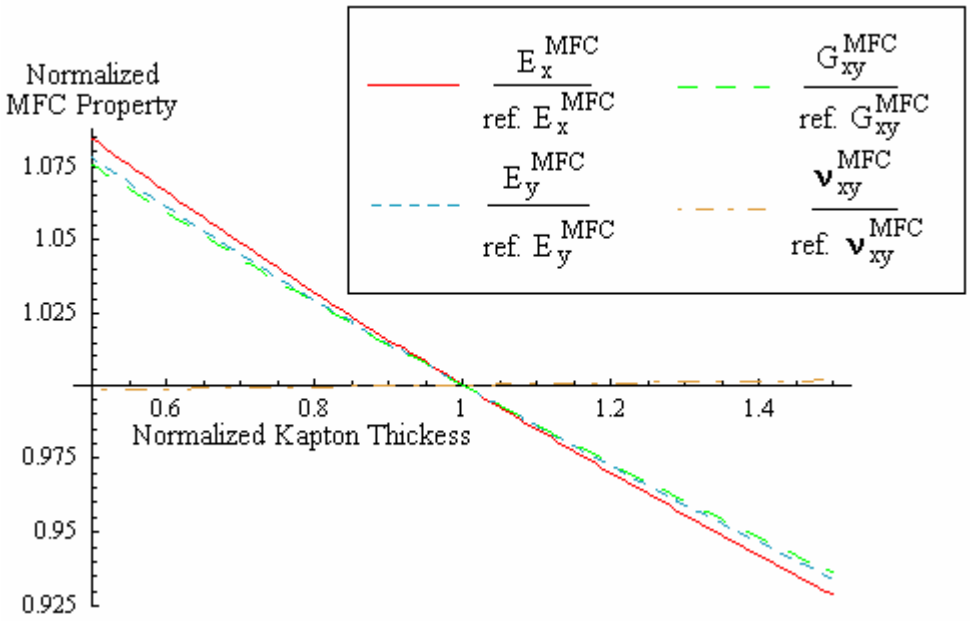

Figure 4.3: Apparent Moduli of the MFC for Variations in Kapton Thickness

Figure 4.4 shows the effective properties of the MFC as a function of the thickness of the acrylic adhesive layer, which bonds the copper foil to the Kapton substrate. Again, the Poisson's ratio of the MFC is not at all sensitive to the thickness of the acrylic layers. On the other hand, the three moduli of the MFC, which vary in a nearly linear fashion with acrylic thickness, are not very sensitive to changes such thickness variations. In fact, even a ± 20% variation in acrylic thickness results in only about a ± 1% difference in E_x, E_y, and G_{xy} of the MFC.

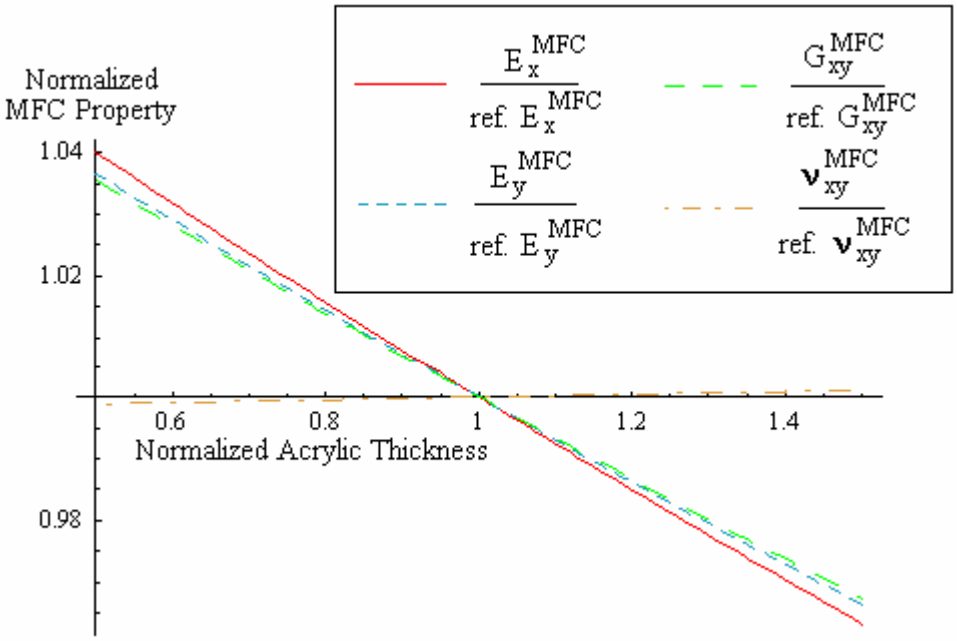

Figure 4.4: Apparent Moduli of the MFC for Variations in Acrylic Thickness

Next, the fiber-reinforced copper/epoxy electrode finger layer thickness is considered. Figure 4.5 shows the MFC property variations for different copper layer thicknesses. More interesting behavior is seen for these apparent properties due to the orthotropic nature of this layer. For example, the Poisson's ratio of the MFC is the most dependent on copper layer thickness. This relationship makes sense, because the thicker the copper electrodes, the more stiff metal there is to resist transverse contraction when the MFC is loaded in the *x*-direction. Likewise, an increase in copper thickness would tend to make the MFC stiffer in that direction, which is depicted as an increase in E_y. Even

still, the overall behavior of the MFC is not incredibly sensitive to such variations in copper thickness, as a ± 20% variation in the independent variable results in less than about a ± 5% change in this apparent property.

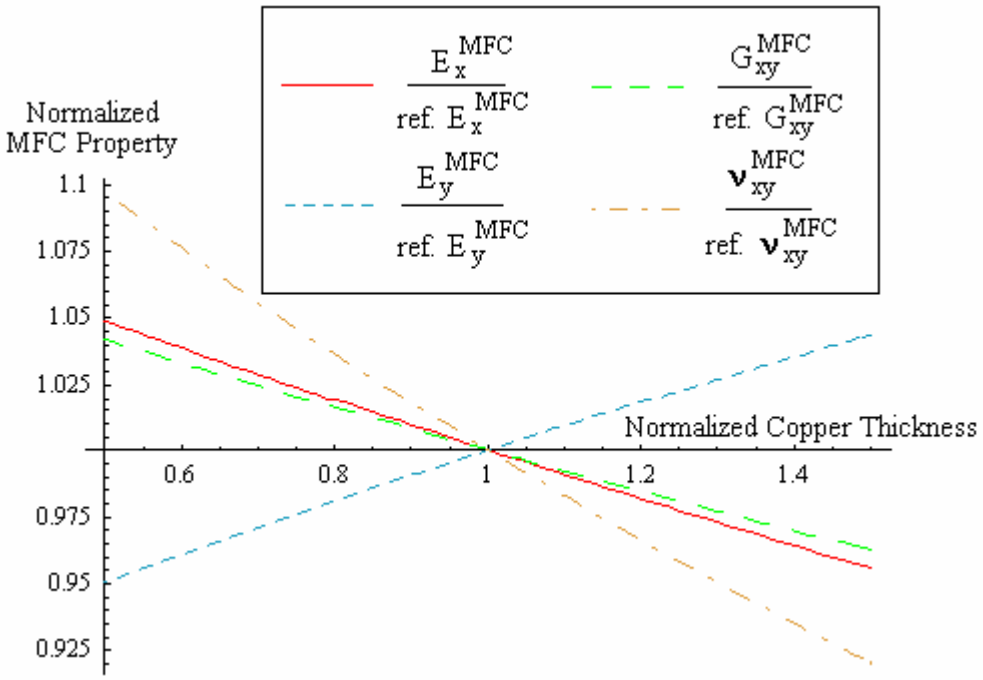

Figure 4.5: Apparent Moduli of the MFC for Variations in Copper Thickness

Lastly, the variations in the thickness of the PZT/epoxy fiber-reinforced layer are considered. The PZT sheet that the fibers are cut from can be purchased at any reasonable thickness, anywhere from about 0.05 mm (0.002 in.) upwards. Care must be taken not to select too thick of a PZT because then the electrical field is not adequately distributed into the fibers. Initial experimentations have shown that in excess of around 0.2 mm (0.008 in.), electromechanical free-strain behavior begins to degrade rapidly with thickness.

Figure 4.6 shows a nonlinear relationship between the properties of the MFC and the thickness of the PZT layer. The longitudinal and in-plane shear moduli appear to be the most sensitive to such changes, particularly when the PZT thickness is decreased. For

example, a 20% decrease in thickness produces almost a 10% decrease in these two effective properties. Increases in thickness produce about half as much deviation in the same properties of the MFC. As for the other two effective parameters of the MFC, E_y and ν_{xy}, they vary by only a few percent for equivalent increases or decreases in the PZT thickness.

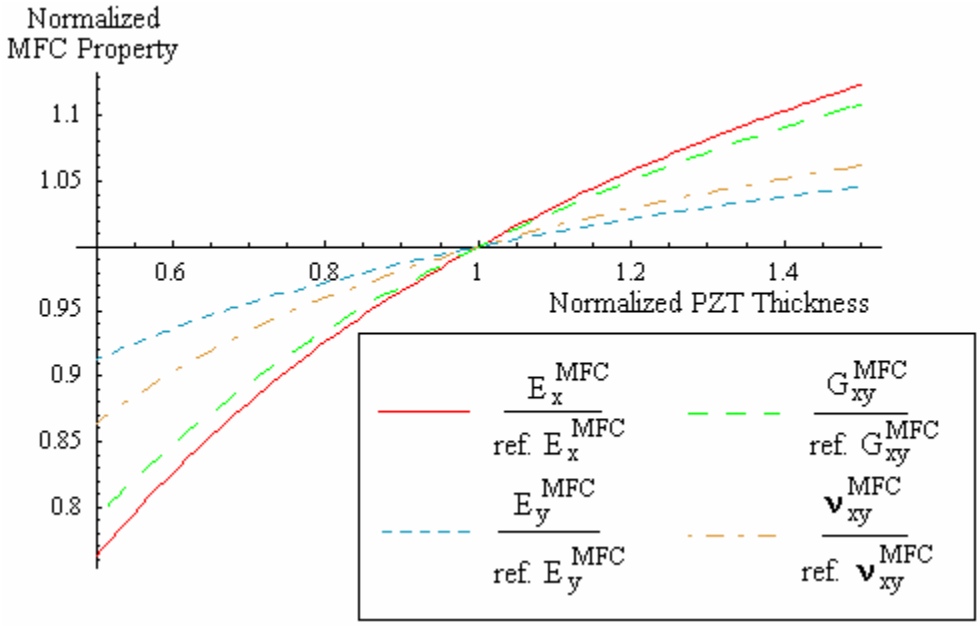

Figure 4.6: Apparent Moduli of the MFC for Variations in PZT Thickness

4.4 Variations in Constituent Material Properties:

In the preceding sections, the effective short-circuit orthotropic mechanical properties of the MFC are plotted as a function of geometric parameters that can be controlled during manufacturing. As a result, the MFC can be designed such that the apparent properties are tailored to obtain a desired performance. In this section, these properties are plotted as a function of variations in the different constituent material properties, while all of the geometric variables maintain their nominal reference design values. While some material properties are obtained from the supplier directly and known to be reliable, some properties values had to be obtained for "typical" or "comparable" materials. The latter set of data is less reliable as the properties are generic handbook values or given

as a range of possible values. As a result, the impact of these required material properties on the overall, apparent E_x, E_y, G_{xy}, and ν_{xy} of the MFC is predicted over a range of ± 50% of the nominal value. If a particular property is seen to impact these effective properties a great deal but comes from the set of less reliable data, then future researchers will know that more material testing is needed for these models.

4.4.1 Kapton Material Properties

The first material whose properties are considered is Kapton. Figure 4.7 shows the effective properties of the MFC as a function of the Kapton modulus, while Figure 4.8 has the Poisson's ratio of Kapton as the independent variable. Since the required modulus and Poisson's ratio were readily available from the material supplier [DuPont Bulletin GS-96-7], it is only realistic to consider small deviations from the nominal value.

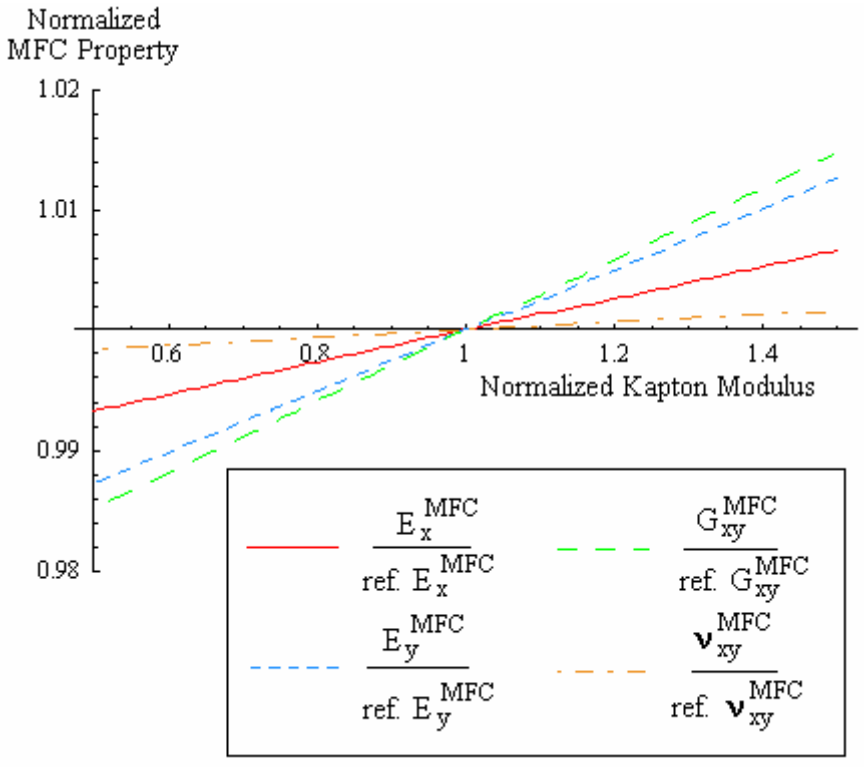

Figure 4.7: Apparent Orthotropic Moduli of the MFC for Variations in Kapton Modulus

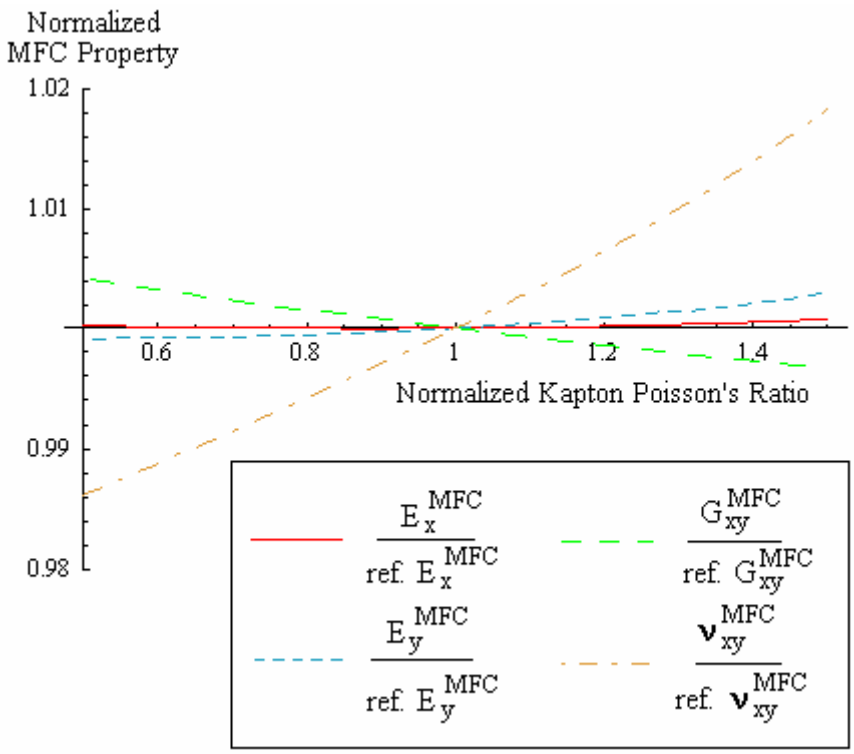

Figure 4.8: Apparent Moduli of the MFC for Variations in Kapton Poisson's Ratio

From the first of these two figures, a nearly linear relationship is observed between the desired moduli and the modulus of Kapton. Also, it is clear that variations in this property do not impact the overall behavior a great deal, because even a 20% change in Kapton modulus results in less than 1% change in the MFC properties. In the second figure, a slight nonlinear relationship is observed between the properties and the independent variable. However, again there is little dependence of the MFC behavior on variations in the Poisson's ratio of Kapton. From these plots and the availabitliy of reliable data on Kapton from the supplier, no further study of this material is required for linear-elastic behavior.

4.4.2 Acrylic Material Properties:

The next material whose properties are considered is acrylic, which is used to bond the copper electrodes to the Kapton substrate. This acrylic adhesive is proprietary to DuPont, so they do not publish any technical data on its properties, composition, or

processing. Thus the uncertain material properties of a generic acrylic are used, and the actual value could vary somewhat from the selected nominal value.

Figure 4.9 shows the effective properties of the MFC as a function of the acrylic modulus, while Figure 4.10 has the Poisson's ratio of acrylic as the independent variable. From the small scale on the *y*-axis, it is clear that uncertainties in the acrylic modulus have very little effect on the overall behavior of the MFC. In addition, the Poisson's ratio of the acrylic also has almost no effect on the predicted apparent mechanical properties of the MFC actuator. Even large variations in these two material properties would result in less than a 1% change in the MFC parameters. This result is promising since the exact values of the acrylic properties are not readily available at this point in time.

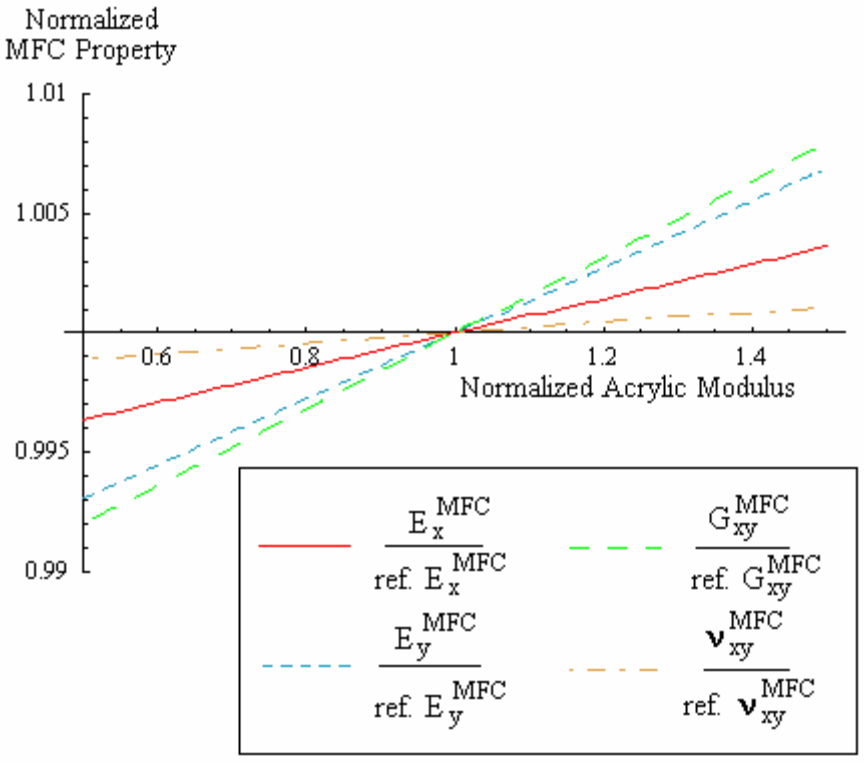

Figure 4.9: Apparent Orthotropic Moduli of the MFC for Variations in Acrylic Modulus

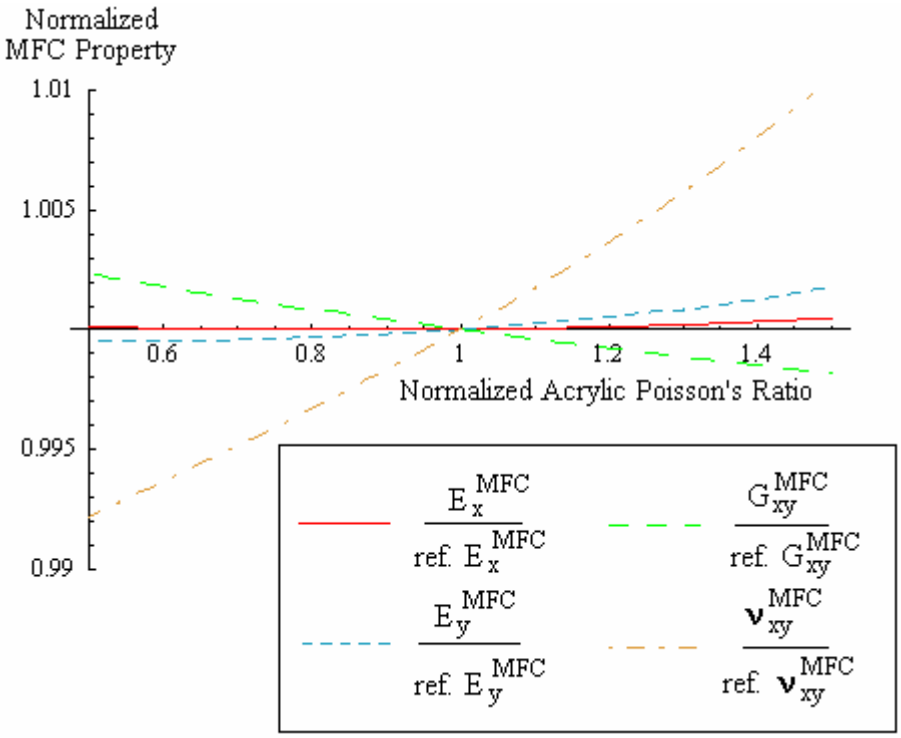

Figure 4.10: Apparent Moduli of the MFC for Variations in Acrylic Poisson's Ratio

4.4.3 Copper Material Properties:

Next, variations in the copper material properties are considered. Again, DuPont does not publish any technical data on this particular copper, so the material properties of a generic copper are used, and the actual value could vary somewhat from the selected nominal materials handbook value. Since copper is a metal, there is often some discrepancy between bulk material properties and those of a rolled or sputtered thin foil. Nevertheless, copper is a well-characterized metal so most properties from handbooks should be reasonably reliable as they typically only vary by a few percent.

Figure 4.11 shows the effective properties of the MFC as a function of the copper modulus, while Figure 4.12 has the Poisson's ratio of copper as the independent variable. From the first of these figures, it is clear that the longitudinal and shear moduli of the MFC are not sensitive to variations in the copper modulus.

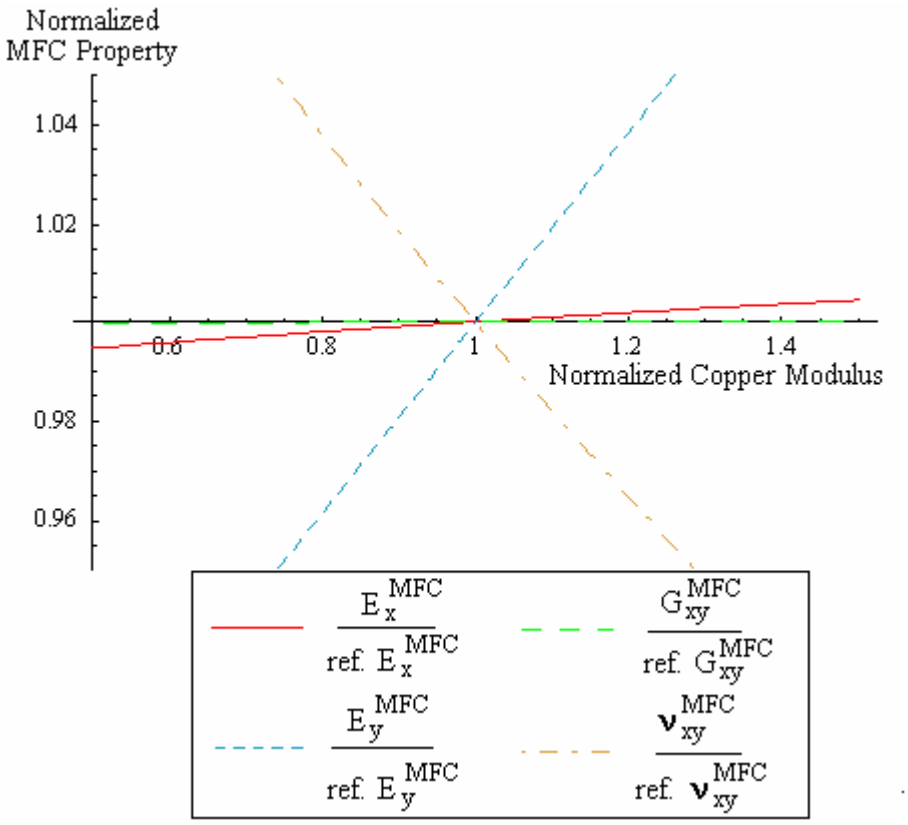

Figure 4.11: Apparent Moduli of the MFC for Variations in Copper Modulus

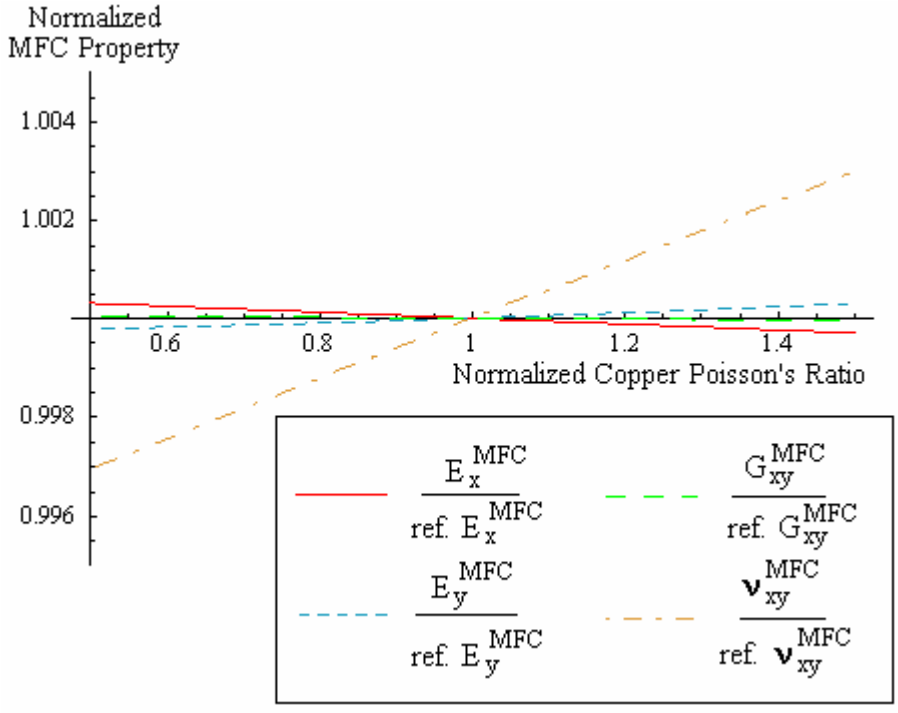

Figure 4.12: Apparent Moduli of the MFC for Variations in Copper Poisson's Ratio

However, the apparent transverse modulus and Poisson's ratio of the MFC is a bit more sensitive to such uncertainties, where a ± 20% change in the copper modulus results in about a ± 5% change in these two predicted parameters. Next, the tiny scale on the *y*-axis of Figure 4.12 shows that none of the MFC properties vary even with large changes in the Poisson's ratio of copper.

4.4.4 Epoxy Material Properties:

Now, variations in the epoxy material properties are considered. The epoxy used for the MFC is made by Loctite, and they do not give any mechanical properties for this epoxy. So, again, the material properties of a generic structural epoxy aere used, and the actual value could vary somewhat from the selected nominal materials handbook value. Since there are many types of structural epoxies commercially available, the range of values for these properties can be quite large (on the order of ± 25% from the nominal value herein), thus the results from these particular plots will be quite important.

With that, Figure 4.13 shows the effective properties of the MFC as a function of the epoxy modulus, while Figure 4.14 has the Poisson's ratio of epoxy as the independent variable. From the first of these figures, it is clear that the longitudinal modulus of the MFC is not sensitive to variations in the epoxy modulus. Likewise, changes in the Poisson's ratio of the MFC are not largely dependent on uncertainties in this material property. However, the apparent transverse and shear moduli of the MFC are extremely sensitive to such uncertainties, where a ± 20% change in the epoxy modulus results in about ± 10% and ± 15% change in these two predicted parameters, respectively. Next, Figure 4.14 shows that neither the longitudinal nor transverse moduli of the MFC change much in response to variations in the epoxy Poisson's ratio. However, the shear modulus and Poisson's ratio of the MFC are somewhat sensitive to such changes, where a ± 20% change in the independent variable results in approximately a 3% change in both parameters.

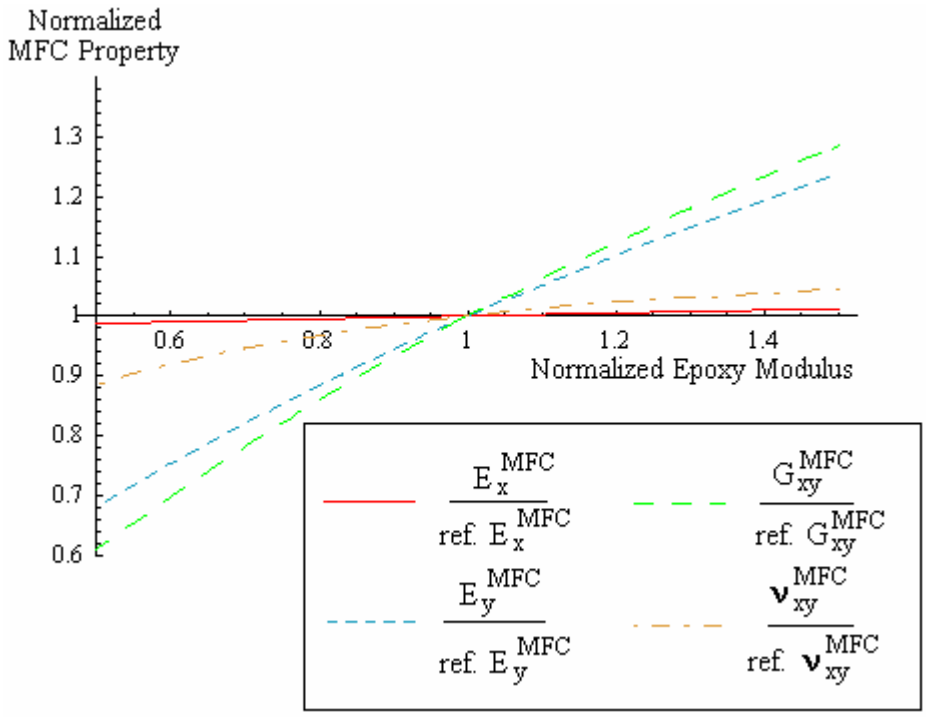

Figure 4.13: Apparent Orthotropic Moduli of the MFC for Variations in Epoxy Modulus

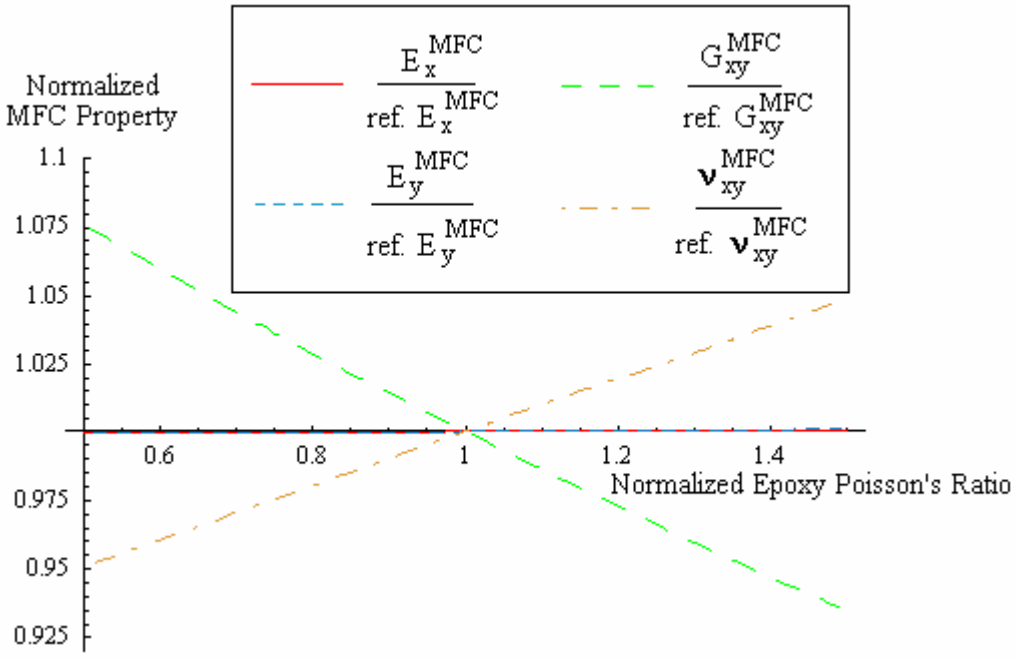

Figure 4.14: Apparent Moduli of the MFC for Variations in Epoxy Poisson's Ratio

4.4.5 Bulk PZT Material Properties

The last set of material properties to be considered for potential uncertainty is that of the poled PZT material. Since this material is transversely isotropic in a state of plane stress, there are variations in four material properties that must be considered. The nominal values for these properties are obtained from Jaffe and Berlincourt [1965]. While being almost forty years old, this document remains the industry standard for properties of piezoceramics. Figure 4.15 shows the effective properties of the MFC as a function of the modulus of the PZT in the poling direction. Clearly, the transverse, shear and Poisson's ratio of the MFC do not change much with even extreme variations in the poling direction PZT modulus. However, as may be expected, E_x of the MFC is highly sensitive to fluctuations in the PZT modulus in the poling direction.

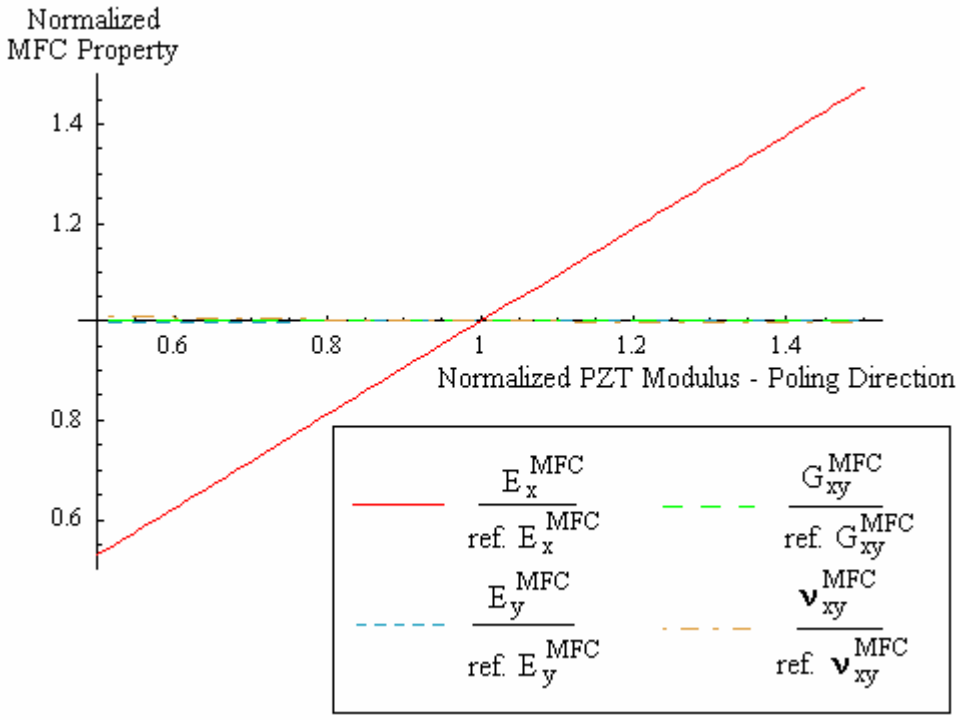

Figure 4.15: Apparent Moduli of the MFC for Variations in PZT Poling Direction Modulus

Next, Figure 4.16 shows the effective MFC properties as a function of the PZT modulus transverse to the poling direction. From this figure, it is clear that E_x and G_{xy} of the MFC

are not sensitive to variations in the modulus of the PZT transverse to the poling direction. While E_y and ν_{xy} of the MFC exhibit a noticeably nonlinear relationship to this property, the latter still only varies slightly over reasonable range of PZT modulus values. However, E_y can in fact vary about ± 5% for a ± 20% variation in the independent variable.

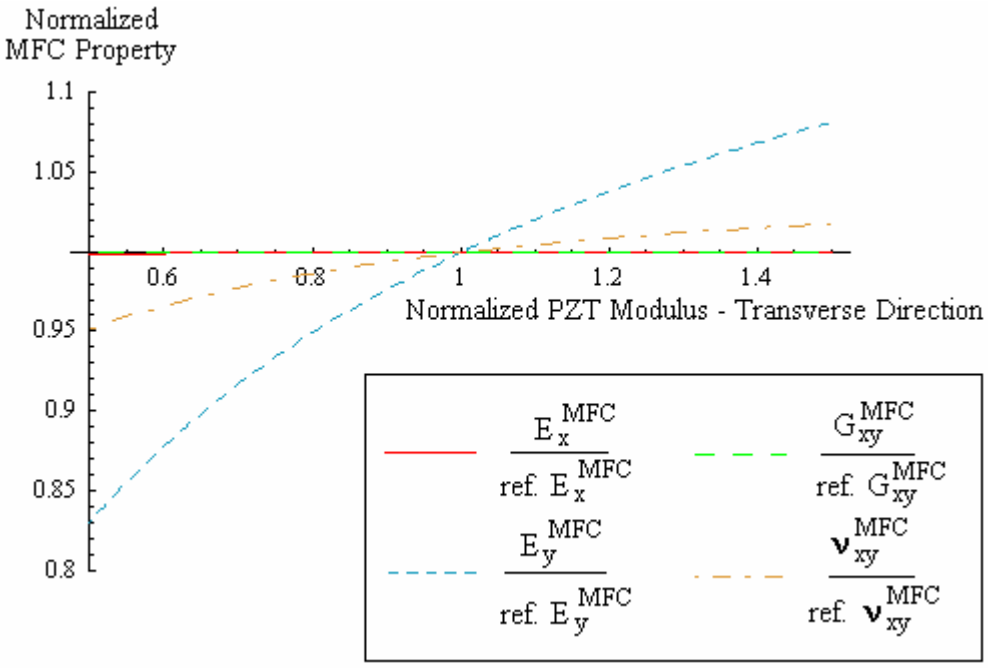

Figure 4.16: Apparent Orthotropic Moduli of the MFC for Variations in the PZT Transverse Modulus

Figure 4.17 depicts the effective MFC properties as a function of the in-plane Poisson's ratio of the PZT material. Clearly, the only property of the MFC that is sensitive to variations in this independent variable is the effective major Poisson's ratio, ν_{xy}. This effective property varies nearly linearly with the independent variable, such that a ± 5% variation results in about a ± 5% change in predicted ν_{xy}.

The last material property under consideration is the in-plane shear modulus of the poled PZT fibers. From Figure 4.18, the longitudinal and transverse moduli and Poisson's ratio of the MFC do not depend on this shear modulus at all. A careful

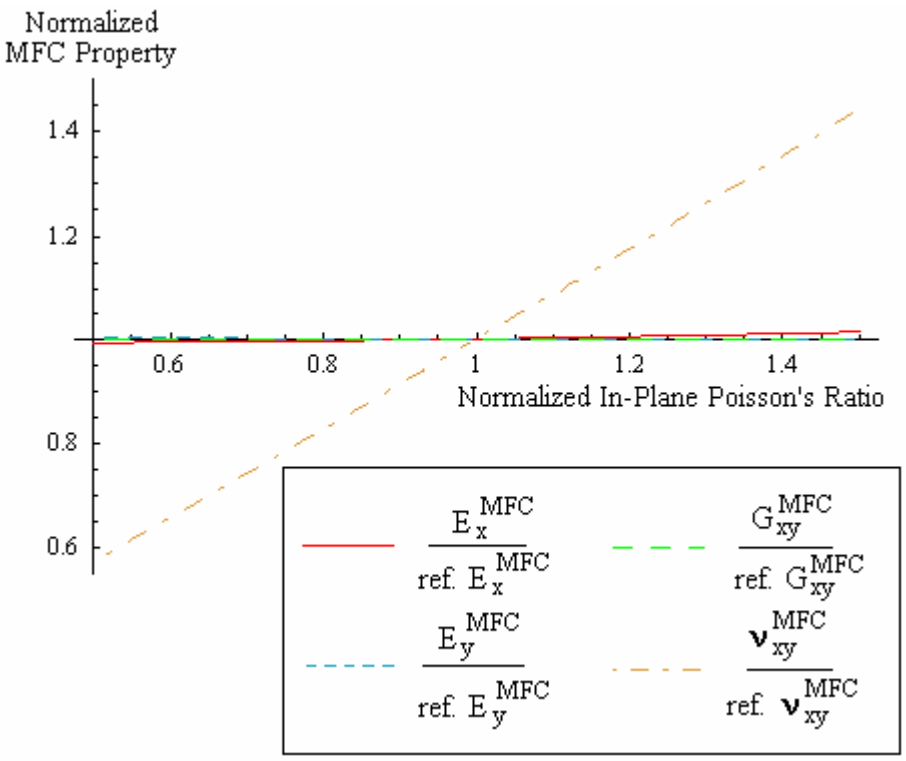

Figure 4.17: Apparent Orthotropic Moduli of the MFC for Variations in the PZT In-Plane Poisson's Ratio

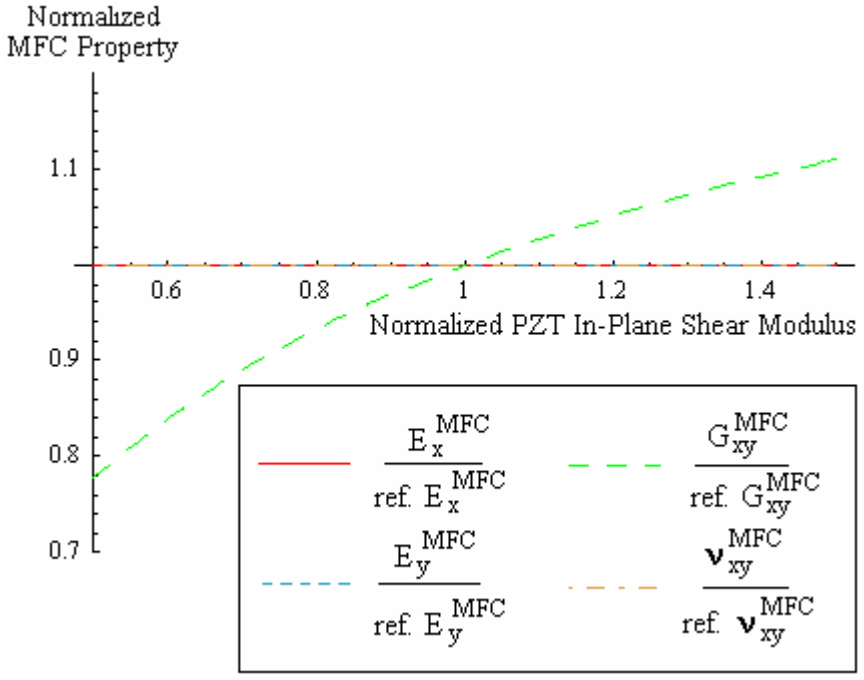

Figure 4.18: Apparent Orthotropic Moduli of the MFC for Variations in the PZT In-Plane Shear Modulus

examination of the compliance tensor for an orthotropic material shows that the various shear responses are related through only a shear modulus, as none of the other compliances contribute to the shear deformation. In contrast, Figure 4.18 indicates a strong, nonlinear dependence of G_{xy} of the MFC on the in-plane shear modulus of the poled PZT fibers. In particular, a ± 20% variation in the independent variable results in about a ± 10% change in the predicted MFC shear modulus.

4.4.6 Summary of Material Property Uncertainty Analysis:

This section uses a more quantitative method to determine how variations in constituent material properties affect the apparent MFC properties. From the plots above where a material property is allowed to vary as the independent variable, the derivative around the nominal value was calculated. The derivative was approximated by finding the slope through two data points, one at one percent above and the other one percent below the nominal value of that particular property. Since most of the relationships are nearly linear, this method of approximation returns reasonably accurate results.

The calculated derivatives (multiplied by 1000) are presented in Table 4.1 for each of the constituent material properties of interest and for each of the four independent apparent properties of the MFC. A large tabulated value is indicative of a large impact of that variable on the predicted MFC property. The most significant factors have been highlighted, and a few important conclusions are made. First, the Kapton and acrylic material properties do not affect the predicted behavior of the MFC in a significant manner. Thus the handbook values used for acrylic are acceptable for future research, while the reliable figures from DuPont for Kapton are equally as suitable. Next, the copper modulus only significantly impacts properties in the *y*-direction. Such a conclusion is reasonable because the electrodes are aligned in this direction. The Poisson's ratio of copper is not a significant factor in these models, and since its value is well-established, no further consideration is needed. From the table, the clearly

dominant properties are those of the PZT and epoxy. The modulus of the epoxy is of particular concern for two reasons. First, the properties of the MFC are shown to be particularly sensitive to variations in this property. Second, a good value for this property was not available from the material supplier. Finally, changes in the transversely isotropic properties of the PZT fibers were found to *only* significantly impact those in their respective directions. That is, the longitudinal modulus of the MFC is highly sensitive to changes in the PZT poling direction modulus, while the in-plane shear modulus of the MFC is quite sensitive to the in-plane shear modulus of the PZT material.

Table 4.1: Derivative of Effective MFC Moduli at Nominal Material Property Value

Material Property Allowed to Vary	Slope at nominal value (x1000)			
	E_x	E_y	G_{xy}	ν_{xy}
Kapton Modulus	13.49	25.49	29.72	3.257
Kapton Poisson's Ratio	0.3913	3.530	-7.542	30.58
Acrylic Modulus	7.290	13.82	15.93	2.248
Acrylic Poisson's Ratio	0.2793	2.104	-4.130	17.28
Copper Modulus	9.624	192.5	0.3551	-182.9
Copper Poisson's Ratio	-0.6010	0.5188	-0.0840	6.048
Epoxy Modulus	24.48	545.5	659.1	135.1
Epoxy Poisson's Ratio	0.223	1.142	-140.1	98.12
PZT Poling Direction Modulus	944.5	3.591	0	-10.56
PZT Transverse Modulus	0.625	219.0	0	52.91
PZT Shear Modulus	20.25	-3.246	867	0.0
PZT Poisson's Ratio	0	0	0.0	295

4.5 Summary:

This chapter presents a quantitative investigation into how the effective orthotropic engineering properties, E_x, E_y, υ_{xy}, and G_{xy}, of the MFC under short-circuit conditions for linear-elastic behavior vary with both geometric design variables and uncertainty in constituent material properties. First, the fiber volume fractions of the electrode and

PZT fiber layers can be altered during processing to achieve particular desired properties for the final MFC package. Also, some design changes can be made to the effective MFC properties by selecting different copper-clad Kapton electrode sheets and PZT layer thicknesses. As for variations in material properties, the Kapton and acrylic values are found to be satisfactory. A small amount of investigation could be done for the copper properties, but on a thin-film rather than a bulk material basis. The PZT material properties are indeed critical to obtaining accurate predictions, but the most complete and well-accepted values from the literature and material suppliers are used for the present study. Most importantly, the properties of the epoxy need to be better characterized since uncertainty in the epoxy modulus affects E_y, υ_{xy}, and G_{xy} of the MFC in a quite significant manner and reliable values from the material supplier are not available. From Table 3.4, the largest percent errors were in the transverse and in-plane shear moduli of the MFC. These properties are well-known to be matrix-dominated, so a large source of error in the predicted values could be from having unreliable epoxy properties. Future researchers in search of higher fidelity models will want to begin with mechanical property testing of the structural epoxy used for their MFC manufacturing.

Chapter 5

Nonlinear Piezoelectric Response of the Macro Fiber Composite to Monotonically Increasing Electric Fields

5.1 Introduction:

To this point, the current modeling and experimental characterization of MFC actuators has dealt with only mechanical behavior under constant, i.e. zero, electric field boundary conditions, imposed in practice by short-circuiting the actuator's power leads. While the parameters obtained from this type of analysis are critical for a complete electromechanical characterization of the MFC, the actuation capability of the device is inherently disregarded. Thus, in this chapter and the next, the MFC is subjected to a variety of driving voltages and mechanical stresses in order to characterize its nonlinear actuation capability. This chapter will focus on the response to a monotonic increase in actuation voltage, while the next will deal with the hysteretic response to harmonic excitations. After a review of literature pertinent to the nonlinear response of piezoceramics to monotonic loads, a nonlinear piezoelectric model is developed. The complete experimental characterization procedure is then outlined, and the resulting experimental data is used to determine the relevant model parameters for

the reference configuration MFC actuator. The same set of experimental data is used in a slightly different manner to develop the models in Chapter 6.

5.2 Background on Nonlinear Piezoelectric Behavior:

From their study of crystal structures, Pierre and Jacques Curie discovered the piezoelectric effect in 1880. Piezoelectricity, whose prefix *piezo-* is derived from the Greek word for *to press*, is an interaction between electrical and mechanical systems. The direct or generator piezoelectric effect is when a material produces an electrical polarization in response to an applied mechanical stress. In contrast, the converse or motor piezoelectric effect occurs when a material develops a mechanical strain in response to an applied electric field. The basic, linear piezoelectric behavior under various mechanical and electrical configurations was outlined in a simplified manner in trade manuals such as Piezo Systems, Inc. [1998] and Morgan Matroc, Inc. [1997]. However, a much more rigorous and academic version of piezoelectricity was presented in the text by Ikeda [1996].

The IEEE Standard on Piezoelectricity [ANSI/IEEE, 1987] is the comprehensive guide for piezoelectric materials. All aspects of linear piezoelectric behavior are presented, including various forms of the constitutive equations, crystallography applied to piezoelectric crystals, and vibratory behavior of rods, disks and, plates. Nonlinear topics are also mentioned briefly, however it is noted that quasistatic measurements or piezoceramics are subject to considerable variation based upon the magnitude of the mechanical stress or applied electric field, and that measurements taken at resonance are typically more accurate. However, better results are obtained under some sort of periodic excitation, rather than a strictly static application of electric field. Other covered topics of interest to the current work are determination of the elastic, piezoelectric, and dielectric constants.

In his classic paper, Toupin [1956] reviewed relevant topics in kinematics of a continuum, theory of stress, and the Maxwell-Faraday electrostatics. Then, the notion of two-point tensor fields and how they apply to continuum mechanics was presented as part of a review of Euclidian tensorial notation. He then developed the general theory of static electroelasticity for a continuum using a variational approach, which resulted in seven nonlinear differential equations in seven unknowns. These equations were then specialized for an isotropic dielectric ellipsoid and an infinite slab exposed to a uniform electric field. Then, the general theory was again specialized by assuming a special form of the stored energy function so that a comparison with existing approximation techniques for stress and electric field relationships in dielectrics could be made.

Tiersten produced a wealth of literature dealing with the behavior of piezoelectric materials. His earlier work dealt with linear piezoelectric theory and the vibration of piezoelectric plates [Tiersten, 1969]. Later, he presented a simplified form of the work by Toupin by utilizing a different thermodynamic function in place of the internal stored energy function and by expressing the electrostatic field in terms of the electric scalar potential. The result was a rotationally invariant description of thermoelectroelasticity consisting of five differential equations in five unknown variables, and only four equations and unknowns if thermal effects are ignored [Tiersten, 1971]. This nonlinear formulation was then reduced to a 2-dimensional approximation and applied to relatively thin [Tiersten, 1993a] and very thin [Tiersten, 1993b] piezoelectric plates, which are subjected to large electric fields. In these particular works, the strains were considered to be small, but the nonlinearities arose from higher-order representation of the electric fields. The work dealing with relatively thin plates was analogous to thin plate theory, while that dealing with very thin plates was comparable to membrane theory, in which bending stiffness is ignored.

Chattopadhyay, Gu, and Liu [1999] modeled smart composite box beams, which represented helicopter rotor blades, where the piezoelectric actuation was represented as a nonlinear induced strain from monolithic piezoceramics. The nonlinearities resulted from the application of strong actuation voltages; hence the model was linear in displacement gradients, but cubic in electric field. A first-order Taylor series was proposed to represent the weakly nonlinear actuation behavior, where the piezoelectric strain constants depended on the actual strain in the actuator and was determined from the experimental results given by Crawley and Lazarus [1989]. Furthermore, about 4% and 10% more tip deflection of the beam was predicted using the nonlinear actuation model for graphite/epoxy and glass/epoxy, respectively. The difference in these values implied that nonlinear actuation effects became more important on less stiff structures, as the glass/epoxy was more flexible than the graphite/epoxy. This finding is significant for researchers working with Gossamer-type structures.

Bent [1997] also briefly covered the nonlinear actuation behavior exhibited by the AFC under high electric fields (~25 kV/cm peak-to-peak). He found that the effective piezoelectric strain constants, d_{33} and d_{31}, varied greatly with electric field for free-strain tests, but only by a small amount when incorporated into a laminate. Because the nonlinearities were much less distinct when restrained, he concluded that that the nonlinearities were strain-based, rather than electric field-based. Consequently, the strain-based nonlinearities of the piezoceramic led to lower actuation authority than predicted from a linear theory. He recommended for future work, that the actuators be tested near the stress levels that they will be asked to perform under, which constitutes a major portion of the current work.

Joshi [1992] derived both linear and nonlinear forms of the piezoelectric constitutive equations from a thermodynamic standpoint, employing an expression for the Gibbs potential, where the stress, electric field, and temperature are the independent variables. The second-order model was reduced a bit by ignoring nonlinear mechanical

behavior, as ceramics are considered linearly-elastic to failure. Nonlinear dielectric properties were also neglected. However, the second-order electrical effects were found to be important for high electric fields, particularly under combined electrical and mechanical loading.

In a work of critical importance to the current effort [Tan and Tong, 2002b], a one-dimensional model for nonlinear electromechanical behavior was developed for round cross-section piezoceramic fiber-reinforced composites based on experimental results. The effects of stress applied in the fiber direction on the strain-field loops was investigated for several types of piezoelectric materials and composites. The stress-field behavior was also investigated as a function of piezoelectric fiber volume fraction, and applied strain level in the fiber direction.

Wang et al. [1999] used a second-order nonlinear model for the piezoceramic, where both the mechanical and electrical higher order behavior was included. Such a model was expressed such that the typical linear piezomechanical parameters, i.e. stiffnesses and piezoelectric strain constants, were both functions of stress and electric field. The nonlinear mechanical behavior resulted in stiffness changes that ultimately changed the natural frequencies of a RAINBOW actuator. The nonlinear model also more closely predicted the tip deflection and blocking force of a cantilevered beam with an attached RAINBOW actuator.

Thornburgh and Chattopadhyay [2001] presented a fully-coupled piezomechanical model for composite laminates which included nonlinear piezoelectric effects for embedded or surface mounted sensors and actuators. A higher-order laminate theory was used to include transverse shear effects for thicker laminates, and a fourth-order electric potential distribution was used to be compatible with the higher-order strain. Their model was developed using Hamilton's principle, and then discretized to provide a finite element formulation. The model was used to predict the deflections of several

smart structures, including a cantilevered plate and a graphite-epoxy-PZT sandwich, which was then compared with experimental data. It was found that the fully-coupled model was better at predicting the deformation of the structure. Furthermore, the d_{ij} parameters were represented from experimental data in two ways, as linear functions of both strain and electric field. It was found that the model using a coupled, nonlinear strain-based piezoelectric strain parameters provided a better fit to the data than the electric field-based model.

Cao and Evans [1993] subjected ferroelectric ceramics to high compressive stresses which resulted in nonlinear deformations and consequently reductions in actuation performance. Phenomonoligical nonlinear constitutive laws were developed from experimental data for several different material systems, and the mechanical nonlinearities were attributed to ferroelastic domain switching. Also, electrically "hard" PZT sustained higher mechanical loads without significant permanent deformations, while "soft" PZT exhibited a great deal of residual deformation even under much lower stress levels. These trends were significant as both materials were listed as having approximately the same "yield" strength. The overbearing conclusion is that hard PZT material is much better suited to handle high stress applications with lower likelihood of depoling. In contrast, relaxor ferroelectrics were shown to perform very well under large stresses without displaying significant nonlinear deformation or hysteresis. Thus, these types of devices were recommended for high-force, high-displacement actuation.

Fang and Li [1999] tested the piezoelectric behavior of PZT subjected to electromechanical loading, where the mechanical loading was compressive in nature. The short-circuit stress-strain performance was also tested. Experimental results showed the strain-field butterfly loops, stress-strain curves and also the electric displacement-electric field loops under various compressive stresses. The electromechanical behavior was seen to be linear under low stress and field levels,

while nonlinearities occur at higher load levels. Discussion of the domain switching behavior was developed into a criteria model for such behavior.

Chaplya and Carman [2001] characterized the electromechanical behavior of PZT-5H subjected to large electrical and mechanical loads. The application of a mechanical prestress was seen to change the dielectric and piezoelectric response of the specimen, which was attributed to non-180° domain wall motion. Key results presented strain-field and polarization-field curves as a function of compressive prestress, and the motion of the domain walls was described at points on these curves.

5.3 Reversible Nonlinear Piezoelectric Model:

At this point, a nonlinear piezoelectric constitutive model is proposed, and the experimental data will be used afterwards to determine the material properties of the reference MFC corresponding to this model. In Chapters 5 and 6, standard piezoelectric subscript notation will be followed, instead of the standard composites notation used in Chapters 2 and 3. This change of coordinates is depicted in Figure 5.1.

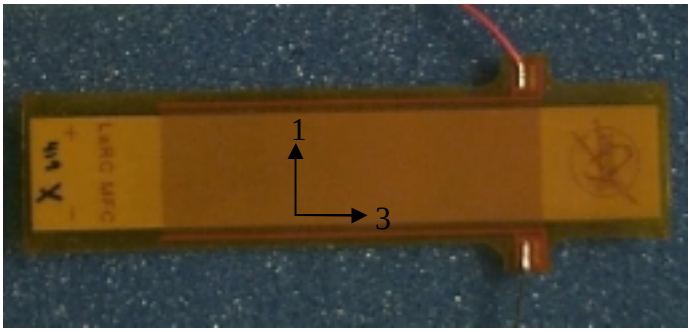

Figure 5.1: MFC Load-Actuation Test Specimen and Piezoelectric Coordinate System

Following the nonlinear derivation of Joshi [1992], the Gibbs thermodynamic potential is given as

$$G = U - \sigma_{ij}\varepsilon_{ij} - E_k\hat{D}_k - TS \tag{5.1}$$

where U is the internal energy, σ_{ij} is the stress tensor, ε_{ij} is the strain tensor, E_k is the electric field vector, $\hat{D}_k$ is the electric displacement vector, T is the absolute temperature and S is the entropy. For this derivation, stress, electric field and temperature are considered to be the independent variables. Thus, the total differential of the Gibbs potential is

$$\mathrm{d}G = \mathrm{d}U - \sigma_{ij}\mathrm{d}\varepsilon_{ij} - \varepsilon_{ij}\mathrm{d}\sigma_{ij} - E_k\mathrm{d}\hat{D}_k - \hat{D}_k\mathrm{d}E_k - T\mathrm{d}S - S\mathrm{d}T \tag{5.2}$$

but for an adiabatic reversible system, the differential of the internal energy is

$$\mathrm{d}U = \sigma_{ij}\mathrm{d}\varepsilon_{ij} + E_k\mathrm{d}\hat{D}_k + T\mathrm{d}S \tag{5.3}$$

Substitution of Equation 5.3 into 5.2 yields the following simplified expression for the total differential of the Gibbs potential:

$$\mathrm{d}G = -\varepsilon_{ij}\mathrm{d}\sigma_{ij} - \hat{D}_k\mathrm{d}E_k - S\mathrm{d}T \tag{5.4}$$

Expansion of Equation 5.4 using a first-order Taylor series gives

$$\mathrm{d}G = \left(\frac{\partial G}{\partial \sigma_{ij}}\right)_{E,T}\mathrm{d}\sigma_{ij} + \left(\frac{\partial G}{\partial E_k}\right)_{\sigma,T}\mathrm{d}E_k + \left(\frac{\partial G}{\partial T}\right)_{\sigma,E}\mathrm{d}T \tag{5.5}$$

where the subscripts on the partial derivatives indicate a constant value of the specified independent variables. Comparison of the last two equations shows that the dependent variables can be expressed as

$$\varepsilon_{ij} = -\left(\frac{\partial G}{\partial \sigma_{ij}}\right)_{E,T} \qquad \hat{D}_k = -\left(\frac{\partial G}{\partial E_k}\right)_{\sigma,T} \qquad S = -\left(\frac{\partial G}{\partial T}\right)_{\sigma,E} \tag{5.6}$$

At this point, temperature changes will be neglected to match the scope of the current work, thus rendering the entropy quantity irrelevant. Since a nonlinear formulation is desired, the total differential of the dependent variables are related to the independent variables by including second-order terms in the Taylor series expansion, thus

$$\begin{aligned} \mathrm{d}\varepsilon_{ij} &= \left(\frac{\partial \varepsilon_{ij}}{\partial \sigma_{lm}}\right)_E \mathrm{d}\sigma_{lm} + \left(\frac{\partial \varepsilon_{ij}}{\partial E_n}\right)_\sigma \mathrm{d}E_n \\ &+ \frac{1}{2}\left[\left(\frac{\partial^2 \varepsilon_{ij}}{\partial \sigma_{lm}\partial \sigma_{pq}}\right)_E \mathrm{d}\sigma_{lm}\mathrm{d}\sigma_{pq} + \left(\frac{\partial^2 \varepsilon_{ij}}{\partial E_n \partial E_r}\right)_\sigma \mathrm{d}E_n \mathrm{d}E_r + 2\left(\frac{\partial^2 \varepsilon_{ij}}{\partial \sigma_{lm}\partial E_n}\right)\mathrm{d}\sigma_{lm}\mathrm{d}E_n\right] \end{aligned} \tag{5.7}$$

and

$$\begin{aligned} \mathrm{d}\hat{D}_k &= \left(\frac{\partial \hat{D}_k}{\partial \sigma_{lm}}\right)_E \mathrm{d}\sigma_{lm} + \left(\frac{\partial \hat{D}_k}{\partial E_n}\right)_\sigma \mathrm{d}E_n \\ &+ \frac{1}{2}\left[\left(\frac{\partial^2 \hat{D}_k}{\partial \sigma_{lm}\partial \sigma_{pq}}\right)_E \mathrm{d}\sigma_{lm}\mathrm{d}\sigma_{pq} + \left(\frac{\partial^2 \hat{D}_k}{\partial E_n \partial E_r}\right)_\sigma \mathrm{d}E_n \mathrm{d}E_r + 2\left(\frac{\partial^2 \hat{D}_k}{\partial \sigma_{lm}\partial E_n}\right)\mathrm{d}\sigma_{lm}\mathrm{d}E_n\right] \end{aligned} \tag{5.8}$$

The following common linear electromechanical material properties are defined from the above two equations as

$$s^E_{ijlm} = \left(\frac{\partial \varepsilon_{ij}}{\partial \sigma_{lm}}\right)_E \qquad \varepsilon^\sigma_{kn} = \left(\frac{\partial^2 \hat{D}_k}{\partial E_n}\right)_\sigma \qquad d_{ijn} = \left(\frac{\partial \varepsilon_{ij}}{\partial E_n}\right)_\sigma = \left(\frac{\partial \hat{D}_k}{\partial \sigma_{ij}}\right)_E \tag{5.9}$$

and are referred to as the elastic compliance, dielectric permittivity, and piezoelectric strain coefficients, respectively. The newer, nonlinear properties are defined as

$$s^{E}_{ijlmpq} = \left(\frac{\partial^2 \varepsilon_{ij}}{\partial \sigma_{lm} \partial \sigma_{pq}} \right)_E \qquad d_{ijnr} = \left(\frac{\partial^2 \varepsilon_{ij}}{\partial E_n \partial E_r} \right)_\sigma = \left(\frac{\partial^2 \hat{D}_k}{\partial \sigma_{lm} \partial E_n} \right)$$

$$\varepsilon_{knr} = \left(\frac{\partial^2 \hat{D}_k}{\partial E_n \partial E_r} \right)_\sigma \qquad \kappa_{ijlmn} = \left(\frac{\partial^2 \varepsilon_{ij}}{\partial \sigma_{lm} \partial E_n} \right) = \left(\frac{\partial^2 \hat{D}_k}{\partial \sigma_{lm} \partial \sigma_{pq}} \right)_E \tag{5.10}$$

and called the nonlinear elastic compliance, electrostriction, nonlinear dielectric permittivity and elastostriction coefficients, respectively. Here, Equations 5.7 and 5.8 are second-order Taylor expansions that represent the difference between an arbitrary point of interest and a reference point. Taking the reference point to be stress and electric field-free yields the two remaining dependent variables, strain and electric displacement:

$$\varepsilon_{ij} = s^{E}_{ijlm}\sigma_{lm} + d_{ijn}E_n + \frac{1}{2}s^{E}_{ijlmpq}\sigma_{lm}\sigma_{pq} + \frac{1}{2}d_{ijnr}E_nE_r + \kappa_{ijlmn}\sigma_{lm}E_n \tag{5.11}$$

and

$$\hat{D}_k = d_{klm}\sigma_{lm} + \varepsilon^{\sigma}_{kn}E_n + \frac{1}{2}\kappa_{klmpq}\sigma_{lm}\sigma_{pq} + \frac{1}{2}\varepsilon^{\sigma}_{knr}E_nE_r + d_{klmn}\sigma_{lm}E_n \tag{5.12}$$

Since piezoceramics are known to be linearly-elastic to failure and the experimental procedure was limited mostly to loads within the linear-elastic region, the nonlinear elastic compliance and permittivity will be disregarded. This assumption reduces Equations 5.11 and 5.12 to

$$\varepsilon_\alpha = s^{E}_{\alpha\beta}\sigma_\beta + d_{\alpha n}E_n + \frac{1}{2}d_{\alpha nr}E_nE_r + \kappa_{\alpha\beta n}\sigma_\beta E_n \tag{5.13}$$

and

$$\hat{D}_k = d_{k\beta}\sigma_\beta + \varepsilon^{\sigma}_{kn}E_n + \frac{1}{2}\kappa_{k\beta\gamma}\sigma_\beta\sigma_\gamma + d_{k\beta n}\sigma_\beta E_n \tag{5.14}$$

where reduced notation has been adopted in which Greek subscripts are one through six and others range from one to three. Since the current effort deals only with the actuator form of these relations, Equation 5.13, it will now be investigated for use with a piezoceramic material poled in the 3-direction. The elastic compliance matrix, which was investigated in previous chapters, is expressed as

$$\left[s^E\right] = \begin{bmatrix} s_{11} & s_{12} & s_{13} & 0 & 0 & 0 \\ s_{12} & s_{11} & s_{13} & 0 & 0 & 0 \\ s_{13} & s_{13} & s_{33} & 0 & 0 & 0 \\ 0 & 0 & 0 & s_{44} & 0 & 0 \\ 0 & 0 & 0 & 0 & s_{44} & 0 \\ 0 & 0 & 0 & 0 & 0 & \frac{1}{2}(s_{11} - s_{12}) \end{bmatrix} \tag{5.15}$$

and its corresponding stress vector is

$$\left[\sigma\right] = \left[\sigma_1, \sigma_2, \sigma_3, \sigma_4, \sigma_5, \sigma_6\right]^T \tag{5.16}$$

The piezoelectric strain constant matrix is

$$\left[d\right] = \begin{bmatrix} 0 & 0 & d_{31} \\ 0 & 0 & d_{31} \\ 0 & 0 & d_{33} \\ 0 & d_{15} & 0 \\ d_{15} & 0 & 0 \\ 0 & 0 & 0 \end{bmatrix} \tag{5.17}$$

and its corresponding electric field vector is

$$[E] = [E_1, E_2, E_3]^T \tag{5.18}$$

The electrostriction coefficients are

$$[d_{\alpha nr}] = \begin{bmatrix} d_{111} & d_{122} & d_{133} & 0 & 0 & 0 \\ d_{122} & d_{111} & d_{133} & 0 & 0 & 0 \\ d_{133} & d_{133} & d_{333} & 0 & 0 & 0 \\ 0 & 0 & 0 & d_{423} & 0 & 0 \\ 0 & 0 & 0 & 0 & d_{423} & 0 \\ 0 & 0 & 0 & 0 & 0 & \frac{1}{2}(d_{111} - d_{122}) \end{bmatrix} \tag{5.19}$$

and the quadratic electric field vector is

$$E_n E_r = [E_1^2, E_2^2, E_3^2, E_2 E_3, E_1 E_3, E_1 E_2]^T \tag{5.20}$$

The elastostriction coefficients are

$$\kappa_{\alpha\beta n} = \begin{bmatrix} \kappa_{111} & \kappa_{121} & \kappa_{131} & 0 & 0 & 0 & \kappa_{121} & \kappa_{121} & \kappa_{132} & 0 & 0 & 0 & \kappa_{131} & \kappa_{132} & \kappa_{133} & 0 & 0 & 0 \\ \kappa_{121} & \kappa_{121} & \kappa_{132} & 0 & 0 & 0 & \kappa_{121} & \kappa_{113} & \kappa_{131} & 0 & 0 & 0 & \kappa_{132} & \kappa_{131} & \kappa_{133} & 0 & 0 & 0 \\ \kappa_{131} & \kappa_{132} & \kappa_{133} & 0 & 0 & 0 & \kappa_{132} & \kappa_{131} & \kappa_{133} & 0 & 0 & 0 & \kappa_{133} & \kappa_{133} & \kappa_{333} & 0 & 0 & 0 \\ 0 & 0 & 0 & \kappa_{441} & 0 & 0 & 0 & 0 & 0 & 0 & 0 & 0 & 0 & 0 & 0 & \kappa_{443} & 0 & 0 \\ 0 & 0 & 0 & 0 & 0 & 0 & 0 & 0 & 0 & 0 & \kappa_{441} & 0 & 0 & 0 & 0 & 0 & \kappa_{443} & 0 \\ 0 & 0 & 0 & 0 & 0 & 0 & 0 & 0 & 0 & 0 & 0 & 0 & 0 & 0 & 0 & 0 & 0 & \kappa_{663} \end{bmatrix} \tag{5.21}$$

and the corresponding stress-electric field cross product vector is

$$\sigma_\beta E_n = [\sigma_1 E_1, \sigma_2 E_1, \sigma_3 E_1, \sigma_4 E_1, \sigma_5 E_1, \sigma_6 E_1, \sigma_1 E_2, \sigma_2 E_2, \sigma_3 E_2, \sigma_4 E_2, \sigma_5 E_2, \sigma_6 E_2, \sigma_1 E_3, \sigma_2 E_3, \sigma_3 E_3, \sigma_4 E_3, \sigma_5 E_3, \sigma_6 E_3]^T \tag{5.22}$$

These matrices can be further reduced for the specific case of the MFC under general loading. The use of interdigitated electrodes renders E_1 and E_2 zero, hence the only nonzero electric field is E_3. Also, since the MFC is a thin, planar actuator in a state of plane stress, only σ_1, σ_3 and σ_6 are nonzero, corresponding to stresses in the PZT fiber direction, transverse to the PZT fibers (in-plane), and in-plane shear stress, respectively. With these simplifications in mind, Equation 5.13 is written in full form as

$$\varepsilon_1 = s_{11}\sigma_1 + s_{13}\sigma_3 + d_{31}E_3 + \frac{1}{2}d_{133}E_3^2 + \kappa_{131}\sigma_1 E_3 + \kappa_{133}\sigma_3 E_3 \tag{5.23}$$

$$\varepsilon_2 = s_{12}\sigma_1 + s_{13}\sigma_3 + d_{31}E_3 + \frac{1}{2}d_{133}E_3^2 + \kappa_{132}\sigma_1 E_3 + \kappa_{133}\sigma_3 E_3 \tag{5.24}$$

$$\varepsilon_3 = s_{13}\sigma_1 + s_{33}\sigma_3 + d_{33}E_3 + \frac{1}{2}d_{333}E_3^2 + \kappa_{133}\sigma_1 E_3 + \kappa_{333}\sigma_3 E_3 \tag{5.25}$$

$$\varepsilon_6 = s_{66}\sigma_6 + \kappa_{663}\sigma_6 E_3 \tag{5.26}$$

Equation 5.24 represents the out-of-plane strain for the coordinate system defined in Figure 5.1, which is of little interest for the planar actuation of the MFC. Consequently, this equation and its unknown parameters will not be investigated any further. As for the other equations, determination of the unknown material parameters is required for a full planar characterization. The compliance terms, s_{ij}, are already known from the work presented in Chapters 2 and 3. However, as described in the next section, the experimental procedure for this initial effort involved only a unidirectional application of load parallel to the PZT fibers (3-direction). Thus σ_1 and σ_6 are also zero for this initial experimental characterization effort, rendering the determination of κ_{131} and κ_{663}

impossible, although κ_{133} can be found from Equation 5.23. Such measurements would require application of a biaxial state of stress with in-plane shear, or possibly an off-axis specimen, as was used in Chapter 3 to measure the in-plane shear behavior. Such complex states of stress are beyond the scope of this effort. With the uniaxial state of stress, the constitutive equations that govern the electromechanical behavior of the MFC are reduced to

$$\varepsilon_1 = s_{13}\sigma_3 + d_{31}E_3 + \frac{1}{2}d_{133}E_3^2 + \kappa_{133}\sigma_3 E_3 \tag{5.27}$$

$$\varepsilon_3 = s_{33}\sigma_3 + d_{33}E_3 + \frac{1}{2}d_{333}E_3^2 + \kappa_{333}\sigma_3 E_3 \tag{5.28}$$

The remaining parameters, d_{31}, d_{33}, d_{133}, d_{333}, κ_{133}, and κ_{333} give the most important parameters required for structural actuation problems using this actuator in the primary direction of actuation, along the PZT fibers. With the short-circuit stiffnesses in hand, an experimental procedure is presented in the next section to determine these six unknown parameters.

5.4 Experimental Procedure:

In order to characterize the nonlinear electromechanical behavior of the MFC actuator, five reference specimens were tested at the NASA Langley Research Center. The test procedure consisted of measuring the strain in the device while applying a series of actuation voltages at a constant, low frequency while the MFC was held at various constant applied mechanical loads by a hydraulically driven and controlled MTS universal testing machine. A schematic of the experimental setup is seen in Figure 5.2, and will be discussed in more detail below.

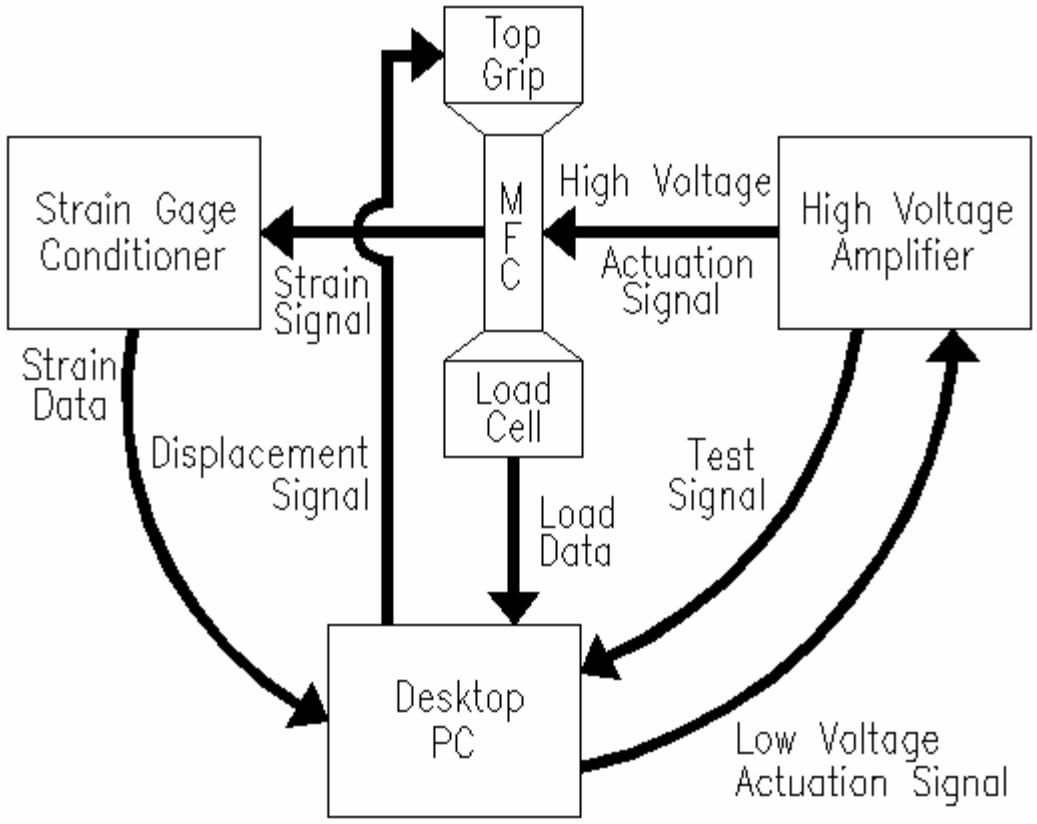

Figure 5.2: Experimental Setup

The sections below describe preparation of the specimens and the experimental equipment, setup and procedure required to collect the appropriate actuation data for both Chapters 5 and 6.

5.4.1 Specimen Preparation:

The reference MFC tensile-test specimen designed for the current effort is shown in Figure 5.1. The 3-direction corresponds to the PZT fiber direction, which is also the direction of piezoelectric poling and the direction of applied load for the experimental procedure described herein. The 1-direction is parallel to the copper electrode fingers and transverse to the PZT fibers/poling direction. The sample preparation and manufacturing procedure for these actuation tensile test specimens is the same as that

described in Chapter 3 and Appendix C. Strain gages capable of measuring both longitudinal and transverse strains simultaneously, type CEA-13-250WQ-350 from Vishay Measurements Group, were aligned with the 1-3 coordinate system seen in Figure 5.1. The gages were bonded to the center of the top and bottom of each MFC tests specimen using M-Bond AE-15 strain gage epoxy, which was cured at 150°F for two hours as suggested by the manufacturer. Strain gage leads were then attached using solder. Sandpaper tabs were added to the tab-ends of the MFC to prevent slipping of the specimen while in the grips of the tensile-testing machine.

5.4.2 Experimental Procedure:

The top tab of the specially prepared specimens described above was loaded into the top hydraulic grip of the computer-controlled MTS tensile-testing machine and the PZT fibers aligned such that the load was applied parallel to the 3-direction as seen in Figure 5.3.

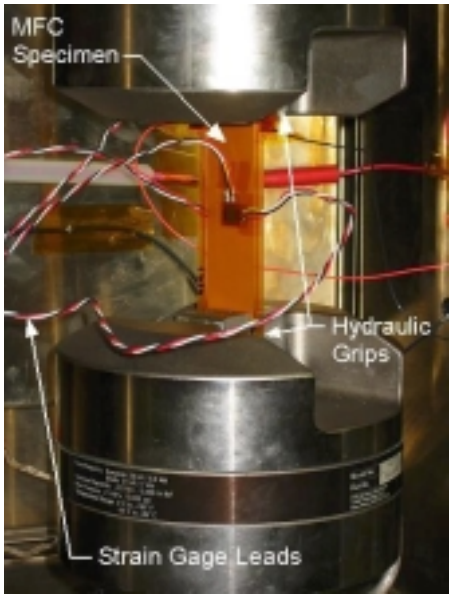

Figure 5.3: MFC Specimen Loaded into MTS Machine

The MFC leads were then connected to a high-voltage amplifier, seen in Figure 5.4, in conjunction with a software function generator on the PC set up to control this experiment and record the necessary data. Special care was taken to properly insulate and restrain the high-voltage leads where they enter the test chamber and attach to the specimen, as they are potentially hazardous.

Figure 5.4: High-Voltage Amplifier

The strain gage leads were then connected to Vishay Model 3800 Wide Range Strain Indicators, seen in Figure 5.5, which relay strain data to the computer.

With only the top tab of the properly connected strain-gauged specimen closed into the top hydraulic grip of the testing machine, the MTS TestStar IIs computer software controlled the load and voltage profiles remainder of the test while recording several channels of data; specifically test time, ambient temperature, applied load, 1 and 3-direction strains from the top and bottom gages and applied voltage and current, with each constant load and voltage level forming its own data file. First, the free-strain

behavior of the actuator was measured by actuating the specimen under Voltage Sequences 1, 2, and 3 as defined in Table 5.1.

Figure 5.5: Vishay Model 3800 Wide Range Strain Indicators

Table 5.1: Sinusoidal Voltage Sequences 1, 2, and 3 at 0.1 Hz

Voltage Sequence		
1	**2**	**3**
DC Offset Voltage		
Start → 0 →	250 →	500
Peak to Peak Voltage at 0.1 Hz		
250	250	250
500	500	500
750	750	750
1000	1000	1000
1250	1250	1250
	1500	1500
	1750	1750
		2000
		2250

Five sinusoidal electrical cycles at a frequency of 0.1 Hz were applied to the actuator at each peak-to-peak value before proceeding to the next level. These particular voltage sequences were chosen such that the MFC is never subjected to less than -650 or more than 1650 volts, which have been found to depole or cause electrical failure, respectively, in the device. The increase of the peak-to-peak and offset voltages follows the arrows in the table, and there was a 5 minute voltage-hold at the new offset value to allow the actuator to stabilize before proceeding. The voltage-time relationship applied to actuator test specimen is shown in Figure 5.6. It should be noted that the time-gaps in Figure 5.6 are where the peak-to-peak voltages were decreased from the maximum to investigate global hysteresis effects. It was decided after the experiments were complete that such behavior would be beyond the scope of the current report, although a portion of this data is used briefly in Chapter 6. Application of such lower peak-to-peak cycles does not effect future performance of the actuator significantly as PZT material is known to exhibit the "wiping out" effect [Mayergoyz, 1991].

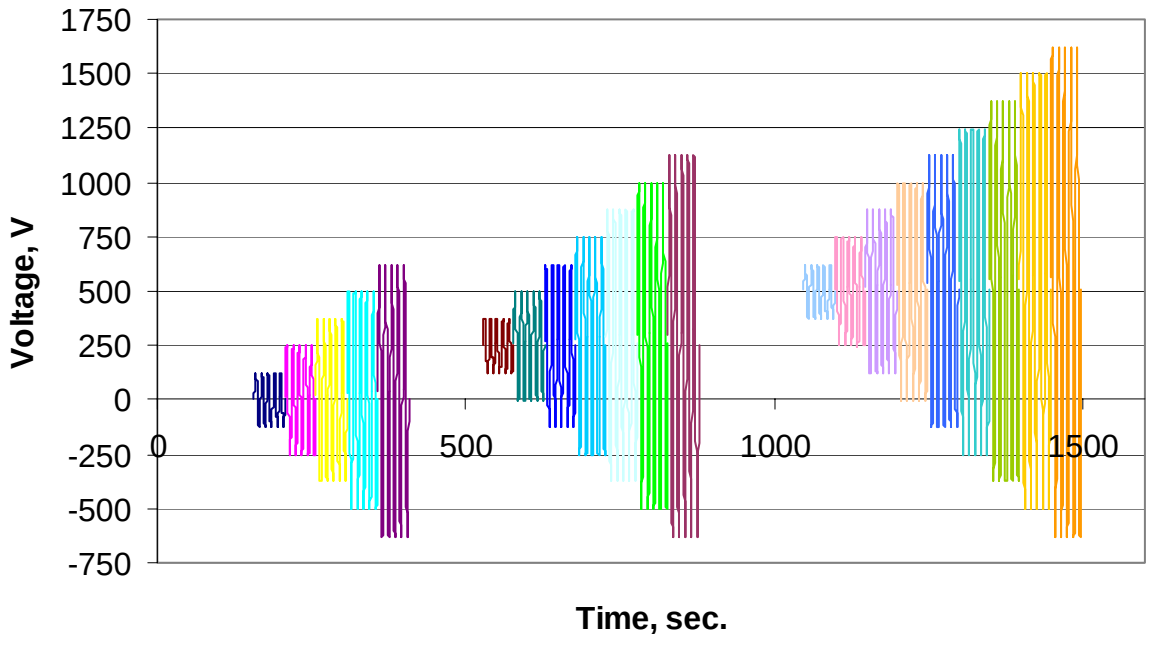

Figure 5.6: Typical Actuation Voltage Profiles

The low frequency of 0.1 Hz was chosen for three main reasons. First, such a frequency allows for the measurement of the quasistatic response, free from frequency-dependent behavior of the piezoceramic. Also, low frequency tests minimize electrical loading rate-effects in the material [ANSI/IEEE, 1987]. Lastly, actuation at such a low frequency allows the hydraulically-controlled testing machine to maintain a constant applied mechanical stress.

After the free-strain measurements were complete, the bottom grip was closed and the specimen loaded in tension to predetermined levels, which were then held constant by the hydraulic machine while the MFC was actuated under Voltage Sequences 1, 2, and 3 at each load level. The incremental load levels were chosen based on the tensile stress-strain relationship developed in Chapter 3 for the PZT fiber direction. The selected load levels are given in Table 5.2, and depicted on the short-circuit stress-strain curve in Figure 5.7.

Table 5.2: Load Levels and Calculated Average Stress on Specimen Cross-Section

Load		Stress	
Pounds	Newtons	PSI	MPa
0	0	0	0
1	4.4	84.03	0.579
10	44.5	840.34	5.794
20	89.0	1680.7	11.59
30	133.4	2521.0	17.38
40	177.9	3361.3	23.18
50	222.4	4201.7	28.97
52	231.3	4369.7	30.13
54	240.2	4537.8	31.29
56	249.1	4705.9	32.45
58	258.0	4873.9	33.60
60	266.9	5042.0	34.76

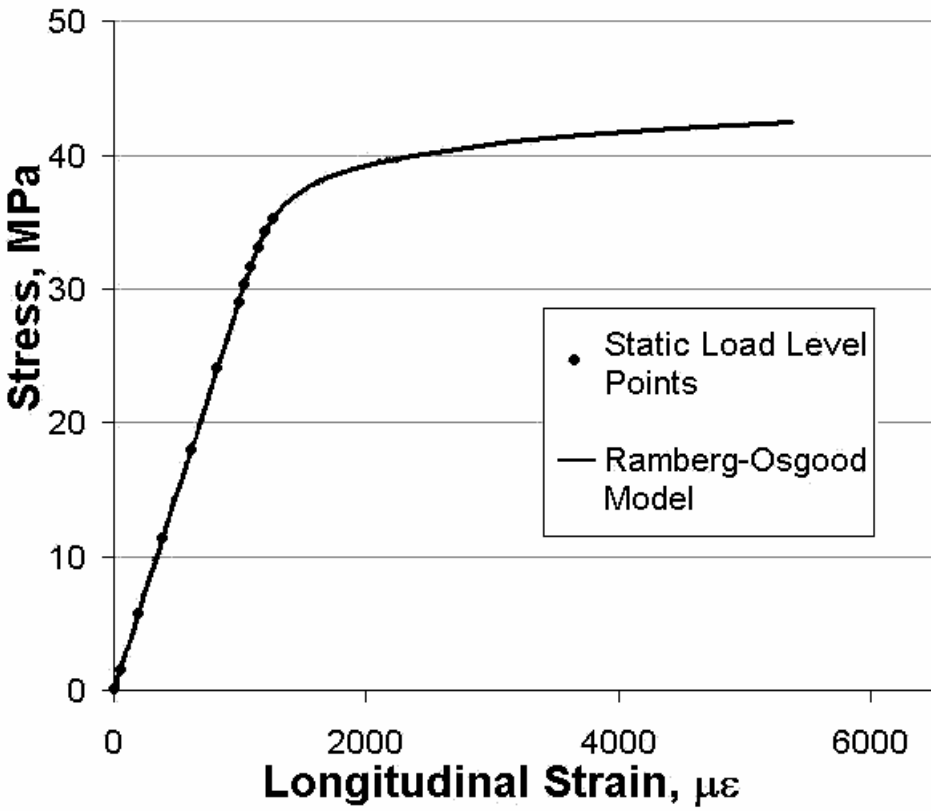

Figure 5.7: Ramberg-Osgood 3-Direction Stress-Strain Relationship and Constant Load Levels for Actuation Testing

Higher loads were not tested as specimen failure (electrical or mechanical) was prominent at such levels. As was the case for the voltage sequences, the load level was stepped down from the maximum value and the actuation performance recorded, to investigate load-based global hysteresis in the MFC. Likewise, such behavior was later deemed beyond the scope of this work. Furthermore, subjecting the actuator to the maximum load caused some fiber damage, shown by the highest data point on the stress-strain curve in Figure 5.7, which is very close to if not beyond the limit of elastic behavior for the MFC.

Since these data were acquired under the notion of constant mechanical stress, it is important to verify that the MTS closed-loop controller was able to properly maintain the desired constant stress levels. Figure 5.8 shows the stress (load divided by cross-

sectional area of the specimen perpendicular to the load) measured by the load cell on the MTS testing machine during the test time.

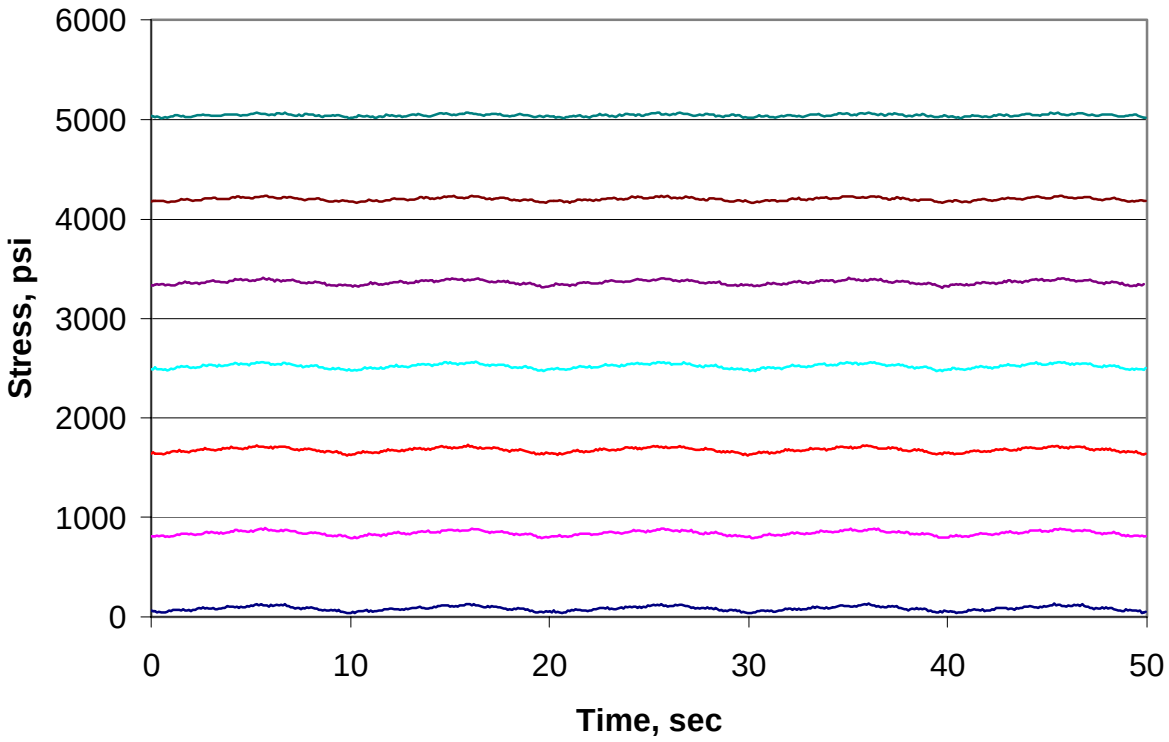

Figure 5.8: Constant Stress Levels Applied to the MFC During Actuation Testing

The particular data in Figure 5.8 is for MFC S/N 487 under 2250 volts peak-to-peak and a 500 VDC offset. Data from the most rigorous voltage sequence is presented because the ability of the control system to maintain a constant load is challenged the most under these conditions; lower voltage profiles are assumed to be easier for the machine to control accurately. Clearly, the loads are constant to within 10%, except for the lowest loads, i.e. 1 pound. Such low loads are in the range of the resolution of the load cell, so the error seen is mostly experimental noise. Thus the data analysis can proceed under the reasonably accurate presumption of constant applied stress level to the MFC actuator.

5.5 Data Analysis:

Given the extent of the testing procedure and the number of specimens, there is a large set of data files that require a close examination as well as some manipulation to obtain the desired quantities. This section serves to clarify how the experimental results are translated into useable engineering quantities for analytical purposes.

5.5.1 General Analysis:

First, given stress values represent nominal average stress on the cross-section of the specimen and are calculated by dividing the load by the area of the cross-section perpendicular to the load direction (0.0119 in^2 or $7.677x10^{-6}$ m^2). The stresses reported in Figure 5.8 are from measured loads, while the stresses used for modeling aspects are nominal stresses based on the chosen constant load levels presented in Table 5.2. Next, the measured directional strains from the top and bottom strain gages are averaged in order to remove any bending strains that are present from clamping the specimen in the hydraulic grips of the MTS testing machine. However, it should be noted that extreme care was taken to minimize the presence of such bending strains. Electric field is also a quantity that must be calculated from the experimental data. The interdigitated electrode pattern of the MFC complicates the electric field shape, as shown qualitatively in Figure 5.9.

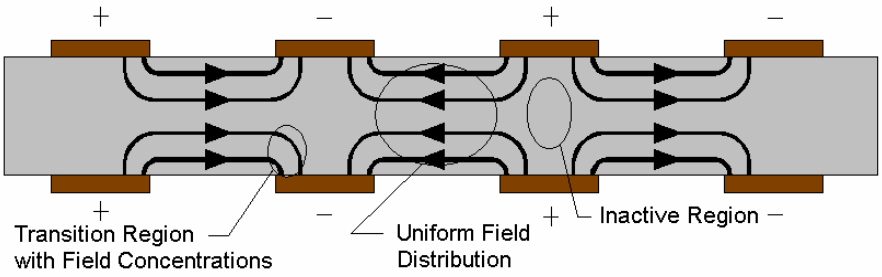

Figure 5.9: Electric Field Distribution for Interdigitated Electrode Pattern

While there exists a fair amount of literature dedicated to calculating such a complex field distribution, to do so here is beyond the scope of this work. Hence, the *average*

electric field, *E*, that is developed in the MFC actuator under the application of voltage *V* is defined as

$$E = \frac{V}{w_{pitch}} \tag{5.29}$$

where w_{pitch} is the center-to-center interdigitated electrode spacing, as illustrated in Figure 5.9. This method for calculating the average electric field is consistent with the other works, and it is from this definition that all of the models and results will be presented herein.

5.5.2 Representative Strain Output Data:

At this point, it is useful to examine a plot of the strain output measured by the strain gages in response to the voltage input shown in Figure 5.6. A typical 3-direction strain-time output plot for the free-strain (zero stress) condition is seen in Figure 5.10, while the 1-direction strains are seen in Figure 5.11. Under a constant applied stress, the curves have a similar shape, but the magnitudes are different, as will be discussed later in this chapter. The three distinct groups correspond to, from left to right, 0 VDC, 250 VDC and 500 VDC offset voltages applied to the actuator. Within each of these three groups, the different colored waves correspond to a different peak-to-peak voltage cycle.

As expected, the transverse actuation of the MFC is smaller in magnitude and opposite in sign compared to in the direction of the PZT fibers. This difference is indicative of the anisotropic actuation capability of this actuator. Such and effect is useful for exciting only certain modes in, for example, a plate structure. In other words, the MFC has the capability to induce a different radius of curvature along one direction of the plate than in another. This feature is *not* exhibited by monolithic actuators with uniform electrode patterns.

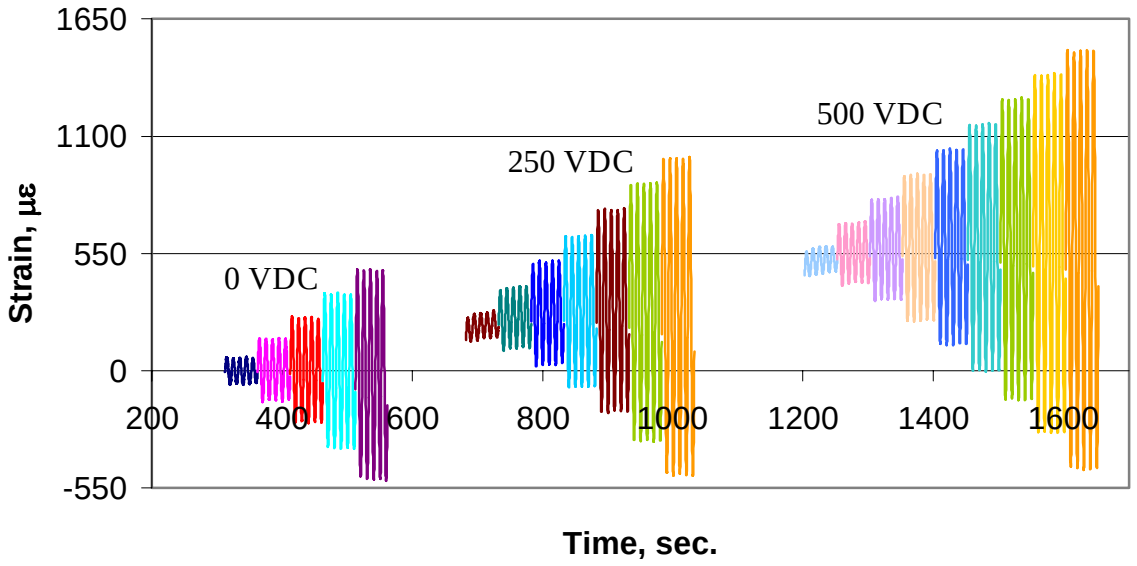

Figure 5.10: Typical 3-Direction Free-Strain Output for Voltage Input of Figure 5.6 for MFC S / N 404

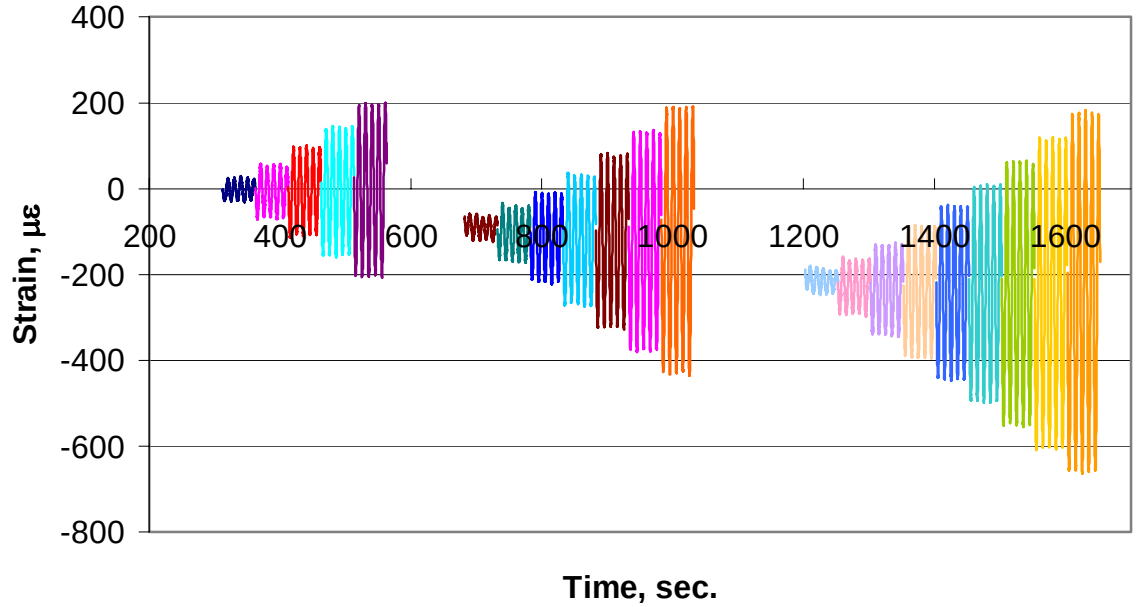

Figure 5.11: Typical 1-Direction Free-Strain Output for Voltage Input of Figure 5.6 for MFC S / N 404

The representative strain outputs from Figures 5.10 and 5.11 roughly oscillate about the same strain level for the three respective offset voltages. Such was the case, in general, for three of the tested MFC specimens, S/N 404, 415, and 424. However, in an effort to obtain a full set of five fully tested specimens, MFC S/N 486 and 487 were manufactured and tested. These two were poled and then actuation-tested on the same day, and were not aged or run-in with electrical cycles properly. As an unexpected result, the strain output data contained a significant amount of piezoelectric drift, as seen in Figures 5.12 and 5.13.

The drift is evident, particularly in the 0 VDC offset case as the data do not oscillate about a horizontal line, but rather, a line slanted downward. The strains tend to drift in the negative direction for the 3-direction response, and in the positive direction for the 1-direction strains. In fact, one can see that when the 250 VDC offset is applied, the measured strain is still negative (positive for the 1-direction). This drift must be artificially removed from the data in order to obtain a meaningful characterization.

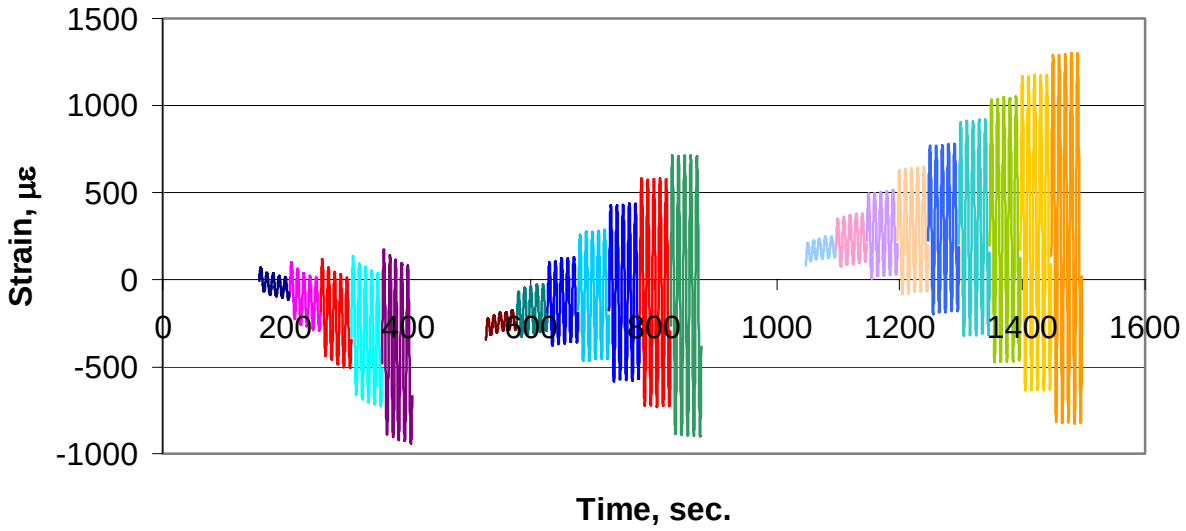

Figure 5.12: 3-Direction Free-Strain Output for Voltage Input of Figure 5.6 for MFC S/N 487 Showing Significant Piezoelectric Drift

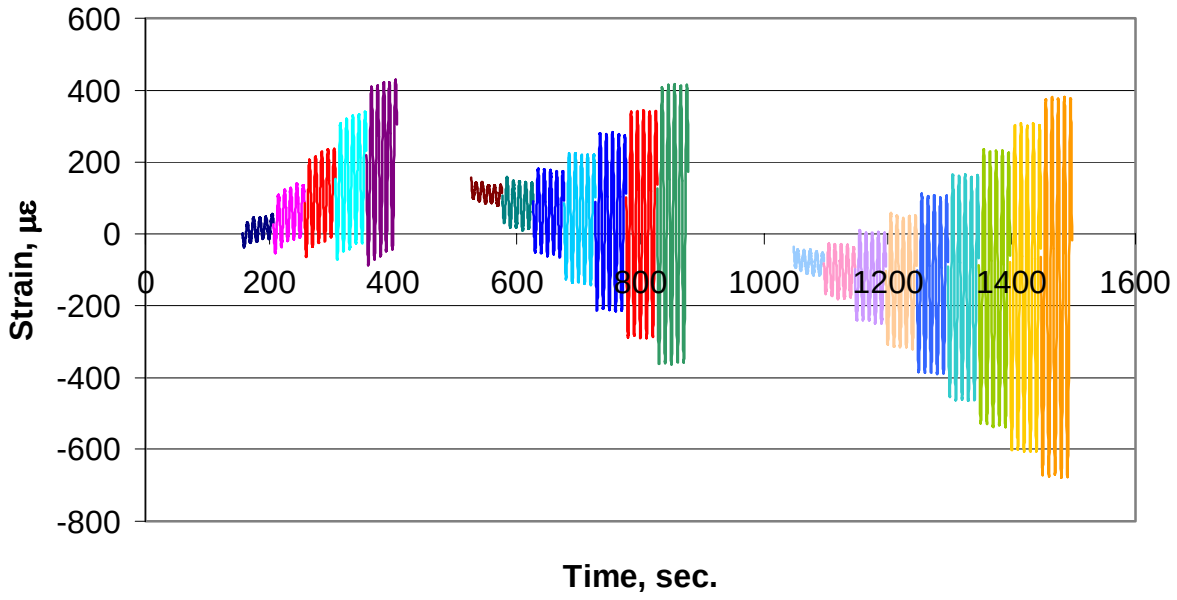

Figure 5.13: 1-Direction Free-Strain Output for Voltage Input of Figure 5.6 for MFC S/N 487 Showing Significant Piezoelectric Drift

5.5.3 Drift Removal and Quadratic Regression – Free-Strain:

This section focuses on removing the drift from the collected data and then performing the necessary quadratic regressions on the data to identify the material parameters for the model developed in Section 5.3. During the course of these experiments, it was found that less drift occurs if a specimen is allowed to sit with its power leads unattached to a power source for an extended amount of time, or if the specimen is run-in under a moderate voltage profile for a few thousand electrical cycles. Either method allows the piezoelectric behavior to settle, thus reducing ageing effects.

5.5.3.1 Zero VDC Offset Voltage – Free-Strain:

While the strain-time response is presented in Figures 5.10 through 5.13, the important piezoelectric parameters are obtained from strain-electric field plots. Representative plots of the entire strain-electric field loop data are shown in Figures 5.14 and 5.15 for MFC S/N 404, 0 VDC, 1250 volts peak-to-peak and zero stress. The initial monotonic response of interest to this chapter is identified.

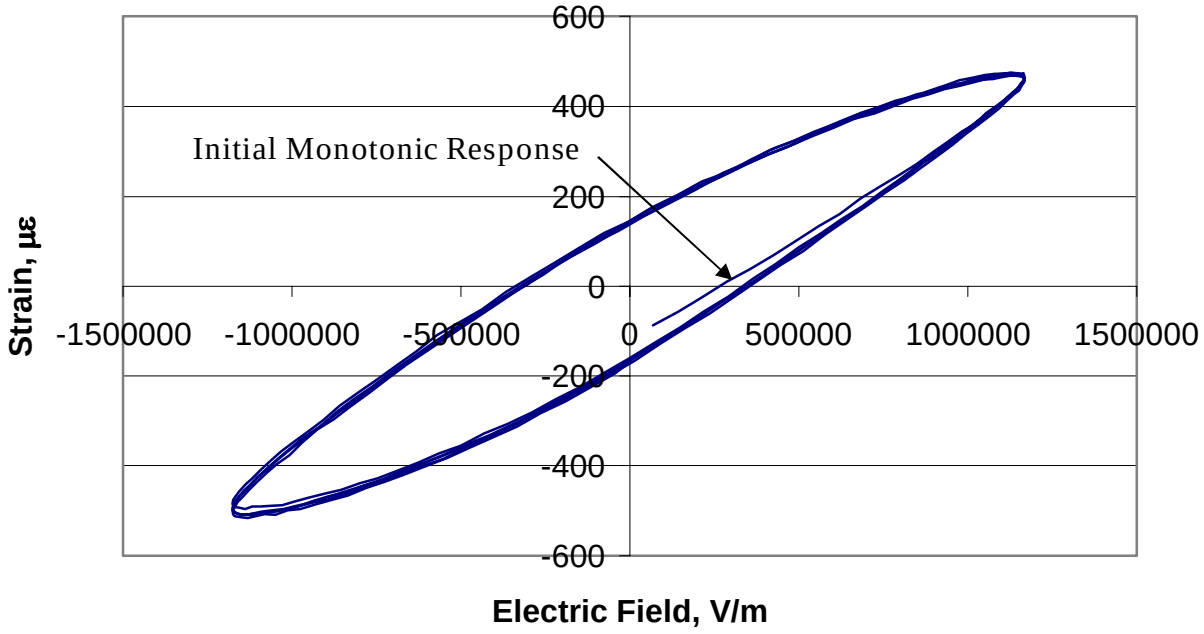

Figure 5.14: 3-Direction Strain-Electric Field Behavior for MFC S/N 404, 1250 volts Peak-to-Peak, 0 MPa

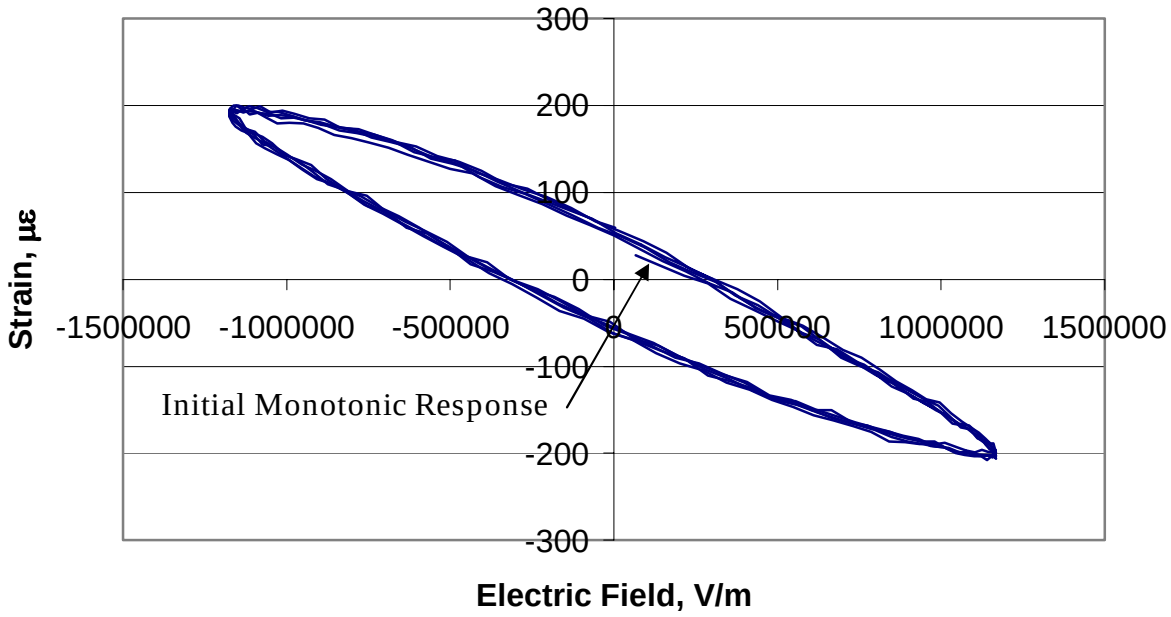

Figure 5.15: 1-Direction Strain-Electric Field Behavior for MFC S/N 404, 1250 volts Peak-to-Peak, 0 MPa

The initial response data is isolated by including only those for increasing electric field, except the peak six points which correspond to the changing of direction of the input sine wave. Inclusion of those six data points would induce a nonlinear appearance to the data that is not part of the response, but rather the output following an extremely curved input (top of the sine wave). Nevertheless, the data from the most linear part of the voltage input wave has some nonlinearity that should be investigated. With these data in hand, a second-order polynomial fit is performed in Microsoft Excel on the strain-field data according to the nonlinear model from Section 5.3, which indicates a quadratic relationship between these two variables. Representative plots of these data are shown in Figures 5.16 and 5.17 for MFC S/N 404 under free stress conditions and 0 VDC offset voltage. The various quadratic regression equations and their curves are also seen in the figures, and as expected, the fits match the data closely.

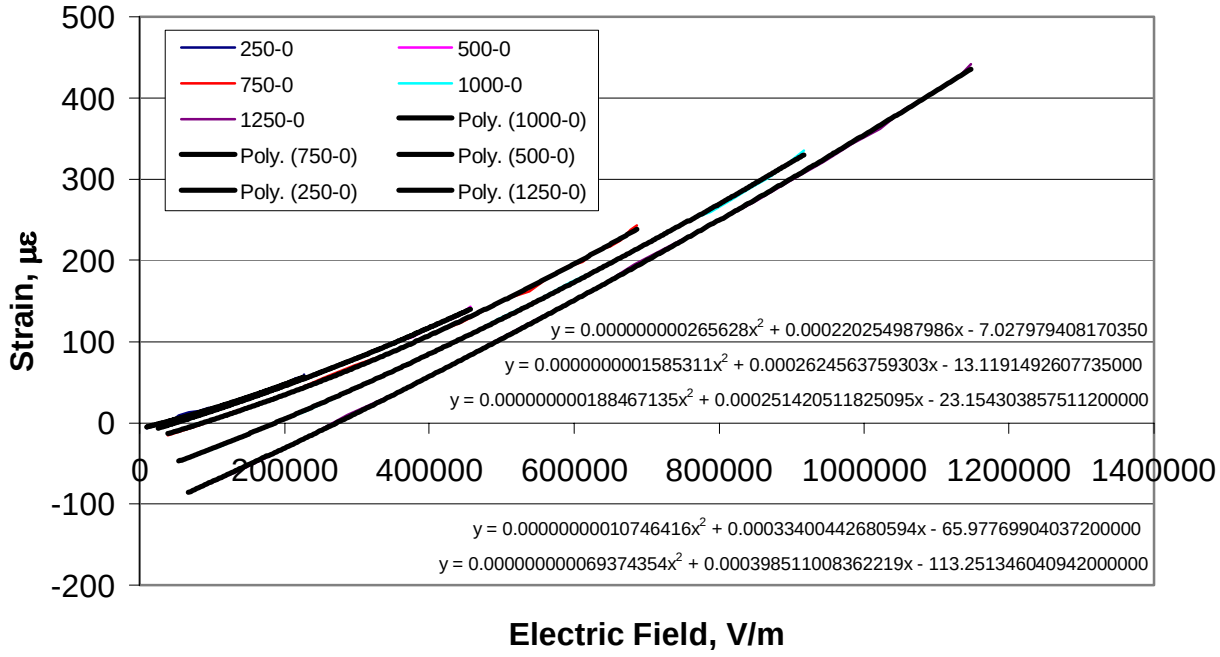

Figure 5.16: 3-Direction Initial Monotonic Strain-Electric Field Behavior for MFC S/N 404, 0 VDC Offset, 0 MPa (Raw, Unshifted Data)

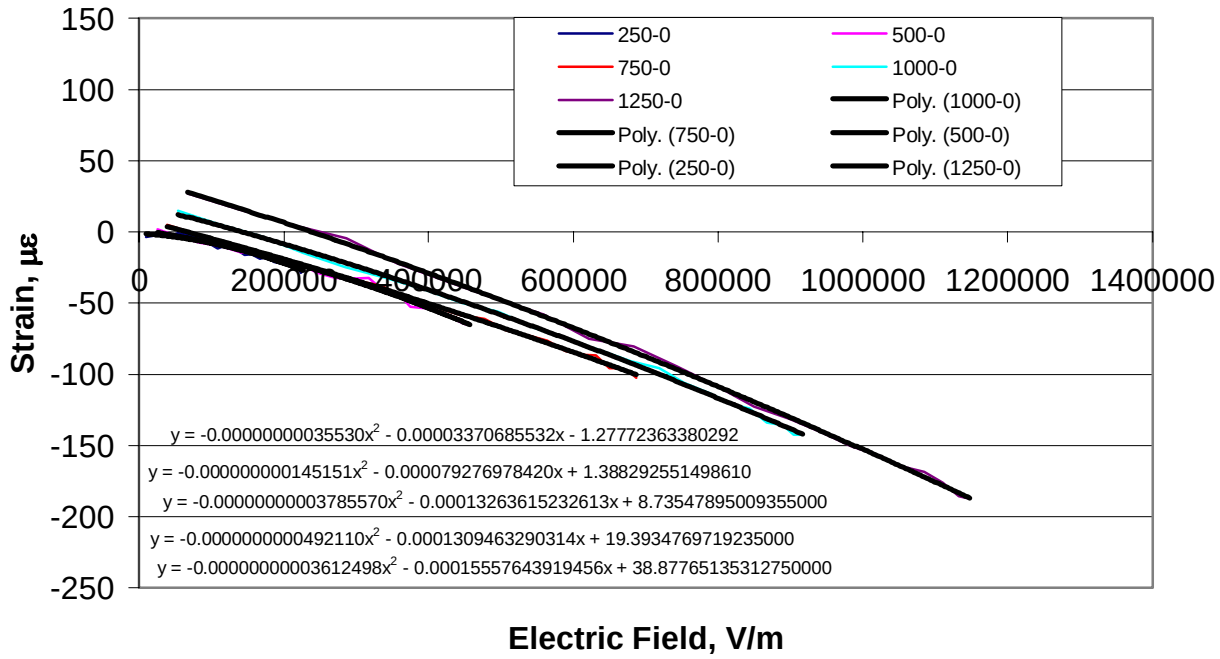

Figure 5.17: 1-Direction Initial Monotonic Strain-Electric Field Behavior for MFC S/N 404, 0 VDC Offset, 0 MPa (Raw, Unshifted Data)

From these plots of the raw data, the unwanted piezoelectric drift is also evident, seen clearly by the large spacing between the curves. However, using the quadratic regression fits, this drift can be removed and a uniform analysis presented. The method for drift removal is applied as follows for each of the five test specimens, irregardless of the amount of drift present in the data. For the case of 0 VDC offset, the intercepts with the strain-axis calculated from the quadratic regression analysis are used to shift the data vertically so that it extrapolates along its own curve through the origin. To fit the shifted data, the linear and quadratic parameters from the regression analysis are averaged for the five peak-to-peak voltage cases (250, 500, 750, 1000, and 1250 volts peak-to-peak), and a curve using these averaged parameters is plotted over the applicable electric field range where there fit is presumed to pass through the origin. Representative shifted data and the fit from the averaged linear and quadratic fitting parameters are presented in Figures 5.18 and 5.19. Clearly, the data from all of the peak voltage profiles is well represented by the average parameter fit.

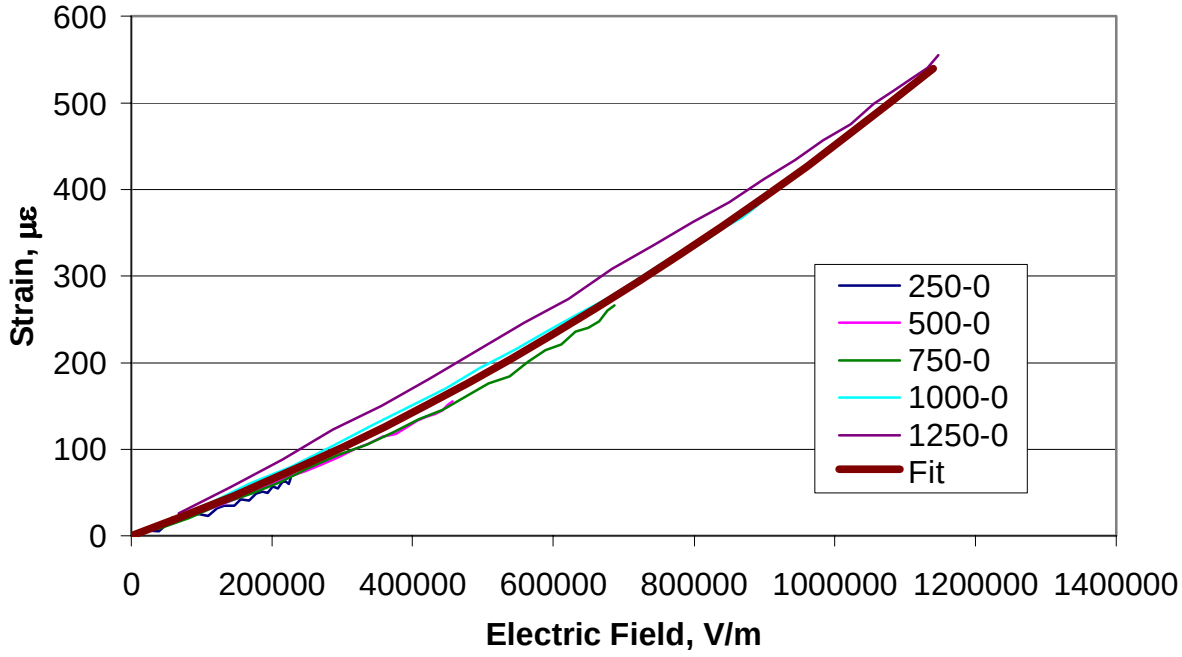

Figure 5.18: 3-Direction Initial Monotonic Strain-Electric Field Behavior for MFC S/N 404, 0 VDC, 0 MPa

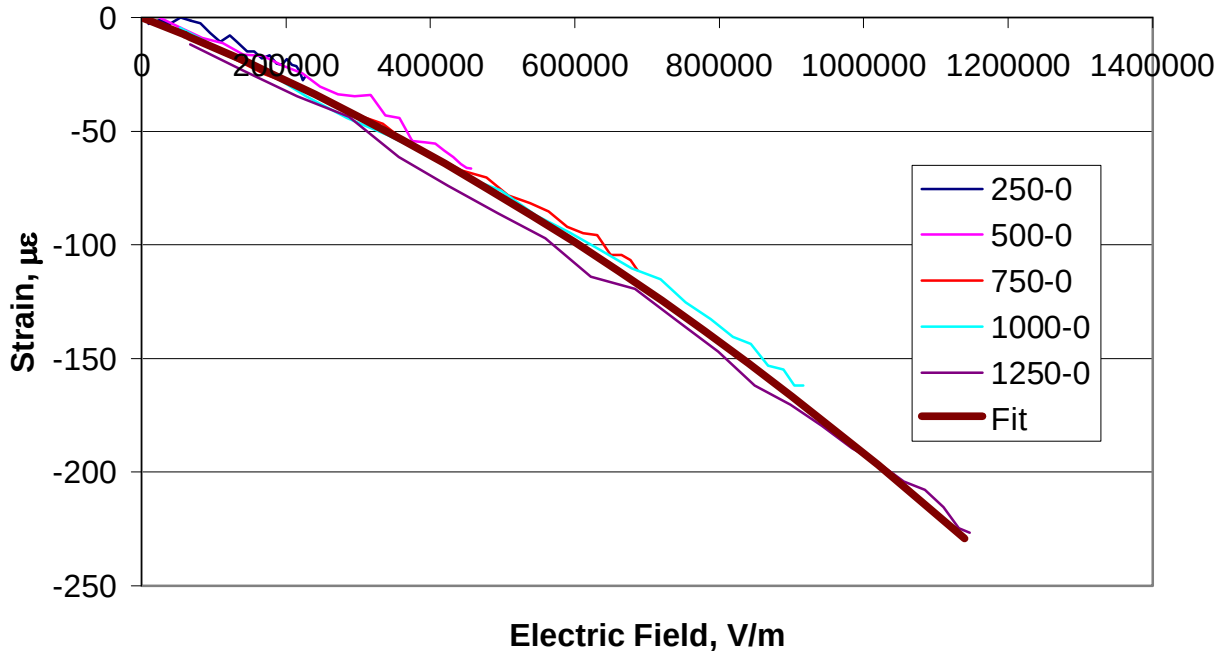

Figure 5.19: 1-Direction Initial Monotonic Strain-Electric Field Behavior for MFC S/N 404, 0 VDC, 0 MPa

With the average linear and quadratic parameters in hand, it is necessary to relate them to the desired unknown constants identified from Equations 5.27 and 5.28. For the case of free-strain (zero stress, as has been investigated and plotted so far), the constitutive relations, Equations 5.27 and 5.28 reduce to

$$\varepsilon_1 = d_{31}E_3 + \frac{1}{2}d_{133}E_3^2 \tag{5.30}$$

$$\varepsilon_3 = d_{33}E_3 + \frac{1}{2}d_{333}E_3^2 \tag{5.31}$$

Next, the regression equations for free-strain in Figures 5.16 and 5.17 have the form

$$\begin{aligned} \varepsilon_1 &= a_1E_3 + a_{11}E_3^2 \\ \varepsilon_3 &= a_3E_3 + a_{33}E_3^2 \end{aligned} \tag{5.32}$$

where the *a* constants obtained from the regression analysis are clearly related the piezoelectric strain and electrostrictive constants, d_{31}, d_{33}, d_{133}, and d_{333}, from Equations 5.30 and 5.31 by

$$\begin{aligned} d_{31} &= a_1 \qquad & d_{133} &= 2a_{11} \\ d_{33} &= a_3 \qquad & d_{333} &= 2a_{33} \end{aligned} \tag{5.33}$$

Comprehensive results for these model parameters for the reference MFC configuration tested are presented and discussed in Section 5.6, after the remainder of the data is analyzed.

5.5.3.2 Nonzero VDC Offset Voltage – Free-Strain:

In order to obtain enhanced performance from the MFC, larger actuation voltages are applied through the use of offset DC voltages in addition to the sinusoidal signals, as

discussed above. The application of such biasing changes both the shape and the starting points for the strain-field relationship. Additionally, the drift that may have occurred at 0 VDC offset must be corrected taken into account. The data analysis begins the same way that the 0 VDC offset case did for free-strain, with a quadratic regression analysis performed on the raw strain data in Microsoft Excel. Representative plots of the raw data are seen below, but the quadratic regression equations and curves have been omitted for clarity.

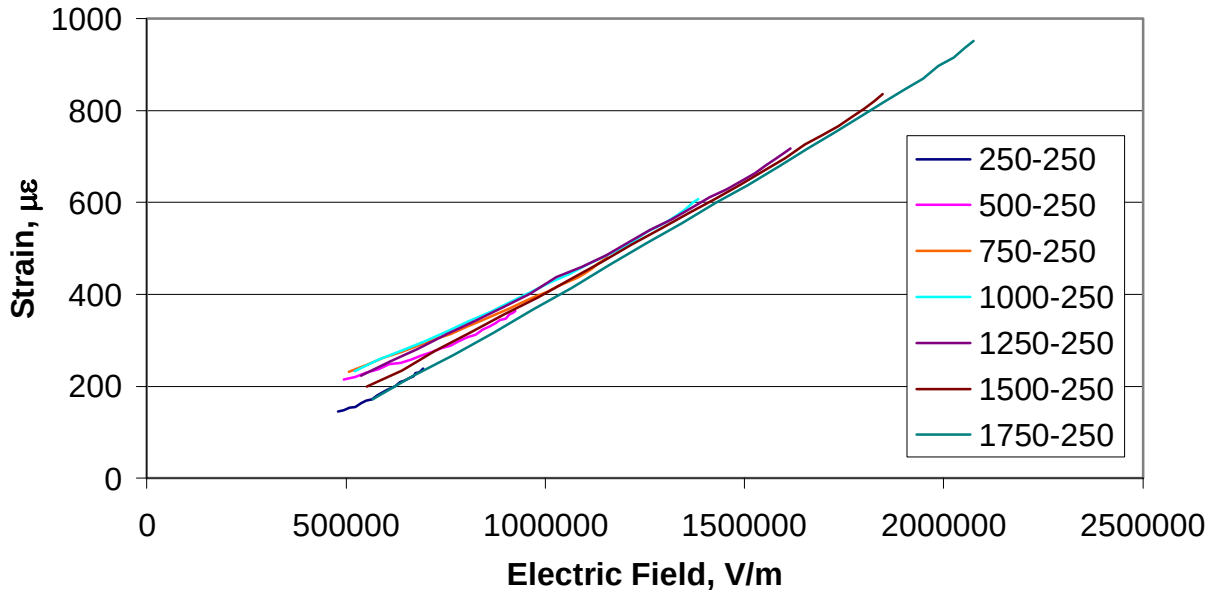

Figure 5.20: 3-Direction Initial Monotonic Strain-Electric Field Behavior for MFC S/N 404, 250 VDC Offset, 0 MPa (Raw, Unshifted Data)

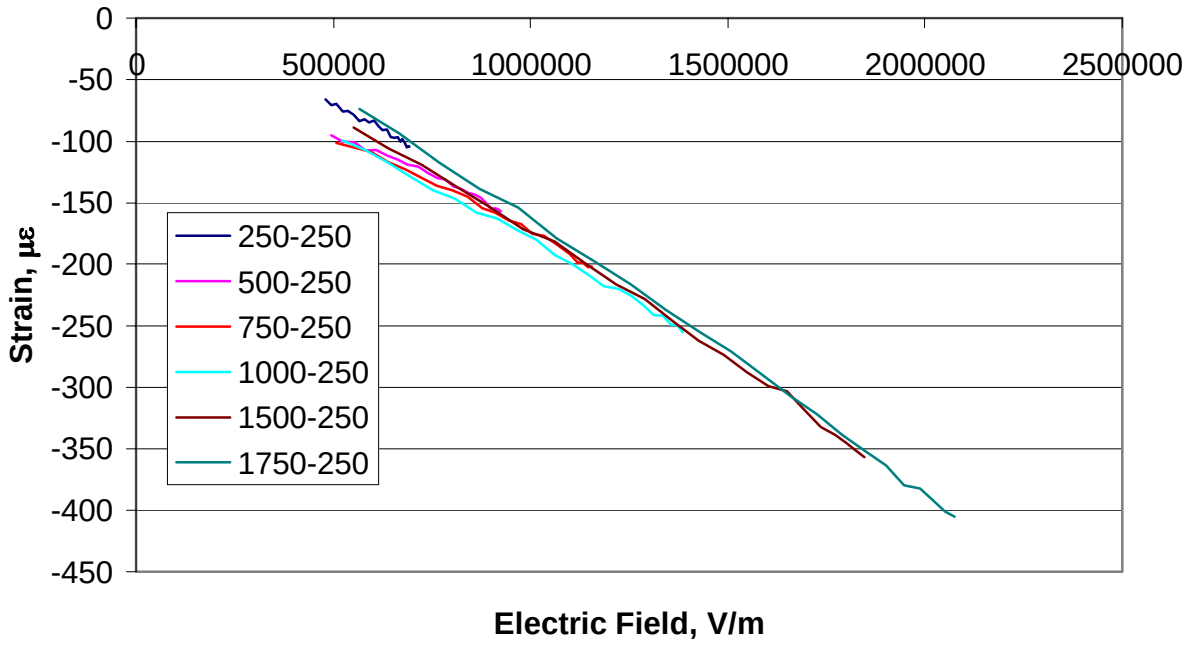

Figure 5.21: 1-Direction Initial Monotonic Strain-Electric Field Behavior for MFC S/N 404, 250 VDC Offset, 0 MPa (Raw, Unshifted Data)

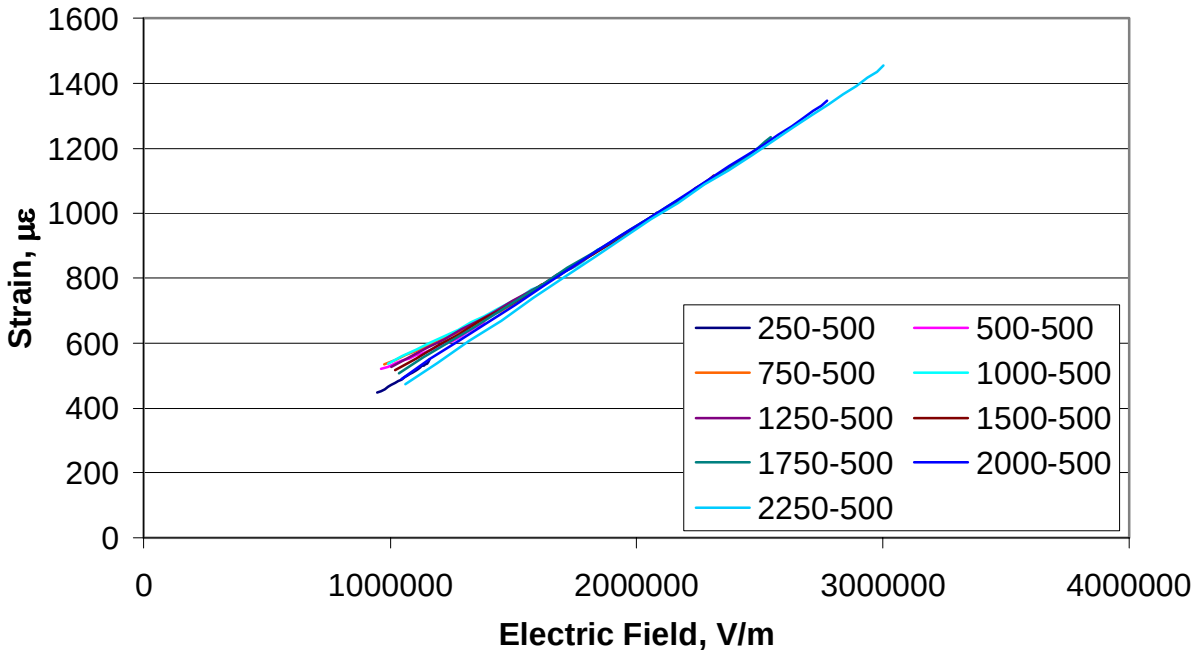

Figure 5.22: 3-Direction Initial Monotonic Strain-Electric Field Behavior for MFC S/N 404, 500 VDC Offset, 0 MPa (Raw, Unshifted Data)

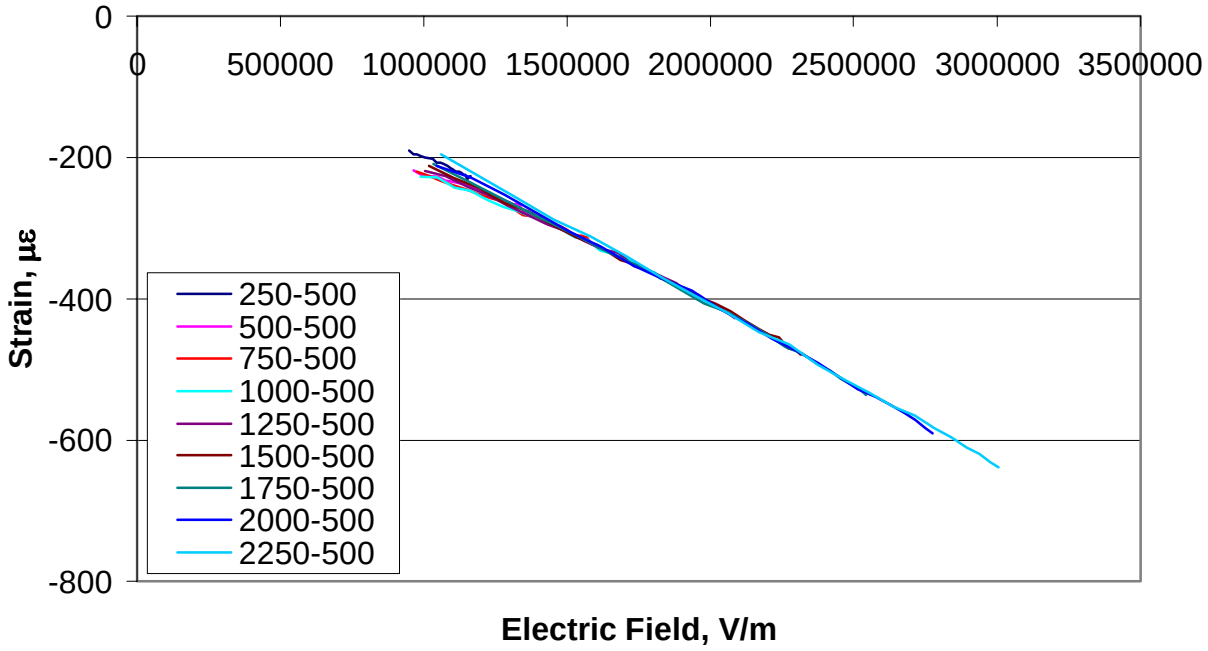

Figure 5.23: 1-Direction Initial Monotonic Strain-Electric Field Behavior for MFC S/N 404, 500 VDC Offset, 0 MPa (Raw, Unshifted Data)

From the four figures above, a few interesting features are noted. First, the application of a DC biasing voltage to the MFC actuator makes the strain-electric field response much more linear than was the case for 0 VDC offset. In fact, the 500 VDC offset results are even more linear than those for the 250 VDC offset case. Next, the strain-field curves are much closer together under a DC biasing voltage, indicating a stabilization of the actuation performance. The curves tend to come together at fields just above the DC offset field. Again, this effect is even more pronounced in the 500 VDC measurements. The last important feature that is noted from these plots is that the 250, 500, and 750 volt peak-to-peak cases should be discarded from the overall fit of the data. This omission is acceptable for two reasons. First, the shape and behavior at these lowest three voltage cycles is much more nonlinear than the higher voltage counterparts, but they only cover a small region of the relevant electric fields. To extend their more-curved behavior over the entire field range of interest would not be a reasonable assumption, and would skew the resulting average behavior to produce a highly inaccurate model. Secondly, since the behavior of these three lowest cycles is bound between the 1000 volt peak-to-

peak and the maximum peak-to-peak voltage cases, 1750 volts peak-to-peak for 250 VDC and 2250 volts peak-to-peak for 500 VDC, the fit for the higher profiles will automatically provide a good fit to the low voltage profiles. With these points in mind, the following steps are applied to the data from all five of the MFC specimens under both free-strain and nonzero stress conditions, the latter of which will be covered in more detail later. The goal of the following procedure is to remove any piezoelectric drift from the data so that the quadratic parameters obtained from the regression analysis will properly predict the output strain from the MFC when it is actuated under both a DC and a harmonic excitation voltage.

Step 1: Calculate the most reliable steady-state strain value for the 0 VDC offset case by averaging the midrange strain values between the peak and the valley of each of the five electrical cycles at the highest voltage profile, which is 1250 volts, peak-to-peak.

Step 2: Calculate the steady-state strain value for the particular offset case (250 VDC or 500 VDC) by averaging the midrange strain values between the peak and the valley of each of the five electrical cycles at the highest, most stable voltage profile at the particular offset voltage, 1750 volts peak-to-peak for the 250 VDC case or 2250 volts peak-to-peak for the 500 VDC case.

Step 3: Calculate the magnitude of the distance between these two steady-state strain values, bearing in mind that one may be negative and the other positive. This distance is equal to the static strain produced by the application of the biasing voltage. The data for the offset case should be shifted so that the average of the starting points for the various voltage curves at the offset voltage is equal to this static strain value. This shifting is done by following the next four steps.

Step 4: Perform a quadratic regression analysis on the raw strain data, including intercept with the strain-axis. Use these equations to determine the extrapolated value at the offset field (250 VDC or 500 VDC), and then average these values for the 1000 volt peak-to-peak and above cases. The 250, 500, and 750 volt peak-to-peak cases are disregarded in this average for the reasons stated above.

Step 5: For all voltage curves, calculate how much that curve must be shifted vertically so that it would start at the static strain caused by the DC offset, as calculated in Step 3.
Step 6: Calculate the average of these required shifting differences for the 1000 volt peak-to-peak and higher curves. The raw strain data is all shifted vertically by this amount in a separate spreadsheet column.
Step 7: The quadratic and linear regression parameters should be averaged for the 1000 volt peak-to-peak and higher curves, and then a second-order fit of the data should be calculated using these averaged parameters.

The data manipulation procedure outlined above has been applied to the experimental data for the five reference MFC specimens. The representative free-strain data for nonzero biasing voltages is presented in the four figures below, along with the calculated fit from the averaged regression parameters. As expected, the fit does a good job of representing the voltage data regardless of the peak-to-peak voltage.

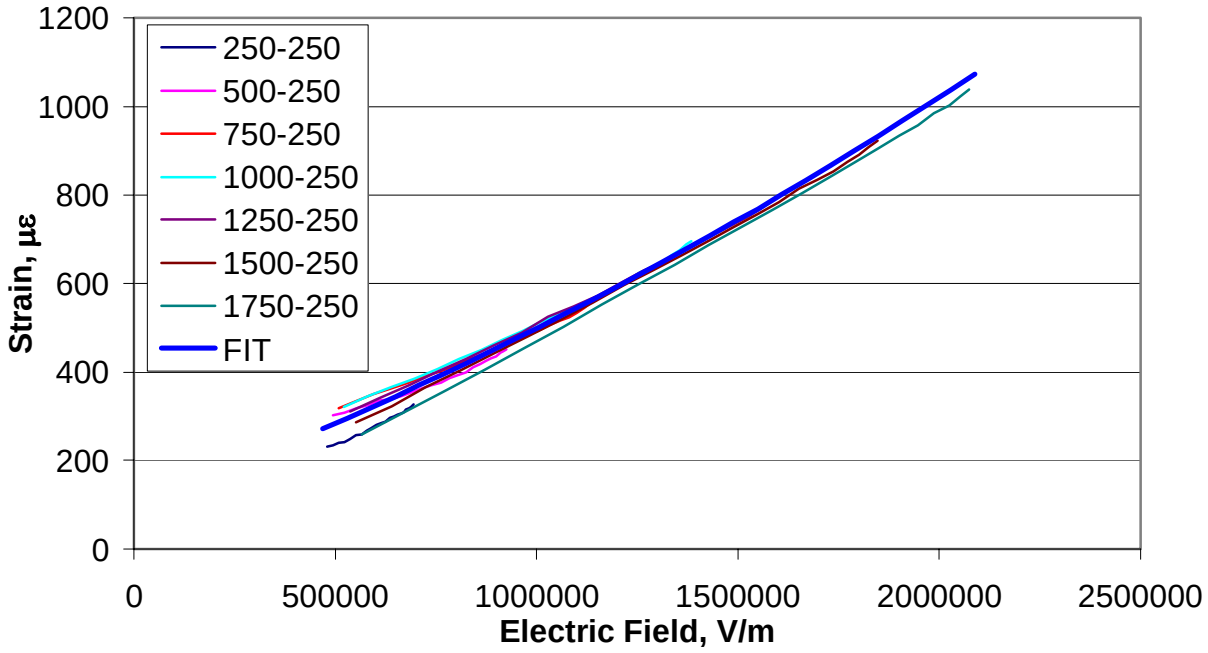

Figure 5.24: 3-Direction Monotonic Strain-Electric Field Behavior for MFC S/N 404, 250 VDC Offset, 0 MPa

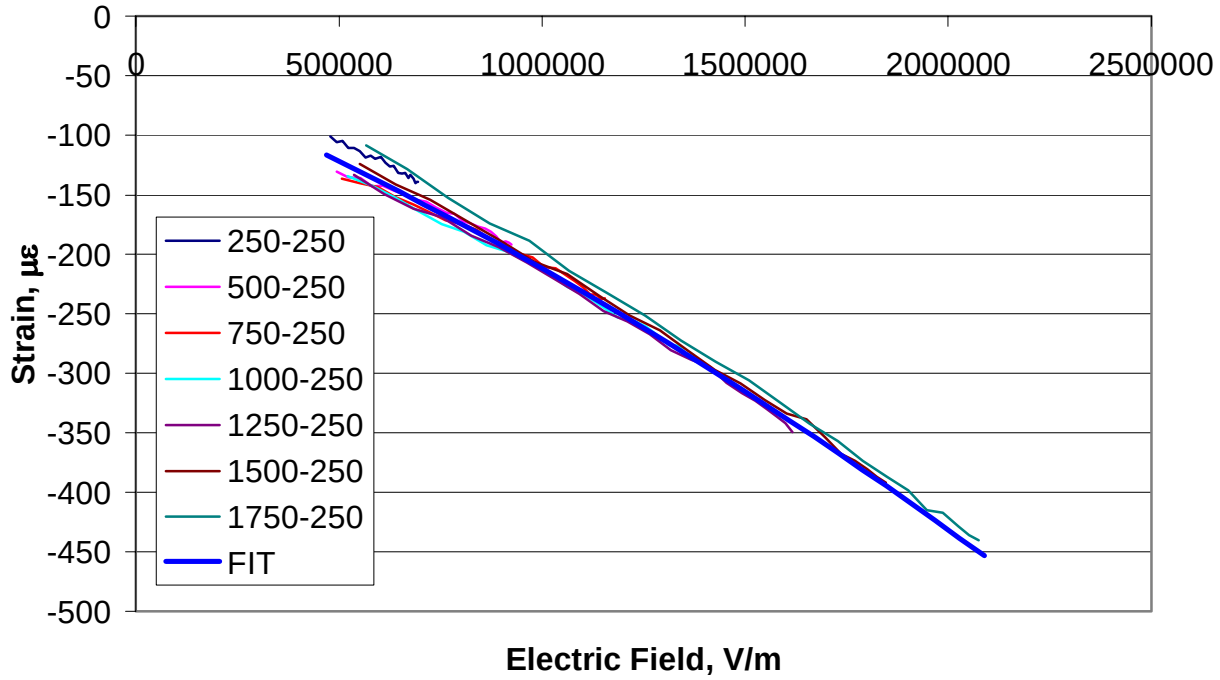

Figure 5.25: 1-Direction Monotonic Strain-Electric Field Behavior for MFC S/N 404, 250 VDC Offset, 0 MPa

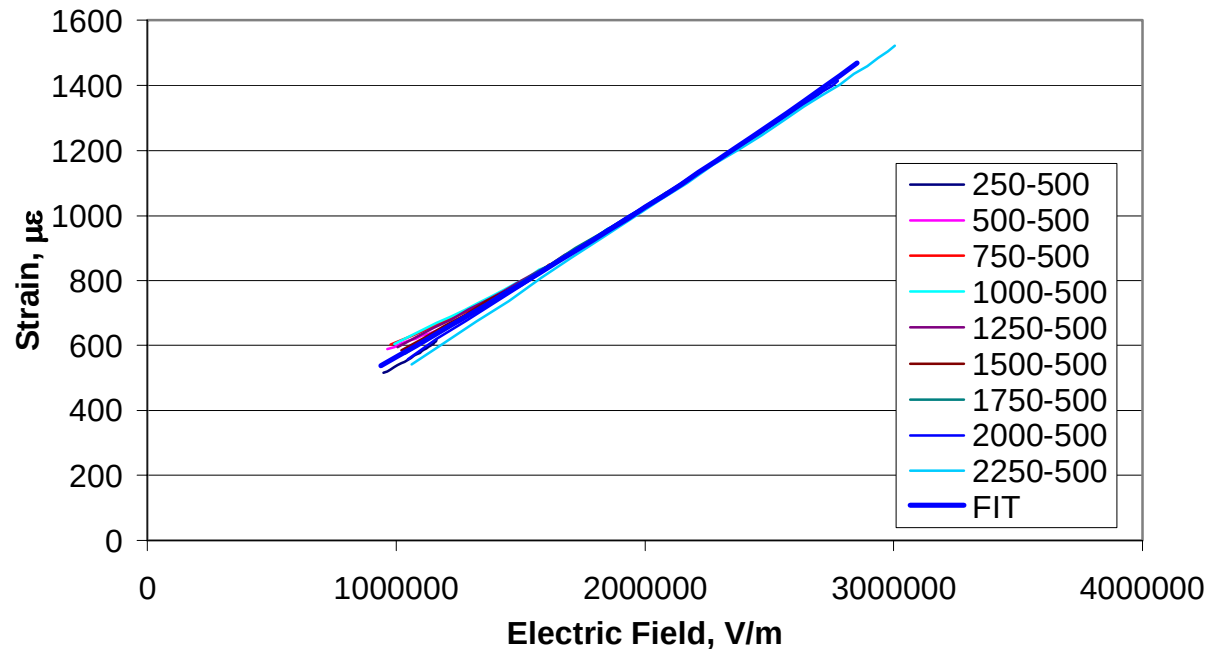

Figure 5.26: 3-Direction Monotonic Strain-Electric Field Behavior for MFC S/N 404, 500 VDC Offset, 0 MPa

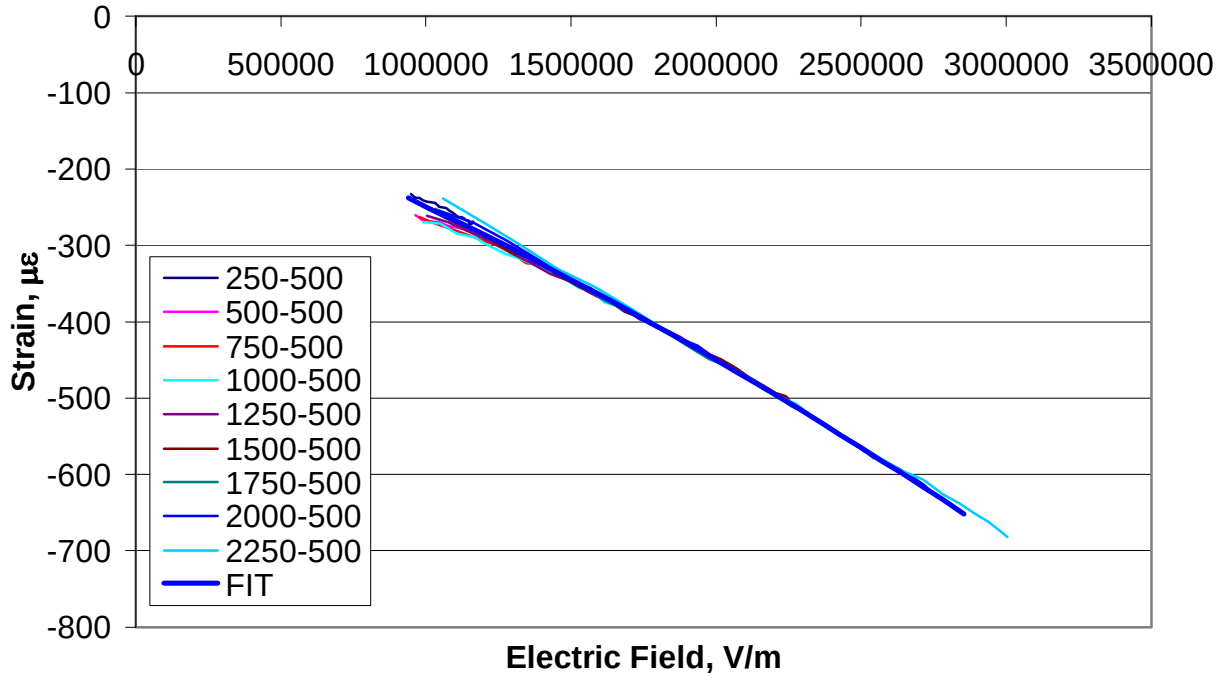

Figure 5.27: 1-Direction Monotonic Strain-Electric Field Behavior for MFC S/N 404, 500 VDC Offset, 0 MPa

From the plots above, it appears that there is a linear relationship between the DC biasing voltage and the resulting static strain. That is, the average static strain from the five specimens at 500 VDC is twice that of the 250 VDC case. In order to accommodate the presence of this static strain induced by the DC biasing voltage, this strain can simply be added onto the other strain components in the constitutive relations, Equations 5.27 and 5.28, or for a more general and useful model, the governing equations can be modified slightly, resulting in, for the case of zero applied stress

$$\varepsilon_1 = d_{31}E_3 + \frac{1}{2}d_{133}E_3^2 + d_{1DC}E_{offset} \tag{5.34}$$

$$\varepsilon_3 = d_{33}E_3 + \frac{1}{2}d_{333}E_3^2 + d_{3DC}E_{offset} \tag{5.35}$$

The material parameters, d_{33}, d_{31}, d_{333}, d_{133}, d_{1DC}, and d_{3DC} extracted from the data in this section are presented in Section 5.6, along with the other results from the data analysis in the remainder of this chapter.

5.5.4 Drift Removal and Quadratic Regression – Constant Applied Stress:

To this point, actuation characterization has focused on the free-strain (zero stress) response of the MFC to various electrical fields. Such a starting point is reasonable because the true piezoelectric and electrostrictive parameters are defined for a constant stress condition, as specified in Equation 5.9 and 5.10. Typically this "constant stress" is zero, because the device is characterized under free-strain conditions. This conditions is the easiest to meet in a laboratory, just as the short-circuit condition is the easiest way experimentally to impose a "constant electric field" for stiffness parameter measurements. However, it is commonplace in the literature to define "effective" constants for actuation devices under frequently encountered situations. Indeed, from the experimental data collected, it is also possible to determine these "effective" constants under various constant applied mechanical stresses. Such results can aid greatly in various forms of nonlinear analysis, by determining stress, strain or electric field-based changes in so called "materials constants."

To this end, a similar quadratic analysis to that presented above for free-strain conditions is now performed on the data acquired under the constant loads presented in Section 5.4.2 and Table 5.2.

When the bottom grip of the MTS testing machine is closed and a constant nonzero load applied to the actuator, the strain gages measure the total strain, which consists of both mechanical and actuation strain components. In order to investigate only the actuation strains, the elastic portion must be subtracted from the measured strain data. The superposition of strains is a reasonable assumption because the load levels are within the linear elastic range on the stress-strain curve, as verified in Figure 5.7. Instead of

calculating the elastic component of the total strain, the measured strains were simply shifted down so that the first data point, corresponding to the 250 volt peak-to-peak, 0 VDC offset case, begins at zero strain. Once this adjustment has been made to the data, the strain-time output plots look similar to those in Figures 5.10 and 5.11. Also, some specimens show signs of piezoelectric drift, which tended decrease with increased static load. Nevertheless, any drift is removed in the same fashion as above for the case of free-strain.

5.5.4.1 Zero VDC Offset Voltage – Constant Applied Stress:

As was the case before, the initial monotonic portion of the strain-field loops is isolated for the nonzero load cases, similar to that of Figures 5.14 and 5.15, for 0 VDC offset voltage. Again, the raw data is fit using a quadratic regression analysis and shifted as discussed in Section 5.5.3.1 so that the data extrapolated through the origin along their respective curves. The parameters are averaged for all of the peak-to-peak voltage profiles, and a fit generated over the entire applicable field range. This procedure is applied to the data from all five specimens at all of the tested constant load cases.

Rather than present the results from each load case, only a few representative plots are shown, at 10 lb (5.6 MPa), 40 lb (23.2 MPa), and 60lb (34.8 MPa), for the two orthogonal direction of strain. However, a complete characterization was performed, and the resulting parameters are tabulated in Section 5.6.

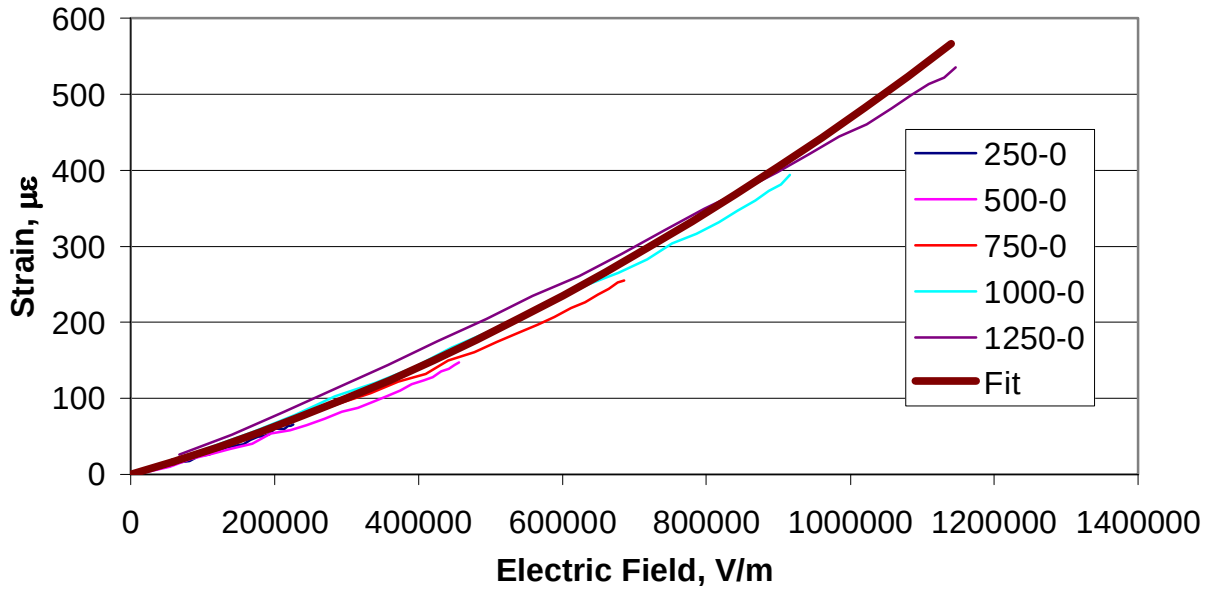

Figure 5.28: 3-Direction Monotonic Strain-Electric Field Behavior for MFC S/N 404, 0 VDC Offset, 5.6 MPa (10 lb)

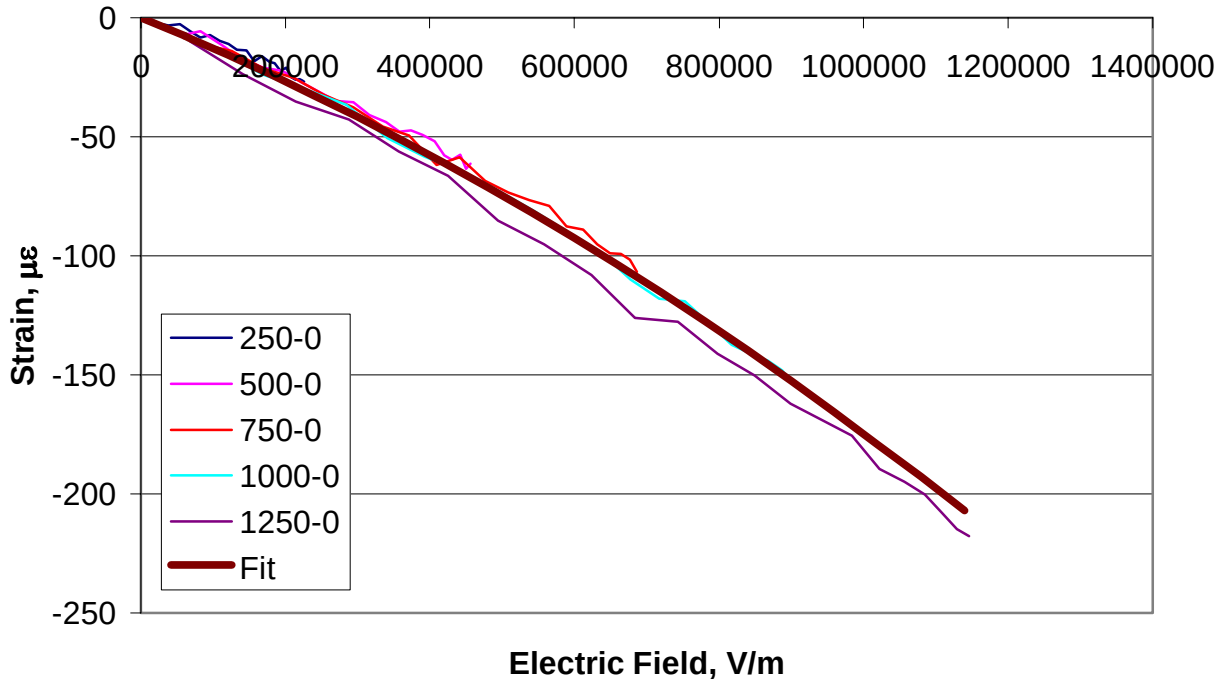

Figure 5.29: 1-Direction Monotonic Strain-Electric Field Behavior for MFC S/N 404, 0 VDC Offset, 5.6 MPa (10 lb)

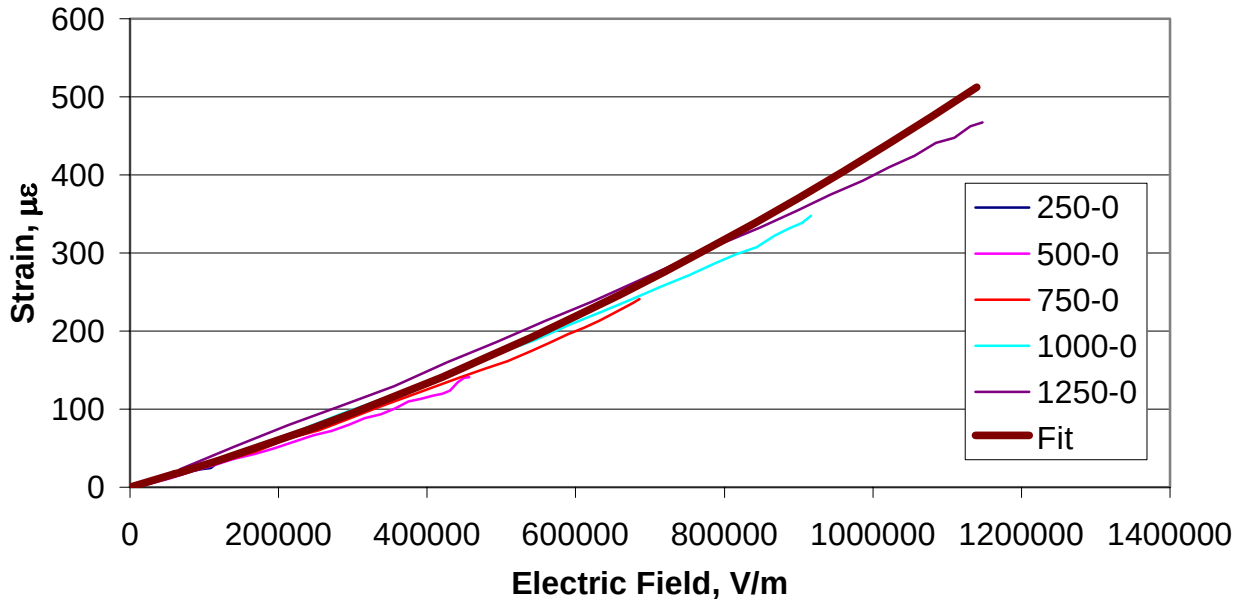

Figure 5.30: 3-Direction Monotonic Strain-Electric Field Behavior for MFC S / N 404, 0 VDC Offset, 23.2 MPa (40 lb)

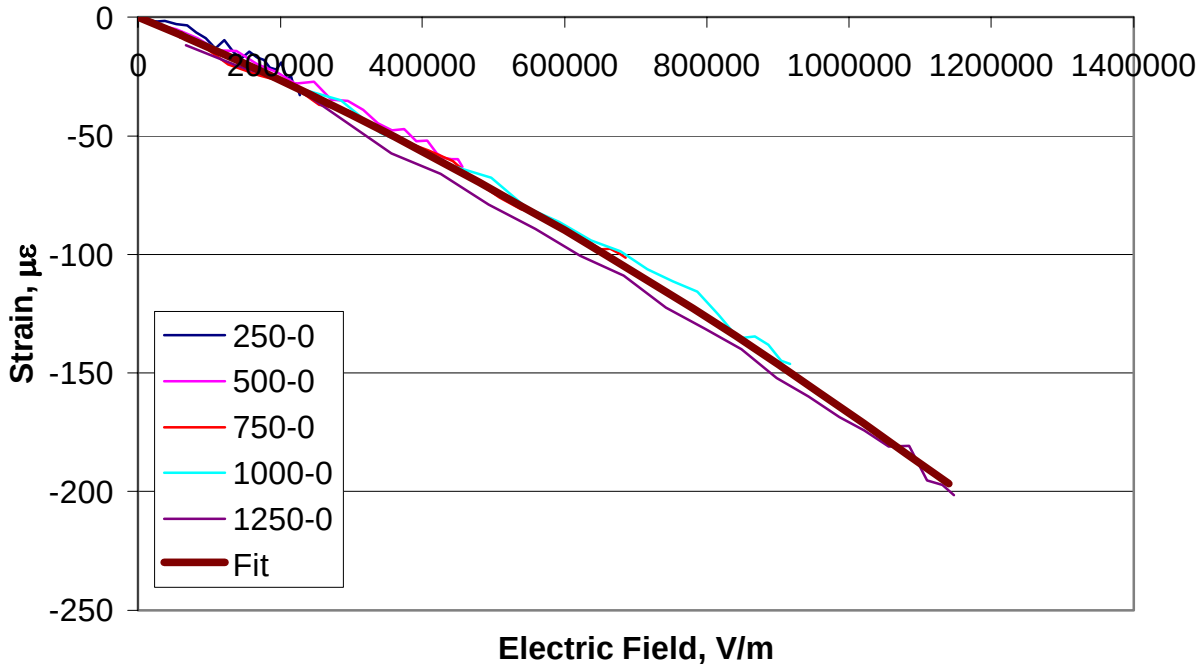

Figure 5.31: 1-Direction Monotonic Strain-Electric Field Behavior for MFC S / N 404, 0 VDC Offset, 23.2 MPa (40 lb)

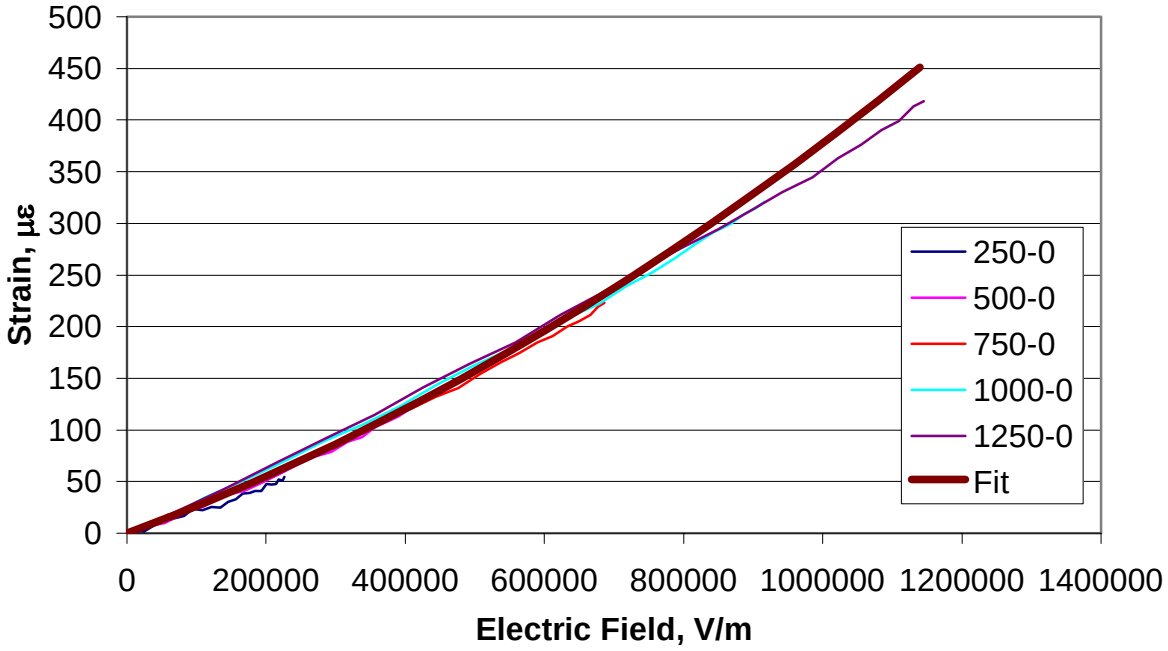

Figure 5.32: 3-Direction Monotonic Strain-Electric Field Behavior for MFC S/N 404, 0 VDC Offset, 34.8 MPa (60 lb)

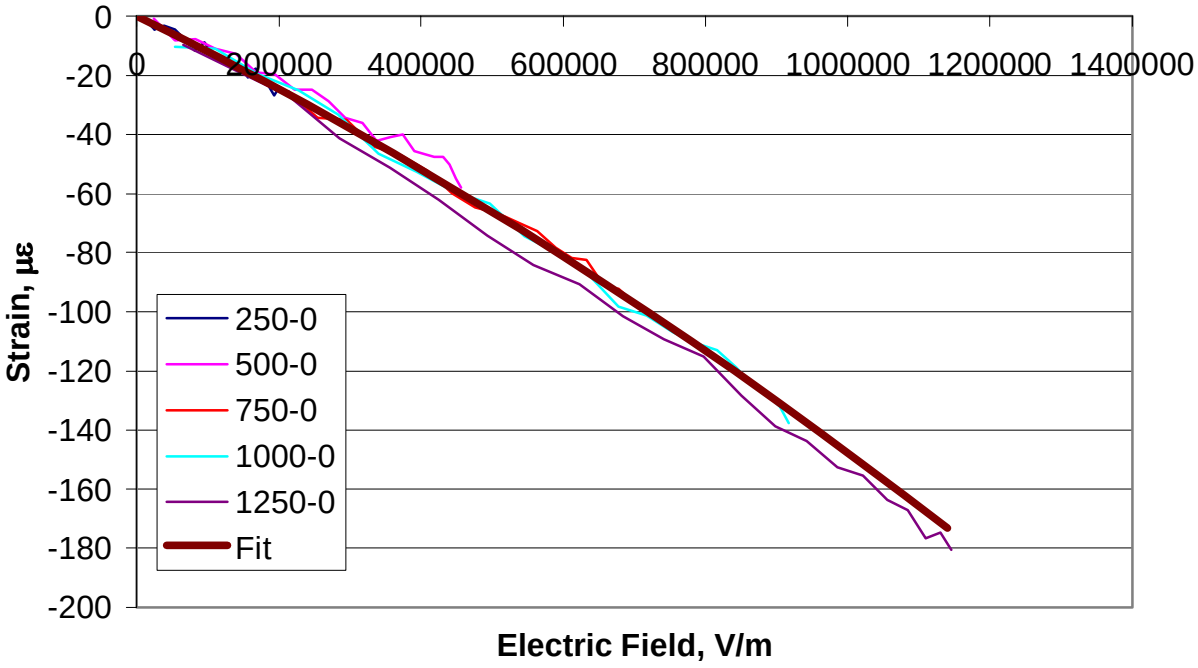

Figure 5.33: 1-Direction Monotonic Strain-Electric Field Behavior for MFC S/N 404, 0 VDC Offset, 34.8 MPa (60 lb)

5.5.4.2 Nonzero VDC Offset Voltage – Constant Applied Stress:

As was the case for free-strain actuation, offset DC voltages are used in addition to the sinusoidal voltages to obtain enhanced performance from the MFC under nonzero constant applied stresses. Likewise, the application of such biasing changes both the shape and the starting points for the strain-field relationship. Additionally, the drift that may have occurred at 0 VDC offset must be corrected taken into account. The data for the nonzero load cases begins the same way that the 0 VDC offset case did for free-strain, with a quadratic regression analysis performed on the raw strain data in Microsoft Excel. Such raw data plots are omitted in the interest of brevity. The seven data shifting steps outlined in Section 5.5.3.2 are also applied to the data for this section. However, for the 1-direction response, the regression parameters for the 250 volt peak-to-peak case were discarded for the same reasons discussed above. The resulting plots showing the data and the averaged curve fits are shown below for MFC S/N 404 under 250 and 500 VDC offsets under 10, 40, and 60 pound load cases.

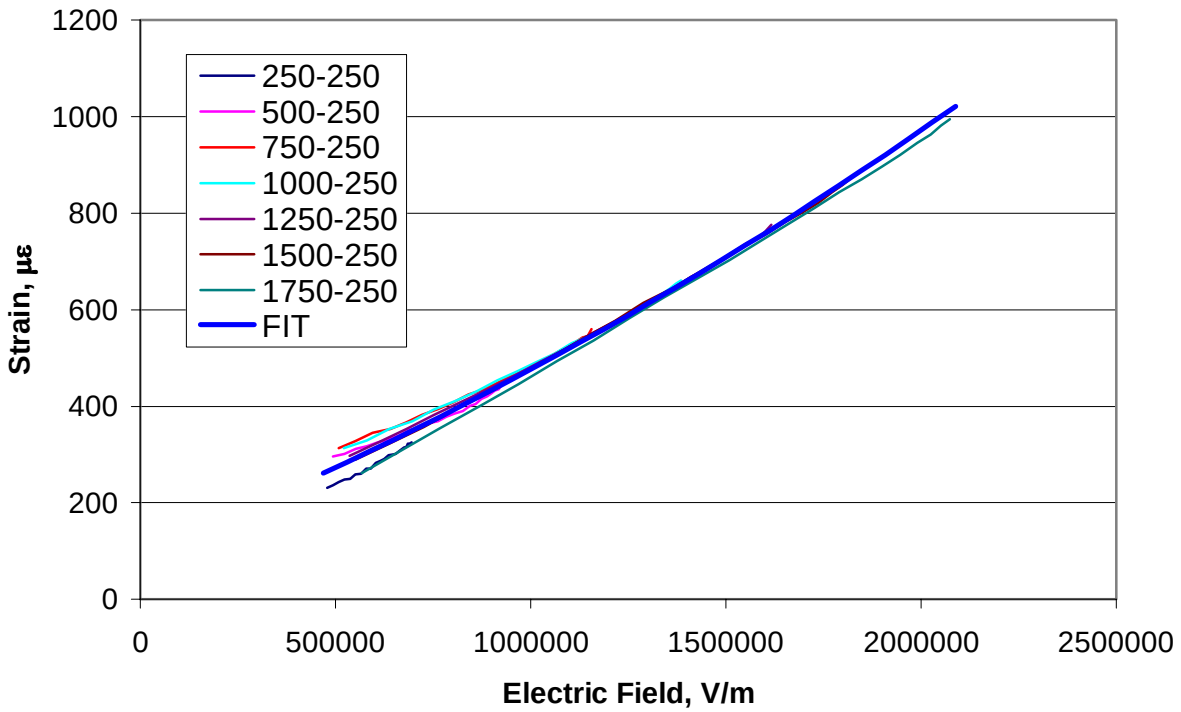

Figure 5.34: 3-Direction Monotonic Strain-Electric Field Behavior for MFC S/N 404, 250 VDC Offset, 5.6 MPa (10 lb)

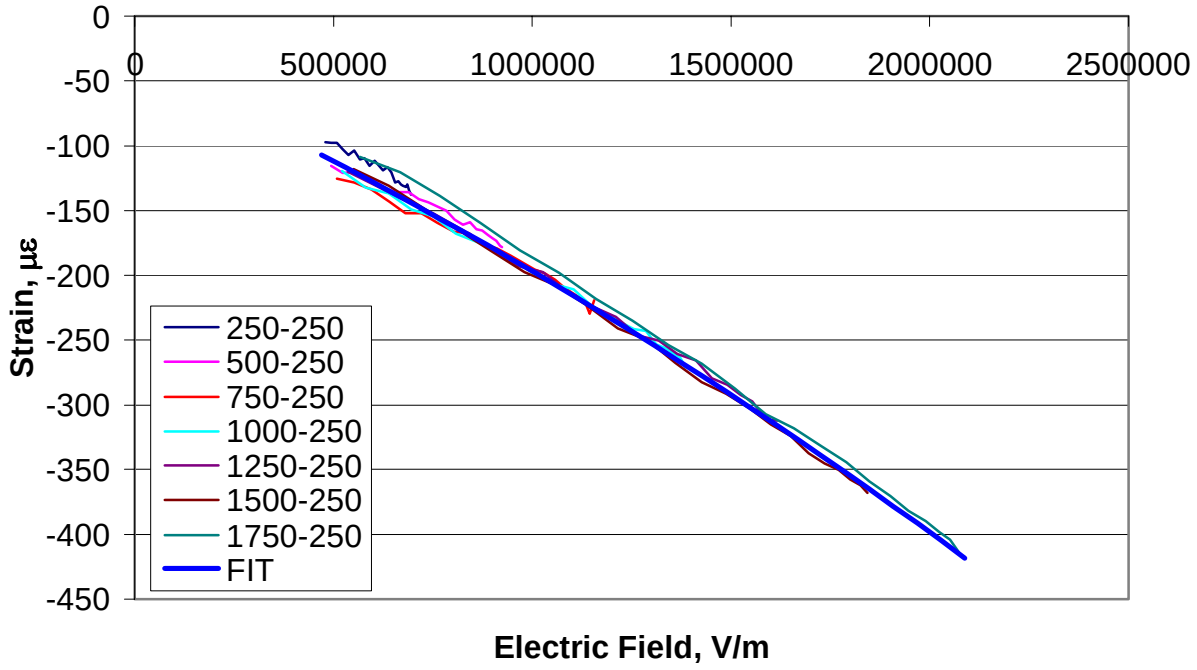

Figure 5.35: 1-Direction Monotonic Strain-Electric Field Behavior for MFC S/N 404, 250 VDC Offset, 5.6 MPa (10 lb)

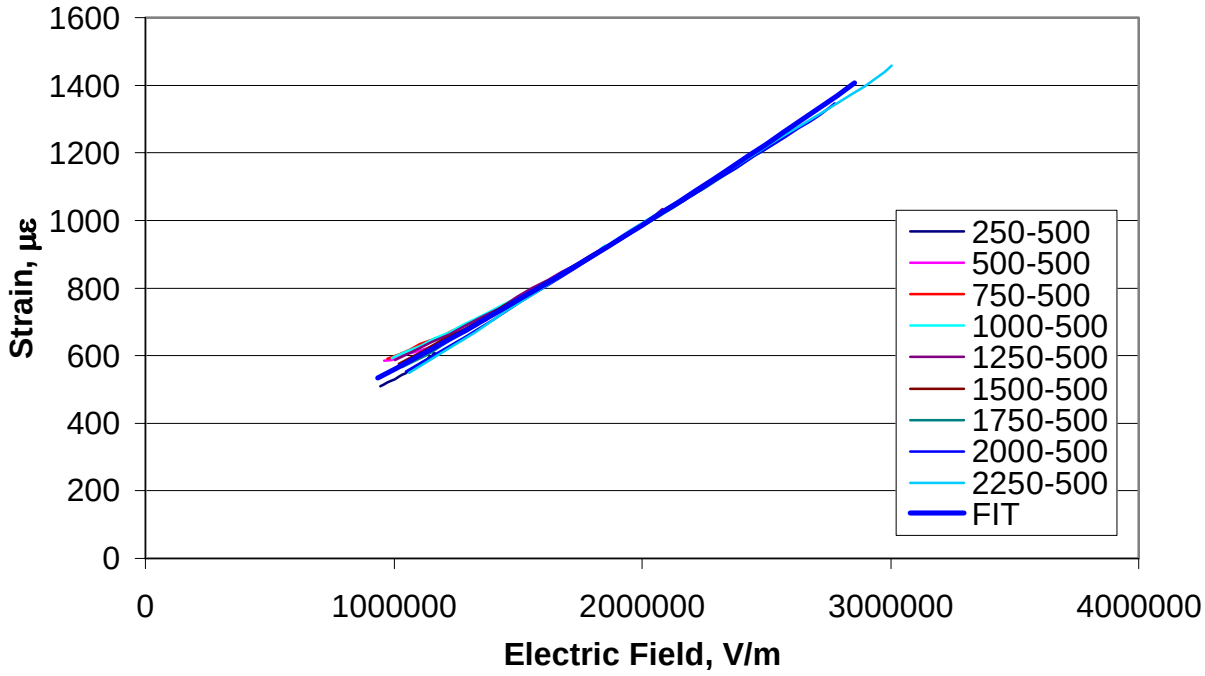

Figure 5.36: 3-Direction Monotonic Strain-Electric Field Behavior for MFC S/N 404, 500 VDC Offset, 5.6 MPa (10 lb)

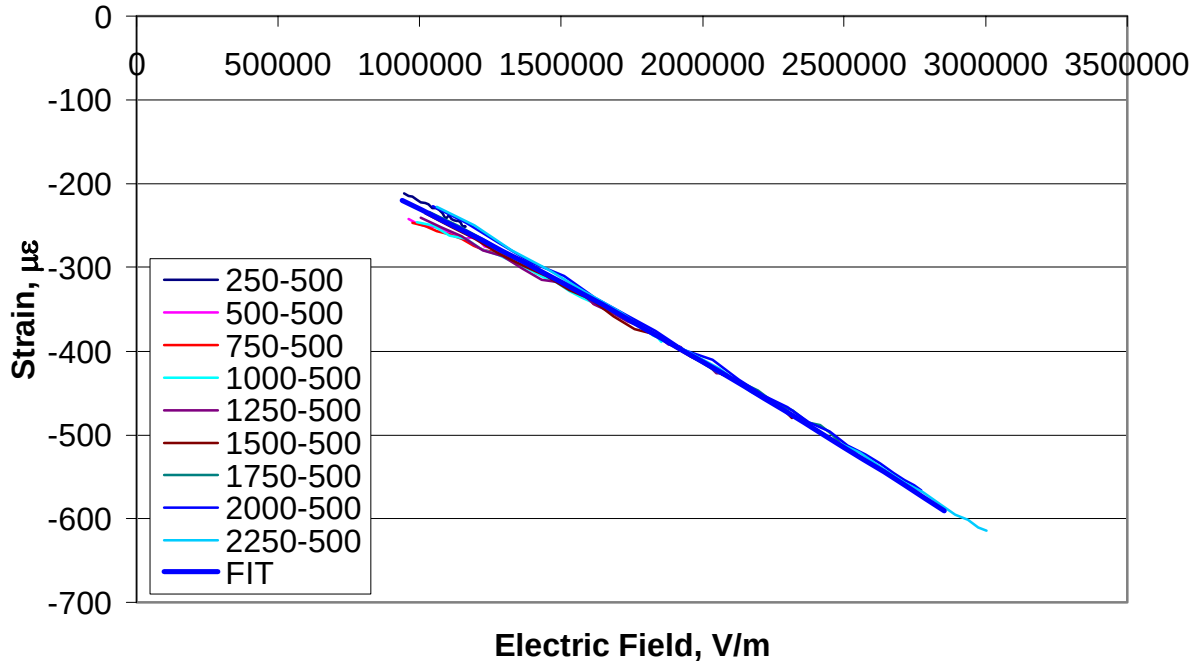

Figure 5.37: 1-Direction Monotonic Strain-Electric Field Behavior for MFC S/N 404, 500 VDC Offset, 5.6 MPa (10 lb)

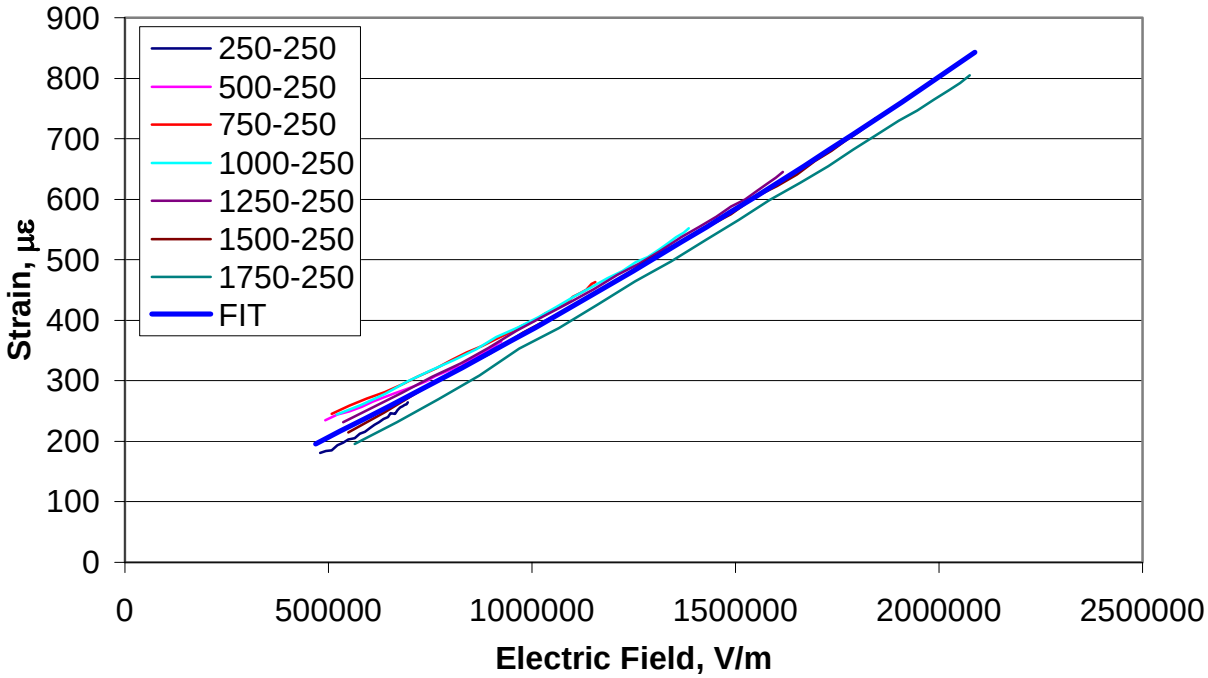

Figure 5.38: 3-Direction Monotonic Strain-Electric Field Behavior for MFC S/N 404, 250 VDC Offset, 23.2 MPa (40 lb)

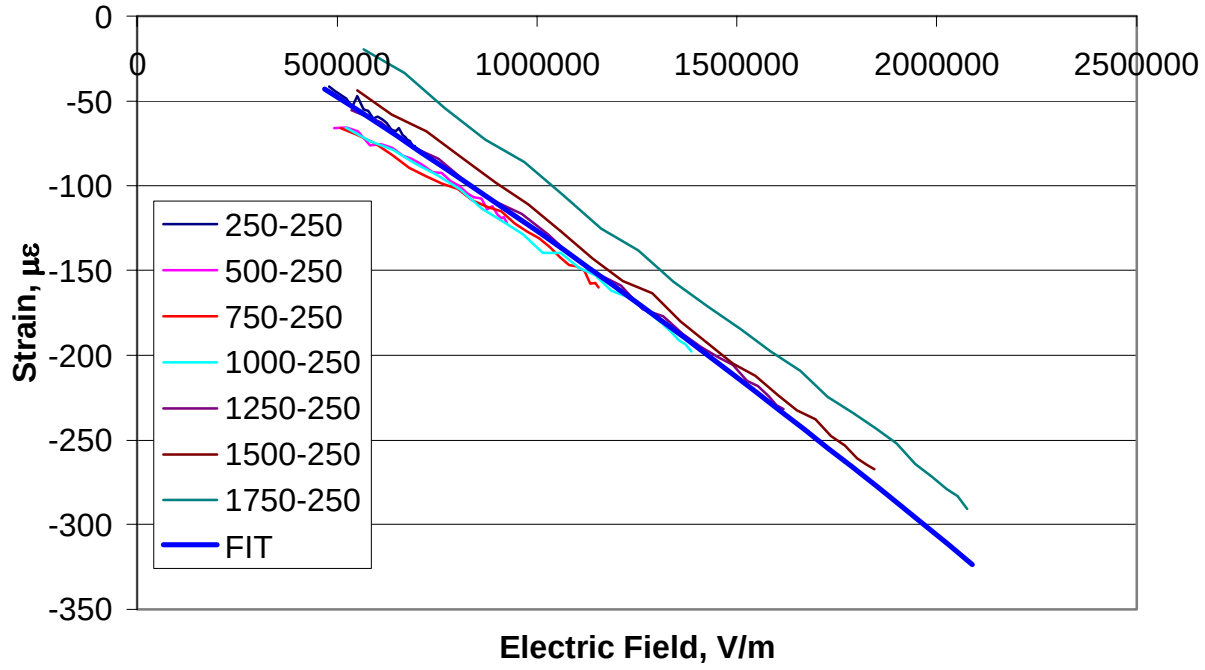

Figure 5.39: 1-Direction Monotonic Strain-Electric Field Behavior for MFC S/N 404, 250 VDC Offset, 23.2 MPa (40 lb)

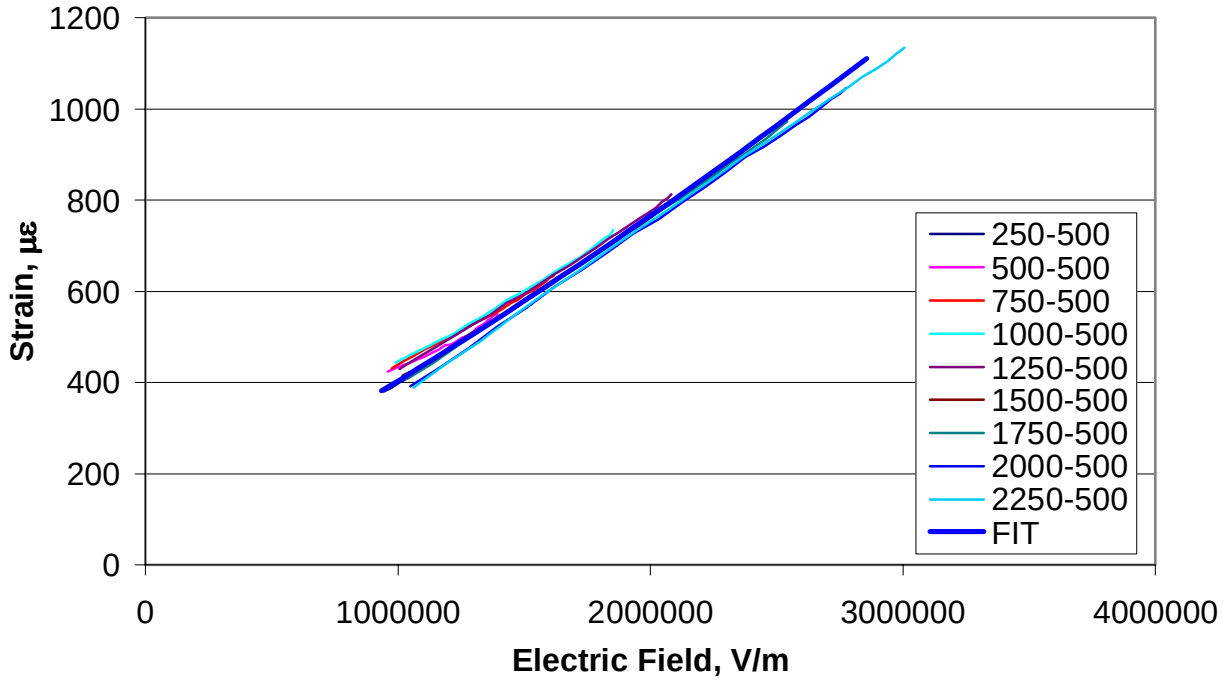

Figure 5.40: 3-Direction Monotonic Strain-Electric Field Behavior for MFC S/N 404, 500 VDC Offset, 23.2 MPa (40 lb)

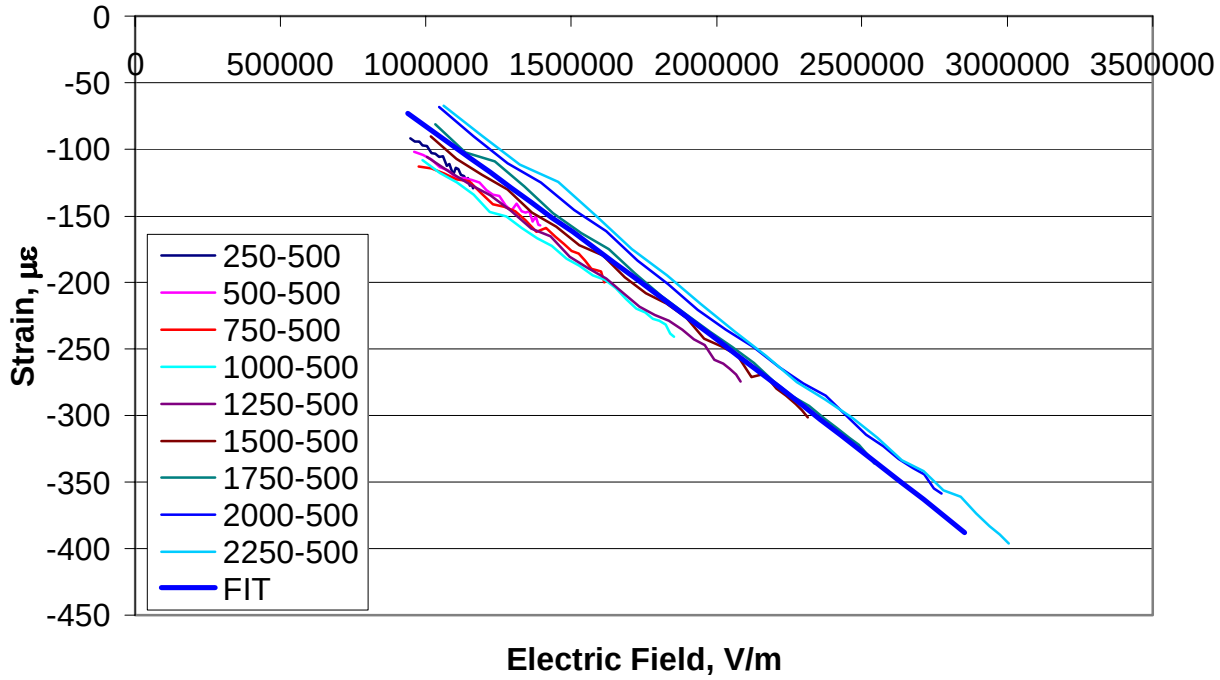

Figure 5.41: 1-Direction Monotonic Strain-Electric Field Behavior for MFC S/N 404, 500 VDC Offset, 23.2 MPa (40 lb)

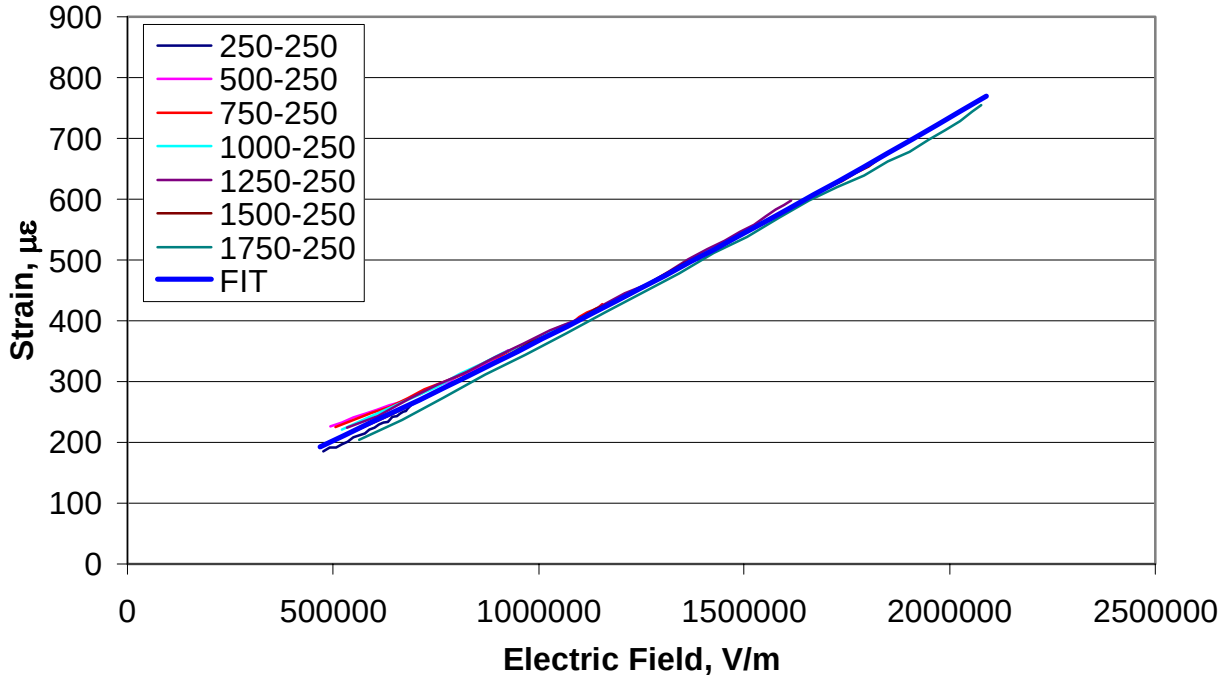

Figure 5.42: 3-Direction Monotonic Strain-Electric Field Behavior for MFC S/N 404, 250 VDC Offset, 34.8 MPa (60 lb)

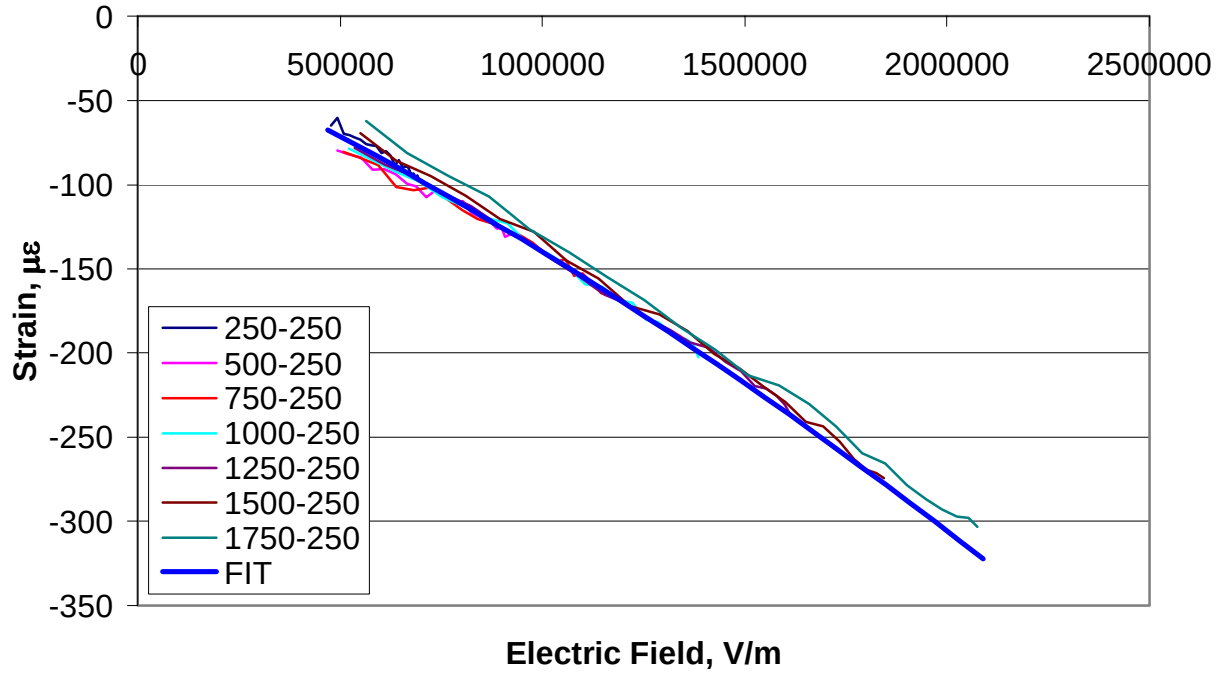

Figure 5.43: 1-Direction Monotonic Strain-Electric Field Behavior for MFC S/N 404, 250 VDC Offset, 34.8 MPa (60 lb)

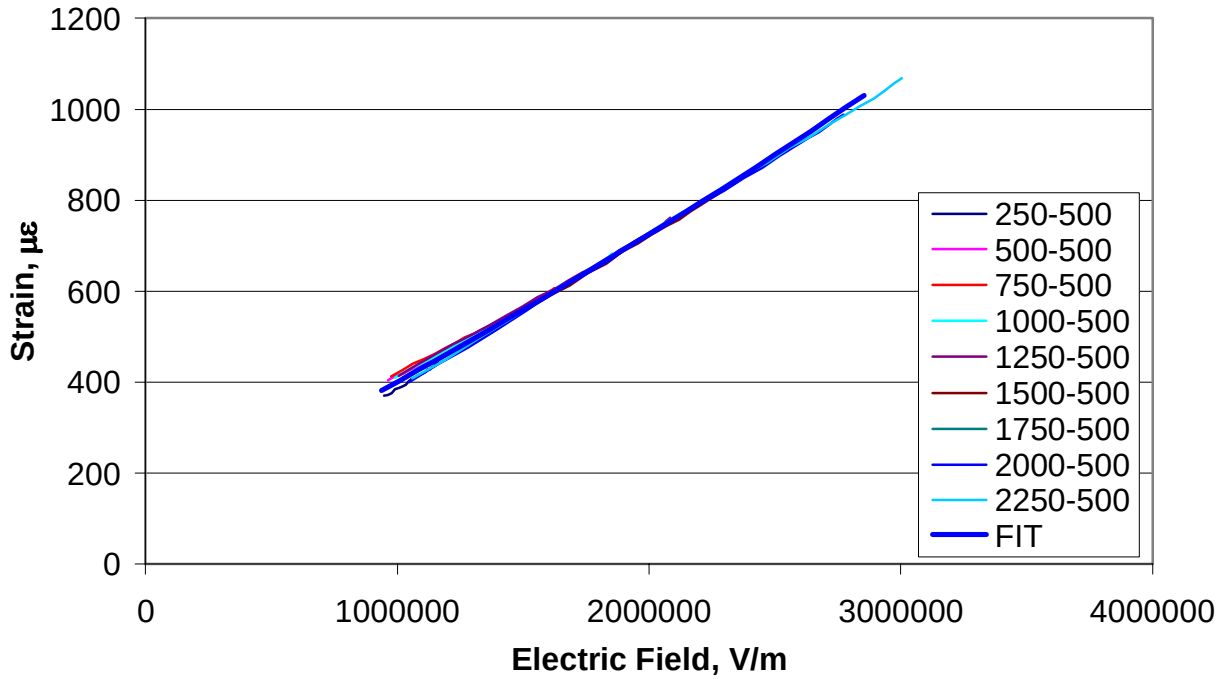

Figure 5.44: 3-Direction Monotonic Strain-Electric Field Behavior for MFC S/N 404, 500 VDC Offset, 34.8 MPa (60 lb)

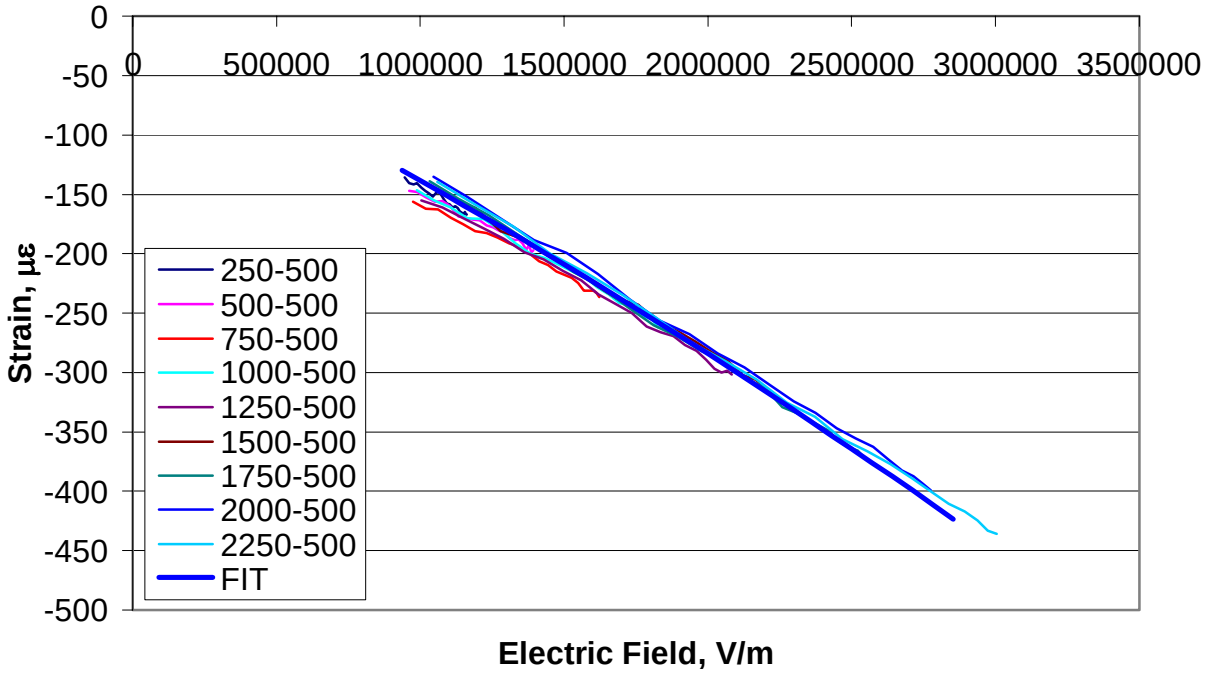

Figure 5.45: 1-Direction Monotonic Strain-Electric Field Behavior for MFC S / N 404, 500 VDC Offset, 34.8 MPa (60 lb)

As expected, the regression curves do a good job representing the data regardless of the sinusoidal voltage amplitude. As was the case for free-strain performance, the actuation behavior becomes quite linear under the presence of increasing DC biasing voltage and constant nonzero applied stress. Also, there again appears to be a linear relationship between the DC biasing voltage and the resulting static strain. Thus, this static strain is again simply added onto the other strain components, as shown in Equations 5.34 and 5.35.

From the data and regression analyses outlined above, the effective material parameters under various constant applied nonzero stresses, d_{33}, d_{31}, d_{333}, d_{133}, d_{1DC}, and d_{3DC} are extracted and presented in Section 5.6.

5.5.5 Calculation of the Elastostrictive Constants:

At this point, a great deal of attention has been paid to the d_{ij} and d_{ijk} parameters under different stress and field conditions. However, the task remains to determine the

elastostrictive parameters identified in the constitutive relationship, Equations 5.27 and 5.28. In these equations, the compliances s_{33} and s_{13} are measured in Chapter 3, and the piezoelectric strain and electrostrictive constants are determined above and presented in Section 5.6. Now, the elastostrictive constants, κ_{133} and κ_{333} can be calculated using the experimental stress-strain curves measured at constant nonzero electric field as presented in Appendix E. With a point selected from the longitudinal stress – longitudinal strain and longitudinal stress - transverse strain curves at constant electric field, E_3, σ_3, ε_1, and ε_3 are known, as are d_{33}, d_{31}, d_{333}, and d_{133} from the earlier analysis. Thus, the constitutive relationship can be solved explicitly for κ_{133} and κ_{333}:

$$\kappa_{133} = \frac{\varepsilon_1 - s_{13}\sigma_3 - d_{31}E_3 - \frac{1}{2}d_{133}E_3^2}{\sigma_3 E_3} \tag{5.36}$$

$$\kappa_{333} = \frac{\varepsilon_3 - s_{33}\sigma_3 - d_{33}E_3 - \frac{1}{2}d_{333}E_3^2}{\sigma_3 E_3} \tag{5.37}$$

For the current research effort, the values of these elastostrictive constants can vary a great deal, as they are calculated from parameters that have been seen to change with stress, strain and electric field. Thus, care should be taken to calculate these parameters for the particular operating conditions that the actuator will experience. However, the values for κ_{133} and κ_{333} are many orders of magnitude lower than the piezoelectric strain and electrostrictive constants, thus their impact is small compared to the other terms in the constitutive equation. Nevertheless, for the current effort, the proper stress-strain curves under constant nonzero electric field were measured for MFC voltages from 250 volts to 1500 volts in 250 volt increments, and at mean stress levels corresponding to 20, 30, and 40 pound loads, for MFC S/N 429. Thus the necessary stress-strain-field data is available for accurate calculations of the elastostrictive constants over almost the entire

applicable stress-electric field range of interest. For example, Figure 5.46 shows the measured stress-strain curves at a constant electric field of 937 kV / m (500 volts).

From this figure, the lowest stress point is at 11.8 MPa, a longitudinal strain of 0.000866, a transverse strain of -0.000354 (shifted to 0.000751 and -0.000295 respectively to remove nonzero strains in gages at the beginning of the experiment). For this load and DC field level, d_{33}, d_{31}, d_{333}, and d_{133} have the values 3.44×10^{-10} m / V, -1.57×10^{-10} m / V, 5.15×10^{-17} m^2 / V^2, and -3.41×10^{-17} m^2 / V^2. The compliances are assumed to not vary with electric field, and are constant in the linear-elastic region, thus the average experimental values of -1.06×10^{-11} m^2 / N and 3.4×10^{-11} m^2 / N for s_{13} and s_{33} are used, respectively. Thus, with Equations 5.36 and 5.37, the elastostrictive parameters for these conditions, κ_{133} and κ_{333}, are calculated to be -6.77×10^{-19} m^3 / NV and 2.45×10^{-19} m^3 / NV, respectively.

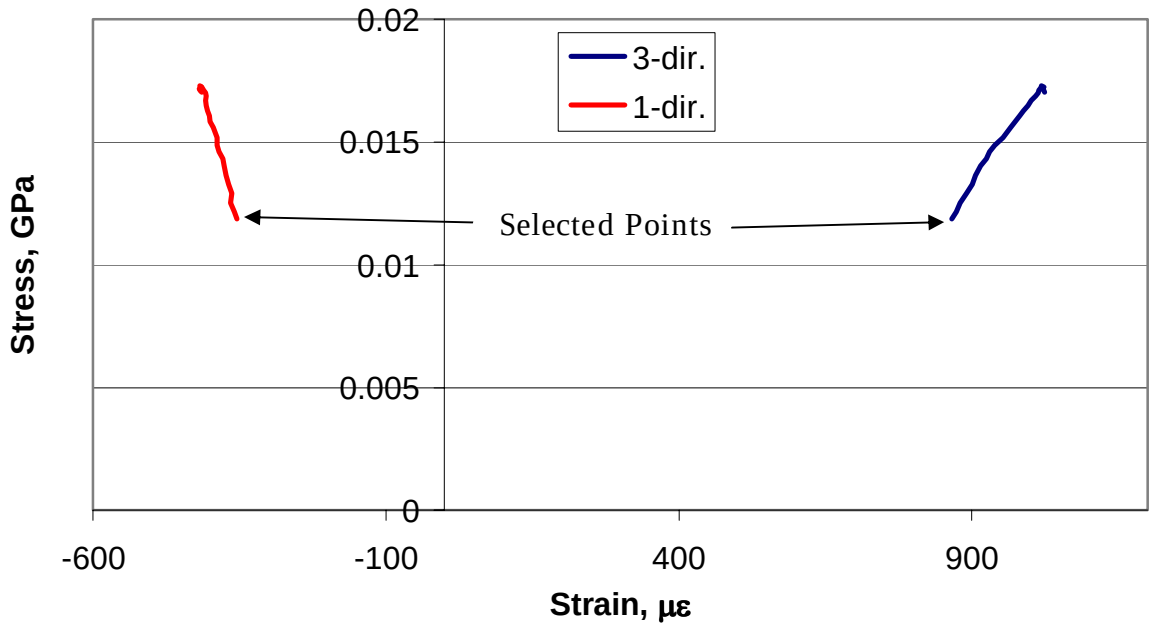

Figure 5.46: Stress-Strain Curves at Const. Electric Field for MFC S / N 429

5.6 Experimental Results:

Thus far, a detailed data analysis has been outlined to determine the nonlinear piezoelectric parameters for the reference MFC geometry under various constant

applied mechanical stresses and both constant and low frequency sinusoidal electric field magnitudes. This section provides the results of this data analysis. In Tables 5.3 through 5.6 below, the relevant nonlinear piezoelectric strain and electrostrictive parameters are presented. According to the nonlinear model, these parameters measured under free-strain conditions are those required for most analyses, however, this effort has strived to measure "effective" actuation parameters under various nonzero stress levels. Both highly useful sets of parameters are provided below. All values represent the mean values for the five MFC specimens tested, and it should be noted that the standard deviations are omitted for the nonzero stress levels, yet they are similar in magnitude to those for the free-strain cases.

5.6.1 Free-Strain (Zero Stress) Actuation Parameters:

Table 5.3 shows the nonlinear actuation parameters measured for the reference MFC geometry from this chapter under free-strain conditions, according to the modified constitutive relations, Equations, 5.34 and 5.35.

Table 5.3: Piezoelectric Strain Constants for Reference MFC, Free-Strain Case

Characterization Parameter	DC Offset Voltage					
	0 VDC		250 VDC		500 VDC	
	Value	Std. Dev.	Value	Std. Dev.	Value	Std. Dev.
d_{33}, m/V	2.72E-10	2.0E-11	3.38E-10	1.1E-11	3.80E-10	3.0E-11
d_{31}, m/V	-1.33E-10	1.6E-11	-1.50E-10	7.8E-12	-1.70E-10	1.7E-11
d_{333}, m^2/V^2	3.96E-16	6.9E-17	1.34E-16	4.1E-17	5.68E-17	1.0E-17
d_{133}, m^2/V^2	-1.51E-16	3.9E-17	-7.30E-17	2.3E-17	-3.92E-17	8.1E-18
d_{3DC}, m/V	N/A	N/A	9.21E-13	7.5E-14	9.30E-13	8.9E-14
d_{1DC}, m/V	N/A	N/A	-4.37E-13	4.92E-14	-4.63E-13	6.1E-14

From this table, a few interesting trends are noticed. First, the absolute value of d_{33} and d_{31} increase under higher DC offset voltages, which indicates that the MFC is a more efficient actuator under such combined electrical loading. Also, the absolute values of

the electrostrictive constants, which are a measure of the degree of nonlinearity of the actuation performance, decrease under increased DC biasing voltages. This relationship mirrors that seen in the numerous actuation figures from this chapter, where the strain-field behavior of the MFC becomes much more linear under higher DC offset voltages. Lastly, the values used to calculate the induced DC offset strain, d_{3DC} and d_{1DC}, are nearly identical, which means that this offset strain is a linear function of DC biasing voltage, at least within the zero to 500 volt range investigated herein.

5.6.2 Constant Nonzero Stress Actuation Parameters:

Tables 5.4 through 5.6 present the nonlinear actuation parameters measured for the reference MFC geometry from this chapter under nonzero constant mechanical stress levels. The three tables correspond to the three DC biasing voltages applied to the actuators, namely 0, 250, and 500 VDC. These parameters are technically "apparent" values since they are measured under such mechanical loads. However, they are quite useful for practical structural actuation problems.

Table 5.4: Piezoelectric Strain Constants for Reference MFC, Constant Stress, 0 VDC

Load, lb (N)	0 VDC Offset Voltage			
	d_{33}, m/V	d_{31}, m/V	d_{333}, m^2/V^2	d_{133}, m^2/V^2
0	2.72E-10	-1.33E-10	3.96E-16	-1.51E-16
1 (4.45)	2.72E-10	-1.34E-10	4.22E-16	-1.48E-16
10 (44.5)	2.70E-10	-1.30E-10	4.41E-16	-1.49E-16
20 (89.0)	2.72E-10	-1.34E-10	4.22E-16	-1.37E-16
30 (133)	2.74E-10	-1.30E-10	3.68E-16	-1.36E-16
40 (178)	2.66E-10	-1.31E-10	3.63E-16	-1.18E-16
50 (222)	2.63E-10	-1.34E-10	3.13E-16	-9.74E-17
52 (231)	2.64E-10	-1.29E-10	2.97E-16	-1.08E-16
54 (240)	2.57E-10	-1.31E-10	2.81E-16	-1.14E-16
56 (249)	2.48E-10	-1.32E-10	3.17E-16	-9.96E-17
58 (258)	2.48E-10	-1.26E-10	2.95E-16	-1.11E-16
60 (267)	2.38E-10	-1.21E-10	2.97E-16	-1.14E-16

Table 5.5: Piezoelectric Strain Constants for Reference MFC, Constant Stress, 250 VDC

Load, lb (N)	250 VDC Offset Voltage					
	d_{33}, m/V	d_{31}, m/V	d_{333}, m^2/V^2	d_{133}, m^2/V^2	d_{3DC}, m/V	d_{1DC}, m/V
0	3.38E-10	-1.50E-10	1.34E-16	-7.30E-17	9.21E-13	-4.37E-13
1 (4.45)	3.47E-10	-1.44E-10	1.30E-16	-7.61E-17	8.99E-13	-4.33E-13
10 (44.5)	3.36E-10	-1.45E-10	1.24E-16	-7.02E-17	8.96E-13	-4.23E-13
20 (89.0)	3.34E-10	-1.46E-10	1.09E-16	-6.37E-17	8.56E-13	-4.08E-13
30 (133)	3.26E-10	-1.46E-10	9.38E-17	-5.72E-17	7.95E-13	-3.83E-13
40 (178)	3.19E-10	-1.45E-10	7.40E-17	-4.80E-17	7.10E-13	-3.19E-13
50 (222)	3.12E-10	-1.36E-10	5.76E-17	-4.62E-17	5.00E-13	-2.69E-14
52 (231)	3.19E-10	-1.32E-10	5.43E-17	-5.20E-17	6.77E-13	-1.95E-13
54 (240)	3.09E-10	-1.35E-10	5.47E-17	-4.73E-17	8.22E-13	-2.60E-13
56 (249)	2.93E-10	-1.34E-10	6.18E-17	-4.65E-17	7.25E-13	-2.75E-13
58 (258)	2.89E-10	-1.33E-10	5.94E-17	-4.56E-17	7.15E-13	-2.82E-13
60 (267)	2.80E-10	-1.22E-10	5.93E-17	-5.00E-17	7.07E-13	-2.76E-13

Table 5.6: Piezoelectric Strain Constants for Reference MFC, Constant Stress, 500 VDC

Load, lb (N)	500 VDC Offset Voltage					
	d_{33}, m/V	d_{31}, m/V	d_{333}, m^2/V^2	d_{133}, m^2/V^2	d_{3DC}, m/V	d_{1DC}, m/V
0	3.80E-10	-1.70E-10	5.68E-17	-3.92E-17	9.30E-13	-4.63E-13
1 (4.45)	3.73E-10	-1.58E-10	6.06E-17	-4.32E-17	8.96E-13	-4.34E-13
10 (44.5)	3.55E-10	-1.55E-10	5.86E-17	-3.95E-17	8.97E-13	-4.31E-13
20 (89.0)	3.44E-10	-1.57E-10	5.15E-17	-3.41E-17	8.60E-13	-4.25E-13
30 (133)	3.40E-10	-1.50E-10	3.84E-17	-3.24E-17	8.09E-13	-4.04E-13
40 (178)	3.19E-10	-1.53E-10	3.35E-17	-2.28E-17	7.63E-13	-3.23E-13
50 (222)	3.10E-10	-1.34E-10	3.03E-17	-3.04E-17	4.43E-13	7.33E-14
52 (231)	3.13E-10	-1.38E-10	2.47E-17	-2.71E-17	6.73E-13	-2.10E-13
54 (240)	3.00E-10	-1.38E-10	2.79E-17	-2.62E-17	8.38E-13	-2.73E-13
56 (249)	2.93E-10	-1.35E-10	2.88E-17	-2.73E-17	7.01E-13	-2.73E-13
58 (258)	2.86E-10	-1.29E-10	2.91E-17	-2.96E-17	7.32E-13	-2.96E-13
60 (267)	2.77E-10	-1.24E-10	3.10E-17	-3.11E-17	7.38E-13	-2.84E-13

From the three tables above, a few interesting trends are noted. First, the absolute values of the linear coefficients are seen to decrease with increasing stress level, which indicates that the actuation capacity of the actuator is reduced from the unloaded to the highly stressed condition. Such behavior has been noted for piezoelectric actuators attached to or embedded in a host structure. Next, the absolute values of the electrostrictive coefficients decrease rapidly with increased stress, which means that the

MFC behaves in a more linear manner when loaded mechanically. Lastly, the static strain coefficients are noted to be effectively independent of the offset voltages used in this study, and also are seen to decrease with constant applied stress. This latter type of behavior is a good indication of the reduced actuation capability of the MFC under mechanical loads, which could be encountered as part of an intelligent structure, such as a plate or beam.

5.6.3 Elastostrictive Constants

Section 5.5.5 discusses the calculation of the elastostrictive parameters once the operating conditions are known. While this feature may appear to be a limitation of the model, the values of these parameters are smaller than even the second order electrostrictive coefficients. Thus the inclusion of elastostrictive behavior in the model under combined electromechanical loading is somewhat secondary in nature, thus it is acceptable to ignore its contribution initially to assess the operating conditions of the actuator, and then calculate them as needed to fine-tune a structural actuation model. Additionally, as discussed earlier, the calculation of the elastostrictive constants requires additional stress-strain measurements under constant nonzero electric fields. While a few such measurements were made in the interest of completeness, a rigorous characterization is beyond the scope of the current research effort.

5.7 Summary:

Chapter 5 thoroughly investigates the nonlinear actuation behavior of the reference MFC actuator under monotonically increasing electric fields under a variety of mechanical load/stress levels. A nonlinear model is developed, and the important piezomechanical coefficients are identified and measured for such combined loading behavior. In addition to determining reliable experimental values for these parameters, trends in their behavior are noted in Section 5.6. The MFC is found to have reduced actuation authority under increased mechanical loads, yet is found to behave in a more linear fashion than under zero stress. Also, the application of a DC biasing voltage

greatly improves the actuation behavior of the device by not only producing more linear strain-field behavior, but also increasing the linear piezoelectric strain coefficients.

It should be noted that the values for the MFC presented in this chapter are a bit lower than both bulk PZT values and to those published in the literature for the MFC. One would expect the MFC, which is comprised of PZT fibers in an epoxy matrix, to have a lower d_{33} and d_{31} than bulk PZT (bulk values, 390×10^{-12} m/V and -190×10^{-12} m/V, respectively, for low fields [CTS Wireless, 2000]). However, much of the bulk actuation authority is retained for the MFC. Also, the results in this chapter are somewhat lower than other published MFC values, (400×10^{-12} m/V and -170×10^{-12} m/V, respectively under no bias, and 460×10^{-12} m/V and -210×10^{-12} m/V, respectively under 500 VDC bias [Wilkie, 2003]). As seen in Figures 5.14 and 5.15, the initial monotonic curve is somewhat different than the behavior under cyclic electric loads, which is how the other published values are determined. A great deal of attention is paid to this initial response because simple static structural actuation models are both common in the field of intelligent structures and useful for comparing different types of actuators.

Another useful feature of the model developed and parameters identified in this chapter is that they do not depend on the maximum electric field value applied to the actuator. The model does require a sense of the load levels that the MFC will operate under, which can be estimated rather easily, and whether or not a DC biasing voltage will be used. The latter requires additional hardware and preparation, and is thus known well in advance. Once these two operational parameters are known (load and biasing voltage), the MFC can be subjected to monotonically increasing fields at will, and the model in this chapter will accurately predict its response.

Chapter 6

Hysteretic Response of the Macro Fiber Composite to Low-Frequency Harmonic Electrical Excitation

6.1 Introduction:

In Chapter 5, the response of the reference MFC to a monotonic increase in electric field is investigated under various static mechanical loads and DC offset voltages. Such characterizations lead to numerical values for important piezoelectric coefficients that fully describe the reversible nonlinear behavior by way of a derived nonlinear constitutive model. In this chapter, the total response to a harmonic electrical field input is investigated. As mentioned briefly in the last chapter, the typical output of a piezoceramic material subjected to even moderate cyclic electric fields is a hysteresis loop. In this chapter, these loops will be investigated in two ways. First, a linear regression analysis will be performed on the loops, essentially discarding the hysteretic nonlinearity, but allowing the linear piezoelectric strain coefficients to be measured as a function of electric field and applied tensile stress amplitudes. These parameters can be used to develop nonlinear structural actuation models. The second method applied to

the hysteresis loops is a classical Preisach model, which uses an experimentally measured database to predict the branches of the hysteresis loops for a known input. Such a model is useful because it can predict the behavior for many inputs after only measuring a select few responses.

6.2 Background on Piezoelectric Hysteresis:

Much of the literature pertaining to the irreversible nonlinear behavior (hysteresis) of piezoceramics deals with polarization hysteresis and the associated "butterfly" loops, which occur in a strain-electric field plot when a raw piezoceramic is poled back and forth by large-value positive and negative electric fields. Such polarization effects in piezoceramic materials were investigated by Smith and Ounaies [1999]. They developed nonlinear polarization relationships for piezoceramic materials subjected to moderate to high actuation voltages based on the quantification of reversible and irreversible domain wall motion in response to applied electric fields. These types of nonlinear models were deemed essential to utilizing the full potential of piezoceramic actuators, and since the differential equation models were based on physical phenomenon, they were useful for both characterization and prediction of polarization levels for a wide range of operating conditions. Additionally, the model was shown to be invertable, which facilitates the development of an inverse compensator for linear control design.

In a follow-up work, Smith, Ounaies, and Wieman [2001] modeled rate-dependent mechanisms that contribute to hysteresis in piezoceramics being poled at low frequencies. They noted that reduction in coercive field and polarization values become more prominent at higher frequencies (above ~0.1 Hz). This change was modeled by determining the probability that dipoles achieve the energy required to overcome energy barriers and switch orientation under an electric field. While these works were significant contributions to nonlinear piezoelectric theory, they focused on material polarization, rather than the strain-field actuation behavior of the poled piezoceramic.

Kamlah [2001] also investigated hysteresis effects in piezoceramic materials undergoing poling as well as tensile loading and unloading. He began by discussing the microstructure of the material, and presenting micromechanical and phenomenological modeling efforts from the relevant literature. Then he developed a constitutive model for the main large-signal hysteretic behavior and employed the model using a finite element analysis of a piezoceramic stack. The benefits of the model included a detailed understanding of the residual stresses in the material after poling.

Fang and Li [1999] tested the response of monolithic PZT piezoceramic to combined electromechanical loads, where the electrical loads were cyclic and the mechanical loading was only compressive in nature. The effect of compressive stress on the strain-electric field and electric displacement-electric field hysteresis loops was depicted. Higher stress levels were seen to reduce the amount of hysteretic behavior. In addition, a domain-switching model was outlined.

While the hysteretic behavior discussed above is important to the field of piezoelectrics, it does not address the nonlinear behavior of a poled piezoceramic subjected to large positive and slightly negative electric fields, which do not cause reversal of the polarization direction. For the field of intelligent materials, this type of nonlinear behavior has a much more practical application. It is in this context that this chapter is developed. There are two main approaches to describing piezoelectric hysteresis, the Rayleigh Law and the Preisach model, both of which originated in the study of magnetics.

A good description of the Rayleigh Law was given by Damjanovic and Demartin [1996] as it applies to the direct piezoelectric effect. There, the dependence of the piezoelectric coefficient on the amplitude of alternating compressive stress was investigated for a variety of piezoceramic materials. A nonlinear Rayleigh material parameter was defined and measured experimentally in order to capture the hysteresis effect.

However, this model was developed with the inherent limitation to low amplitude mechanical stresses, which presumably restricts the material to linear-elastic mechanical behavior. In a follow-up paper, Damjanovic [1997] expanded the earlier investigation for PZT piezoceramic. The experimental results suggested that the hysteretic and dependence of the piezoelectric coefficients on stress was primarily due to pinning of non-180° domain walls. Frequency-dependence of the piezoelectric coefficients was also investigated.

The most widely applicable hysteresis models were developed from the Preisach description, which was originally developed for the study of magnetics [Mayergoyz, 1991]. Preisach models have since been utilized in many other scientific areas, such as adsorption, superconductors, magnetostrictors, and electrorheological (ER) fluids [Han et al., 2003], among others. For the current research effort, the application of the Preisach model for piezoceramic applications is of primary interest. An important text in this field was written by Mayergoyz [1991], whose model was developed without a specific physical application in mind so that it can be applied to practically any hysteretic phenomenon.

Robert, Damjanovic and Setter [2001] investigated the quadratic variation of the longitudinal piezoelectric coefficient with electric field and the resulting hysteresis loop under a variety of biasing compressive stresses. Along with stress amplitude-dependent parameters and the introduction of a viscous term, the model was able to match the experimental hysteresis loop for the direct piezoelectric effect.

Robert et al. [2001] used a collection of distributed bistable units along with the Preisach approach to describe the hysteretic response of piezoelectric materials. The microscopic effects of moving a domain wall in a stochastically-described pinning field were discussed, as are the resulting field-dependent piezoelectric coefficients. The effects of DC field and thresholds for nonlinear behavior were also investigated qualitatively.

Hu and Mrad [2003] applied a classical Preisach model to describe the hysteretic behavior of stacked piezoceramic actuators. Their intent was to assess the suitability of the classical model under a wide range of mechanical loads and electrical excitation frequencies. After developing the classical Preisach model, experimental measurements were made to form the required database of displacements under zero applied load and low excitation frequency. This model and database were then used to predict displacements under increasing mechanical loads and frequencies. They found that the classical form of this model was highly accurate when the load and frequency variations were small. That is, the model worked well when the conditions are similar to those for which the data base was developed.

Ge and Jouaneh [1995] presented a fairly rigorous development for a modified version of a classical Preisach model for piezoceramic actuators. The classical model required the hysteresis loops to be congruent, that is, hysteresis loops for a given minimum and maximum input voltage have the same shape and are identical, save for a vertical translation parallel to the strain/displacement axis. This modification allowed the response of the device to be predicted for only positive-valued electric field excitations under free-strain conditions. An experimental procedure was developed to acquire the necessary data base, and to measure the response of the stack actuators. Using this database, the model was found to accurately predict the piezoelectric response to both sinusoidal and triangular wave voltage inputs. In a follow-up paper, Ge and Jouaneh [1997] develop a modified general Preisach model for stack piezoelectric actuators and used the model in a linearizing control scheme. The generalized form of this model removed the congruency requirement mentioned above for the hysteresis loops. The first and second-order reversal curves were experimentally measured to acquire the needed database. The model was then used to predict the output for an exponentially decaying sinusoidal input and an arbitrary, noncyclic input. The maximum error for the model was found to be only 2.3% and 2.7% (for the two input signals, respectively) over the entire applicable range. A model-based linearization scheme using a PID

feedback controller was also developed using the Preisach model for the piezoceramic transducer. This application removed the hysteresis nonlinearity and allowed the output to follow the input more closely.

6.3 Experimental Procedure and Collected Data:

As mentioned in the previous chapter, the experimental setup and procedure for this chapter is the same as that of Section 5.4. That is, sinusoidal, low-frequency voltages of various amplitudes under various DC biasing voltages were applied to the MFC actuator under a variety of constant, unidirectional tensile stresses. A typical voltage input profile for 0 VDC bias is repeated in Figure 6.1.

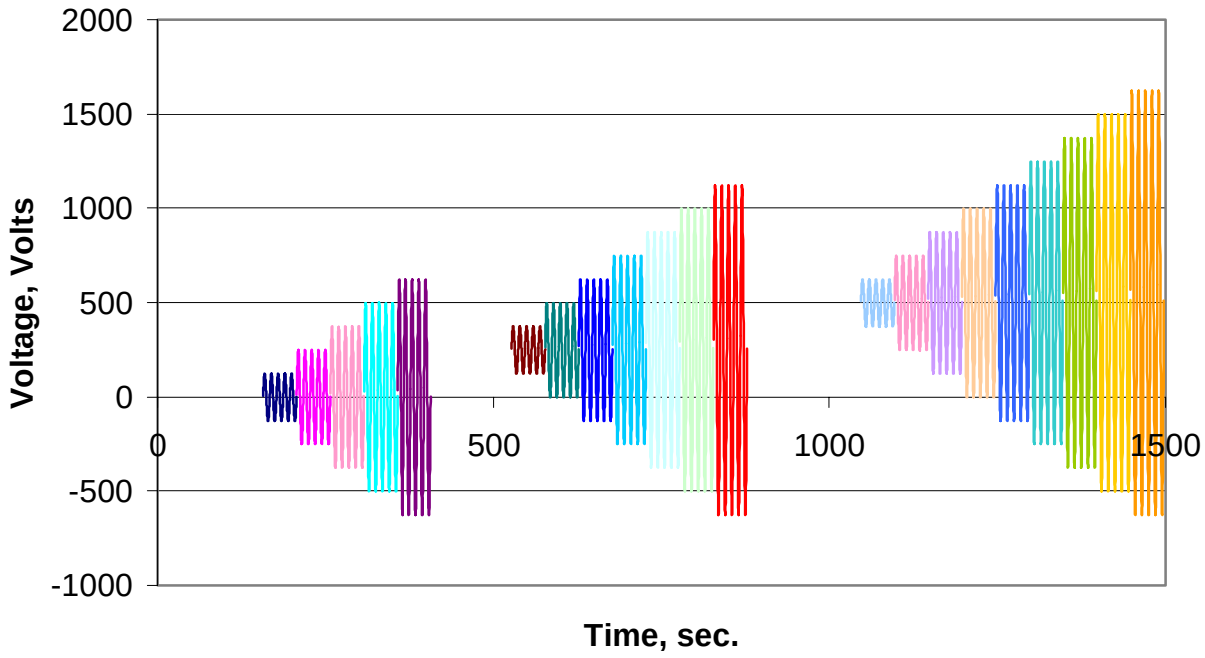

Figure 6.1: Typical Actuation Voltage Profiles

From this input to the MFC, the in-plane strain responses were measured, and sample plots of the 3 and 1-direction strain-electric field responses are repeated here from Figures 5.14 and 5.15.

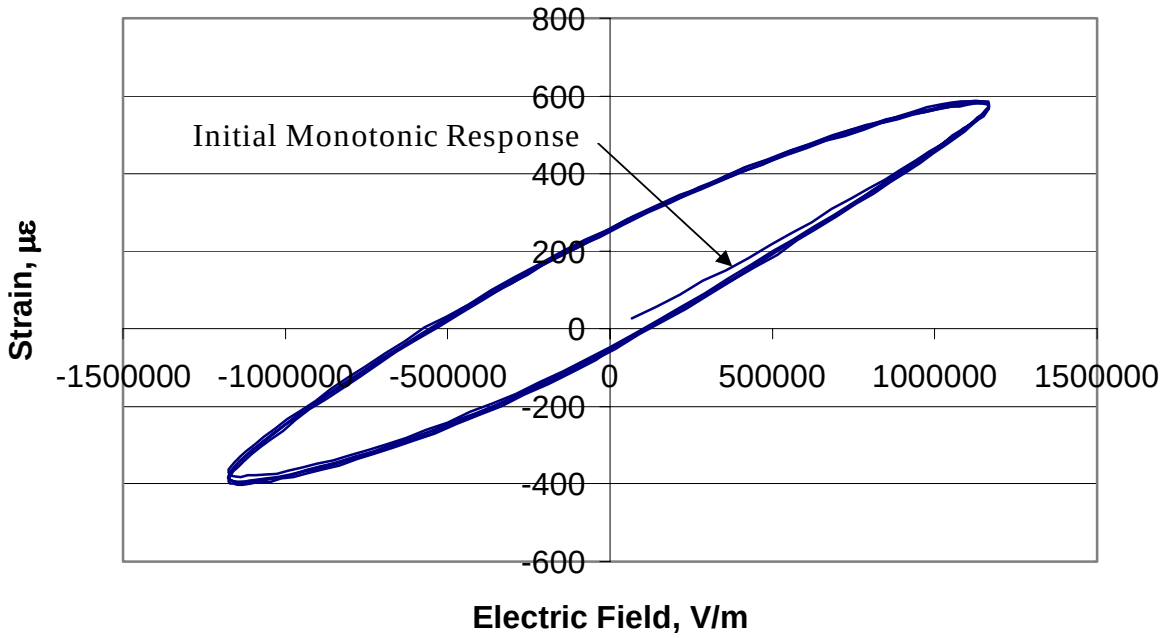

Figure 6.2: 3-Direction Strain-Electric Field Behavior for MFC S/N 404, 1250 Volts Peak-to-Peak, 0 VDC, 0 MPa

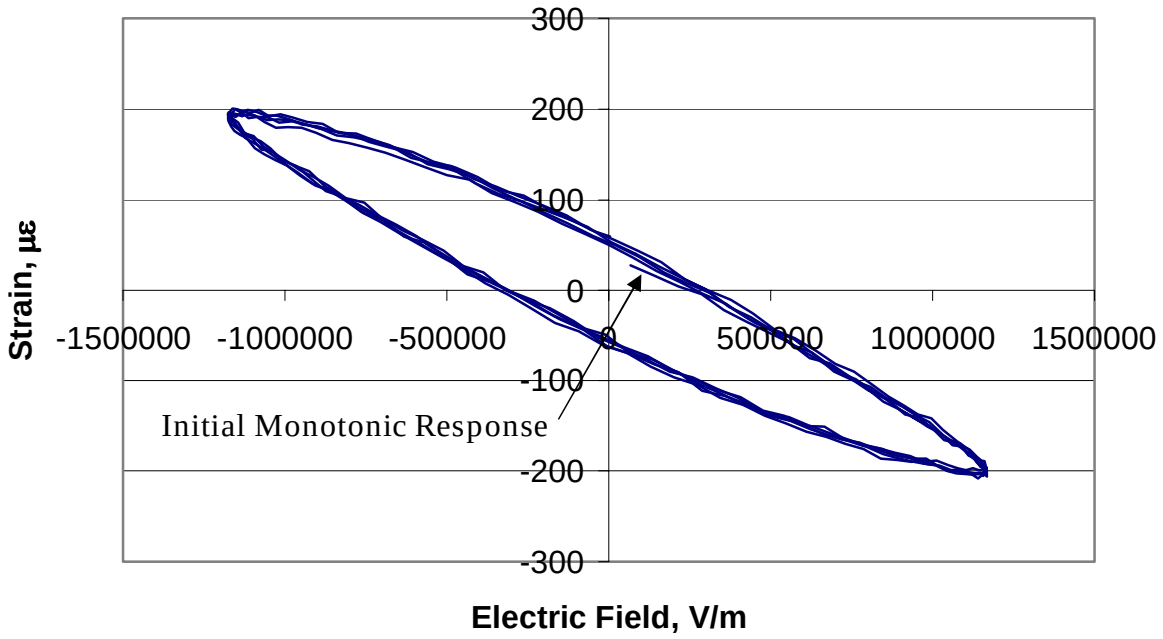

Figure 6.3: 1-Direction Strain-Electric Field Behavior for MFC S/N 404, 1250 Volts Peak-to-Peak, 0 VDC, 0 MPa

As was seen in Chapter 5, some of the experimental specimens suffer from large amounts of piezoelectric drift. This drift is perhaps more pronounced when an entire set of five hysteresis loops are plotted for a given voltage amplitude. Thus, in order to deal with the most stable data possible, only the fifth electrical cycle of data is used for the analysis in this chapter, for both the linear regressions and Preisach modeling. The shifted data calculated in Chapter 5 for monotonic actuation is used for the peak-to-peak analysis. However, a peak-to-peak analysis inherently removes any shifting, drift or elastic strain due to the applied mechanical load. Also, since the experiment was conducted at the single low frequency of 0.1 Hz, frequency-dependent and high frequency responses will not be investigated. Rather, the current effort deals with only the quasi-static response, which is quite useful for initial investigations for intelligent structures.

6.4 Peak-to-Peak Actuation Strain Behavior:

One of the best ways to judge the actuation performance of a piezoceramic–based device is to measure the amount of strain that it is capable of producing under the influence of a variety of external variables. In the current effort, the reference MFC is tested under various voltages while subjected to different constant mechanical loads. In this section, the measured peak-to-peak strains are presented for the 1 and 3-directions, and trends in these important actuation parameters are investigated. The peak-to-peak strains are calculated as the maximum recorded strain minus the minimum recorded strain for the fifth electrical cycles at a given DC offset and peak-to-peak voltage, thus ensuring examination of the most stable piezoelectric behavior possible.

6.4.1 Free-Strain Performance:

The first step in characterizing the performance of a piezoceramic-based device is to ascertain its ability to deform under zero applied stress. Thus, the free-strain performance is measured by applying the three voltage sequences specified in Table 5.1 with the specimen suspended vertically with only the top grip of the testing machine

closed, as described in detail in Section 5.4. The results from this free strain characterization are presented below in Figures 6.4 through 6.6. The bold curves in these figures depict the measured peak-to-peak strain output from the MFC test specimens in both the 1 and 3-directions as a function of the peak-to-peak voltage applied to the interdigitated electrodes with 0, 250, and 500 VDC biasing voltages, respectively. Each curve represents the average of five identical test specimens, and the error bars indicate the sample standard deviation above and the below the mean. The light, dashed curves represent the other biasing voltages, but without error bars.

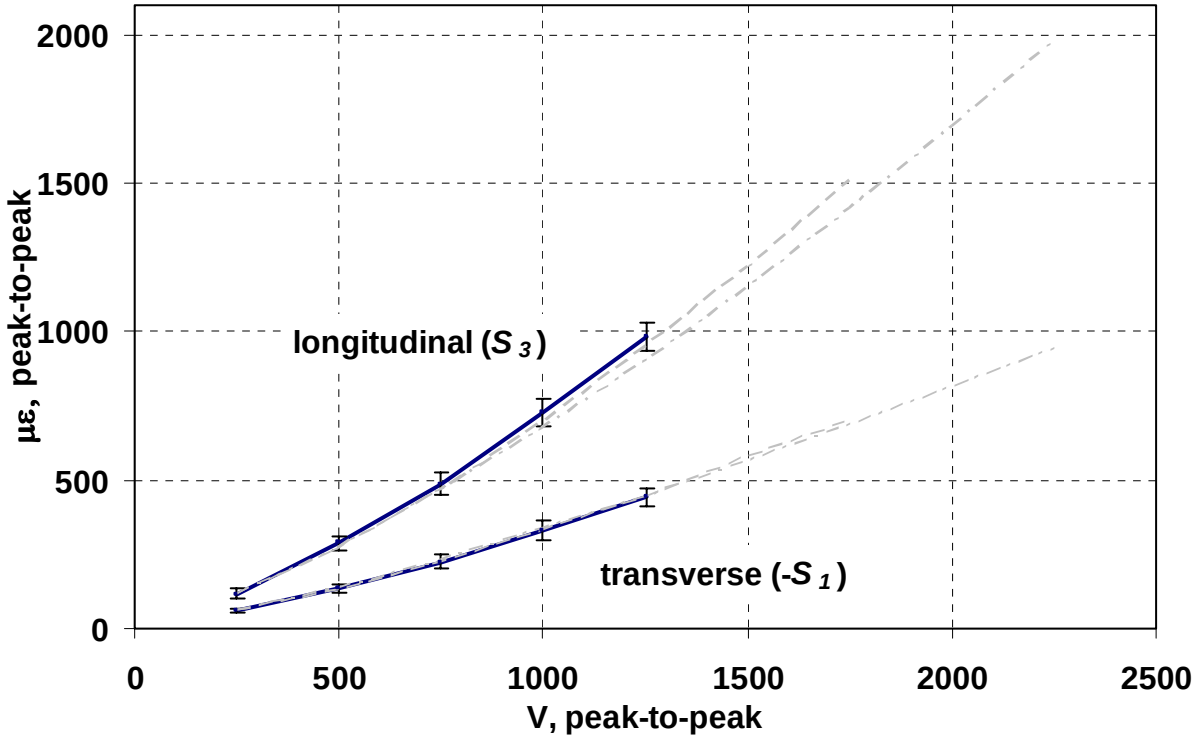

Figure 6.4: Peak-to-Peak Strain Output for the MFC Actuator, Free-Strain Conditions, 0 VDC Bias

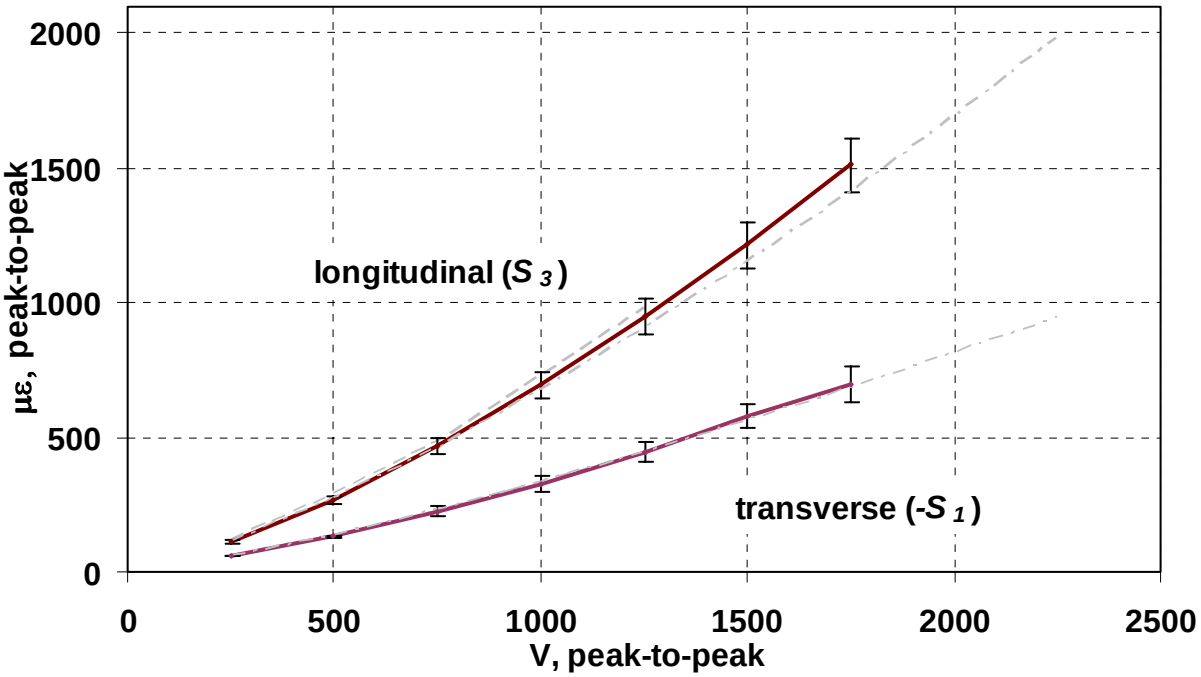

Figure 6.5: Peak-to-Peak Strain Output for the MFC Actuator, Free-Strain Conditions, 250 VDC Bias

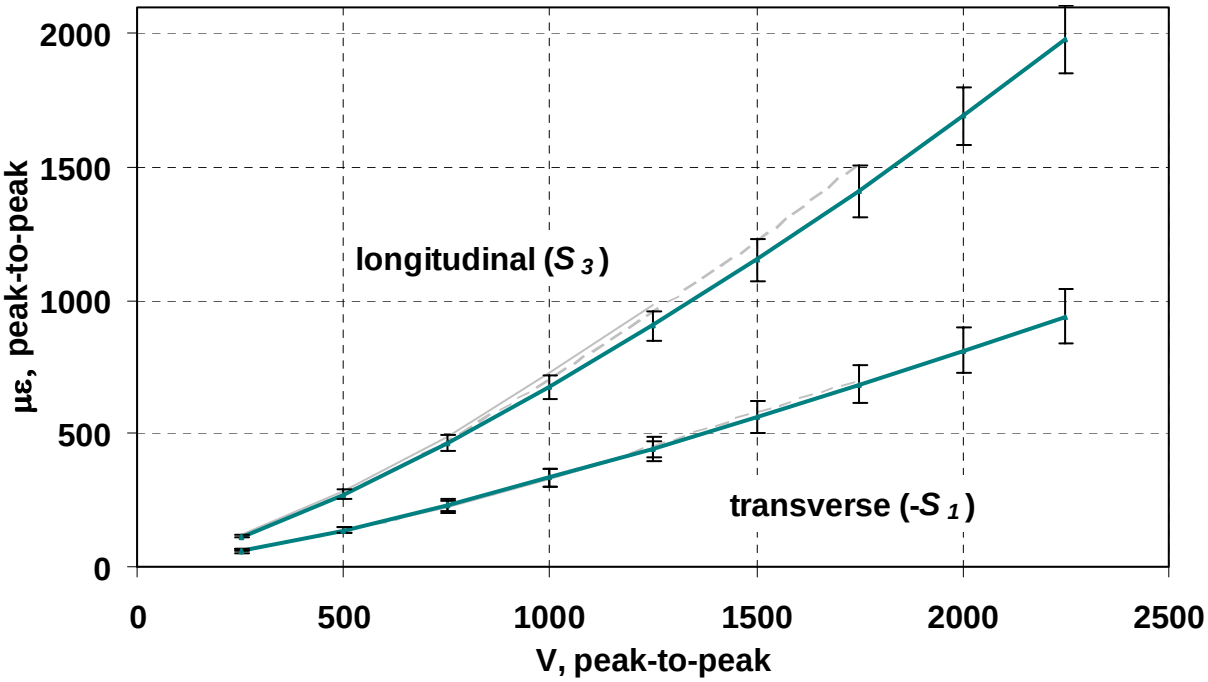

Figure 6.6: Peak-to-Peak Strain Output for the MFC Actuator, Free-Strain Conditions, 500 VDC Bias

Inspection of these plots shows many important trends. First, each of the three biasing voltage curves in the two orthogonal directions lie on approximately the same curve, which indicates that the offset voltage does not significantly effect the nature (shape) of the free-strain behavior of the device, but rather allows one to obtain higher strain outputs by actuating under higher maximum voltages. Next, the relatively small size of the error bars indicates the high degree of repeatability exhibited by the MFC in terms of induced strain. Lastly, the curves indicate a nonlinear relationship between the applied voltage and induced strain. This behavior is likely attributed to variable piezoelectric domain behavior under either low or high electric fields.

In the interest of investigating trends in the MFC's performance both from these figures and from a numerical standpoint, the recorded strain data from is recast in the form of Table 6.1.

Table 6.1: Peak-to-Peak Actuation Strains for Free-Strain

Values	Peak to Peak Electrode Voltage, Volts								
	250	500	750	1000	1250	1500	1750	2000	2250
0 VDC Offset									
3-Dir. P-P Strain, με	117.6	286.4	485.8	725.0	982.3	N/A			
Std. Dev.	13.7	23.7	37.1	48.1	44.9				
1-Dir. P-P Strain, με	61.1	137.2	224.4	331.1	441.2				
Std. Dev.	9.0	13.4	22.6	33.7	31.1				
250 VDC Offset									
3-Dir. P-P Strain, με	111.1	266.8	465.2	694.3	949.4	1215.1	1510.5	N/A	
Std. Dev.	8.7	16.8	30.3	47.2	65.1	87.0	99.0		
1-Dir. P-P Strain, με	58.6	131.2	223.6	327.9	446.7	581.1	699.2		
Std. Dev.	2.5	5.9	19.2	30.0	39.1	44.6	66.9		
500 VDC Offset									
3-Dir. P-P Strain, με	114.0	271.6	462.8	674.1	904.8	1151.4	1411.4	1692.2	1981.8
Std. Dev.	4.6	18.4	30.3	44.6	57.1	78.0	96.3	111.1	128.7
1-Dir. P-P Strain, με	61.1	136.8	231.0	334.9	443.6	562.5	684.8	812.7	940.1
Std. Dev.	4.8	10.4	21.3	31.4	42.5	56.5	72.9	86.6	100.6

6.4.2 Nonzero Constant Stress Performance:

While the peak-to-peak strain measurements investigated above for free-strain conditions are a good indicator of the proper functioning and actuation capability of the MFC, this device is typically subjected to some sort of external mechanical stress by virtue of being bonded to or embedded in a host structure. Therefore, it is also important to understand how the actuation strain output is influenced by the presence of such loads. In a manner similar to the free-strain measurements above, Figures 6.7 through 6.9 below depict the relationship between the actuation strains and the peak-to-peak electrode voltage as a function of constant nonzero applied load. The families of curves begin with the free-strain curve, for purposes of comparison, and increase through to the sixty pound load case.

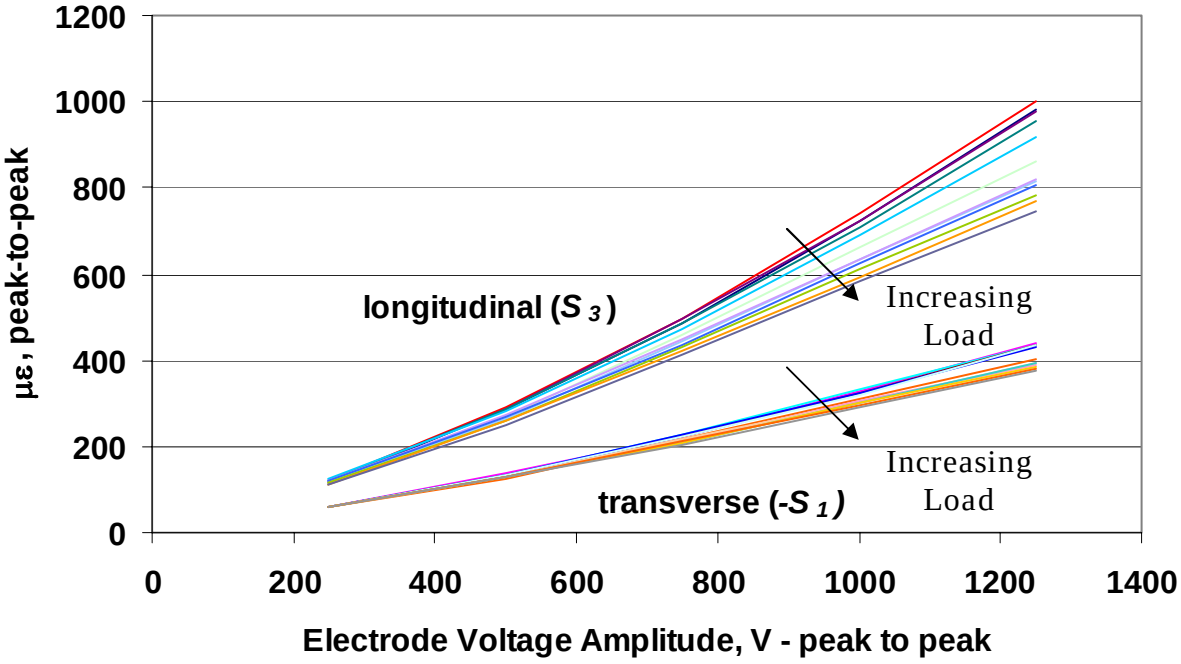

Figure 6.7: Peak-to-Peak Strain Output for the MFC Actuator, 0 VDC Offset and Various Peak-to-Peak Electrode Voltages, Constant Nonzero Stress Levels

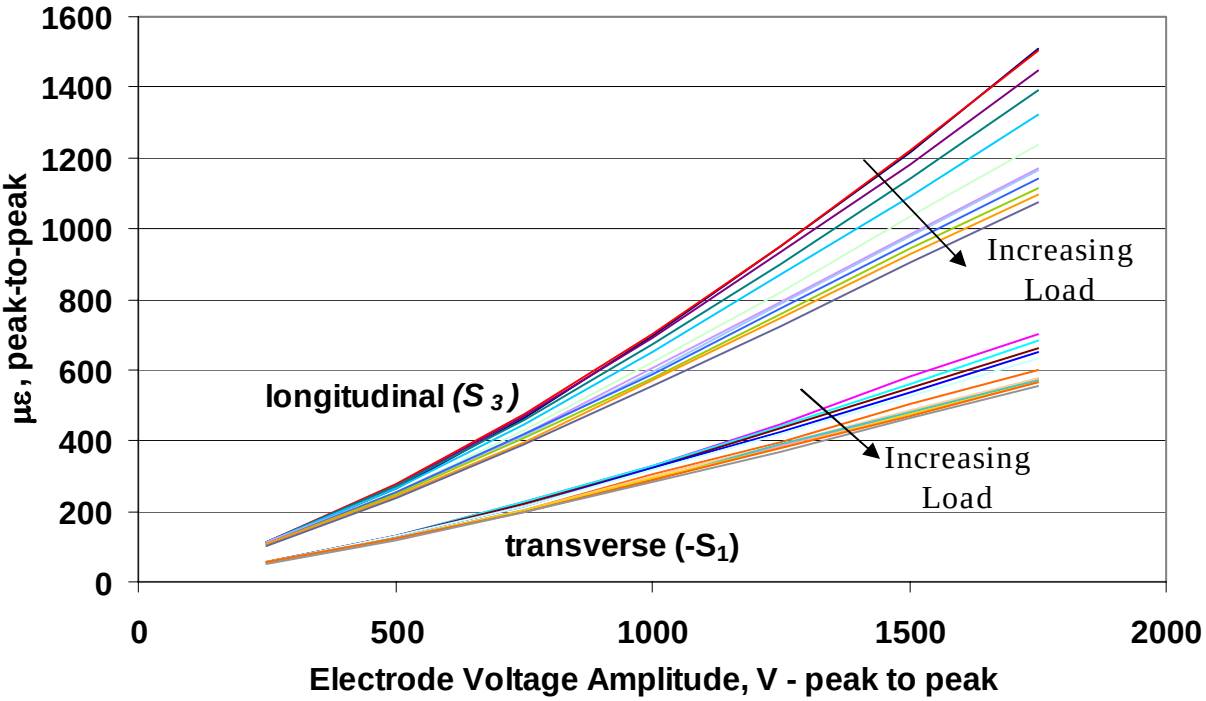

Figure 6.8: Peak-to-Peak Strain Output for the MFC Actuator, 250 VDC Offset and Various Peak-to-Peak Electrode Voltages, Constant Nonzero Stress Levels

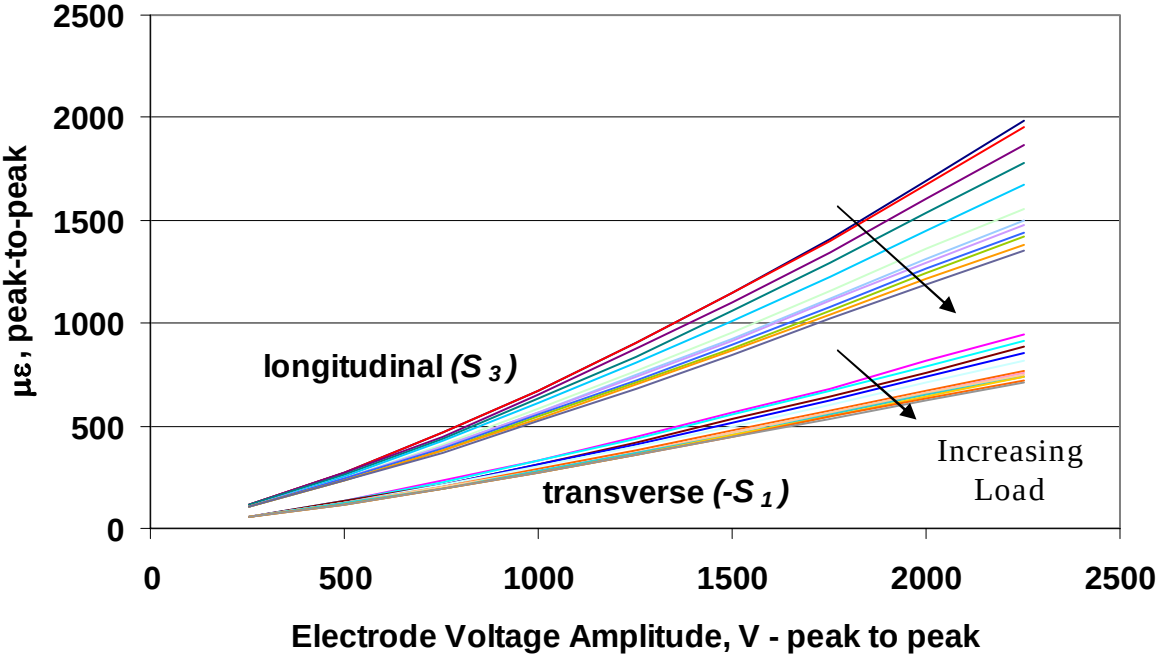

Figure 6.9: Peak-to-Peak Strain Output for the MFC Actuator, 250 VDC Offset and Various Peak-to-Peak Electrode Voltages, Constant Nonzero Stress Levels

From the three figures above, several interesting trends are noted. First, as expected, the peak-to-peak strain increases at higher peak-to-peak excitations. However, this increase is clearly nonlinear, and is a result of material nonlinearities which arise in the form of nonconstant material parameters, as discussed in detail in the next section. Also, the application of a DC biasing voltage allows for a large increase in available peak-to-peak strain output, while slightly increasing the nonlinearity of these curves. Lastly, the application of constant nonzero mechanical loads within the linear-elastic region causes the evenly spaced curves for equal load increments. However, the marked decrease in strain output is not an elastic effect, but rather the presence of increasing mechanical loads degrades the ability of the actuator to induce strain.

6.5 Effective Piezoelectric Strain Coefficients, d_{33} and d_{31}:

In this section, a linear regression analysis is preformed on the measured strain-field data. As stated above, only the fifth and presumably most stable hysteresis loop is considered. In this section, the shifted strains as calculated in Chapter 5 are analyzed. However, since only the slopes of the data are required, the shifting i.e. vertical locations of the curves are not relevant. A typical plot with the linear regression line and equation for MFC S/N 404 under free-strain conditions with a 0.1 Hz sinusoidal excitation voltage of 1250 volts peak-to-peak and no DC biasing voltage is shown in Figure 6.10.

Physically, the slope of a linear regression through these loops represents the effective piezoelectric strain parameters (d_{33} and d_{31}) for the given test conditions, i.e. constant stress and peak-to-peak electric field levels. In the interest of simplicity, and following a precedent set in the literature [Bent, 1997], these parameters are calculated as

$$d_{33}^{eff} = \frac{3-direction\ peak-to-peak\ strain}{applied\ peak-to-peak\ electric\ field} \tag{6.1}$$

$$d_{31}^{eff} = \frac{1-direction\ peak-to-peak\ strain}{applied\ peak-to-peak\ electric\ field} \tag{6.2}$$

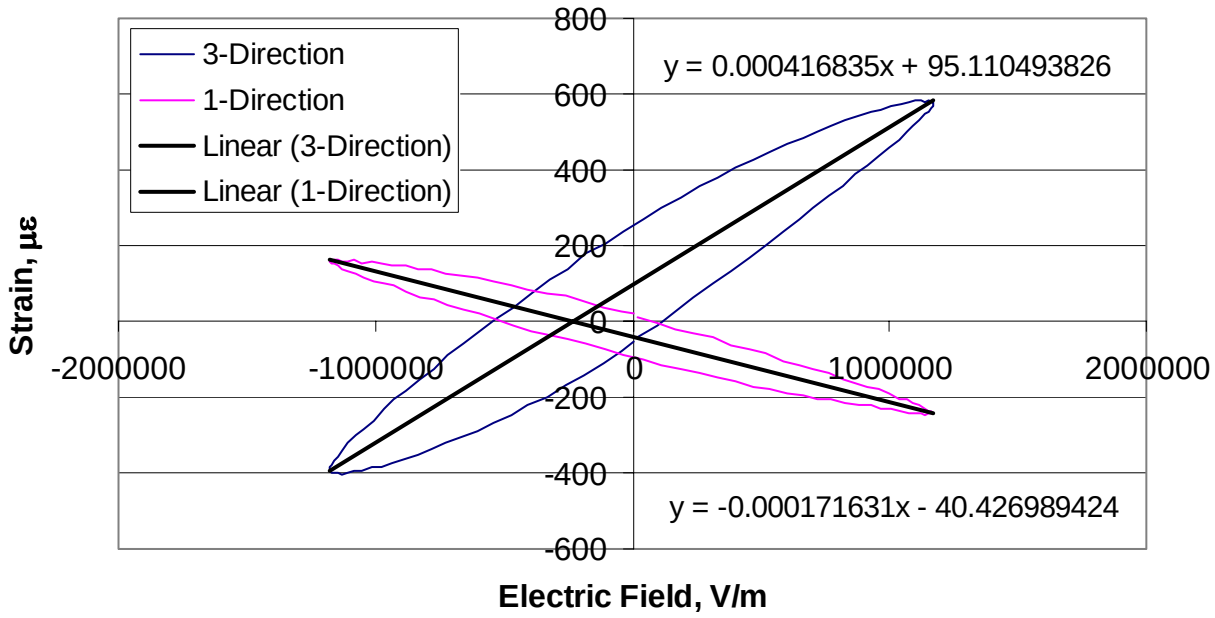

Figure 6.10: Typical Strain - Electric Field Plot for MFC

6.5.1 Piezoelectric Strain Coefficients for Zero Stress (Free-Strain):

As was discussed in Chapter 5, the piezoelectric strain coefficients, d_{33} and d_{31}, for a piezoelectric material are defined at a constant stress, which is typically taken to be zero for the sake of easy laboratory measurements. With this standard in mind, the data analysis methodology presented above is used to investigate trends in these piezoelectric strain coefficients under free-strain mechanical boundary conditions. These effective properties are calculated in Microsoft Excel for each of the DC biasing voltages at each of the constant mechanical load levels (nonzero loads presented in Section 6.5.2). Figures 6.11 through 6.13 show these parameters as a function of the peak-to-peak voltage applied to the interdigitated electrodes for 0, 250, and 500 VDC, respectively. The results represent the mean of the five specimens, and the error bars indicate the sample standard deviation above and below the mean. The light, dashed curves represent the other biasing voltages, but error bars are omitted for clarity.

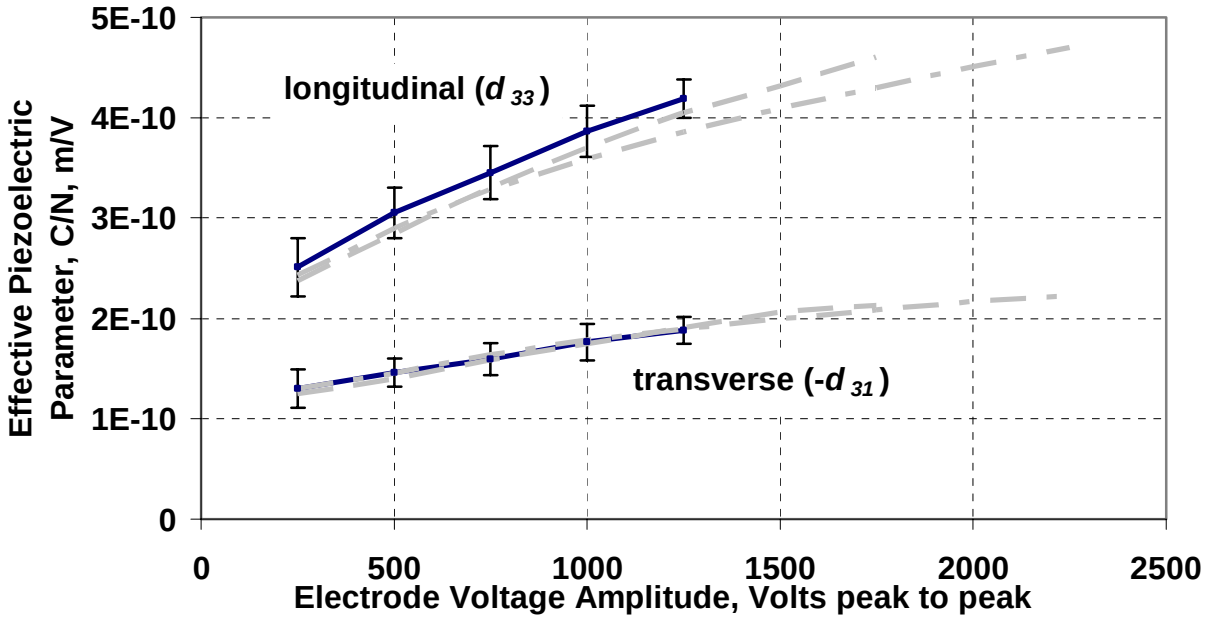

Figure 6.11: Effective Piezoelectric Strain Parameters for the MFC Actuator, Free-Strain Conditions, 0 VDC Bias

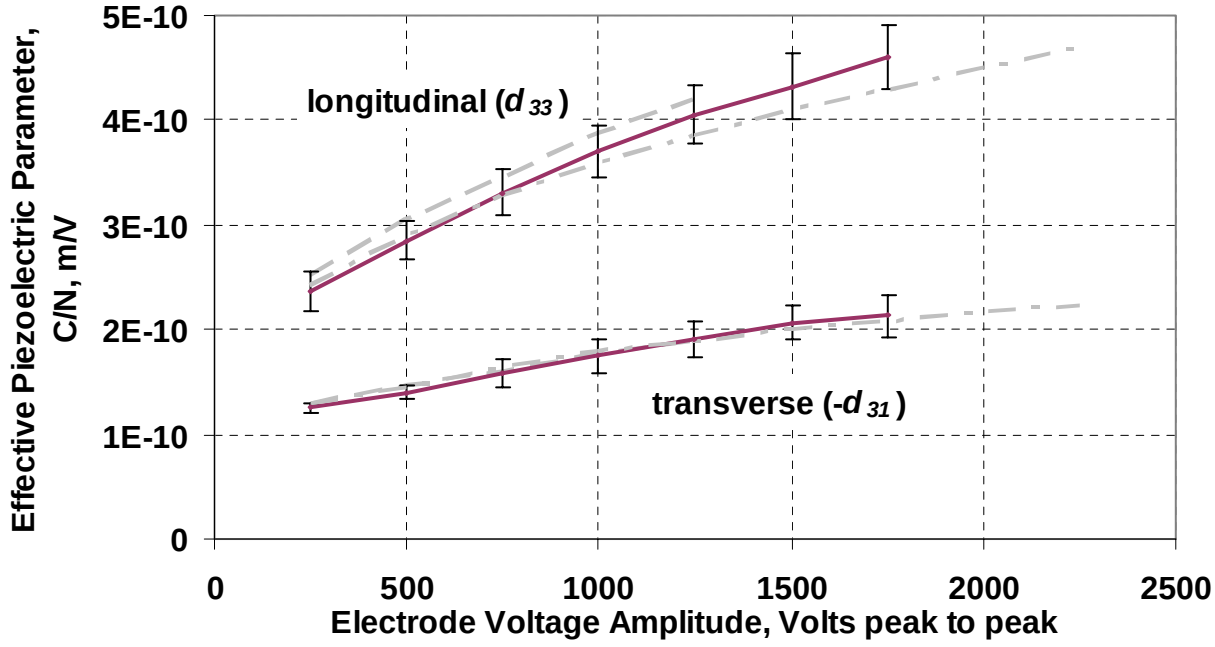

Figure 6.12: Effective Piezoelectric Strain Parameters for the MFC Actuator, Free-Strain Conditions, 0 VDC Bias

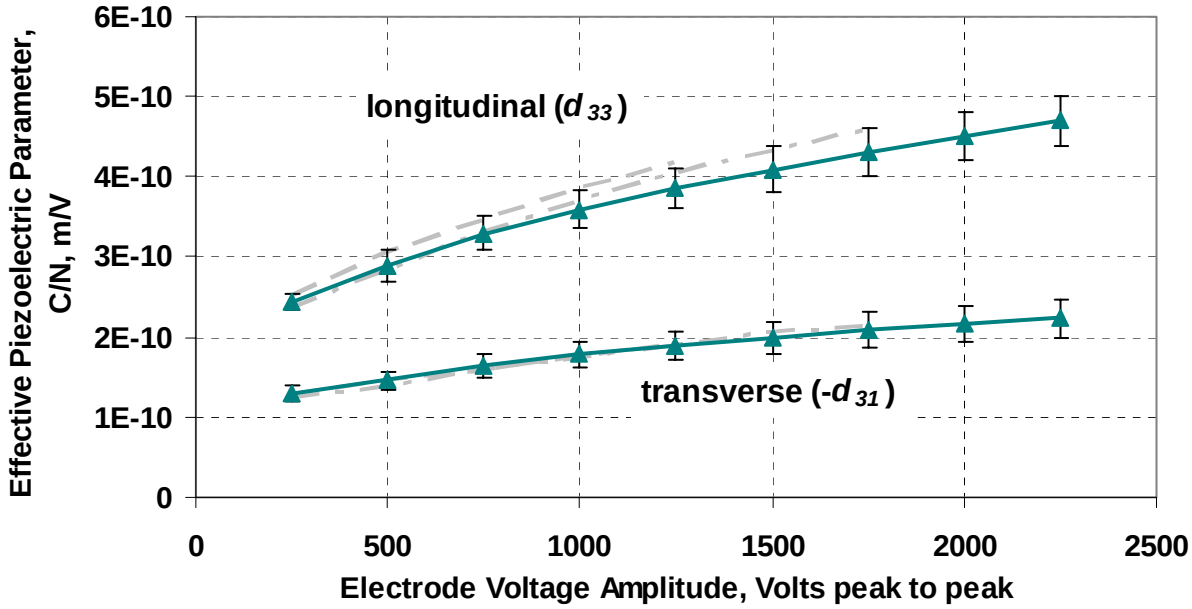

Figure 6.13: Effective Piezoelectric Strain Parameters for MFC Actuator for Free-Strain with 500 VDC Bias

Inspection of these curves reveals many important features. First, the d_{31} curves are all practically co-linear, indicating that this particular parameter is not sensitive at all to the biasing voltage. However, the d_{33} curves show a small amount of spread between the various biasing voltages. Next, the small standard deviations again indicate the high level of repeatability exhibited by the MFC. Additionally, there is some indication of nonlinear changes in the *d* parameters; however, the most important feature is that these parameters are highly dependent on the applied voltage. If the device is subjected to low fields, the performance is good, however, under much higher fields, d_{33} can double in magnitude, while d_{31} can increase by as much as about 50%. Such large changes in these key parameters must be included into structural actuation models in order to produce accurate structural deflections.

The results from the three figures above are presented for ease of use in Table 6.2 below. In addition to the graphical and tabulated results, it would be useful to future researchers to have an equation that represents how d_{33} and d_{31} vary with the peak-to-peak voltages, as seen in Figures 6.11 through 6.13. Such second-order equations were

generated in Microsoft Excel, but these equations should be used with care because they are expressed in terms of *peak-to-peak voltage* amplitude. Only one equation is given for d_{31} because it does not depend greatly upon the DC offset voltage, which is not the case for d_{33}.

Table 6.2: Piezoelectric Strain Parameters for Free-Strain

Values	Peak to Peak Electrode Voltage, Volts								
	250	500	750	1000	1250	1500	1750	2000	2250
0 VDC Offset									
d_{33}, m/V	2.51E-10	3.06E-10	3.45E-10	3.87E-10	4.19E-10	N/A			
Std. Dev.	2.9E-11	2.5E-11	2.6E-11	2.6E-11	1.9E-11				
d_{31}, m/V	-1.30E-10	-1.46E-10	-1.60E-10	-1.77E-10	-1.88E-10				
Std. Dev.	1.9E-11	1.4E-11	1.6E-11	1.8E-11	1.3E-11				
250 VDC Offset									
d_{33}, m/V	2.37E-10	2.85E-10	3.31E-10	3.70E-10	4.05E-10	4.32E-10	4.60E-10	N/A	
Std. Dev.	1.9E-11	1.8E-11	2.2E-11	2.5E-11	2.8E-11	3.1E-11	3.0E-11		
d_{31}, m/V	-1.25E-10	-1.40E-10	-1.59E-10	-1.75E-10	-1.91E-10	-2.07E-10	-2.13E-10		
Std. Dev.	5.3E-12	6.2E-12	1.4E-11	1.6E-11	1.7E-11	1.6E-11	2.0E-11		
500 VDC Offset									
d_{33}, m/V	2.43E-10	2.90E-10	3.29E-10	3.60E-10	3.86E-10	4.09E-10	4.30E-10	4.51E-10	4.70E-10
Std. Dev.	9.8E-12	2.0E-11	2.2E-11	2.4E-11	2.4E-11	2.8E-11	2.9E-11	3.0E-11	3.1E-11
d_{31}, m/V	-1.30E-10	-1.46E-10	-1.64E-10	-1.79E-10	-1.89E-10	-2.00E-10	-2.09E-10	-2.17E-10	-2.23E-10
Std. Dev.	1.0E-11	1.1E-11	1.5E-11	1.7E-11	1.8E-11	2.0E-11	2.2E-11	2.3E-11	2.4E-11

$$d_{33}(0VDC) = -4.9x10^{-17} V_{p-p}^2 + 2.41x10^{-13} V_{p-p} + 1.949x10^{-10} \qquad 250V \le V_{p-p} \le 1250V$$

$$d_{33}(250VDC) = -3.85x10^{-17} V_{p-p}^2 + 2.26x10^{-13} V_{p-p} + 1.827x10^{-10} \qquad 250V \le V_{p-p} \le 1750V$$

$$d_{33}(500VDC) = -2.97x10^{-17} V_{p-p}^2 + 1.837x10^{-13} V_{p-p} + 2.03x10^{-10} \qquad 250V \le V_{p-p} \le 2250V$$

$$d_{31} = 1.484x10^{-17} V_{p-p}^2 - 8.52x10^{-14} V_{p-p} - 1.066x10^{-10} \qquad 250V \le V_{p-p} \le 2250V \qquad (6.3)$$

6.5.2 Piezoelectric Strain Coefficients for Nonzero Stress:

While it is critical to understand the ability of the MFC to deform in the absence of applied mechanical stress, it is typically used as either an integrated or surface-bonded actuator which is subjected to various loads. Therefore, it is important to characterize the changes in actuation authority as the applied load is increased from zero. In this

section, the effective piezoelectric strain coefficients are presented for nonzero applied constant stresses. Figures 6.14 through 6.16 show trends in the effective d_{33} and d_{31} parameters as a function of peak-to-peak electrode voltage applied to the MFC as the load increases from zero up to fifty pounds in ten pound increments, and then up to sixty pounds in two pound increments. The data points represent the average of the five specimens. However, the error bars have been omitted for clarity. The numerical values for both the two coefficients and their sample standard deviations are presented in Appendix G.

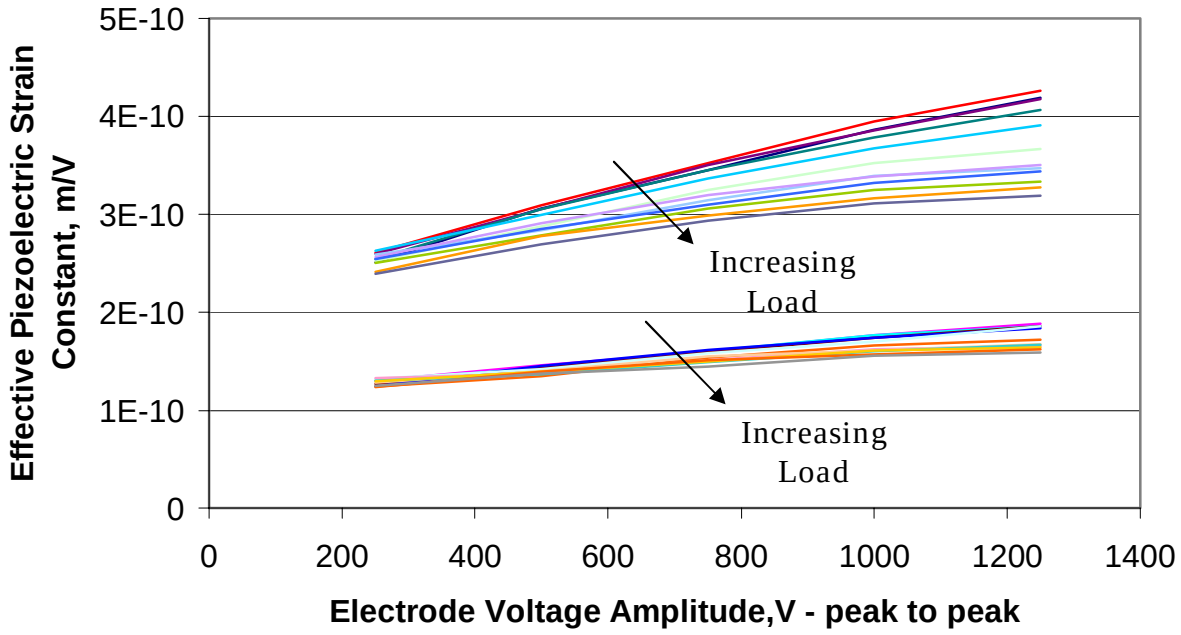

Figure 6.14: Effective d_{33} and d_{31} Values for 0 VDC Offset and Various Peak-to-Peak Electrode Voltages and Constant Stress Levels

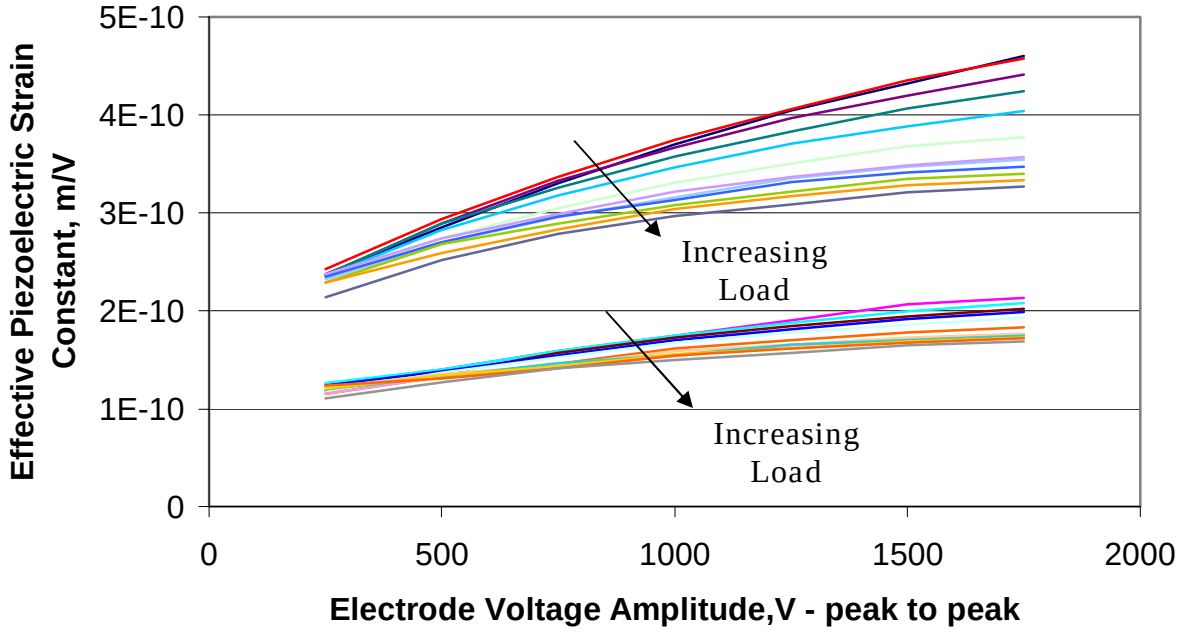

Figure 6.15: Effective d_{33} and d_{31} Values for 250 VDC Offset and Various Peak-to-Peak Electrode Voltages and Constant Stress Levels

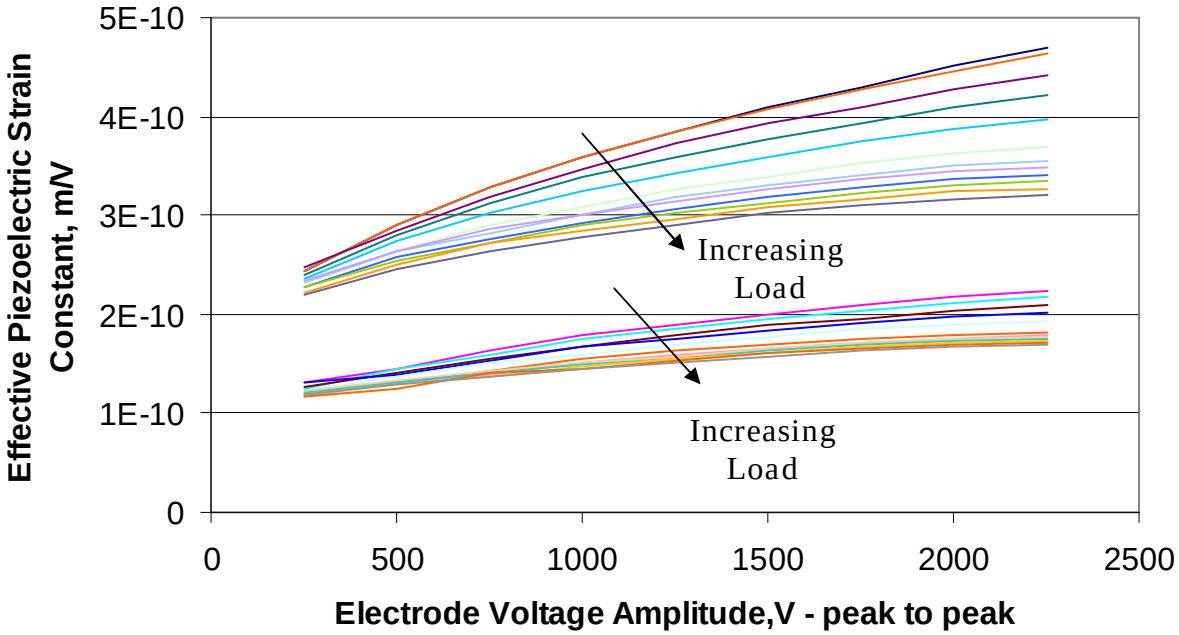

Figure 6.16: Effective d_{33} and d_{31} Values for 500 VDC Offset and Various Peak-to-Peak Electrode Voltages and Constant Stress Levels

From these plots, a few interesting trends are noted. First, it is clear that the higher the excitation voltage, the more actuation capability the MFC exhibits. This effect is true for both harmonic and DC voltages. Said another way, material nonlinearities arise because d_{33} and d_{31} are not constant. For example, under such a wide range of applied voltages, d_{33} varies by up to a factor of two, while about a 50% increase is noted in d_{31}. Since the MFC was tested primarily in the linear elastic region, the families of curves are evenly spaced for a constant increase in mechanical load. Also, d_{31} is less sensitive to increases in both actuation voltage and applied mechanical stress, which stands to reason since the load is applied perpendicular to the strain associated with d_{31}.

6.6 Preisach Hysteresis Loop Modeling:

In the field of intelligent materials, it is a well known fact that piezoelectric materials can exhibit a large amount of hysteresis behavior. This type of behavior is referred to as "irreversible nonlinearity," while the monotonic responses investigated in Chapter 5 are called "reversible nonlinearities." The main distinction between these two types of nonlinearities is that the latter is presumed to follow the same curve for both increasing and decreasing inputs, while the former deals with different behavior for increasing or decreasing input functions. Consider the input and output for the generic hysteretic transducer shown in Figure 6.17.

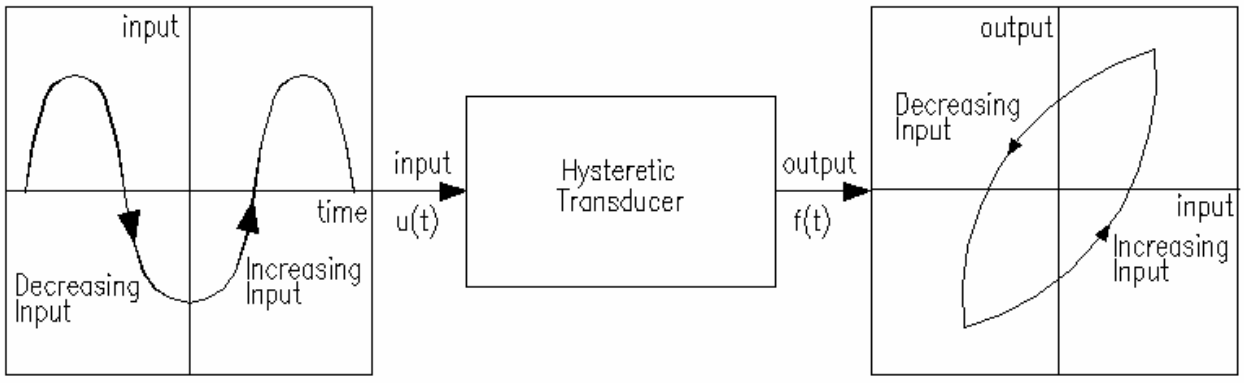

Figure 6.17: Input-Output for Hysteretic Transducer

The output of this device is hysteretic, that it, its output has different branches where the change from one branch to another occurs after a local input extrema. In other words, the particular output curve depends on whether the input is increasing or decreasing. This feature results in a more complicated mathematical description because for a given value of the input, there can be more than one possible output value. It should also be pointed out that this type of behavior is referred to as *static* hysteresis because time/rate effects for the transducer are not included. That is, the time-variation of the input is presumed to be slow enough to not induce dynamic behavior in the device.

Within this set of static hysteresis, there are two subsets of behavior, namely, hysteresis with *local* memory and hysteresis with *nonlocal* memory. For hysteresis nonlinearities with local memory, the future outputs depend only on the current value of the input, whereas the future output for those with nonlocal memories depends on both the current value of the input as well as the previous extremum values of the input. It is well known from the literature that piezoelectric materials exhibit hysteresis with nonlocal memory [Ge and Jouaneh, 1995], hence, only this type of behavior is discussed further herein.

One of the most popular methods for describing such hysteretic behavior is referred to as the Preisach model, which is investigated thoroughly for the remainder of this chapter as it pertains to the experimentally observed behavior of the MFC actuator.

6.6.1 Justification for Implementation of the Classical Preisach Model:

The classical Preisach model, as it has come to be called, was first developed for work with magnetic materials. However, as time went on, it was realized that this model could be applied to other materials and devices that exhibit hysteresis-type behavior. For some of these applications, modifications to the classical model must be made in order to adequately represent more complex hysteretic behavior, such as reversible

nonlinearity. The results of such modifications are referred to as *generalized* Preisach models. As may be expected, the classical model is more straightforward and mathematically easier to implement, but, in order for the classical model to be applicable, two necessary and sufficient conditions must be met by the observed behavior. These two conditions are referred to as the "wiping out" effect and the "congruency" of the minor hysteresis loops. The first of these two effects is clearly satisfied for piezoelectric materials, in that when subjected to a local input extremum, the effects of all previous lesser extremum are erased, or, "wiped out." That is, if a piezoelectric is subjected to the electric field input shown in Figure 6.18, the indicated peaks and valleys will not have an impact on future outputs.

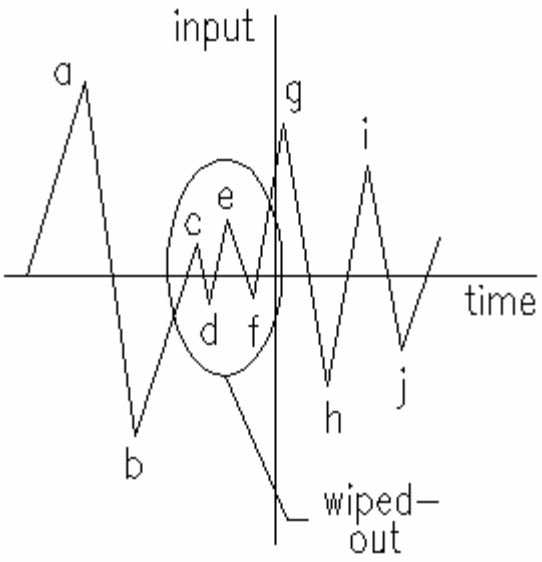

Figure 6.18: "Wiping-Out" Behavior for Piezoelectrics and the Classical Preisach Model

Mathematically speaking, the classical Preisach model only stores the alternating series of dominant input extrema [Mayergoyz, 1991]. This type of behavior is generally known to occur for piezoelectrics.

The second necessary and sufficient condition for the classical Preisach model to be applicable is that of congruency. The congruency requirement specifies that the shape

and inclination of the minor hysteresis loops, which are formed by variations between consecutive local maximum and minimum values, have to be the same for equal extremum no matter when they are encountered in time. Figure 6.19 illustrates congruent minor hysteresis loops. Congruency is satisfied because the minor loops have the same shape and inclination, but are separated only by a vertical translation along the output axis.

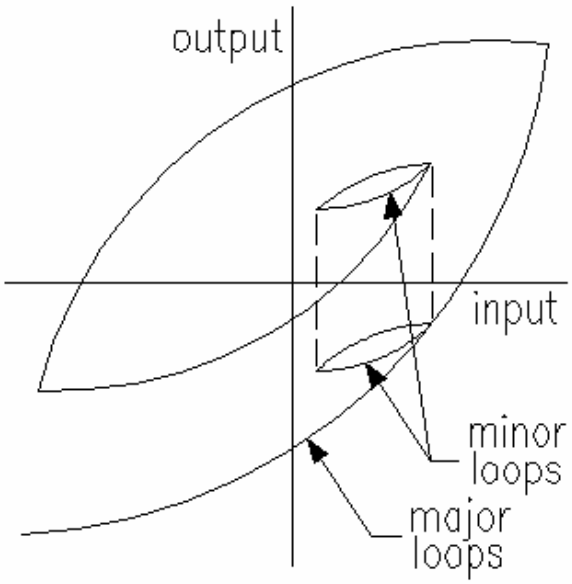

Figure 6.19: Congruency of Minor Hysteresis Loops

For piezoelectric materials, the congruency requirement is satisfied under certain external conditions. Hu and Mrad [2003] found a piezoceramic stack to exhibit congruency for the minor loops if the applied mechanical load is constant or varies by only a small amount. They also noted that the classical model is applicable so long as the applied frequency is constant or exhibits a very small bandwidth. In another work, Ge and Jouaneh [1995] applied the classical model for piezoceramics as they are only interested in the major hysteresis loops, which are created by increasing the electric field input to the material from zero to some maximum value. Hence, the classical model can be used for piezoceramics subjected to various amplitude periodic input electric field signals. For the current work pertaining to the MFC actuator, each of the

three conditions above are satisfied; the applied mechanical loads are indeed constant, as is the input frequency (0.1 Hz is also low enough to meet the static Preisach requirement), and the response was measured for a periodic input with various amplitudes. However, during the experimental procedure, the MFC was subjected to both positive and negative electric fields, yet care was taken not to apply a negative field in excess of the coercive field, which would cause depoling of the actuator. As will be seen below, the classical Preisach model used in the literature for piezoelectrics must be modified to include such inputs. Furthermore, much of the work in magnetics allows for negative-valued inputs, but presumes that the maximum and minimum values are equal in magnitude but opposite in sign. For the case of nonzero static DC biasing voltages applied to the MFC herein, the maximum and minimum input values can have both different signs and magnitudes. This added complication will be accounted for in the derivation which follows. Having met these other requirements, the current effort continues by looking at a mathematical and geometric implementation of the classical Preisach model.

6.6.2 Derivation of the Classical Preisach Model:

The derivation of the classical Preisach model will follow that presented by Mayergoyz [1991]. While it will ultimately be applied to predict the actuation behavior of the MFC tested throughout this work, the model is derived for a generic hysteretic transducer with time-dependent input and output, $u(t)$ and $f(t)$, respectively, as seen in Figure 6.17. The model will also be developed in such a manner that does not require the maximum and minimum values of the input signal to be equal but of opposite signs, and does not require the input signal to only be greater than or equal to zero. With this approach in mind, the Preisach model can be described as a combination of an infinite set of hysteresis operators, $\gamma_{\alpha\beta}\, u(t)$, times the Preisach weighting function, $\mu(\alpha, \beta)$ and integrated over all appropriate values of α and β. The hysteresis operator is depicted graphically in Figure 6.20.

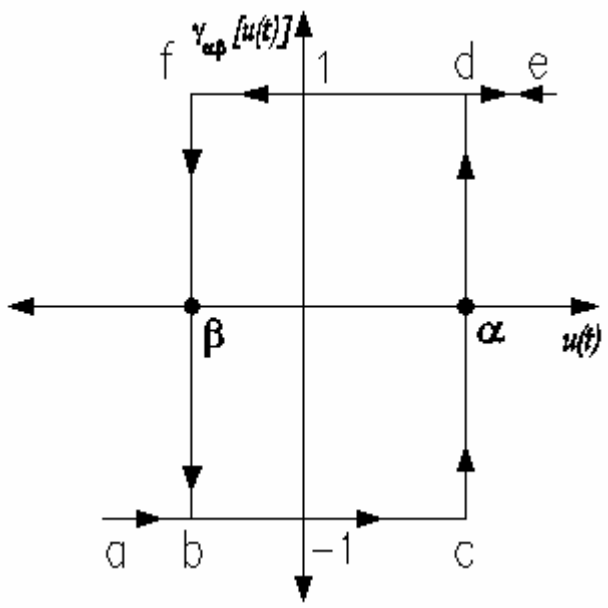

Figure 6.20: Preisach Hysteresis Operator

Here, α and β represent switching values of the input, that is, points where the first time derivative of the input changes signs. In general, the Preisach hysteresis operator can take only one of two values, 1 or -1, as shown in the Figure 6.20. Such behavior allows this operator to function as a switch, where for inputs less than α, the value of the operator is -1. This value remains unchanged as the input is increased along path a-b-c-d-e, changing its value to 1 when the switching value α is reached. The operator remains at 1 until the input is reversed, at which time the path e-d-f-b-a is followed, including changing of the operator value back to -1 when the input is decreased below the switching value β. It should be noted that for this most general case, α and β can have either positive or negative values, and it is presumed that α is always greater than or equal to β, which is reasonable for practical applications, including piezoelectric behavior. It should be noted that sometimes the 1 and -1 output values are modified so that $\gamma_{\alpha\beta}$ takes either 1 or 0, specifically for the case of piezoelectric devices subjected to only positive electric fields. However, the experiments described in the current work clearly excite the MFC actuator with both positive and negative voltages. Thus, the traditional values of 1 or -1 are preserved herein.

With a geometric idea of this switching behavior, the Preisach model is written mathematically as

$$f(t) = \iint_{\alpha \geq \beta} \mu(\alpha, \beta)\gamma_{\alpha\beta}u(t)d\alpha\, d\beta \tag{6.4}$$

where *f(t)* is the time-dependent output of the transducer and $\mu(\alpha, \beta)$ is the Preisach weighting function to be determined later from experimental data.

6.6.2.1 Geometric Interpretation of Preisach Model:

Instead of proceeding with a purely mathematical description of the classical Preisach model, it is more straightforward to approach it with a geometric interpretation. From Equation 6.4, it is clear that input values α and β are restricted to a half-plane by virtue of the inequality restriction on the double integral. Also, each switching operator is uniquely defined by only one point (α, β) in this plane. Thus, the α - β half-plane, the line $\alpha = \beta_0$, and the line $\beta = \alpha_0$ form the limiting triangle, *T*, depicted in Figure 6.21, where the point (α_0, β_0) is the limiting (or maximum and minimum, respectively) value for the input signal.

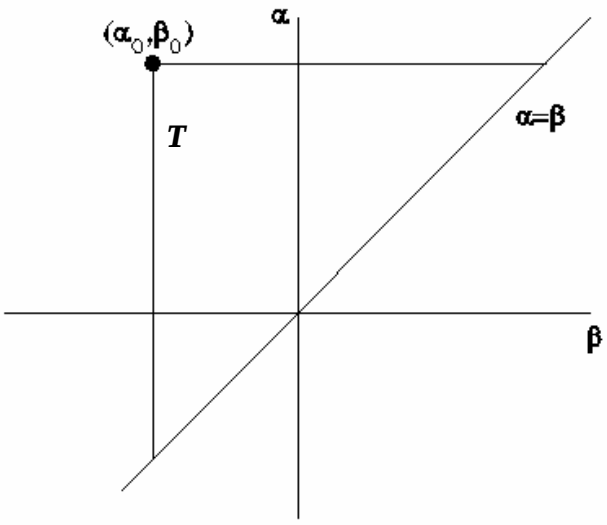

Figure 6.21: α - β Half-Plane, Limiting Triangle *T*, With α_0 Not Necessarily Equal to β_0

To begin, consider the input to be at some value less than β_0. Thus all of the $\gamma_{\alpha\beta}$ operators are equal to -1 and the transducer is negatively saturated (or, at its most negative point). Now, the input is increased monotonically towards a maximum value u_1, which corresponds to the line $\alpha = u(t)$ moving vertically, as seen in Figure 6.22.

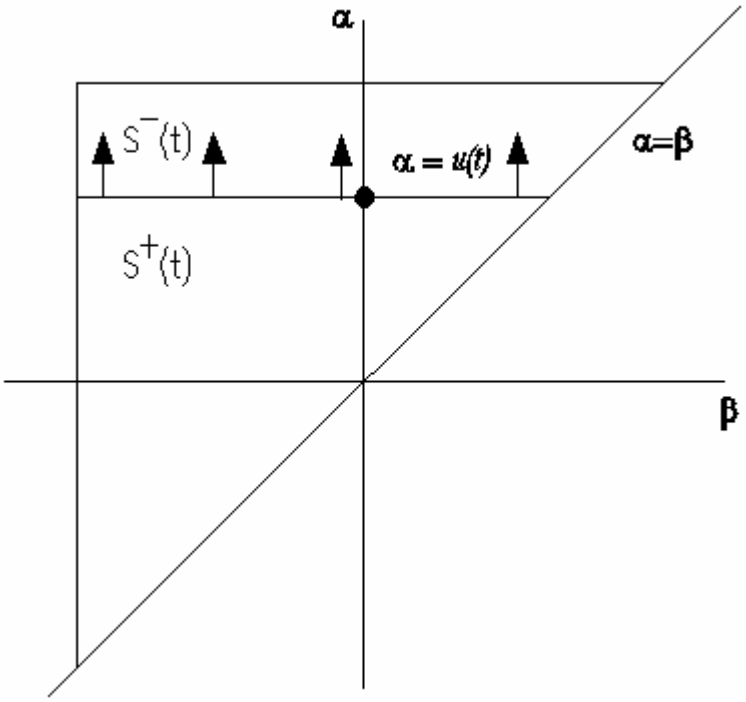

Figure 6.22: α - β Half-Plane for Increasing Input Signal

As the input is increased, all of the $\gamma_{\alpha\beta}$ with switching values α less than the current value of $u(t)$ change to take the value 1. Once the maximum u_1 is reached, the limiting triangle is divided into two distinct regions, one where the $\gamma_{\alpha\beta}$ are positive, denoted herein as $S^+(t)$ and the other denoted $S^-(t)$ where this operator still has the value -1. This condition is depicted in Figure 6.23.

Next, assume that the input is monotonically decreased, corresponding graphically to the vertical line $\beta = u(t)$ moving left through the limiting triangle T. The resulting boundary between $S^+(t)$ and $S^-(t)$, called $L(t)$, then takes the shape seen in Figure 6.24.

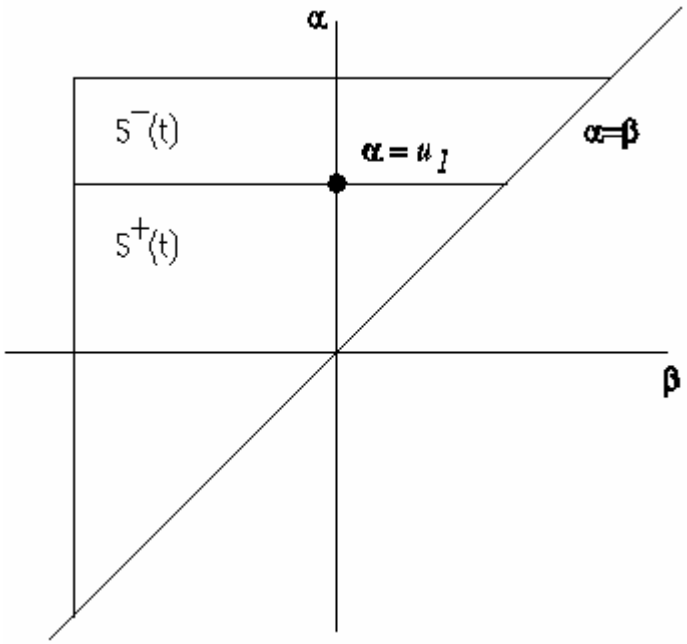

Figure 6.23: α - β Half-Plane for Increasing Input Signal

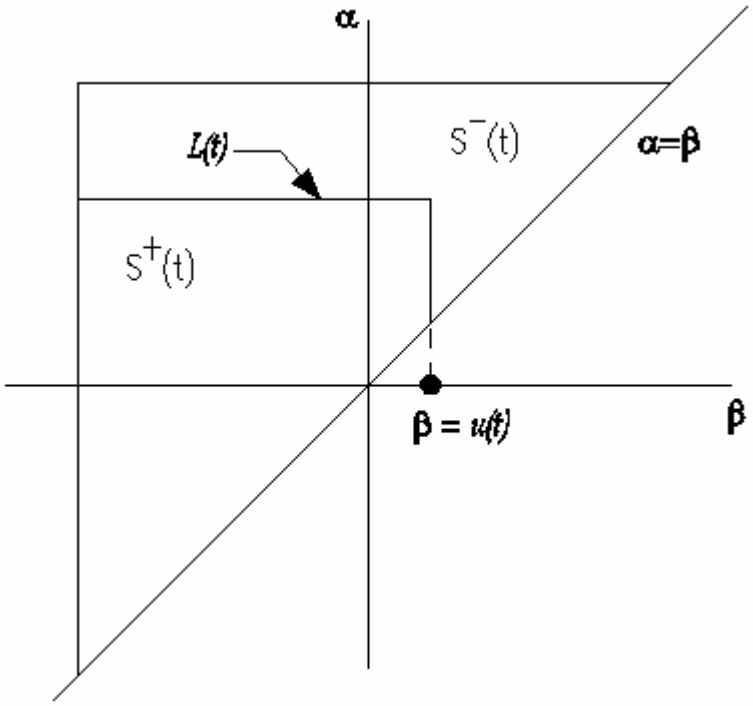

Figure 6.24: α - β Half-Plane for Decreasing Input Signal with $S^{+}(t)$ - $S^{-}(t)$ Interface $L(t)$

For this decrease in input, all of the $\gamma_{\alpha\beta}$ with switching values above the current value $u(t)$ are switched down to take a values of -1 until the local minimum u_2 is reached. At this time, let the input again increase to a local maximum value of u_3, which is less than u_1. Such a condition is depicted in Figure 6.25.

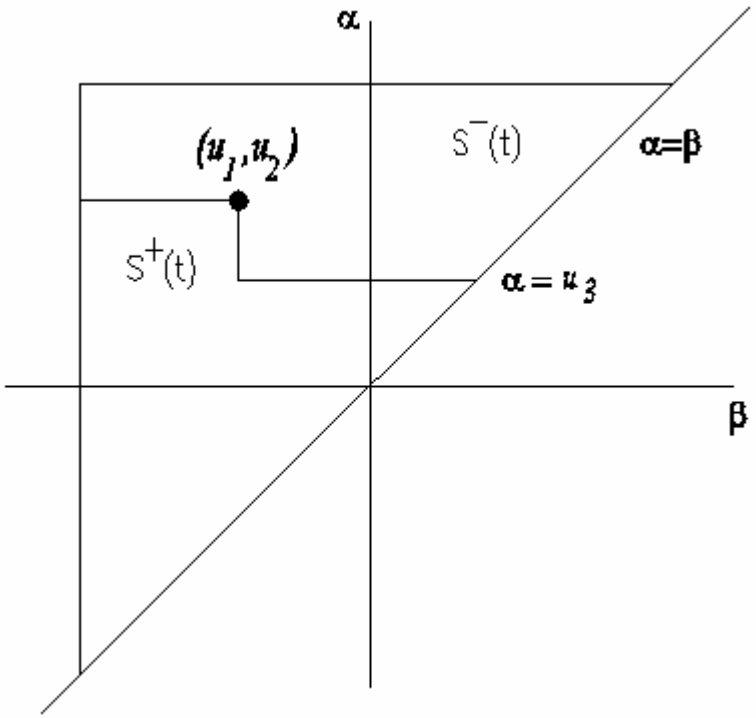

Figure 6.25: α - β Half-Plane for Increasing Input Signal Less Than u_1

Here, wiping out property can be visualized quite clearly. If u_3 was greater than u_1, then the vertical line $\alpha = u_3$ would be the highest link of the boundary $L(t)$ and the effect of the input u_1 would clearly be obscured, or, wiped out. Lastly, for the geometric interpretation of the Preisach model, allow the input to again decrease to a local minimum value u_4 that is greater than u_2. Such a condition is depicted in Figure 6.26. Clearly, the limiting triangle T is still divided into a positive and negative regions, $S^+(t)$ and $S^-(t)$, whose interface is a step function, $L(t)$, whose vertices correspond to the stored input extrema (those not wiped out).

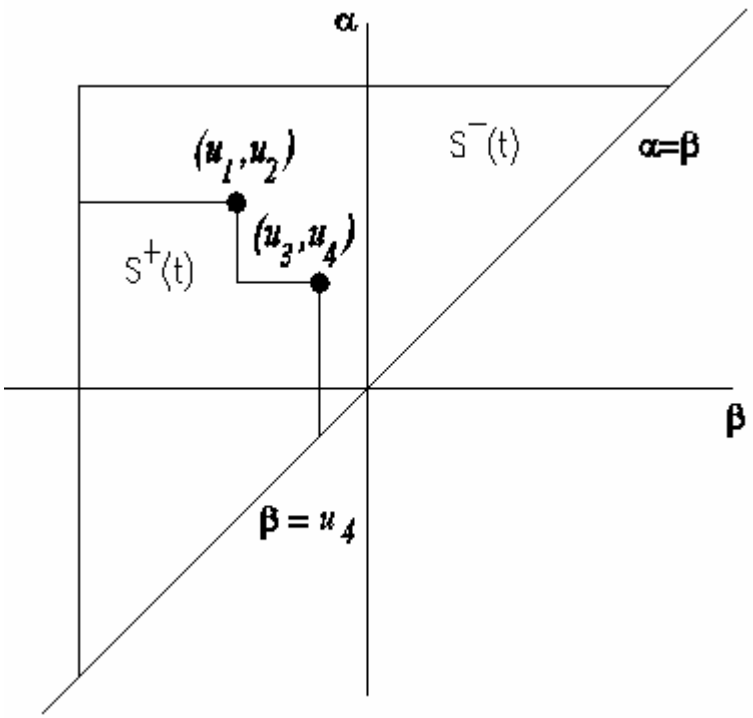

Figure 6.26: α - β Half-Plane for Decreasing Input Signal Greater Than u_2

From these figures, it is clear that the double integral over the α - β half-plane in Equation 6.4 can be divided into two separate double integrals, such that the output is given by

$$f(t) = \iint_{S^+(t)} \mu(\alpha, \beta)\gamma_{\alpha\beta}u(t)\,d\alpha\,d\beta \; + \; \iint_{S^-(t)} \mu(\alpha, \beta)\gamma_{\alpha\beta}u(t)\,d\alpha\,d\beta \tag{6.5}$$

Since the hysteresis operator has only two values, 1 and -1, corresponding to the two regions, $S^+(t)$ and $S^-(t)$, respectively, it can be replaced in the integrands, resulting in

$$f(t) = \iint_{S^+(t)} \mu(\alpha, \beta)\,d\alpha\,d\beta \; - \; \iint_{S^-(t)} \mu(\alpha, \beta)\,d\alpha\,d\beta \tag{6.6}$$

At this point, the geometric interpretation has removed the hysteresis operator $\gamma_{\alpha\beta}$ from the output equation. The next step is to determine the as yet unknown Preisach weighting function, $\mu(\alpha, \beta)$.

6.6.2.2 Experimental Procedure for Ascertaining the Weighting Function:

The Preisach weighting function required for Equation 6.6 can be determined from experimental data for first-order reversal curves. An analytical approach to interpreting this data is presented in this section, while a more accurate numerical method (for discreet data) is presented in the next section.

Both of these methods are technically sound and can be utilized effectively depending on the nature of the data on hand. However, both methods require the same experimental set of first-order reversal curves to be generated, as depicted in Figure 6.27.

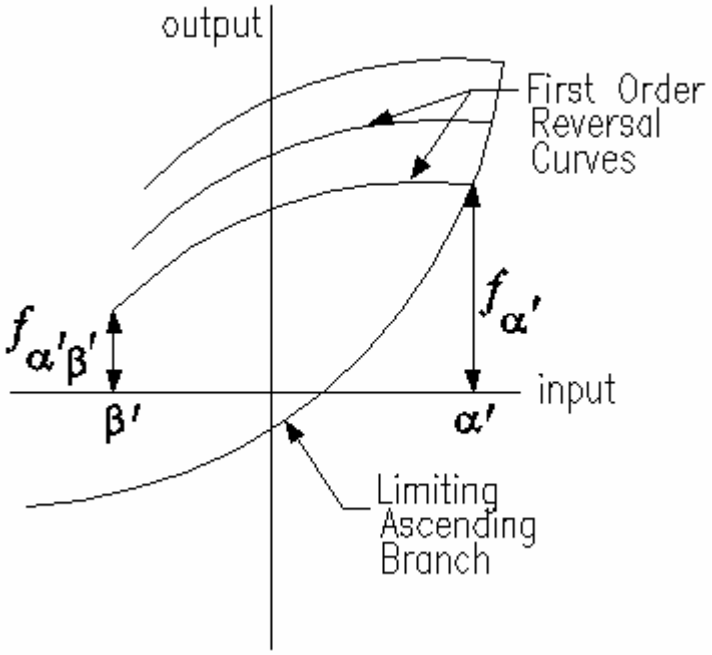

Figure 6.27: *f(t) – u(t)* Diagram for Increasing Input to α' and Subsequently Decreasing Input to β' Showing Output Values $f_{\alpha'}$ and $f_{\alpha'\beta'}$

These curves are measured experimentally as follows. First, the input should start at a value that is below β_0 (but not low enough to depole a piezoceramic), and then increased monotonically until it reaches a predetermined switching value, α'. During this initial increase, the limiting ascending branch is followed. This curve is referred to as such since the input started at a value less than β_0 and thus there are typically no curves below it. The output of the transducer when the input reaches α' is referred to as $f_{\alpha'}$, as depicted on the limiting ascending branch in Figure 6.27. Upon reaching α', the input is monotonically decreased to a value β', whereupon the output value at this point on the first-order reversal curve is denoted $f_{\alpha'\beta'}$. The decreasing curves are called first-order reversal or transition curves because they occur after the first reversal of the input, and are thus attached to the limiting ascending branch.

The collected data should indicate clearly the values of $f_{\alpha'}$ and $f_{\alpha'\beta'}$, as they are critical to the implementation of the Preisach model. Likewise, the above experimental procedure should be repeated for many values of α' and β'. Each reversal curve that is measured will uniquely define the response of the transducer at a point (α', β') in the α - β half-plane. Increasing the number of points that are defined through experimentation will increase the accuracy of the model when it is used after the experimental phase is complete.

Even though the experimental procedure applied to the MFC, which was outline in Chapter 5, is somewhat different than that presented above, a partial set of first-order reversal curves can be extracted from the data on hand. This data analysis procedure will be covered in detail when this Preisach model is implemented for the MFC load-actuation testing later.

The experimental procedure outlined above, namely increasing the input to α' and then decreasing to β', produces the α-β diagram shown in Figure 6.28.

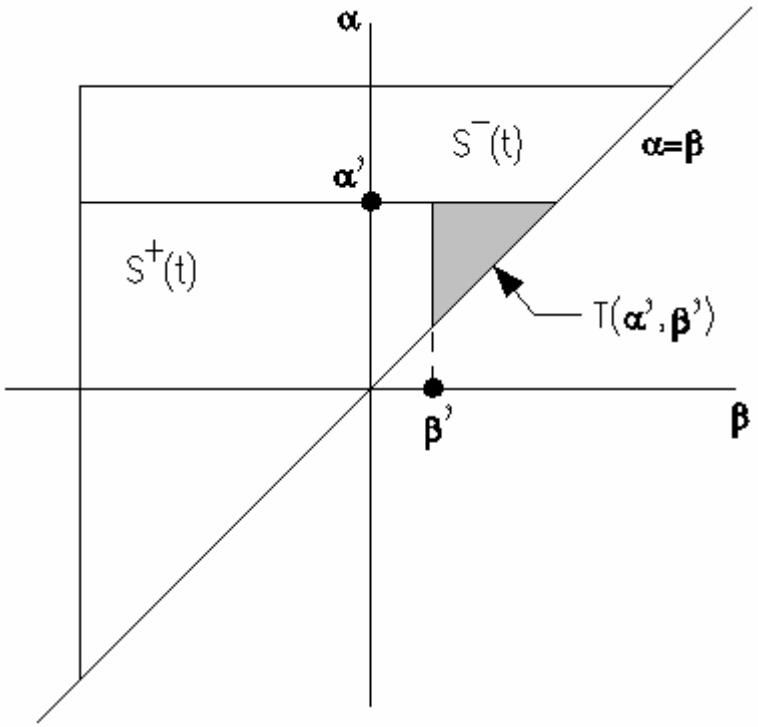

Figure 6.28: α - β Half-Plane Corresponding to First-Order Reversal Curve α' β'

In order to facilitate the determination of the weighting function, $\mu(\alpha, \beta)$, the following function F is defined as half the difference between the output values on the ascending branch and the first-order decreasing branch:

$$F(\alpha', \beta') = \frac{1}{2}\left(f_{\alpha'} - f_{\alpha'\beta'}\right) \tag{6.7}$$

Next, from Figure 6.28, the monotonic decrease of the input results in the addition of $T(\alpha', \beta')$ to the set $S^{-}(t)$ and subtracts the same area from the set $S^{+}(t)$. So, with Equation 6.6, the Preisach model matches the outputs along the first-order reversal curves if the weighting function obeys the relationship

$$f_{\alpha'\beta'} - f_{\alpha'} = -2 \iint_{T(\alpha', \beta')} \mu(\alpha, \beta)\, d\alpha\, d\beta \tag{6.8}$$

From these two previous equations, Equation 6.7 can be rewritten as

$$F(\alpha', \beta') = \iint_{T(\alpha', \beta')} \mu(\alpha, \beta) d\alpha \, d\beta \tag{6.9}$$

This integral can be broken up into two separate integrals over the appropriate α'- β' range, such that

$$F(\alpha', \beta') = \int_{\beta'}^{\alpha'} \int_{\beta'}^{\alpha'} \mu(\alpha, \beta) d\alpha \, d\beta \tag{6.10}$$

Equation 6.10 is then differentiated twice, once with respect to α' and once with respect to β', in order to isolate the Preisach weighting function. The resulting formula gives $\mu(\alpha', \beta')$ in terms of the experimental data with the use of Equation 6.7 as

$$\mu(\alpha', \beta') = -\frac{\partial^2 F(\alpha', \beta')}{d\alpha' \, d\beta'} = \frac{1}{2} \frac{\partial^2 f_{\alpha'\beta'}}{d\alpha' \, d\beta'} \tag{6.11}$$

At this point, the output of a hysteresis transducer can be predicted for a harmonic input using Equations 6.6 and 6.11, along with the experimental data for the first-order descending curves.

6.6.2.3 Numerical Approach to the Preisach Model:

While the previously presented method can be used in theory to predict the hysteretic output of the transducer, it would require both the double integration required by Equation 6.6 and the double differentiation of the experimental data required by Equation 6.10. The former step could become extremely computationally intensive, while the latter would greatly amplify the experimental noise in the data, thus reducing the accuracy of the predicted outputs. For these reasons, a more useful and arguably

easier numerical method is presented in this section to implement the Preisach model from the experimentally obtained first-order reversal curves.

With that, consider Figure 6.29, which shows the limiting triangle *T*, consisting of two regions, $S^+(t)$ and $S^-(t)$, whose interface is a step-shaped function *L(t)*. The α and β coordinates of the vertices are denoted M_k and m_k, respectively, and correspond to local input extrema that have been accumulated for the input history (not wiped-out).

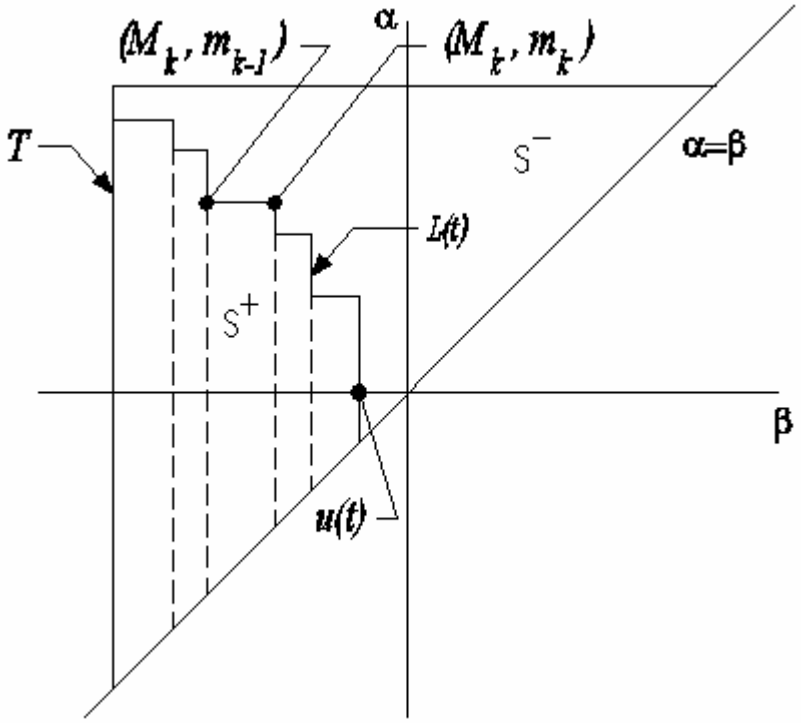

Figure 6.29: α - β Half-Plane with Positive and Negative Regions Having Interface *L(t)*

By adding and subtracting the double integral of the weighting function over the region $S^+(t)$, Equation 6.6 becomes

$$f(t) = 2 \iint_{S^+(t)} \mu(\alpha, \beta)\, d\alpha\, d\beta \; - \iint_{T} \mu(\alpha, \beta)\, d\alpha\, d\beta \tag{6.12}$$

where *T* is the limiting triangle. From Equation 6.9, the limiting triangle is described by

$$\iint_{T} \mu(\alpha, \beta) d\alpha \, d\beta = F(\alpha_0, \beta_0) \tag{6.13}$$

At this point, the positive portion of the α-β half-plane is sectioned into n trapezoids, referred to as Q_k, as seen above in Figure 6.29. As a result, the double integral over this positive region $S^+(t)$ can be replaced by the sum of these trapezoids, which can change in shape or number with time. Thus, the double integral over $S^+(t)$ is rewritten as

$$\iint_{S^+(t)} \mu(\alpha, \beta) \, d\alpha \, d\beta = \sum_{k=1}^{n(t)} \iint_{Q_k(t)} \mu(\alpha, \beta) \, d\alpha \, d\beta \tag{6.14}$$

Figure 6.29 is redrawn below to identify that each Q_k trapezoid is equal to the difference of two triangles, $T(M_k, m_{k-1})$ and $T(M_k, m_k)$.

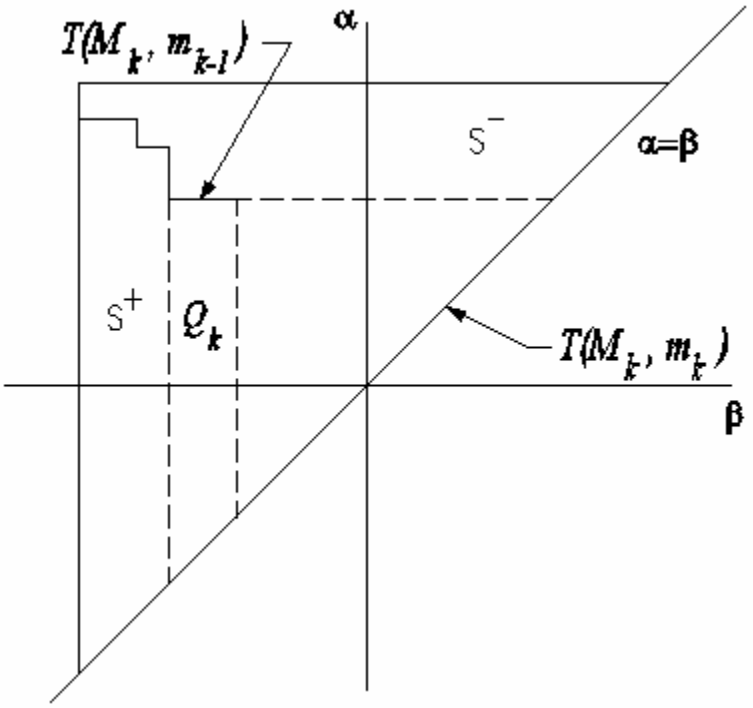

Figure 6.30: α - β Half-Plane Showing Each Q_k Trapezoid Equals the Difference Between Two Triangles, $T(M_k, m_{k-1})$ and $T(M_k, m_k)$

Therefore, the integral over each trapezoid can be expressed as

$$\iint_{Q_k(t)} \mu(\alpha, \beta)\, d\alpha\, d\beta = \iint_{T(M_k, m_{k-1})} \mu(\alpha, \beta)\, d\alpha\, d\beta - \iint_{T(M_k, m_k)} \mu(\alpha, \beta)\, d\alpha\, d\beta \tag{6.15}$$

In Equation 6.15, if k is equal to one, then m_0 is simply equal to β_0. Next, each of these triangles that help define the trapezoids can be expressed by utilizing Equation 6.9 as

$$\iint_{T(M_k, m_{k-1})} \mu(\alpha, \beta)\, d\alpha\, d\beta = F(M_k, m_{k-1}) \tag{6.16}$$

and

$$\iint_{T(M_k, m_k)} \mu(\alpha, \beta)\, d\alpha\, d\beta = F(M_k, m_k) \tag{6.17}$$

Substitution of these two expressions into Equation 6.15, which is in turn substituted into Equation 6.14, produces the output of the hysteretic transducer from Equation 6.12:

$$f(t) = -F(\alpha_0, \beta_0) + 2\sum_{k=1}^{n(t)} \left[F(M_k, m_{k-1}) - F(M_k, m_k)\right] \tag{6.18}$$

From Figure 6.29, m_n is simply equal to the input, $u(t)$. Thus, the summation in Equation 6.18 can be broken up, such that, for a monotonically decreasing input (when the last link of $L(t)$ is a vertical line), the output is

$$f(t) = -F(\alpha_0, \beta_0) + 2\sum_{k=1}^{n(t)-1} \left[F(M_k, m_{k-1}) - F(M_k, m_k)\right] + 2\left[F(M_n, m_{n-1}) - F(M_n, u(t))\right] \tag{6.19}$$

Sometimes, the last link of the interface *L(t)* is a horizontal line corresponding to a monotonically increasing input, as seen in Figure 6.31.

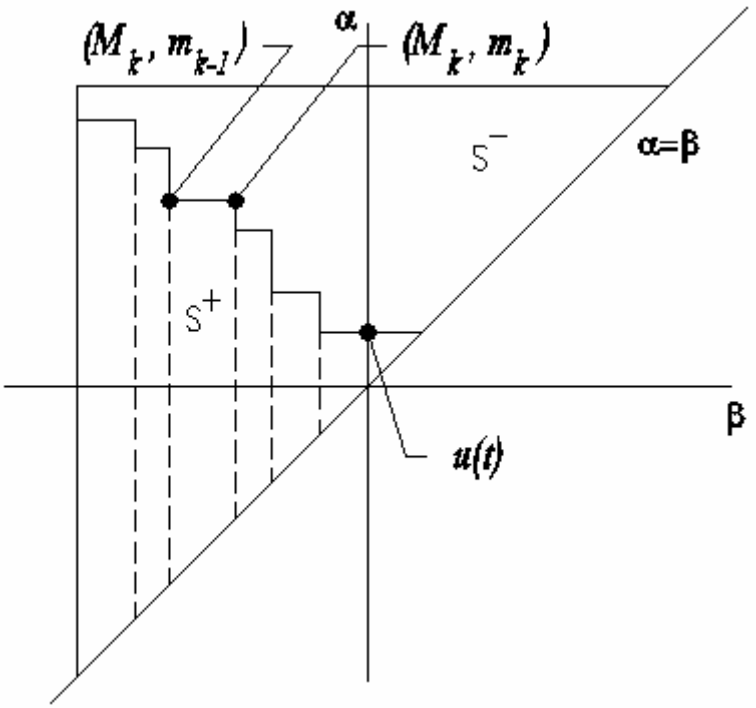

Figure 6.31: α - β Half-Plane with Monotonically Increasing Input

For this case, one can write

$$m_n(t) = M_n(t) = u(t) \tag{6.20}$$

For this particular input, Equation 6.9 can be used to show that

$$F(M_n, m_n) = F(u(t), u(t)) = 0 \tag{6.21}$$

Next, Equation 6.18 is again modified such that the n^{th} case is removed from the summation, and, along with Equations 6.20 and 6.21, the output for a monotonically increasing input is given by

$$f(t) = -F(\alpha_0, \beta_0) + 2\sum_{k=1}^{n(t)-1}\left[F(M_k, m_{k-1}) - F(M_k, m_k)\right] + 2F(u(t), m_{n-1}) \qquad (6.22)$$

At this point, the outputs for increasing and decreasing inputs are specified by Equations 6.19 and 6.22, respectively. However, using the definition of $F(\alpha, \beta)$ from Equation 6.7, these outputs can be expressed in terms of the experimentally collected first-order reversal curves as

$$f(t) = -\frac{1}{2}\left(f_{\alpha_0} - f_{\alpha_0\beta_0}\right) + \sum_{k=1}^{n-1}\left[f_{M_k m_k} - f_{M_k m_{k-1}}\right] + f_{M_n u(t)} - f_{M_n m_{n-1}} \quad for \quad \dot{u}(t) < 0 \qquad (6.23)$$

$$f(t) = -\frac{1}{2}\left(f_{\alpha_0} - f_{\alpha_0\beta_0}\right) + \sum_{k=1}^{n-1}\left[f_{M_k m_k} - f_{M_k m_{k-1}}\right] + f_{u(t)} - f_{u(t) m_{n-1}} \quad for \quad \dot{u}(t) > 0 \qquad (6.24)$$

Equations 6.23 and 6.24 are valid for the general case in which the major hysteresis loop is not symmetric about the input axis, that is, α_0 does not equal β_0. For many practical applications, these two maximum quantities are indeed the same, or, for the case of many piezoelectrics, only positive voltages are applied to the actuator (β_0 equals zero). For the former, the first term in each of the output expressions can be simplified, resulting in

$$f(t) = -f^{+} + \sum_{k=1}^{n-1}\left[f_{M_k m_k} - f_{M_k m_{k-1}}\right] + f_{M_n u(t)} - f_{M_n m_{n-1}} \quad for \quad \dot{u}(t) < 0 \qquad (6.25)$$

$$f(t) = -f^{+} + \sum_{k=1}^{n-1}\left[f_{M_k m_k} - f_{M_k m_{k-1}}\right] + f_{u(t)} - f_{u(t) m_{n-1}} \quad for \quad \dot{u}(t) > 0 \qquad (6.26)$$

Here, f^{+} is the positive saturation value of the output, or the maximum output on the limiting ascending curve. For the case of only positive actuation voltages, the hysteresis

operator $\gamma_{\alpha\beta}$ is modified to take only the values 0 or 1, and the result of this modification is that the first term in Equations 6.23 and 6.24 no longer appears [Hu and Mrad, 2003, and Ge and Jouaneh, 1995].

The case can arise when the response is desired to a certain input that does not fall on a node in the α-β half-plane for which values of $f_{\alpha\beta}$ have not been measured. In this case, a spline interpolation can be used to approximate the required value. If the desired (α, β) pair falls within a rectangular cell on the α-β half-plane, then the interpolation equation is

$$f_{\alpha\beta} \approx C_0 + C_1\alpha + C_2\beta + C_3\alpha\beta \tag{6.27}$$

However, if the desired (α, β) pair is in a triangular cell along the diagonal line $\alpha = \beta$, then the interpolation equation is

$$f_{\alpha\beta} \approx C_0 + C_1\alpha + C_2\beta \tag{6.28}$$

The C_i coefficients are calculated by matching the values of $f_{\alpha\beta}$ for the adjacent four or three nodes, for rectangular or triangular cells, respectively. Such a procedure involves solving a linear system of equations (four equations for rectangular cells, three equations for triangular cells) for the unknown coefficients C_i.

6.6.3 The Classical Preisach Model and the Macro Fiber Composite:

At this point, an explicit formulation of the classical Preisach model is given by Equations 6.23 and 6.24 for the specific case of a piezoceramic actuator subjected to a harmonic input, where consecutive local extrema do not necessarily have equal magnitudes but opposite signs and the local minima are not all required to be great than or equal to zero. Thus, these two equations can be utilized with respect to the

actuation-under-load experimental procedure that was performed on the MFC and detailed in Chapter 5. The focus of this section will be to first extract the necessary first-order reversal curves from the acquired MFC data, and then use this data and the Preisach model to predict the output of the MFC to a voltage input for which experimental results are readily available.

6.6.3.1 First-Order Reversal Curves for the MFC:

The voltage-time input signal to the MFC, *u(t)* in the Preisach model developed above, is depicted in Figure 6.1 above. From the local extrema in this plot, a table of switching values that have been measured is presented below.

Table 6.3: Switching Values for Measured First-Order Reversal Curves for the MFC

M	125	250	375	500	500	625	750	875	1000	1125	1250	1375	1500
m	-125	-250	-375 125	-500 0	0	-625 -125 375	-250 250	-375 125	-500 0	-625 -125	-250	-375	-500

The resulting strain output in both the 1 and 3-directions was measured under various constant mechanical loads. The first-order reversal curve parameters can be found from the experimental data by plotting the output strains as a function of input voltage to the actuator. Electric fields can also be the independent variable for this plot through the use of Equation 5.29. However, since the Preisach model is phenomenological rather than analytical, strain-voltage plots are sufficiently simple and easy to understand in terms of the experimental procedures required to implement the model.

From the data previously collected and analyzed, representative plots for the two in-plane directions are shown below in Figures 6.32 and 6.33. It should be noted that the plotted data has been shifted as outlined in Section 5.5.3.2, and only the fifth cycle data is shown, as it represents the most stable hysteresis loop. Also, these plots have the loops for all three DC biasing voltage cases, 0, 250, and 500 VDC.

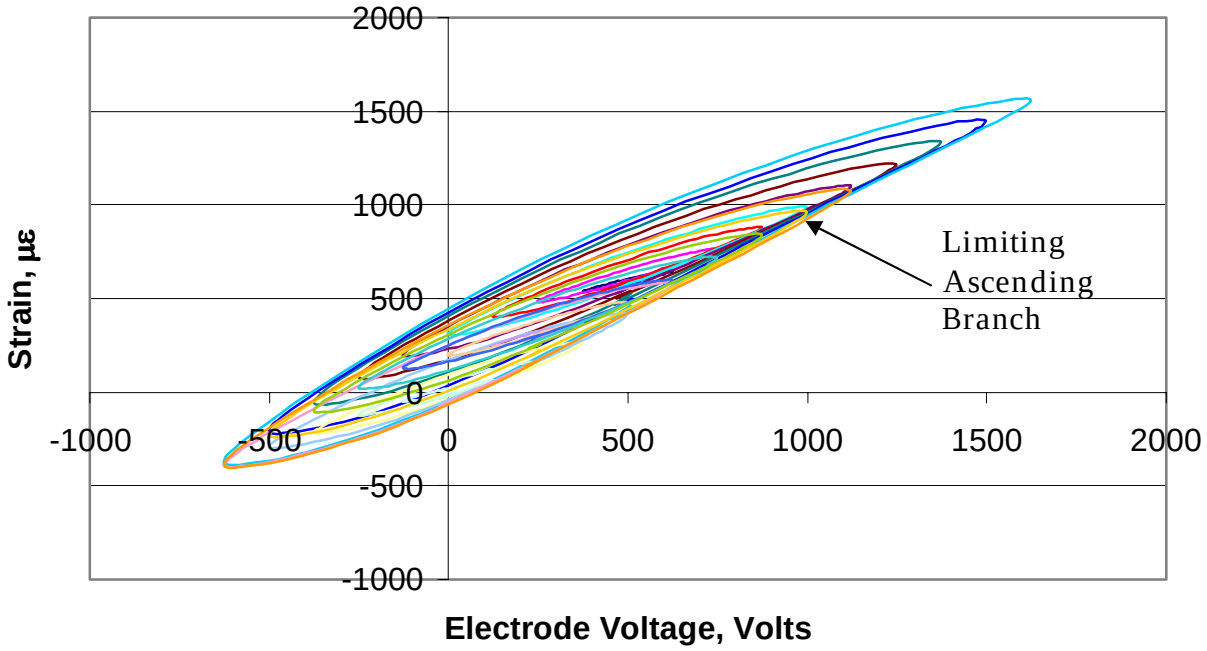

Figure 6.32: First-Order Transition Curves for 3-Direction Strains of MFC S/N 404 under Free Strain Conditions

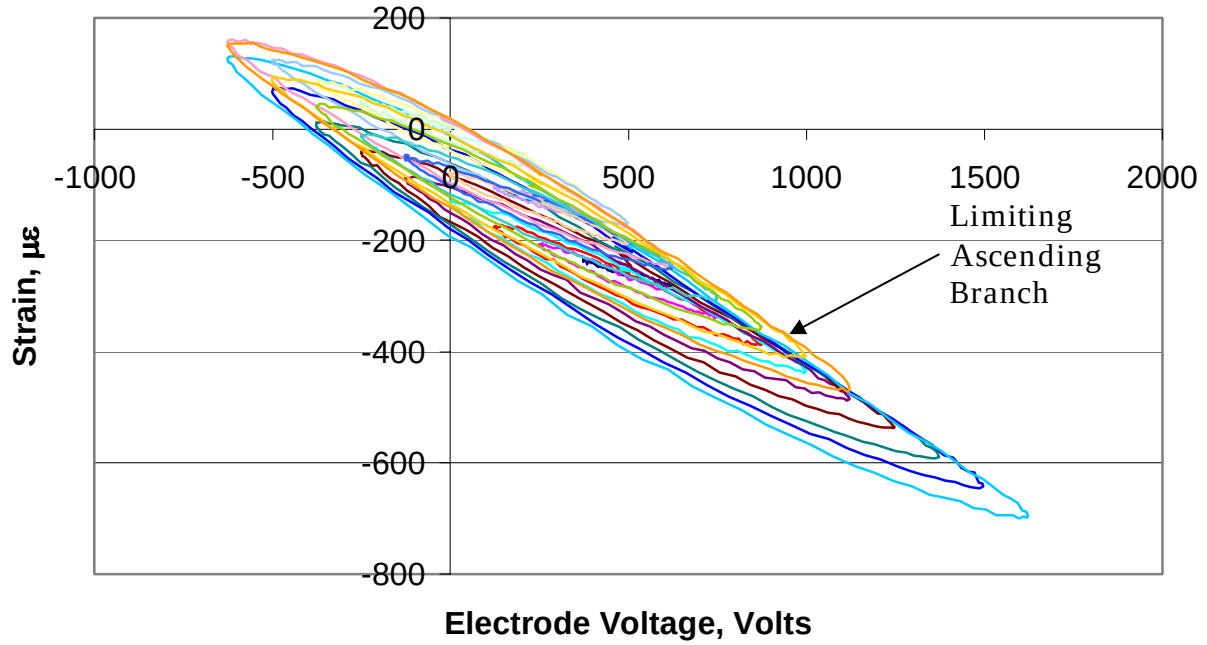

Figure 6.33: First-Order Transition Curves for 1-Direction Strains of MFC S/N 404 under Free Strain Conditions

When the classical Preisach model is typically implemented, the α - β half-plane is covered in a rectangular grid, and then experimental first-order reversal curves are measured at M and m values corresponding to each (M, m) pair at the intersections of the gridlines. Such a figure for the MFC actuation experiments is shown in Figure 6.34.

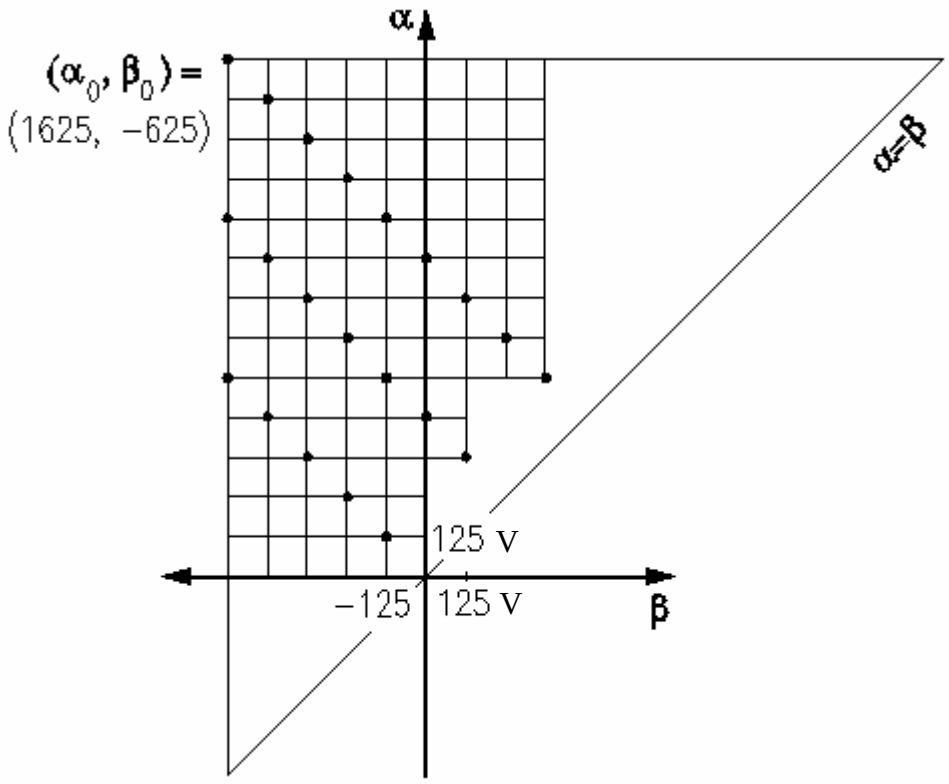

Figure 6.34: α - β Half-Plane Corresponding to the Voltage Input Signal to the MFC

In this figure, the dots represent the (M, m) pairs specified in Table 6.3 that have been measured experimentally in the current effort. Clearly, not all of the possible reversal values within the limiting triangle have been tested, thus interpolation between rectangular or triangular cells would be either impossible or not accurate. Measuring all of the required reversal curves is beyond the scope of this work, yet the classical Preisach model can still be applied by future researchers interested in such detailed actuation analysis for the MFC. Nevertheless, this initial effort at extracting the first-order reversal curves from the data on hand still provides useful values that can

demonstrate the proper implementation and accuracy of this classical Preisach model. Thus, an analysis of the data is now provided such that all of the desired f_M and f_{Mm} values for Equations 6.23 and 6.24 can be extracted with as much accuracy as possible.

The data analysis used to extract the desired parameters f_M and f_{Mm} for the MFC is as follows. The maximum and minimum values of the shifted, fifth electrical cycle data from each peak-to-peak actuation voltage (i.e. the loops in Figures 6.32 and 6.33) are determined for each MFC specimen. These values represent f_M and f_{Mm}, and the limiting triangle in the α-β half-plane corresponds to the maximum voltage sequence, namely 2250 volts peak-to-peak with a 500 VDC biasing voltage. Hence, the point (α_0, β_0) is equal to (1625, -625) volts for the limiting ascending branch. The values from three MFC specimens, namely S/N 404, 415, and 424, are then averaged, and the results and their sample standard deviations are presented in tabular form. The other MFCs that were tested, S/N 486 and 487, exhibited too much drift throughout the electrical cycles to be reliable for their extrema values of strain output, thus their behavior is excluded from this Preisach modeling analysis. It should be noted, however, that the peak-to-peak property analysis presented earlier in this chapter is not affected by piezoelectric drift. Therefore, the data from S/N 486 and 487 is still useful for some types of analyses. For the case of free-strain, the resulting f_M and f_{Mm} are presented in Table 6.4, while the results for nonzero constant applied loads are given in Appendix H.

6.6.3.2 An Application of the Classical Preisach Model to MFC Actuation

From Figure 6.34, it is clear that not all possible or desired first-order reversal curves were measured in the experiments performed on the reference MFC in this effort. However, enough points were measured and enough data collected to give an example of how to use the classical Preisach model developed above to predict the output of the MFC. Referring back to Table 5.1 and the associated discussion of the experimental procedure for actuation performance characterization, after the maximum peak-to-peak voltage profile for each DC offset, strain measurements were recorded at decreasing

Table 6.4: Measured Parameters f_M and f_{Mm} for Preisach Model of MFC Hysteresis, 1 and 3-Direction Actuation for Free-Strain (0 MPa)

M	m	3-Direction				1-Direction			
		f_M, $\mu\varepsilon$	f_{Mm}, $\mu\varepsilon$	f_M - Std. Dev.	f_{Mm} - Std. Dev.	f_M, $\mu\varepsilon$	f_{Mm}, $\mu\varepsilon$	f_M - Std. Dev.	f_{Mm} - Std. Dev.
125	-125	56.54	-52.00	10.09	7.56	25.28	-29.39	2.42	2.59
250	-250	143.3	-127.9	17.61	9.94	56.98	-71.48	6.22	2.60
375	-375	252.7	-209.8	16.38	10.50	95.97	-115.30	10.00	11.39
375	125	353.7	241.7	15.80	5.34	-109.08	-166.26	9.77	8.88
500	-500	387.5	-307.3	32.00	13.82	140.55	-171.87	17.47	16.13
500	0	465.6	202.2	16.97	7.24	-87.70	-217.34	12.40	15.17
625	-625	544.7	-410.8	36.76	12.87	181.47	-245.27	24.21	11.85
625	-125	582.3	133.2	20.69	9.07	-55.98	-268.87	9.13	22.79
625	375	631.7	519.2	17.64	12.31	-250.26	-309.62	21.43	27.23
750	-250	699.6	32.8	25.78	14.28	-14.07	-324.09	6.05	23.76
750	250	740.5	474.3	26.04	4.29	-227.49	-361.38	22.55	30.73
875	-375	821.1	-89.3	32.90	19.77	40.20	-383.29	6.42	30.67
875	125	851.2	401.4	30.83	4.90	-192.41	-412.63	19.23	35.87
1000	-500	933.6	-227.3	39.99	17.88	96.71	-435.38	7.53	35.45
1000	0	958.3	309.3	33.82	6.56	-147.59	-464.72	16.59	39.01
1125	-625	1048	-397.7	46.22	19.63	164.75	-495.08	17.23	36.95
1125	-125	1073	201.5	35.70	12.98	-102.10	-519.77	15.59	43.43
1250	-250	1184	80.6	44.18	13.36	-48.39	-575.72	14.07	50.86
1375	-375	1294	-56.6	49.87	19.97	7.84	-632.23	7.07	55.09
1500	-500	1408	-213.5	52.90	25.56	69.11	-691.65	11.22	63.00
1625	-625	1513	-386.0	61.74	27.16	133.45	-745.48	10.78	65.34

peak-to-peak voltage levels. Such profiles would appear at the bottom of each column of Table 5.1. As mentioned earlier, these measurements were made to investigate such global hysteresis effects, however, such behavior was later deemed beyond the scope of this work. Nevertheless, the classical Preisach model developed in this chapter is excellent for harmonic, decreasing input signals. Thus, in order to illustrate the use of the Preisach model, consider the portion of the voltage input to the MFC actuator shown in Figure 6.35. Such an input can be represented on the α - β half-plane as depicted in Figure 6.36. The dashed lines in Figure 6.35 are not actually part of the

interface link *L(t)*, but rather emphasize that reducing the input to β_0 erases the effects of the other extrema up to that point in time.

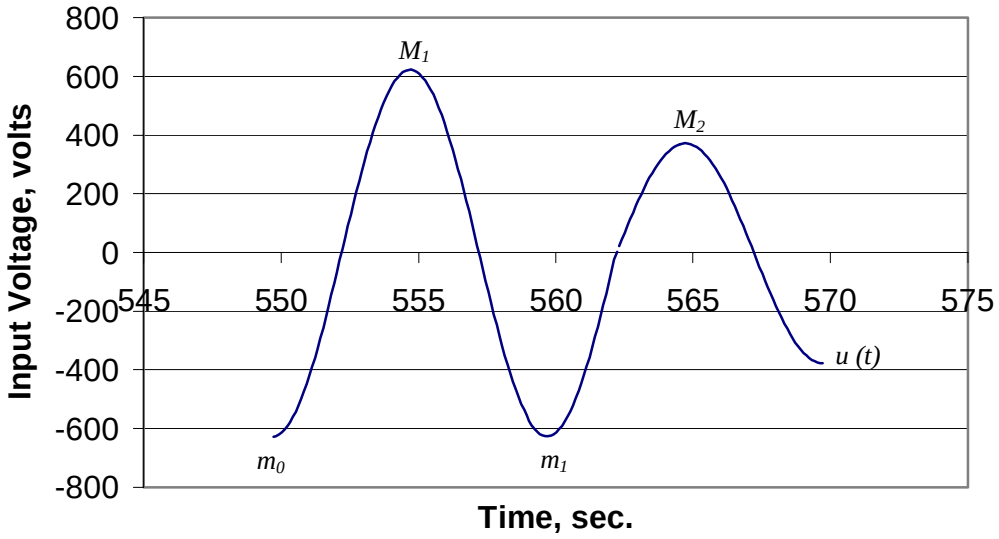

Figure 6.35: Decreasing, Harmonic Voltage Input to the MFC Actuator

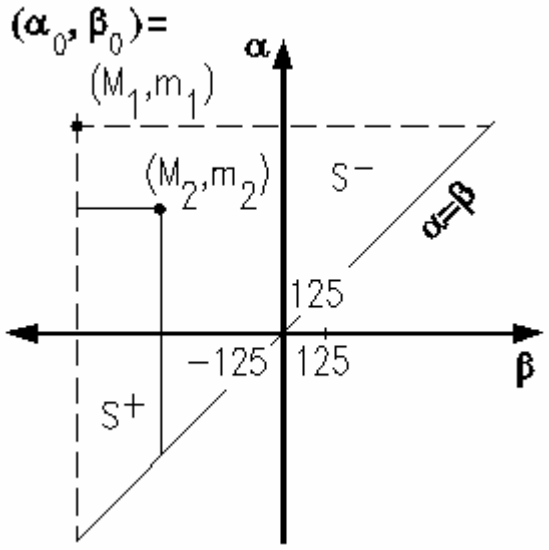

Figure 6.36: α - β Half-Plane Corresponding to the Voltage Input of Figure 6.35

The input signal shown in Figure 6.35 has the limiting triangle defined by (α_0, β_0) equal to (625, 625) volts. There are also two stored consecutive maximum-minimum pairs, thus *n* is equal to 2. Since the final link of the interface *L(t)* is vertical, corresponding to

a decreasing input, Equation 6.23 is used to predict the strain output in the 3-direction. The resulting expression for this input is

$$f(t) = -\frac{1}{2}\left(f_{\alpha_0} - f_{\alpha_0\beta_0}\right) + \left(f_{M_1 m_1} - f_{M_1 m_0}\right) + f_{M_2 u(t)} - f_{M_2 m_1} \tag{6.29}$$

In Figures 6.35 and 6.36, the *M*, *m*, and *u(t)* variables take the values

$$\begin{aligned} m_0 &= \beta_0 = -625\,V \\ M_1 &= \alpha_0 = 625\,V \\ m_1 &= \beta_0 = -625\,V \\ M_2 &= 375\,V \\ u(t) &= -375\,V \end{aligned} \tag{6.30}$$

From Table 6.4, the required f_{Mm} values are

$$\begin{aligned} f_{\alpha_0} &= f_{625} = 544.7\ \mu\varepsilon \\ f_{\alpha_0\beta_0} &= f_{625,-625} = -410.8\ \mu\varepsilon \\ f_{M_1 m_1} &= f_{625,-625} = -410.8\ \mu\varepsilon \\ f_{M_1 m_0} &= f_{625,-625} = -410.8\ \mu\varepsilon \\ f_{M_2 u(t)} &= f_{375,-375} = -209.8\ \mu\varepsilon \\ f_{M_2 m_1} &= f_{375,-625} = -410.8\ \mu\varepsilon \end{aligned} \tag{6.31}$$

It should be noted that in Equation 6.31, the value of $f_{375,-625}$ was not measured directly for the MFC, nor is there sufficient data to interpolate through the use of Equation 6.27. However, this value corresponds to decreasing the input back to β_0, thus the numerical value for $f_{375,-625}$ is taken to be the same as for $f_{625,-625}$. Substitution of these values into Equation 6.29 gives an output value $f(t)$ = -276.8 $\mu\varepsilon$. The value measured for the strain output of the MFC (S/N 404) subjected to the input voltage depicted in Figure 6.35 is

$f(t)$ = -269 $\mu\varepsilon$. Thus the classical Preisach model is seen to accurately predict the output of the MFC subjected to a given harmonic voltage input signal.

6.7 Conclusions:

This chapter utilizes the measured strain-electric field hysteresis loops in two separate but important ways. First, a linear regression analysis is performed on the loops collected under various electrical and mechanical loads. The slope of these lines corresponds to the desired piezoelectric strain coefficients, and since they are measured under different conditions, it is possible to look at how the effective parameters vary. For example, d_{33} is seen to increase in a quadratic manner with increasing peak-to-peak electrode voltage, while d_{31} decreases in a similar manner. The peak-to-peak strain output of the reference MFC is also seen to depend on the peak-to-peak electric field and constant applied mechanical load. Measurement of these parameters is crucial for an accurate characterization of the MFC actuator. The work of this chapter provides both rigorous and statistically sound measurements for the effective strain parameters under a variety of external loading conditions. In addition to the linear regression analysis characterization that is commonly used in the literature to characterize actuation devices, a classical Preisach model is developed predict the strain output of the reference MFC to a harmonic voltage excitation input. However, this model requires a dataset of first-order reversal curves in order to accurately predict the output of the actuator for a completely general input signal. The experimental procedure designed to characterize the monotonic and peak-to-peak performance of the MFC did not lead to the acquisition of a *full* set of first-order reversal curves. However, many data points in the α-β half-plane are measured, and the model is fully developed and an example of its accuracy compared to experimental data is presented. Furthermore, the measurement of the complete set of first-order reversal curves (for free-strain) is straightforward, and the procedure is outlined herein. Thus, future researchers can use some simple experiments and the classical Preisach model developed in this chapter to predict the output of the MFC to a general voltage input.

Chapter 7

Conclusions, Future Work, and Contributions

7.1 Introduction:

This dissertation has presented a thorough investigated into both the linear and nonlinear macroscopic piezomechanical behavior of the MFC actuator. Rather than focusing on the micromechanical interactions between the constituent materials, namely the PZT fibers, epoxy matrix, copper interdigitated electrodes and polymer protective layers, this effort strived to characterize the MFC as a component of an intelligent structural system. Consequently, the quantitative nonlinear behavior characterized herein can be readily employed by the designers of such systems to help reduce structural vibrations and increase shape-control accuracy. Additional topics were also investigated, including the manufacturing processes for the MFC, cure kinetics modeling for its structural epoxy, and voltage and temperature-dependent thermomechanical properties. Such peripheral topics appear in select appendices. This chapter serves to highlight key results and contributions, as well as make recommendations for potential improvements for future researchers.

7.2 Brief Summary of Results:

A model based on rule-of-mixture formulae and classical lamination theory was developed to predict the short circuit linear-elastic properties of the reference MFC, which was found to closely match the experimental results. By extension, this model can be use to design or analyze MFCs having a different geometry. The predicted values of E_x, E_y, G_{xy}, and υ_{xy} for the reference and standard MFC configurations are presented in Table 2.5, while the corresponding measured values for the reference configuration are listed in Table 3.3. The comparison of these two sets of values in Table 3.4 shows a close agreement between the model and experimental results. Even the transverse and shear properties, which are notoriously difficult to predict and measure, are predicted reasonably well by the model.

Nonlinear mechanical behavior under the same short-circuit electrical boundary conditions was also measured and described using various nonlinear phenomenological methods, such as the elastic-linear hardening and Ramberg-Osgood models. The measured parameters for the MFC are presented in Tables 3.5 and 3.6. From the development of these models, the stress-strain transition point from linear to nonlinear behavior can be determined. In general, under short-circuit electrical conditions, the MFC can be presumed to behave in a linear-elastic manner for longitudinal (PZT fiber direction) and in-plane shear strains less than about 1000 $\mu\varepsilon$. The same longitudinal strain range results in an observed constant major Poisson's ratio. For the transverse direction, linear behavior is seen for strains less than about 1500 $\mu\varepsilon$.

The sensitivity of the classical lamination model to variations in PZT and copper fiber volume fractions, layer thicknesses, and constituent material properties was also investigated. The first two sets of parameters can be used to design the MFC to have specific, desired effective orthotropic properties. Also, it was found that the overall linear, short-circuit mechanical properties are quite sensitive to the properties of the structural epoxy used to hold the MFC package together. Such a discovery indicates

that further research is required for its bulk material properties in order to obtain more accurate predictions from the model developed herein, particularly for the transverse and shear behavior.

The peak-to-peak strain output and effective linear piezoelectric strain parameters of the MFC were measured from a peak-to-peak strain-field analysis, for both free-strain conditions as well as constant, nonzero applied loads. The tabulated parameters for free-strain are found in Tables 6.1 and 6.2, while the values for nonzero constant loads are presented in Appendix G. In general, it was found that increasing the constant load decreased the actuation strain ability of the MFC. However, higher excitation amplitudes result in an increase in the apparent piezoelectric strain coefficients.

A second-order nonlinear piezomechanical model was derived for a poled piezoceramic. This model was then used to describe the nonlinear actuation performance of the MFC subjected to an electric field input that increases monotonically from a DC biasing voltage value. The performance of the actuator was characterized under both free-strain and constant nonzero unidirectional applied mechanical loads. The results are found in Tables 5.3 through 5.6.

The classical Preisach model was developed for the general case of a hysteresis transducer subjected to an input signal that has neither equal yet opposite extrema nor cycles between zero and some maximum value. Some of the required first-order reversal curve dataset was extracted from the data collected from for the MFC under zero and nonzero constant mechanical loads, and the tabulated results are presented in Table 6.4 and in Appendix H, respectively.

7.3 Contributions:

Prior to the onset of this research effort, the field of piezoceramic fiber composite actuators with interdigitated electrodes was steadily developing. However, there was a

great deal of excitement over the Macro Fiber Composite because it possessed increased actuation potential while rectifying some of the limitations encountered by other similar devices. However, since the MFC was so new, very little was known about its electromechanical properties. Thus, the primary contribution of this dissertation is the prediction, measurement, and mathematical description of the linear and nonlinear behavior of the MFC, including its highly sought-after linear and nonlinear properties. Below is a more specific list of these contributions.

- The rule-of-mixture and classical lamination theories were used to calculate the short-circuit, linear-elastic mechanical properties of the MFC actuator, namely E_x, E_y, G_{xy}, and υ_{xy}. These properties were then measured and found to be in agreement with the predicted values.
- A sensitivity analysis identified that the linear model developed above was most sensitive to the mechanical properties of the epoxy, which were not well known for this research effort.
- Elastic-linear hardening and Ramberg-Osgood models were developed to represent the nonlinear short-circuit mechanical behavior of the MFC actuator subjected to longitudinal, transverse, and in-plane shear loading. The limits of linear elasticity for short-circuit behavior were also identified.
- A model for the nonlinear response of a piezoelectric material to an initial monotonic increasing voltage input and general in-plane mechanical loads was derived. The corresponding nonlinear material properties (piezoelectric strain, electrostrictive, and elastostrictive coefficients) required by this model for the MFC were measured for the case of free-strain and unidirectional constant nonzero loads.
- The peak-to-peak actuation strains and electric fields were measured, and a linear regression of this data provided the linear piezoelectric strain parameters of the MFC using a well-accepted method for such measurements found in the

literature. The effect values were found to decrease under higher loads, while increasing with larger voltage excitation amplitudes.

- The classical Preisach model was modified so that it can be used to predict strain outputs for the MFC actuation hysteresis loops resulting from voltage profiles with or without equal but opposite maxima and minima. The experimental procedure required to obtain the first-order reversal curves is also identified.

7.4 Publications:

Portions of this dissertation have been presented at various professional conferences and some are to appear in refereed journals. In addition, a patent application was filed through NASA Langley as part of the research associated with this dissertation. Below is a list of these works.

7.4.1 Papers in Refereed Journals:

- Williams, R. B., Inman, D. J. and Wilkie, W. K., "Manufacturing and Cure Kinetics Modeling for Macro Fiber Composite Actuators, Accepted for publication, *Journal of Reinforced Plastics and Composites.*

- Williams, R. B., Schultz, M. R., Hyer, M. W., Inman, D. J. and Wilkie, W. K., "Nonlinear Mechanical Behavior of Macro Fiber Composite Actuators," Accepted for publication, *Journal of Composite Materials.*

- Williams, R. B., Inman, D. J. and Wilkie, W. K., "Temperature-Dependent Coefficients of Thermal Expansion in Macro Fiber Composite Actuators" Accepted for publication, *Journal of Thermal Stresses.*

7.4.2 Forthcoming Papers in Refereed Journals:

- Williams, R. B., Inman, D. J. and Wilkie, W. K., "Nonlinear Monotonic Actuation Properties of Macro Fiber Composite Actuators Under Free-Strain Conditions," to be submitted to *Smart Materials and Structures.*

- Williams, R. B., Inman, D. J. and Wilkie, W. K., "Nonlinear Monotonic Actuation Properties of Macro Fiber Composite Actuators Under Nonzero Constant Mechanical Loads," to be submitted to *Smart Materials and Structures.*

- Williams, R. B., Inman, D. J. and Wilkie, W. K., "Application of the Classical Preisach Model to the Nonlinear Hysteretic Actuation of Macro Fiber Composite Actuators," to be submitted to *Journal of Intelligent Systems and Structures.*

7.4.3 Published Conference Papers:

- Lloyd, J. M., Williams, R. B., Inman, D. J. and Wilkie, W. K., "An Analytical Model of the Mechanical Properties of the Single-Crystal Macro-Fiber Composite Actuator," *Proceedings of SPIE Smart Structures and Materials Symposium*, March 14-18, 2004, Town and Country Resort & Convention Center, San Diego, CA.

- Williams, R. B., Inman, D. J. and Wilkie, W. K., "Nonlinear Actuation Properties of Macro Fiber Composite Actuators," *Proceedings of IMECE'03, 2003 ASME International Mechanical Engineering Congress & Exposition*, November 16-21, 2003, The Marriott Wardman Park Hotel, Washington, D. C.

- Schultz, M. R., Hyer, M. W., Williams, R. B., Wilkie, W. K., and Inman, D. J., "Use of Piezoelectric Actuators to Effect Snap-Through Behavior of Unsymmetric Composite Laminates," *Proceedings of the American Society for Composites 18th Technical Conference,* October 19-22, 2003, Hilton University of Florida Conference Center, Gainesville, FL.

- Williams, R. B., Schultz, M. R., Hyer, M. W., Inman, D. J. and Wilkie, W. K., "Nonlinear Tensile and Shear Behavior of Macro Fiber Composite Actuators," *Proceedings of the American Society for Composites 18th Technical Conference,* October 19-22, 2003, Hilton University of Florida Conference Center, Gainesville, FL.

- Williams, R. B., Inman, D. J. and Wilkie, W. K., "Temperature-Dependent Coefficients of Thermal Expansion in Macro Fiber Composite Actuators," *Proceedings of the 5th International Congress on Thermal Stresses*, June 8-11, 2003, Donaldson Brown Hotel and Conference Center, Blacksburg, VA.

- Williams, R. B., Inman, D. J. and Wilkie, W. K., "Nonlinear Mechanical Behavior of Macro Fiber Composite Actuators," *Proceedings of the Sixth International Conference on Sandwich Structures*, March 31-April 2, 2003, Marriott Marina Hotel, Ft. Lauderdale, FL.

- Williams, R. B., Grimsley, B. W., Inman, D. J. and Wilkie, W. K "Manufacturing and Mechanics-Based Characterization of Macro Fiber Composite Actuators," *Proceedings of the 2002 ASME International Mechanical Engineering Congress & Exposition, ,* November 17-22, 2002, Ernest Morial Convention Center, New Orleans, LA.

- Williams, R. B., Park, G., Inman, D. J. and Wilkie, W. K., "An Overview of Composite Actuators with Piezoceramic Fibers," *Proceedings of IMAC-XX: Conference on Structural Dynamics*, February 4-7, 2002, Westin Los Angeles Airport Hotel, Los Angeles, CA.

7.4.4 Conference Presentations (Abstract-Only):

- Williams, R. B., "An Overview of Composite Actuators with Piezoceramic Fibers," at the *2003 Virginia Space Grant Consortium Student Research Conference*, March 2003, Old Dominion University Peninsula Center, Hampton, VA.
- Williams, R. B., Inman, D. J. and Wilkie, W. K., "Modeling of Temperature Effects in Macro Fiber Composite Actuators" at the 14th *U.S. National Congress of Theoretical and Applied Mechanics*, June 24-27, 2002, Donaldson Brown Hotel and Conference Center, Blacksburg, VA.
- Williams, R. B., "An Overview of Composite Actuators with Piezoceramic Fibers," at the *2002 Virginia Space Grant Consortium Student Research Conference*, March 25, 2002, Old Dominion University Peninsula Center, Hampton, VA.

7.4.5 Patents:

- "Single Crystal Piezoelectric Fiber Composite Actuator and Method for Making Same", *NASA Invention Disclosure LAR 16520-1,* August 2002 along with W. Keats Wilkie, Daniel J. Inman and James W. High.

7.5 Recommendations for Future Work:

This work has identified the relevant properties and characterized the nonlinear actuation behavior of the MFC to the point that intelligent structure designers can apply these results directly to their modeling efforts. While this work represents a large step in such characterization efforts, there are ways in which it can be improved by future researchers whose goal is more accurate modeling of the MFC or structures that incorporate these actuators.

Other than a superficial treatment of micromechanics of fiber-reinforced composites, this work does not address any sort of micromechanical formulation. Thus, the most important step for future researchers is the development of micromechanical models to predict the effective piezoelectric constants for the MFC. While some of these models

do exist, they have not been applied to the MFC specifically, for either short-circuit or piezoelectric coefficients. Potentially, there are more accurate models than the rule-of-mixtures used herein (although ROM is a reasonable first-approximation for a single layer of rectangular fibers). Also, while the effective nonlinear piezoelectric strain coefficients were measured for the reference MFC, other geometries will have different properties. Thus, the development of a micromechanics model to accurately predict these values would be extremely useful. In addition, these models will be able to predict physical and material properties such as permittivity and capacitance, so that sensor application of the MFC can be further investigated. Also, addition work is required to represent the electric field distribution for the interdigitated electrode patterns.

The specimens used to measure the transverse response and E_y in Chapter 3, as shown in Figure 3.4, are not as long as desired for tensile testing. The tabs are close together, so the state of stress is not exactly uniaxial due to end/gripping effects. For future measurement efforts, longer E_y specimens should be designed in order to obtain more accurate values for both this modulus, as well as the minor Poisson's ratio, υ_{yx}.

The sensitivity analysis presented in Chapter 4 identified that more reliable values for the mechanical properties of the epoxy matrix are needed. These should be tested from tensile/shear specimens consisting of only cured epoxy. Such tests are common for polymer processing engineers, and the results would produce better estimates for the MFC mechanical properties, particularly for transverse and shear loading.

The experimental procedure designed to measure the actuation performance of the MFC, as described in Chapter 5, used sinusoidal input signals. However, it would have been better to use a saw tooth shaped wave input, because the sinusoidal waves induce some apparently nonlinear behavior, in particular near its extrema points. This type of input requires some of the monotonically increasing data to be discarded. Also, the

sinusoidal input was chosen to oscillate at a constant low frequency, regardless of the amplitude of the signal. This procedure introduces rate effects, although they are thought to be negligible at low frequencies. A better input would maintain a constant sweep rate, rather than frequency.

Also, from an intelligent structures point of view, it would be useful to perform some characterization experiments for a laminate consisting of the MFC sandwiched between passive, structural layers. Such a smart laminate would subject the MFC to more realistic elastic constraints along both surfaces of the actuator, rather than just at the tabbed ends. Such experiments will lead naturally to thorough investigations of using the MFC as an actuator at is either bonded to or embedded in a host structure. The anisotropic actuation of the MFC enables one to directly twist a structure, while its anisotropic mechanical properties allow for indirect twist-actuation through laminate twist-extension coupling. Additionally, measurement and modeling of the open-circuit properties of the MFC will aid future researchers who intend to use this device as a sensing component of an intelligent structure.

In Chapter 5, some "aging" effects were noted for MFC S/N 486 and 487, which resulted in a great deal of piezoelectric drift. As pointed out earlier, these two specimens were poled and immediately subjected to the actuation testing, while the others were poled, and stored for a period of time before actuation testing. In the future, specimens should either be allowed to settle normally or "run-in" under some sort of moderate actuation voltage, perhaps 1000 volts peak-to-peak at a frequency of 50 hertz. Such a procedure would tend to stabilize the actuation behavior of the MFC.

While the Preisach model developed in this work is quite useful, future researcher can measure a more complete set of α-β gridpoints, corresponding to more first-order reversal curves. In particular, more β values should be measured.

Overall, this work has thoroughly characterized the macroscopic nonlinear behavior of the MFC under various mechanical and electrical loading conditions. However, no attempt has been made to explain the physical sources of this nonlinearity, which lie within the microstructure of the piezoceramic. Nevertheless, there exists a wealth of literature dealing with modeling such behavior. Clearly, a full literature review of this topic is not called for herein, but it is worth noting how the observed nonlinearities are presumed to arise from microstructural behavior.

Papers by Fang and Li [1999] and Hall [2001] describe large scale nonlinearities, namely large polarization-electric field hysteresis loops and strain-electric field butterfly loops, by modeling the switching of ferroelectric domains. This type of behavior, caused by high fields or stresses, is indicative of the material being unpoled and repoled in the opposite direction. Such works are useful for the general study of piezoceramic materials, but are not as much for piezoelectric actuators, which typically do not consider depoling of the device. Models for domain switching generally have some sort of energy-based switching criterion, which states that when a dipole reaches a certain energy level, it will reverse its orientation.

For the experiments herein, the MFC is sometimes subjected to low to moderate negative electric fields during the harmonic excitation described in Chapter 5. Initial experimentation at NASA Langley has shown that when the MFC is subjected to only positive electric fields, its peak-to-peak free-strain performance is less than when subjected to slightly negative electric fields. The application of slightly negative fields is thought to elicit some additional non-180° domain rotation that does not occur under unipolar positive electric fields. Furthermore, it is clearly seen that the amount of nonlinearity observed for the MFC decreases under higher DC biasing voltages. Such application of a constant, positive electric field would increase the difficulty for a domain to switch its orientation, even when the electric field is cycled through the moderately negative region.

At moderately high fields, the reversible nonlinearities modeled in Chapter 5 are said to be the result of small domain wall motions [Hall 2001]. At higher fields, above a threshold value, large scale domain wall motion is possible across an array of pinning defects, which causes the irreversible hysteretic behavior considered in Chapter 6. Constant electric field or mechanical stress is thought to cause partial domain switching, which can add to the apparent change in properties [Chaplya and Carman, 2001].

The last topic recommended for future investigation is establishing a reasonable boundary for linear piezoelectric behavior of the MFC. From the short-circuit tests in Chapter 3, fiber damage occurs around a total PZT-fiber direction strain of 1100 $\mu\varepsilon$. This onset of mechanical nonlinearity results in damage to the actuator that severely reduces its actuation capability. This limit to linearity is thought to be higher than that of monolithics because fibers tend to be stronger than bulk material, and the fibers in the MFC share loads with the various polymer constituents. From a non-damaged, electric field point of view, nonlinear hysteretic behavior is visible for even the lowest amplitude harmonic excitations. The amount of hysteresis is seen to decrease under larger electric field amplitudes and mechanical stresses. The same trend is noted for monolithic ceramics.

References

1. ANSI/IEEE Std 176-1987, 1987, *IEEE Standard on Piezoelectricity*, The Institute of Electrical and Electronics Engineers, New York.

2. ASTM Standard "Standard Test Method For In-Plane Shear Response of Polymer Matrix Composite Materials by Tensile Test of a ±45° Laminate," *ASTM D 3518/D 3518-94* (Reapproved 2001).

3. ASTM Standard, "Standard Test Method for Tensile Properties of Polymer Matrix Composite Materials," *ASTM D3039/D 3039M – 00.*

4. Azzouz, M. S., Mei, C., Bevan, J., and Ro, J. J., 2001, "Finite Element Modeling of MFC/AFC Actuators and Performance of MFC," *Journal of Intelligent Material Systems and Structures*, Vol. 12, pp. 601-612.

5. Banks, H. T., Smith, R. C., and Wang, Y., S*mart Material Structures: Modeling Estimation and Control*, John Wiley & Sons, Masson, Paris, 1996.

6. Beckert, W. and Kreher, W. S., 2003, "Modelling Piezoelectric Modules with Interdigitated Electrode Structures," *Computational Materials Science*, Vol. 26, pp. 36-45.

7. Bent, A. A., "Piezoelectric Fiber Composites for Structural Actuation," Master of Science Thesis, Massachusetts Institute of Technology, January 1994.

8. Bent, A. A., "Active Fiber Composites for Structural Actuation," Doctor of Philosophy Dissertation, Massachusetts Institute of Technology, January 1997.

9. Bent, A. A., and Hagood, N. W., 1997, "Piezoelectric Fiber Composites with Interdigitated Electrodes," *Journal of Intelligent Material Systems and Structures*, Vol. 8, No. 11, pp. 903-919.

10. Bent, A. A., Hagood, N. W., and Rodgers, J. P., 1995, "Anisotropic Actuation with Piezoelectric Fiber Composites," *Journal of Intelligent Material Systems and Structures*, Vol. 6, No. 3, pp. 338-349.

11. Bevan, J. S., "Piezoceramic Actuator Placement for Acoustic Control of Panels," Doctor of Philosophy Dissertation, Old Dominion University, December 2001.

12. Bowen, C. R., Bowles, A., Drake, S., Johnson, N., and Mahon, S., 1999, "Fabrication and Finite Element Modelling of Interdigitated Electrodes," *Ferroelectrics*, Vo.l 228, No. 1-4, pp. 257-269.

13. Callister, W. D. Jr., *Materials Science and Engineering: An Introduction*, John Wiley & Sons, New York, 1994.

14. Cao, H. and Evans, A. G., 1993, "Nonlinear Deformation of Ferroelectric Ceramics," *Journal of the American Ceramics Society*, Vol. 76, No. 4, pp. 890-896.

15. Cesnik, C. E. S., and Ortega-Morales, M., 2001, "Active Beam Cross-Sectional Modeling," *Journal of Intelligent Material Systems and Structures*, Vol. 12, pp. 483-496.

16. Cesnik, C. E. S., and Shin, S., 2001, "On the Modeling of Integrally Actuated Helicopter Blades," *International Journal of Solids and Structures*, Vol. 38, pp. 1765-1789.

17. Chamis, C. C. and Sinclair, J. H., 1977, "Ten-deg Off-axis Test for Shear Properties in Fiber Composites," *Experimental Mechanics*, pp. 339-346.

18. Chaplya, P. M., and Carman, G. P., 2001, "Dielectric and Piezoelectric Response of Lead Zirconate-Lead Titanate at High Electric and Mechanical Loads in Terms of non-180° Domain Wall Motion," *Journal of Applied Physics*, Vol. 90, No. 10, pp. 5278-5286.

19. Chattopadhyay, A., Gu, H., and Liu, Q., 1999, "Modeling of Smart Composite Box Beams with Nonlinear Induced Strain," *Composites*: *Part B*, pp. 603-612.

20. Chonan, S., Jiang, Z., and Yamamoto, T., 1996, "Nonlinear Hysteresis Compensation of Piezoelectric Ceramic Actuators," *Journal of Intelligent Material Systems and Structures*, Vol. 7, pp. 150-156.

21. Chopra, I., 2002, "Review of State of Art of Smart Structures and Integrated Systems," *AIAA Journal*, Vol. 40, No. 11, pp. 2145-2187.

22. Continuum Control Corp., 2000, "Electronic Tennis Racket Improves Performance," *Reinforced Plastics*, pp. 4.

23. Crawley, E. F., and de Luis, J., 1987, "Use of Piezoelectric Actuators as Elements of Intelligent Structures," *AIAA Journal*, Vol. 25, No. 10, pp. 1373-1385.

24. Crawley, E. F., and Lazarus, K. B., 1989, "Induced Strain Actuation of Isotropic and Anisotropic Plates," Proceedings, *30th AIAA/ASME/ASCE/AHS/ASC Structures, Structural Dynamics and Materials Conference*, Mobile, AL, pp. 2000-2010.

25. CTS Wireless, 2000, "PZT Piezoelectric Materials, Technical Data (Typical Values)".

26. Cymer Corporate Press Release, 1998, "ACX Wins Prestigious "Corporate Technical Achieement Award from American Ceramic Society".

27. Damjanovic, D., 1997, "Stress and Frequency Dependence of the Direct Piezoelectric Effect in Ferroelectric Ceramics," *Journal of Applied Physics*, Vol. 82, No. 4, pp. 1788-1797.

28. Damjanovic, D. and Demartin, M., 1996, "The Rayleigh Law in Piezoelectric Ceramics," *Journal of Physics D: Applied Physics*, Vol. 29, pp. 2057-2060.

29. Dowling, N. E., *Mechanical Behavior of Materials*, Second Edition, Prentice Hall, New Jersey, 1999.

30. DuPont Films, "High Performance Films: Kapton General Specifications" Bulletin GS-96-7, http://www.dupont.com/corp/markets/aerospace/products/kapton.html.

31. DuPont Films, 1999, "Flexible Circuit Materials: Pyralux LF Copper-Clad Laminates," Bulletin H-73244.

32. Fang, D. and Li, C., 1999, "Nonlinear Electric-Mechanical Behavior of a Soft PZT-51 Ferroelectric Ceramic," *Journal of Materials Science*, Vol. 34, pp. 4001-4010.

33. Flinn, E. D., 1999, "Helicopter blades with a new twist," *Aerospace America*, Vol. 37, No. 9, pp. 40-43.

34. Ge, P. and Jouaneh, M., 1995, "Modeling Hysteresis in Piezoceramic Actuators," *Precision Engineering*, Vol. 17, pp. 211-221.

35. Ge, P. and Jouaneh, M., 1995, "Generalized Preisach Model for Hysteresis Nonlinearity of Piezoceramic Actuators," *Precision Engineering*, Vol. 20, pp. 99-111.

36. Hagood, N. W., and Bent, A. A., 1993, "Development of Piezoelectric Fiber Composites for Structural Actuation," AIAA Paper No. 93-1717-CP, *34th AIAA/ASME/ASCE/AHS/ASC Structures, Structural Dynamics and Materials Conference*, La Jolla, CA, pp. 3625-3638.

37. Hagood, N. W., Kindel, R., Ghandi, K., and Gaudenzi, P., 1993, "Improving Transverse Actuation using Interdigitated Surface Electrodes," SPIE Paper No. 1917-25, *Proceedings of the 1993 North American Conference on Smart Structures and Materials, Albuquerque, NM*, pp. 341-352.

38. Han, Y. M., Lim, S.C., lee, H.G., Choi, S.B., and Choi, H.J., 2003, "Hysteresis Identification of Polymethylaniline-Based ER Fluid Using Preisach Model," *Materials and Design*, Vol. 24, pp. 53-61.

39. High, J. W. and Wilkie, W. K., 2003, "Method of Fabricating NASA-Standard Macro-Fiber Composite Piezoelectric Actuators," NASA/TM-2003-212427,ARL-TR-2833.

40. Hu, H. and Mrad, B., 2003, "On the Classical Preisach Model for Hysteresis in Piezoceramic Actuators," *Mechatronics*, Vol. 13, pp. 85-94.

41. Hyer, M.W., *Stress Analysis of Fiber-Reinforced Composite Materials*, WCB/McGraw Hill, New York, 1998.

42. Ikeda, T., *Fundamentals of Piezoelectricity*, Oxford Science Publications, New York, 1996.

43. Jaffe, H., and Berlincourt, D. A., 1965, "Piezoelectric Transducer Materials," *Proceedings of the IEEE*, Vol. 53, No. 10, pp. 1372-1386.

44. Jenkins, C. H., Editor, 1998, *Manual on Experimental Methods of Mechanical Testing of Composites – Second Edition*, Society for Experimental Mechanics, The Fairmont Press, Georgia.

45. Jha, A. K., "Vibration Analysis and Control of an Inflatable Toroidal Satellite Component using Piezoelectric Actuators and Sensors," Doctor of Philosophy Dissertation, Virginia Tech, July 2002.

46. Janos, B. Z. and Hagood, N. W., 1998, "Overview of Active Fiber Composites Technologies," Proceedings, *6th International Conference on New Actuators – ACTUATOR 98*, Bremen, Germany.

47. Jones, R. M., *Mechanics of Composite Materials, Second Edition*, Taylor & Francis, 1999.

48. Joshi, S. P., 1992, "Non-linear Constitutive Relations for Piezoceramic Materials," *Smart Materials & Structures*, Vol. 1, No. 1, pp. 80-83.

49. Kamlah, M., 2001, "Ferroelectric and Ferroelastic Piezoceramics-Modeling of Electromechanical Hysteresis Phenomena," *Continuum Mechanics and Thermodynamics*, Vol. 13, pp. 219-268.

50. Kim, C., and Koo, K. H., 2002, "Development of a PZT Fiber/Piezo-Polymer Composite Actuator with Interdigitated Electrodes," *KSME International Journal*, Vol. 16, No. 5, pp. 666-675.

51. Lenglet, E., Hladky-Hennion, A.-C., and Debus, J.-C., 2003, "Numerical Homogenization Techniques Applied to Piezoelectric Composites," Journal of the Acoustical Society of America, Vol. 113, No. 2, pp. 826-833.

52. Lin, T. H., Salinas, D. and Ito, Y. M., 1971, "Elastic-Plastic Analysis of Unidirectional Composites," Advancements in Applied Mechanics, Vol. 11, pp. 48-60.

53. Mallik, N., and Ray, M. C., 2003, "Effective Coefficients of Piezoelectric Fiber-Reinforced Composites," *AIAA Journal*, Col. 41, No. 4.

54. Malowicki, M. G., "Active Vibration Isolation Using an Induced Strain Actuator with Application to Automotive Seat Suspensions," Master of Science Thesis, Virginia Tech, June 2000.

55. Manz, H., and Schmidt, K., 2000, "On the Application of Smart Materials in Automotive Structures," Volkswagen AG Vehicle Research, Paper Number Z00.519.2.20.20.

56. MatWeb, 2003, Online Material Property Database, www.matweb.com.

57. Mayergoyz, I. D., *Mathematical Models of Hysteresis*, Springer-Verlag, New York, 1991.

58. Morgan Matroc, Inc, 1997, "Guide to Modern Piezoelectric Ceramics."

59. Moses, R. W., Weiseman, C. D., Bent, A. A., and Pizzochero, A. E., 2001, "Evaluation of New Actuators in a Buffet Loads Environment," Proceedings, *SPIE 8th Annual International Symposium on Smart Structures and Materials*, Newport Beach, CA.

60. den Otter, M. W., 2002, "Approximate Expressions for the Capacitance and Electrostatic Potential of Interdigitated Electrdes," *Sensors and Actuators A*, Vol. 96, pp. 140-144.

61. Perry, C. C., 1969, "Plane-shear Measurement with Strain Gages," *Experimental Mechanics*, pp. 19N-22N.

62. Petit, C. W., May 21, 2001, "Up, Up, and Away – Future Flying Machines will be Faster and More Birdlike," *U.S. News and World Report*, pp. 46-47.

63. Petit, P. H., 1969, "A Simplified Method of Determining the Inplane Shear Stress-Strain Response of Unidirectional Composites," in ASTM STP 460, Philadelphia.

64. Piezo Systems, Inc., 1998, "Catalog #3."

65. Pindera, M.-J., and Herakovich, C. T., 1986, "Shear Characterization of Unidirectional Composites with the Off-Axis Tension Test," *Experimental Mechanics*, Vol. 26, No. 1, pp. 103-112.

66. Poizat, C., and Sester, M., 1999, "Effective Properties of Composites with Embedded Piezoelectric Fibers," *Computational Materials Science*, Vol. 16, pp. 89-97.

67. Robert, G., Damjanovic, Setter, N., 2001, "Preisach Distribution Function Approach to Piezoelectric Nonlinearity and Hysteresis," *Journal of Applied Physics*, Vol. 90, No. 5, pp. 2459-2464.

68. Robert, G., Damjanovic, Setter, N., and Turik, A. V., 2001, "Preisach Modeling of Piezoelectric Nonlinearity in Ferroelectric Ceramics," *Journal of Applied Physics*, Vol. 89, No. 9, pp. 5067-5074.

69. Rotman, D., May/June, 1999, "Materials Science Getting Active – New Ceramics: Smarter, Tougher," *Technology Review*, pp. 25.

70. Ruggiero, E., Park, G., Inman, D. J. and Wright, J., 2002, "Multi-Input, Multi-Output Modal Testing Techniques for a Gossamer Structure," Proceedings, *IMECE 02*, 2002 ASME IMECE Adaptive Structures Symposium, November 17-22, New Orleans, LA.

71. Schultz, M. R., "Use of Piezoelectric Actuators to Effect Snap-Through Behavior of Unsymmetric Composite Laminates," Doctor of Philosophy, Virginia Tech, April 2003.

72. Smith, R. C. and Ounaies, Z., 1999, "A Hysteresis Model for Piezoelectric Materials," ICASE Report No. 99-29, NASA/CR-1999-209368, August 1999.

73. Smith, R. C., Ounaies, Z., and Wieman, R., 2001, "A Model for Rate-Dependent Hysteresis in Piezoelectric Materials Operating at Low Frequencies," ICASE Report No. 2000-26, NASA/CR-2001-211062.

74. Sodano, H. A., Park, G., and Inman, D. J., 2003, "The Use of Macro-Fiber Composites in Structural Vibration Applications," *Mechanical Systems and Signal Processing*, in press.

75. Sun, C. T., and Berreth, S. P., 1988, "A New End Tab Design for Off-Axis Tension Test of Composite Materials," *Journal of Composite Materials*, Vol. 22, pp. 766-779.

76. Sun, C. T. and Chung, I., 1993, "An Oblique End-Tab Design for Testing off-axis Composite Specimens," *Composites*, Vol. 24, No. 8, pp. 619-623.

77. Tan, P, and Tong, L., 2001, "Micro-Electromechanics Models for Piezoelectric-Fiber-Reinforced Composite Materials," *Composites Science and Technology*, Vol. 61, pp. 759-769.

78. Tan, P., and Tong, L., 2002a, "Investigation of Loading Assumptions of the Effective Electroelastic Constants for PFRC Materials," *Composite Structures*, Vol. 57, pp. 101-108.

79. Tan, P., and Tan, P., 2002b, "A One-Dimensional Model for Non-Linear Behaviour of Piezoelectric Composite Materials," *Composite Structures*, Vol. 58, pp. 551-561.

80. Thornburgh, R. P., and Chattopadhyay, A., 2001, "Nonlinear Actuation of Smart Composites Using a Coupled Piezoelectric-Mechanical Model," *Smart Materials and Structures*, Vol. 10, pp. 743-749.

81. Tiersten, H. F., *Linear Piezoelectric Plate Vibrations: Elements of the Linear Theory of Piezoelectricity and the Vibrations of Piezoelectric Plates*, Plenum Press, New York, 1969.

82. Tiersten, H. F., 1971, "On the Nonlinear Equations of Thermoelectroelasticity," *International Journal of Engineering Science*, Vol. 9, pp. 587-604.

83. Tiersten, H. F., 1993a, "Equations for the Extension and Flexure of Relatively Thin Electroelastic Plates Undergoing Large Electric Fields," AMD-Vol. 161/MD-Vol. 42, *Mechanics of Electromagnetic Materials and Structures*, pp. 21-34.

84. Tiersten, H. F., 1993b, "Electroelastic Equations for Electroded Thin Plates Subject to Large Driving Voltages," *Journal of Applied Physics*, Vol. 74, No. 5, pp. 3389-3393.

85. Toupin, R. A., 1956, "The Elastic Dielectric," *Journal of Rational Mechanical Analysis*, Vol. 5, No. 6, pp. 849-915.

86. Wang, Q.-M., Zhang, Q., Xu, B., Liu, R., and Cross, L. E., 2001, “Nonlinear Piezoelectric Behavior of Ceramic Bending Mode Actuators Under Strong Electric Fields,” *Journal of Applied Physics*, Vol. 86, No. 6, pp. 3352-3360.

87. Wilkie, W. K., February 2003, “Engineering Properties for NASA-Standard 7.5 mil CTS 3195HD, 21-5 mil IDE Macro-Fiber Composite Devices (REV. 2/23/03),” personal communication.

88. Wilkie, W. K., Bryant, G. R., High, J. W. et al., 2000, “Low-Cost Piezocomposite Actuator for Structural Control Applications,” Proceedings, *SPIE 7th Annual International Symposium on Smart Structures and Materials*, Newport Beach, CA.

89. Williams, R. B., Grimsley, B. W., Inman, D. J., and Wilkie, W. K., "Manufacturing and Mechanics-Based Characterization of Macro Fiber Composite Actuators, Accepted for Publication in *Journal of Reinforced Plastics and Composites,* August 2003.

90. Williams, R. B., Schultz, M. R., Hyer, M. W., Inman, D. J., and Wilkie, W. K., "Nonlinear Tensile and Shear Behavior of Macro Fiber Composite Actuators," Accepted for Publication in *Journal of Composite Materials,* August 2003.

91. Williams, R. B., Inman, D. J., and Wilkie, W. K., “Temperature-Dependent Coefficients of Thermal Expansion for Macro Fiber Composite Actuators,” Accepted for Publication in *Journal of Thermal Stresses*, February 2004.

92. Zhong, W., Lin, T. H., and Lin, S. R., 1998, “An Elastic-Plastic Micromechanical Analysis of a Cross-Ply Composite,” *Composites Science and Technology*, Vol. 58, pp. 527-537.

Appendix A

Derivation of Rule-of-Mixture Formulae for Orthotropic Laminae

A.1 Introduction:

In Chapter 2, rule-of-mixtures formulae are used to calculate the apparent orthotropic moduli of the various fiber-reinforced laminae. This appendix applies a mechanics of materials approach to derive these formulae for a representative volume element of a fiber-reinforced lamina, based on the approach found in Jones [1999].

A.2 Approach to Derivation:

The mechanics of materials approach to the modeling of composites requires some simplifying assumptions about the behavior of the fiber and matrix materials. First, the strain in the fiber and the matrix are identical in the direction of the fibers, and that they are equal to the total strain of the composite, as shown in Figure A.1. That is, a plane normal to the 1-direction will remain plane after application of the load. Also, when a stress is applied perpendicular to the fiber direction, the stress in the fiber and matrix are equal. Likewise, when the composite is subjected to a shear load, the shear stresses

in the fiber and matrix are again equal. Furthermore, while the matrix material is considered to be isotropic, the equations derived in this section allow for the fiber material properties to be transversely isotropic. That is, the material properties in the fiber direction (1-direction) are different than those in the 2-3 plane, in which the properties are isotropic. With these assumptions in mind, derivation of the desired properties begins.

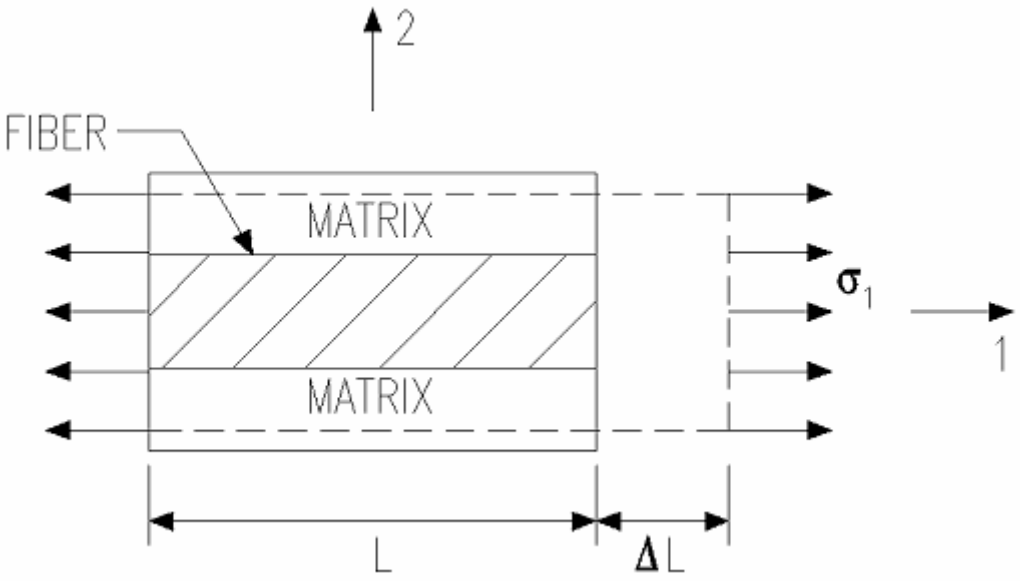

Figure A.1: Representative Volume Element with 1-Direction Load

A.2.1 Derivation of E_1:

For the representative volume element shown in Figure A.1, subjected to a uniaxial stress, σ_1, the strain in the 1-direction, ε_1 is given as

$$\varepsilon_1 = \frac{\Delta L}{L} \tag{A.1}$$

where this strain has been assumed to be the same in the fiber and the matrix. For linear elastic behavior, the stresses in the fiber and matrix are given by

$$\sigma_f = E_f^1 \varepsilon_1 \tag{A.2}$$

and

$$\sigma_m = E_m \varepsilon_1 \tag{A.3}$$

where E is the elastic modulus, the superscript 1 indicates a property in the 1-direction, and the subscript f and m refer to the fiber and matrix properties, respectively. Since the uniaxial stress, σ_1, acts on the total cross-sectional area of the composite, A, and the stress in the fiber and matrix act on their respective cross-sectional areas, A_f and A_m, the resultant force, P, on the composite is given as

$$P = \sigma_1 A = \sigma_f A_f + \sigma_m A_m \tag{A.4}$$

Next, the fiber and matrix stresses from Equation A.2 and A.3 are substituted into Equation A.4, along with the relationship for σ_1

$$\sigma_1 = E_1 \varepsilon_1 \tag{A.5}$$

where E_1 is the desired effective modulus of the composite. Thus, after dividing through by A, the effective modulus is found to be

$$E_1 = E_f^1 \frac{A_f}{A} + E_m \frac{A_m}{A} \tag{A.6}$$

However, the volume fractions, V, of the fiber and matrix are defined as

$$V_f = \frac{A_f}{A} \quad and \quad V_m = \frac{A_m}{A} \tag{A.7}$$

Therefore,

$$E_1 = \mathrm{V}_f E_f^1 + \mathrm{V}_m E_m \tag{A.8}$$

A.2.2 Derivation of E_2:

Next, it is desired to determine the effective modulus of the composite in the 2-direction, E_2. This task is accomplished by loading the composite perpendicular to the fibers, as depicted in Figure A.2.

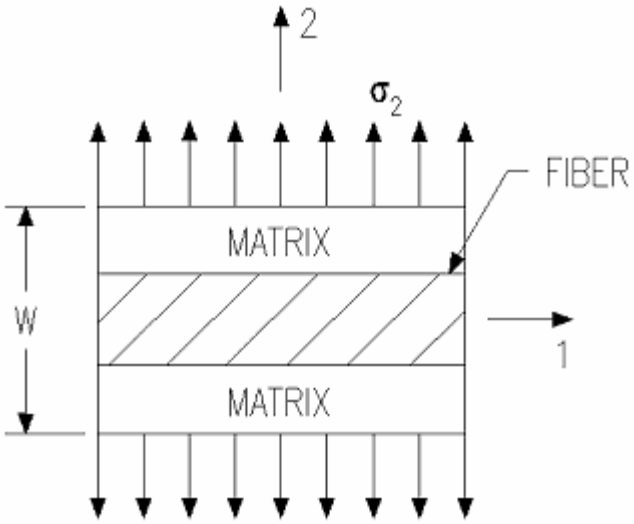

Figure A.2: Representative Volume Element with 2-Direction Load

For such a loading configuration, where the stress in the fiber and matrix have been assumed to be identical, the elastic strains are

$$\varepsilon_f = \frac{\sigma_2}{E_f^2} \tag{A.9}$$

and

$$\varepsilon_m = \frac{\sigma_2}{E_m} \tag{A.10}$$

where the superscript *2* indicates a property in the *2*-direction. Next, since the strain in the fiber acts over the distance $V_f W$ and the strain in the matrix acts over the distance $V_m W$, the total deformation in the 2-direction is simply

$$\varepsilon_2 W = V_f W \varepsilon_f + V_m W \varepsilon_m \tag{A.11}$$

The strains from Equations A.9 and A.10 are now be substituted into Equation A.11, resulting in

$$\varepsilon_2 = V_f \frac{\sigma_2}{E_f^2} + V_m \frac{\sigma_2}{E_m} \tag{A.12}$$

At this point, the stress on the composite can be written in terms of the desired effective modulus in the 2-direction, E_2, as

$$\sigma_2 = E_2 \varepsilon_2 \tag{A.13}$$

With Equation A.12, this stress can be rewritten as

$$\sigma_2 = E_2 \left(V_f \frac{\sigma_2}{E_f^2} + V_m \frac{\sigma_2}{E_m} \right) \tag{A.14}$$

Dividing both sides by $\sigma_2 E_2$ gives

$$\frac{1}{E_2} = \frac{V_f}{E_f^2} + \frac{V_m}{E_m} \tag{A.15}$$

After inverting both sides and multiplying the right hand side by $\frac{E_f^2 E_m}{E_f^2 E_m}$, the desired modulus is found to be

$$E_2 = \frac{E_f^2 E_m}{V_m E_f^2 + V_f E_m} \tag{A.16}$$

A.2.3 Derivation of G_{12}:

The in-plane shear modulus of a fiber-reinforced lamina, G_{12}, is found by assuming that the matrix and fiber shear stresses are the same. Consider a representative volume element loaded by shear stress τ as shown in Figure A.3a

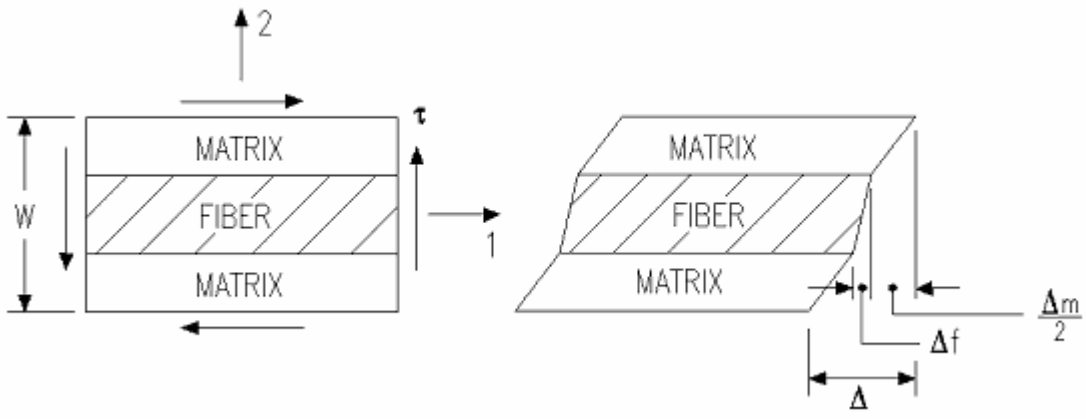

(A) (b)

Figure A.3: (a) Representative Volume Element with Shear Load and (b) Microscopic Deformation of Representative Volume Element

Considering only linear elastic behavior, the shear strains, γ are given as

$$\gamma_f = \frac{\tau}{G_f^{12}} \tag{A.17}$$

and

$$\gamma_m = \frac{\tau}{G_m} \tag{A.18}$$

Examination of the deformation field in Figure A.3b shows that the total shear deformation of the composite can be written as

$$\Delta = \gamma W \tag{A.19}$$

This total deformation is made up of the fiber and matrix deformations, which are

$$\Delta_f = V_f W \gamma_f \tag{A.20}$$

and

$$\Delta_m = V_m W \gamma_m \tag{A.21}$$

Since $\Delta=\Delta_f+\Delta_m$, combination of Equations A.19-A.21 yields

$$\gamma = V_f \gamma_f + V_m \gamma_m \tag{A.22}$$

Noting that the shear strain of the composite is simply equal to the shear stress divided by the desired lamina shear modulus, G_{12}, and with Equations A.17 and A.18, Equation A.22 becomes

$$\frac{\tau}{G_{12}} = V_f \frac{\tau}{G_f^{12}} + V_m \frac{\tau}{G_m} \tag{A.23}$$

Algebraic manipulation then gives

$$G_{12} = \frac{G_f^{12} G_m}{V_m G_f^{12} + V_f G_m} \tag{A.24}$$

A.2.4 Derivation of υ_{12}:

The major Poisson's ratio for a fiber-reinforced lamina, υ_{12}, is found using a representative volume element, shown in Figure A.4, loaded like that used to determine E_1.

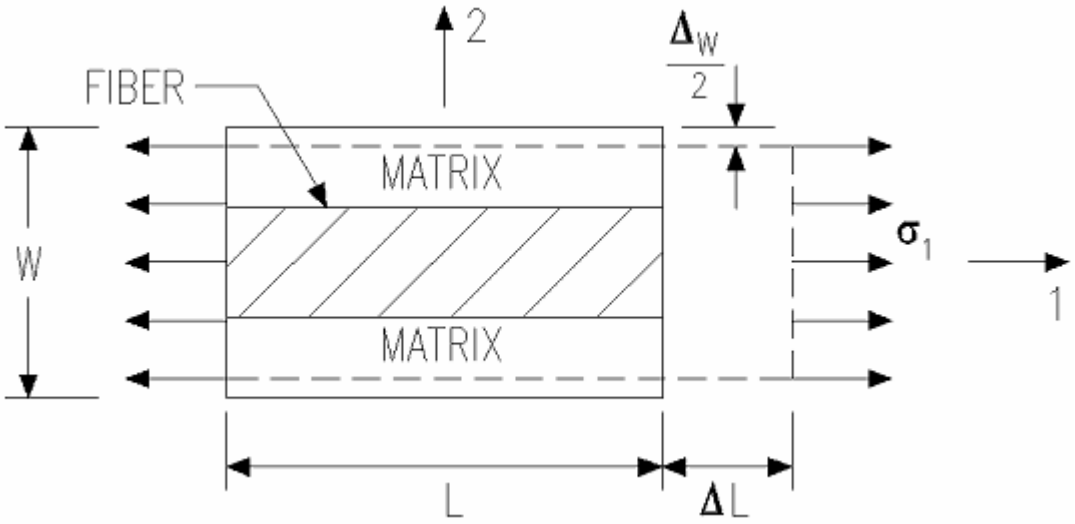

Figure A.4: Representative Volume Element with 1-Direction Load

This quantity is defined as

$$\nu_{12} = -\frac{\varepsilon_2}{\varepsilon_1} \tag{A.25}$$

The total transverse deformation is given as

$$\Delta_w = -W\varepsilon_2 = W\nu_{12}\varepsilon_1 \tag{A.26}$$

However, it is also the sum of the deformations in the fiber and the matrix in the 2-direction:

$$\Delta_w = \Delta_{fW} + \Delta_{mW} \tag{A.27}$$

The quantities on the right hand side of Equation A.27 can be expressed as

$$\Delta_{fW} = WV_f \upsilon_f^{12} \varepsilon_1 \tag{A.28}$$

$$\Delta_{mW} = WV_m \upsilon_m \varepsilon_1 \tag{A.29}$$

Substitution of Equations A.28 and A.29 into Equation A.27, and then using the far right hand side of Equation A.26 gives

$$\nu_{12} = \mathrm{V}_f \nu_f^{12} + \mathrm{V}_m \nu_m \tag{A.30}$$

A.3 Summary:

Appendix A presents derivations for the four effective engineering mechanical properties of an orthotropic lamina with transversely isotropic fibers. The derivations follow the methodology presented in Jones [1999]. These expressions are used in the development of a classical lamination model of the MFC actuator in Chapter 2.

A.4 References:

1. Jones, R. M., *Mechanics of Composite Materials, Second Edition*, Taylor & Francis, 1999.

Appendix B

Mathematica Code for Classical Lamination Model of the Macro Fiber Composite

B.1 Introduction:

In Chapter 2, rule-of-mixtures formulae are used to represent the orthotropic laminae of the MFC actuator. These layers, along with the isotropic ones are then combined using a classical lamination approach. In order to perform these calculations for various MFC geometric configurations, a *Mathematica* computer code is written. This appendix presents this code, which is developed in *Mathematica* Version 4.0.

B.2 *Mathematica* Code:

MFC Property Calculations 15x2x7.5 mil, 5 mil Cu

```
<< Graphics`Colors`
<< Graphics`Legend`
Off[General::spell1]
```

■ **Layer properties**

■ **Electrode Layers**

Kapton

```
tkapton = 2.54 * 10^-5; (*Kapton Thickness, m*)
Ekapton = 2.5; (*Kapton Elastic Modulus, GPa*)
νkapton = 0.34; (*Kapton Poisson's Ratio*)
Gkapton = Ekapton / (2 * (1 + νkapton)); (*Kapton Shear Modulus, GPa*)
ρkapton = 1.42; (*Kapton Density, g/cm^3*)
```

Acrylic Adhesive

```
tacrylic = 1.27 * 10^-5; (*Acrylic Thickness, m*)
Eacrylic = 2.7; (*Acrylic Elastic Modulus, GPa*)
νacrylic = 0.35; (*Acrylic Poisson's Ratio*)
Gacrylic = Eacrylic / (2 * (1 + νacrylic)); (*Acrylic Shear Modulus, GPa*)
ρacrylic = 1.15; (*Acrylic density, g/cm^3*)
```

Copper Electrodes

```
tcopper = 1.778 * 10^-5; (*Copper Thickness, m*)
wcopper = 1.27 * 10^-4; (*Copper Width, m* 5 mil*)
electrodespacing = 5.334 * 10^-4; (*Copper Electrode Spacing, m*)
Ecopper = 117.2; (*Copper Elastic Modulus, GPa*)
νcopper = 0.31; (*Copper Poisson's Ratio*)
Gcopper = Ecopper / (2 * (1 + νcopper)); (*Copper Shear Modulus, GPa*)
```

Epoxy

```
Eepoxy = 3.378; (*Epoxy Elastic Modulus, GPa*)
νepoxy = 0.27; (*Epoxy Poisson's Ratio*)
Gepoxy = Eepoxy / (2 * (1 + νepoxy)); (*Epoxy Shear Modulus, GPa*)
```

■ **PZT Fiber Layer**

■ Calculate Elastic Constants for Each Orthotropic Layer

■ Properties calculated using rule of mixtures.

PZT Fiber Layer

$$E1PZT = VfiberPZT * E11EPZT + VmatrixPZT * Eepoxy;$$

$$E2PZT = \frac{1}{\frac{VfiberPZT}{E22EPZT} + \frac{1-VfiberPZT}{Eepoxy}};$$

$$G12PZT = \frac{Gepoxy * G12fiber}{(1 - VfiberPZT) * G12fiber + VfiberPZT * Gepoxy};$$

$$\nu 12PZT = VfiberPZT * \nu fiber + VmatrixPZT * \nu epoxy;$$

Copper-Epoxy Electrode Layer

$$E1electrode = Vfiberelectrode * Ecopper + Vmatrixelectrode * Eepoxy;$$

$$E2electrode = \frac{1}{\frac{Vfiberelectrode}{Ecopper} + \frac{1-Vfiberelectrode}{Eepoxy}};$$

$$G12electrode = \frac{Gepoxy * Gcopper}{(1 - Vfiberelectrode) * Gcopper + Vfiberelectrode * Gepoxy};$$

$$\nu 12electrode = Vfiberelectrode * \nu copper + Vmatrixelectrode * \nu epoxy;$$

■ Input Laminate Parameters

■ Define number of layers and number of different material types.

```
Nlayers = 8;
Nsets = 4;
layerset[1] = 1;

thick[1] = tkapton;
thick[2] = tacrylic;
thick[3] = tcopper;
thick[4] = tfiber/2;
thick[5] = thick[4];
thick[6] = thick[3];
thick[7] = thick[2];
thick[8] = thick[1];
totalthickness = Sum[thick[i] (*m*), {i, 1, Nlayers}]
```

■ **Define the z values for the top and bottom of each layer**

```
Clear[z]
z = Table[0, {i, 1, Nlayers + 1}];
z[[Nlayers + 1]] = totalthickness / 2;
Do[z[[i]] = Chop[z[[i + 1]] - thick[i]], {i, Nlayers, 1, -1}]
z
```

Kapton Layer (Isotropic)

```
E1[1] = Ekapton;
E2[1] = Ekapton;
G12[1] = Gkapton;
ν12[1] = νkapton;
θ[1] = 0;
θ[8] = 0;
```

Acrylic Layer (Isotropic)

```
E1[2] = Eacrylic;
E2[2] = Eacrylic;
G12[2] = Gacrylic;
ν12[2] = νacrylic;
θ[2] = 0;
θ[7] = 0;
```

Copper-Epoxy Layer (Orthotropic, 90°)

```
E1[3] = E1electrode;
E2[3] = E2electrode;
G12[3] = G12electrode;
ν12[3] = ν12electrode;
θ[3] = 90;
θ[6] = 90;
```

PZT-Epoxy Layer (Orthotropic, 0°)

```
E1[4] = E1PZT;
E2[4] = E2PZT;
G12[4] = G12PZT;
ν12[4] = ν12PZT;
θ[4] = 0;
θ[5] = 0;
```

■ Calculating Laminae Matrices

■ Compliance Matrix, S

```
Sij = Array[S, {3, 3, Nsets}];
Do[S[1, 1, i] = 1/E1[i];
 S[1, 2, i] = -ν12[i]/E1[i];
 S[1, 3, i] = 0;
 S[2, 1, i] = S[1, 2, i];
 S[2, 2, i] = 1/E2[i];
 S[2, 3, i] = 0;
 S[3, 1, i] = 0;
 S[3, 2, i] = 0;
 S[3, 3, i] = 1/G12[i], {i, 1, Nsets}]
Do[
 compliance[i] =
  Partition[Extract[Sij, {{1, 1, i}, {1, 2, i}, {1, 3, i}, {2, 1, i},
     {2, 2, i}, {2, 3, i}, {3, 1, i}, {3, 2, i}, {3, 3, i}}], 3], {i, 1, Nsets}]
```

■ Reduced Stiffness Matrix

```
Do[Q[i] = Inverse[compliance[i]], {i, 1, Nsets}];
MatrixForm[Q[1]];
MatrixForm[Q[2]];
MatrixForm[Q[3]];
MatrixForm[Q[4]];
```

■ Transformation Matrices for Each Layer

```
Do[
 T[i] =
  N[{{Cos[θ[i] Degree]^2, Sin[θ[i] Degree]^2, 2*Sin[θ[i] Degree]*Cos[θ[i] Degree]},
    {Sin[θ[i] Degree]^2, Cos[θ[i] Degree]^2, -2*Sin[θ[i] Degree]*Cos[θ[i] Degree]},
    {-Sin[θ[i] Degree]*Cos[θ[i] Degree], Sin[θ[i] Degree]*Cos[θ[i] Degree],
     Cos[θ[i] Degree]^2 - Sin[θ[i] Degree]^2}}], {i, 1, Nlayers}]
```

■ **In-plane Laminate Extensional Stiffness Matrix, [A]**

```
Clear[A]
extenstiff = Array[A, {3, 3}];
For[i = 1, i ≤ 3, A[i, 1] = Sum_{k=1}^{Nlayers} Extract[qbar[k], {i, 1}] * thick[k]; i++]
Clear[i]
For[i = 1, i ≤ 3, A[i, 2] = Sum_{k=1}^{Nlayers} Extract[qbar[k], {i, 2}] * thick[k]; i++]
Clear[i]
For[i = 1, i ≤ 3, A[i, 3] = Sum_{k=1}^{Nlayers} Extract[qbar[k], {i, 3}] * thick[k]; i++]
Clear[i]
```

■ **Inversion of the [A] Matrix and Calculation of Laminate Engineering Properties**

```
ainv = Inverse[extenstiff];
MatrixForm[ainv]
Ex = 1 / (ainv[[1, 1]] * totalthickness)
Gxy = 1 / (ainv[[3, 3]] * totalthickness)
Ey = 1 / (ainv[[2, 2]] * totalthickness)
νxy = -ainv[[2, 1]] / ainv[[1, 1]]
```

B.3 Summary:

This appendix provides the classical lamination code used to model the Macro Fiber Composite, for the use of future researchers. Its benefits include the ability to change geometric properties for various MFC geometric configurations and to update the material properties should more experimental data become available. The thicknesses of the various layers are also readily changed to allow for the use of other electrode layers or PZT thicknesses. This code also allows the PZT fibers to be oriented at any intermediate angle between 0 and 90 degrees, so long as the copper electrodes always remain perpendicular to the piezoceramic.

Appendix C

Manufacturing of the Macro Fiber Composite

C.1 Introduction:

The present work has focused efforts to characterize the piezomechanical behavior of the Macro Fiber Composite actuator. However, an important step that enabled such research was the development and documentation of innovative manufacturing procedures that lead to increased repeatability and resolution of many initial quality control issues. This appendix serves to outline this assembly procedure so that Macro Fiber Composites could possibly be produced at locations other than NASA Langley, and possibly on a commercial basis, if the required materials were already on hand. However, the current documentation effort ultimately led to a NASA Technical Memorandum [High and Wilkie 2003], which contains a comprehensive manufacturing guide. In addition to the assembly steps presented in this appendix, that document lists detailed vendor information pertaining to procurement of the constituent materials (PZT, epoxy, etched, copper-clad Kapton), incidental tooling and expendables (soldering iron, razor blades, various films and pads, etc.), and discussed operation of

the specialized equipment (vacuum hot press, computer controlled silicon dicing saw, electrical test and poling equipment) required to produce MFCs.

C.2 Preparation of the MFC Layers:

The MFC is assembled by hand and consists of three main layers: the bottom electrode, the PZT fiber layer and the top electrode. This section discusses how each layer is prepared and acquired.

C.2.1 Interdigitated Electrodes:

The top and bottom electrode layers begin a sheet of DuPont Pyralux® LF7062 copper clad laminate. This layered material consists of rolled, annealed copper that is bonded to a Kapton® substrate using a proprietary C-staged acrylic adhesive [DuPont, 1999]. The desired electrode artwork is generated in a computer CAD program, and the resulting PCX files are sent to a company, GC Aero, in Torrance, California. Then they chemically etch away the unwanted copper material to leave behind the desired electrode pattern. The finished, etched sheets are returned, each containing several pairs of bottom and top electrodes. The pair of electrodes is identical, except the top solder tabs have two slots etched away. These slots are shown in the photograph of Figure C.1(a), while the entire bottom electrode is depicted in Figure C.1(b).

Upon receipt of the etched sheets, the individual electrode layers are carefully separated using scissors, and the electrode fingers visually inspected. Any layers with broken, over, or under-etched electrodes should be discarded, as these defects could lead to potentially dangerous electrical failures in the final MFC package. Next, solder is applied to the tabs on both the top and bottom electrode layers. This step will promote good electrical contact between the two electrode sheets in the final assembly. Finally, the copper side of each electrode should carefully be cleaned with isopropyl alcohol and a lint-free tissue, and then dried with inert, pressurized nitrogen gas.

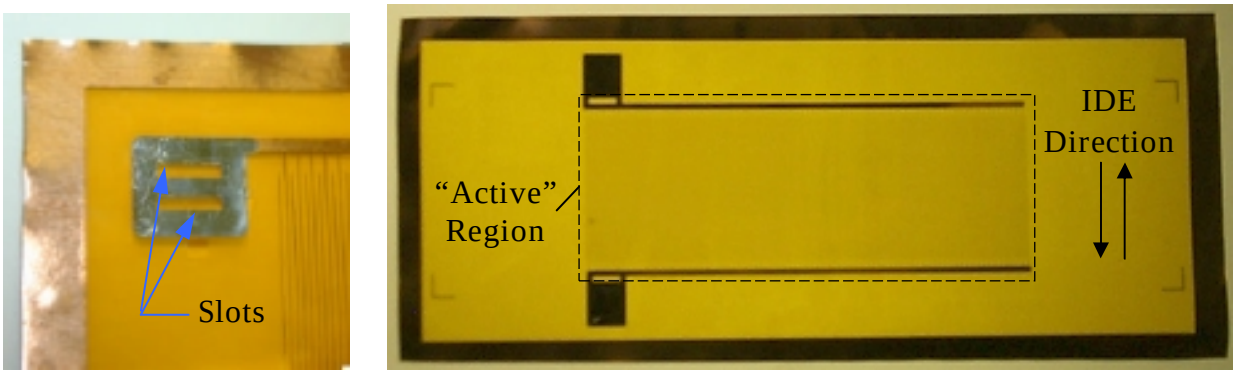

(a) (b)

Figure C.1: (a) Top MFC Solder Tab with Slots and (b) Bottom Interdigitated Electrode

C.2.2 PZT Fiber Layer:

As discussed in Chapter 1, the round, extruded PZT fibers used in the AFC actuator were arranged by hand, which sometimes led to misaligned and broken fibers. Once the decision was made to use rectangular cross-section fibers, the idea was proposed to employ silicon dicing techniques, including the use of plastic wafer dicing tape as a carrier film stretched between plastic grip rings. The plastic wafer dicing tape is purchased from Semiconductor Equipment Corp., while the grip rings are from Perfection Products, Inc.

The MFC PZT fibers begin as a thin, monolithic block of unpoled piezoceramic, purchased from CTS Wireless Components in Albuquerque, New Mexico. The wafer is then adhered to the 0.003 in (0.0762 mm) thick sticky blue carrier film, and then loaded into a computer-controlled silicon wafer dicing saw. This machine uses a 0.00217 in (0.055 mm) thick, water-cooled, diamond impregnated blade to cut back and forth along the length of the piezoceramic block every 0.017 mil (0.432 mm) at a rate of 0.2 in (5.08 mm) per minute. Since the PZT remains adhered to the carrier film during the dicing process, the result is a layer of perfectly aligned fibers with 0.014 in (0.356 mm) wide rectangular cross-sections separated by 0.003 in (0.0762 mm) spaces. The dicing saw and grip ring are shown in Figure C.2.

Figure C.2: Water-Cooled, Computer-Controlled Silicon Wafer Dicing Saw

The diced PZT fibers, attached to the blue carrier film between the grip-rings are seen in Figure C.3. After dicing is complete, a razor blade is used to remove the fibers and film from the rings. At this point, the sticky film holds the fibers in place, ensures that they remain perfectly aligned, and aids in subsequent handling.

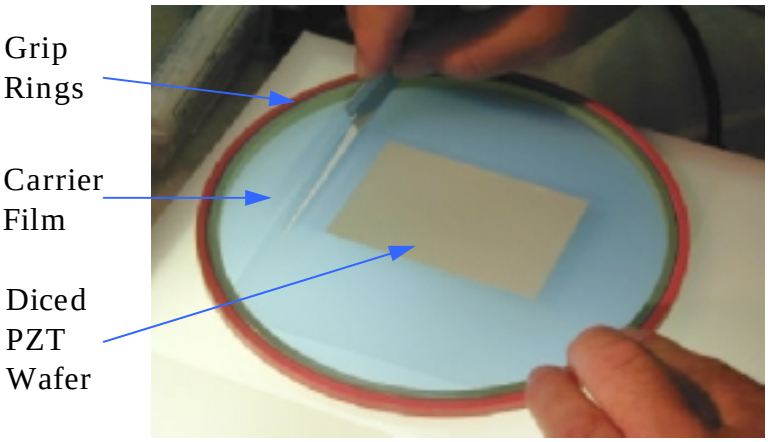

Figure C.3: Rectangular Cross-Section PZT Fibers Attached to Carrier Film

C.2.3 Epoxy Resin

Even though the epoxy is not an individual layer, it is an important component of the MFC actuator. While there are many thermosetting epoxy resin systems commercially

available, NASA uses LOCTITE® DURABOND E-120HP for its superior performance at elevated temperatures around 150°F (66°C). The preferred size is 50 ml tubes with the corresponding applicator gun and mixing nozzles. This is a two-part epoxy that requires curing at an elevated temperature. However, the manufacturer only gives approximate temperature-time cure cycles and did not have any experimental data to share. This lack of information is the impetus for the cure kinetics models that form the second half of this chapter.

C.3 MFC Assembly:

At this point, with the two electrode layers, the PZT fibers, and epoxy in hand, one can begin assembling the layers to form the MFC actuator. Epoxy application and assembly should take place on disposable plastic sheets, such as Pacothane® Plus, to ensure the work area does not accumulate unwanted epoxy.

C.3.1 Bottom Electrode and Fiber Layers

The first step is to apply some mixed epoxy to the side of the bottom electrode that contains the copper interdigitated electrode pattern using the epoxy applicator gun and proper mixing nozzle as depicted in Figure C.4(a). Then, the epoxy is spread into a thin layer by lightly dragging a razor blade parallel to the electrode fingers. The edge of the blade should point *away* from the direction of motion, as seen in Figure C.4(b).

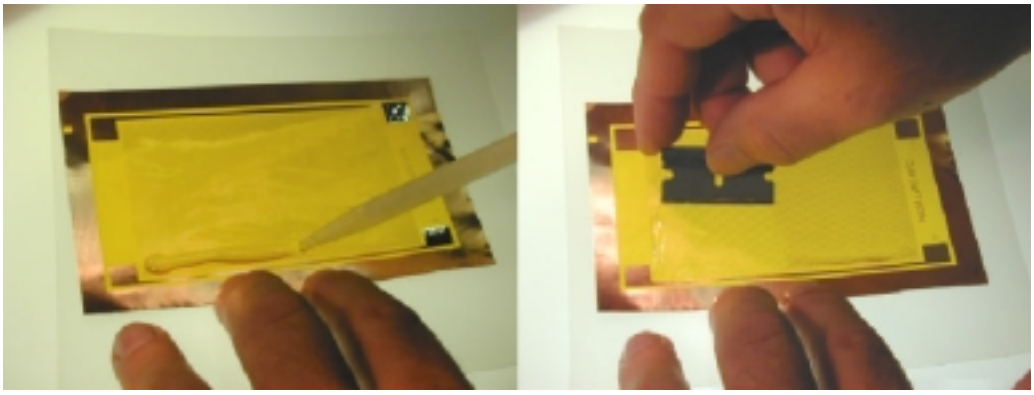

(a) (b)

Figure C.4: (a) Application of Epoxy from Mixing Nozzle and (b) Spreading Epoxy

The epoxy should only be spread over the region containing the interdigitated electrodes at this point to facilitate removing the part from the hot press layers discussed below. Ultimately, the goal of spreading the epoxy in this manner is to force the epoxy *between* the electrodes, but not on top of the copper. While excess epoxy will gather on the razor blade and can be wiped off using a lint-free paper towel, there should be no portions of the electrode area without epoxy.

Next, epoxy is applied to the PZT fiber sheet, which is attached to the blue carrier film. A reasonable amount of epoxy should be applied at one end of the fibers, and then spread in the direction of the fibers using a razor blade. Again, the sharpened edge of the razor should point *away* from the direction of motion for initial spreading and the goal is to force the epoxy completely between the PZT fibers so that there are no air bubbles remaining. After spreading is complete, excess epoxy should be removed from the top of the fibers by making one pass with the razor blade pointing *in* the direction of motion along the fibers. Care should always be taken to not push the blade perpendicular to the fibers, as they could become unattached to the film, misaligned, or even broken. Next, the excess carrier film should be trimmed from around the edges of the PZT fibers using the razor blade.

Now the PZT fiber layer is stacked on top of the bottom layer, such that the piezoceramic is in direct contact with the copper fingers and the electrodes are perpendicular to the PZT fibers, as seen in Figure C.5.

C.3.2 Pre-Cure of the Epoxy:

While the blue carrier film has done an excellent job holding the fibers together during dicing and subsequent handling, it must now be removed. However, a pre-curing step must be undertaken at an elevated temperature in order to partially cure the epoxy, so that the fibers remain securely aligned and attached to the bottom electrode when the blue film is peeled away.

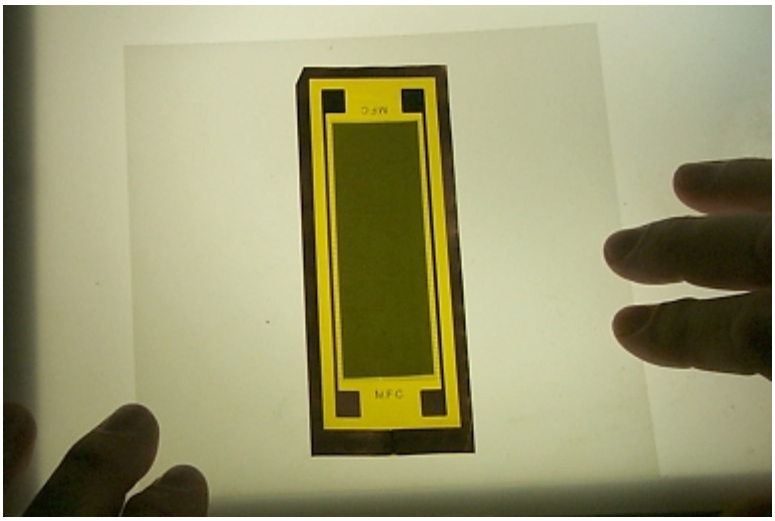

Figure C.5: PZT Fiber Layer Stacked on top of Bottom Electrode

Since this heated partial curing takes place in a vacuum hot-press, the electrode and fibers are first sandwiched into a hot-press book, the bottom half of which is shown in Figure C.6.

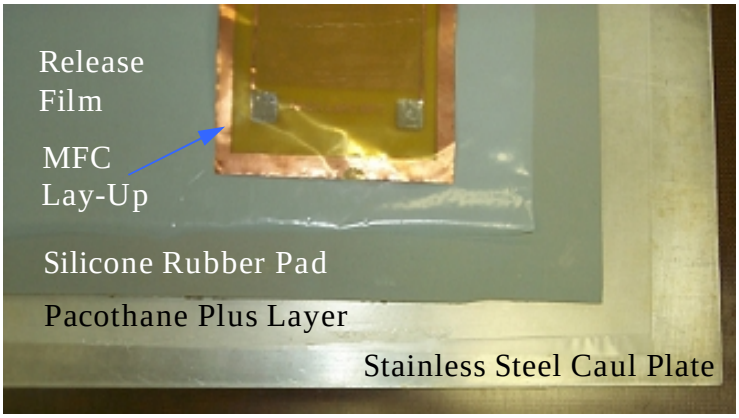

Figure C.6: Hot-Press Book Layers

This collection of various layers of plastic, rubber and stainless steel serves to protect the package and facilitates an even heating of the lay-up. The hot-press book is now placed into the vacuum hot-press, seen with its door open in Figure C.7.

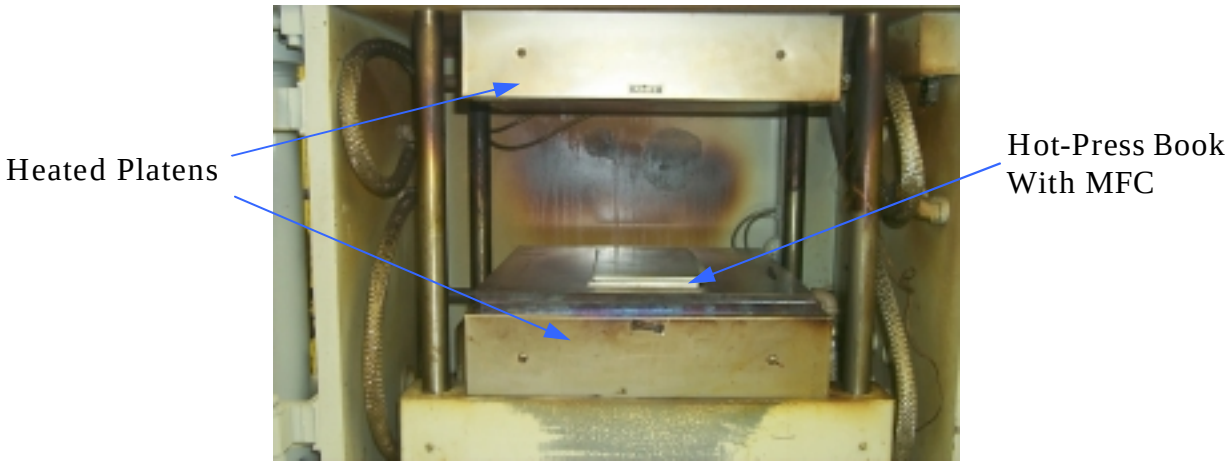

Figure C.7: Vacuum Hot-Press and Assembled Book

With the heated platens off, the vacuum is pumped down to around 27 inches of mercury and held for fifteen minutes in an effort to remove voids from between the fibers and volatiles expelled from the epoxy. Next, while still under vacuum, the heated platens are clamped such that a force of 5000 pounds is applied to the book and the temperature is ramped up to 115 °F at the rate of 8 °F per minute. The lay-up is held at this temperature for just 15 minutes since only a partial cure of the epoxy is desired, and then the platens are returned to room temperature using a water-cooling system and the vacuum pressure removed. The book is then unassembled and the half-MFC package is carefully removed.

C.3.3 Top Electrode Layer:

Before proceeding with the lay-up process, the blue carrier film is now carefully peeled away such that the fibers are not misaligned or damaged. The film should be removed starting at a corner, and then continuing across the width of the fibers, and *then* finally along the length of the fibers at as steep of an angle as possible, as seen in Figure C.8

Next, another layer of epoxy is applied to the top electrode and the exposed surface of the PZT fibers using a razor blade in the same manner described above. However, this time, the epoxy is spread to the edges of the top and bottom electrode to ensure the

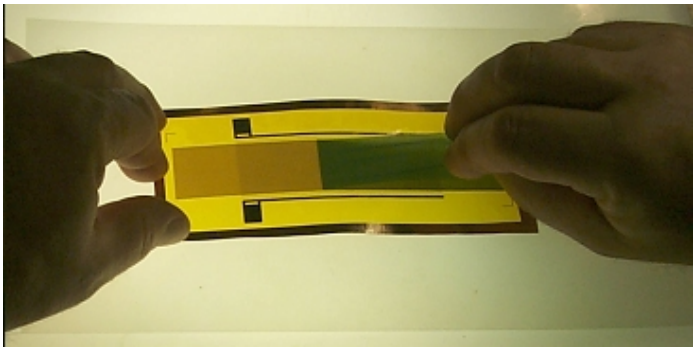

Figure C.8: Removal of Carrier Film

layers are bonded together over their entire surface areas. The only exception is the solder tabs, which should remain free of epoxy. Now, the top electrode layer is placed on top of the fibers such that copper-PZT contact is established and the electrodes are aligned with the interdigitated portion of the bottom layer, as seen in Figure C.9.

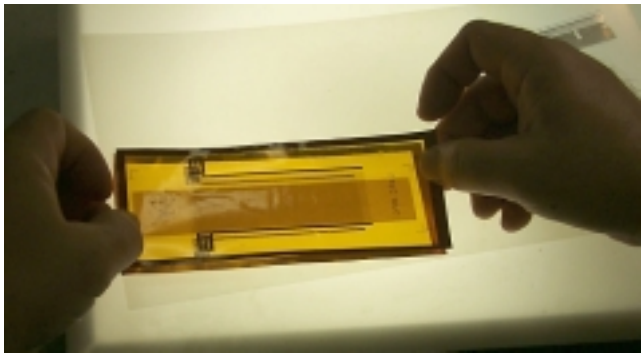

Figure C.9: Placement of Top Electrode Layer

C.3.4 Final Cure of the Epoxy:

Now, the entire MFC package is ready for the final curing process, so it is again placed into the hot-press book and returned to the vacuum hot-press, where the vacuum is applied for another 15-minute period. Then the platens are clamped down and heated as before, only this time the temperature is ramped up to 250 °F at the rate of 17.5 °F per minute and held for two hours. After water-cooling the platens to room temperature, the completed MFC lay-up is removed from the hot-press book. The detailed curing procedures used for the MFC are examined in more detail in Sections C.5.

C.4 Final Preparation:

At this time, all of the three main layers have been laminated together and the MFC is nearing completion. There may be some excess cured epoxy around the perimeter of the part which was expelled during the final cure procedure. If so, it should be removed at this time using a razor blade. Also, at this point, the laminate should be visually inspected to ensure that it is free from any air bubble voids or broken or misaligned PZT fibers. Defects of this type will typically cause electrical failure of the actuator during a later poling process and should be discarded at this point.

C.4.1 Electrical Connectivity between Electrodes:

At this time, the Kapton® can be removed from the slots in the solder tabs of the top electrode layer using a razor blade and an X-acto knife. First, the razor blade is used to cut around the perimeter of the slots, where care is taken to only cut through the top layer of Kapton. The X-acto knife is now used to dig out the Kapton and any remaining epoxy from the slots, as illustrated in Figure C.10.

Figure C.10: Removal of Kapton and Epoxy from Solder Tab Slots

It is recommended that the Kapton/epoxy be removed from all four slots under a microscope. Now, the previously tinned tab on the bottom electrode is exposed, and soldering flux is applied in the slots. Next, extra solder should be placed onto the heated tip of a soldering iron, which is then applied to all of the slots in an effort to melt

the solder on the bottom and top tabs together, thereby ensuring electrical connectivity between the top and bottom electrodes. Care should be taken to get the soldering iron close to the edges of the slots to ensure complete contact.

C.4.2 Final Shaping and Power Lead Attachment:

Next, the actuator is cut to its final shape using a paper cutter or a razor blade with metal forms to ensure straight cuts. Special care should be taken to not sever the solder tabs or to cut into the interdigitated electrode pattern. This final trimming step can be done before removing the Kapton and epoxy from the solder tab slots as detailed in section C.4.1, if desired.

Next, black and red leads are soldered to the tabs. Note that it is only necessary to attach one lead on each side, even though there are four slots. The red lead will indicate the electrical positive terminal, while the black side will be denoted the negative terminal for future electrical connections. A completed MFC actuator with attached leads is shown in Figure C.11.

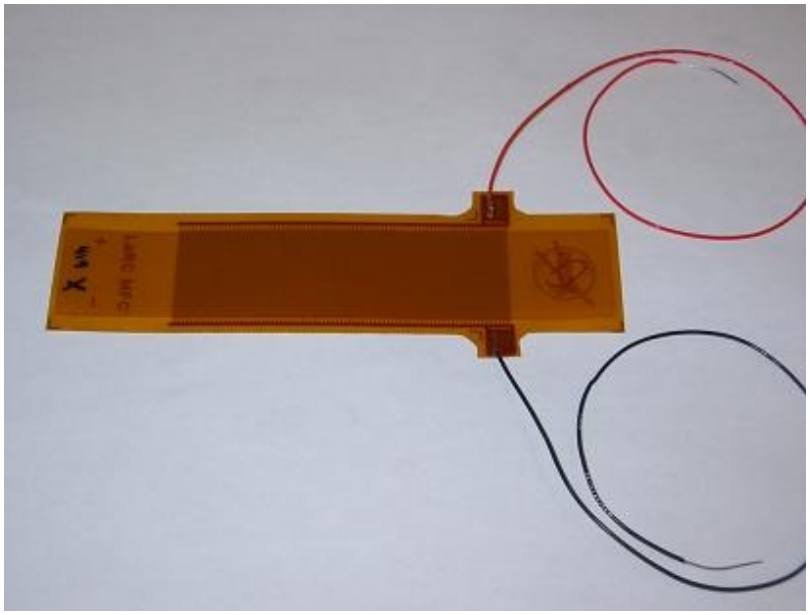

Figure C.11: Completely Assembled MFC Actuator with Leads

C.4.3 Poling and Electrical Inspection

The next step before poling is to assign the device a serial number and use a Hewlett Packard 4192 LF impedance analyzer to measure the capacitance, dissipation factor, impedance, inductance, phase angle, and quality factor of the actuator at 1000 hertz. The serial number and these electrical properties are then recorded in a MFC manufacturing log book. Next, the PZT fibers must be poled in order for the completely assembled MFC actuator to exhibit the desired piezoelectric behavior. Poling is performed by applying a high DC voltage to the actuator for five minutes at room temperature. The positive and negative leads of the actuator should be connected to the corresponding terminals on a high voltage amplifier. The voltage should be increased in one of two ways: if the poling voltage is controlled by hand, then it should be increased in steps of 100 volts, up to 1500 volts, with 15 second intervals between steps, of, if the poling process is computer-controlled, the voltage should be ramped up continually in a linear fashion from zero to 1500 volts over a ninety second time-span. In either case, the voltage is held constant at 1500 volts for five minutes, and then either returned to zero in one step manually, or ramped back down to zero over 90 seconds by the computer.

If there were problems during the manufacturing, such as air bubble voids or particulate contaminates in the laminate, there will typically be an electrical failure at some point during this poling process. The failure will be caused by a short-circuit between adjacent electrode fingers, which will cause the Kapton to burn, blister, and smoke, and will be accompanied by loud popping sounds. The applied voltage should be removed immediately, and the actuator discarded for safety and performance reasons.

After poling is complete, the leads should be shorted together for several seconds to dissipate any remnant charge in the actuator. Finally, after poling, the same electrical properties are measured again and recorded in the log book. At this point in time, the

manufacturing of the MFC actuator is complete, and, assuming no electrical failures were encountered during poling, the device will be fully functional.

C.5 Summary:

Appendix A discusses the acquisition of the layers that make up the MFC actuator, the assembly process for these layers, and subsequent poling of the device to obtain the desired strong piezoelectric behavior. The complete documentation of these procedures led to a NASA Technical Memorandum [High and Wilkie, 2003].

C.6 References:

1. High, J. W. and Wilkie, W. K., "Method of Fabricating NASA-Standard Macro-Fiber Composite Piezoelectric Actuators," NASA/TM-2003-212427,ARL-TR-2833, June 2003.

2. DuPont Films, "Flexible Circuit Materials: Pyralux LF Copper-Clad Laminates," Bulletin H-73244, 1999.

Appendix D

Epoxy Cure Kinetics Modeling

D.1 Introduction:

In addition to completely documenting the manufacturing procedure for the MFC, another initial research goal was to evaluate the current manufacturing process, in a scientific manner, and to identify the potential for cycle-time reductions if the MFC is to be produced in commercial quantities. Thus, Appendix B uses heat-flow experiments in a differential scanning calorimeter to develop a cure kinetics model for the epoxy resin system used with the MFC. This model depicts how the epoxy cures as a function of time and temperature, and is subsequently used to identify potential cure cycle time reductions in the current procedures used to manufacture the MFC.

D.2 Background on Cure Kinetics Modeling:

This appendix deals with cure kinetics modeling of the epoxy matrix used with the MFC actuator. This epoxy serves three vital roles in this actuator, namely, surrounding and protecting the PZT fibers, transferring the induced strain from the fibers to the

structure, and holding the entire actuator package together. Therefore, its proper processing is essential to ensuring high quality, uniform actuators. Little was known about processing of the Loctite E-120 HP resin system used with the MFC, other than a "rule of thumb" cure cycle specified by the manufacturer. Therefore, the current work includes a characterization of this epoxy using techniques developed in previous works.

The foundation for cure kinetics modeling was presented by Loos and Springer [1983]. Here, the definition of the degree of cure and rate of cure were defined and related through a simple temporal integration. Then, experiments in a differential scanning calorimeter were performed and the analysis required to produce rate of cure and degree of cure versus time plots from the data was presented. Formulations to describe the cure kinetic behavior for various types of cure reactions were proposed, and the experimental data were employed to obtain the various empirical parameters. The resulting equation predicted the degree of cure of the epoxy as a function of time and cure temperature. Also, they derived similar resin viscosity models and developed computer programs to simulate the curing and compaction of various composites.

Grimsley et al. [2001] used these techniques to characterize SI-ZG-5A epoxy for application in the vacuum assisted resin transfer molding (VARTM) process, where a typical carbon fiber preform was impregnated with epoxy. Process simulations were carried out using the process model COMPRO© to examine heat transfer and curing kinetics for a fully impregnated panel, neglecting resin flow. The predicted viscosity profile and final degree of cure were found to be in good agreement with experimental observations.

In an extension of the previously mentioned work, the cure kinetics and viscosity of two resins, an amine-cured epoxy system, Applied Poleramic, Inc. VR-56-4 , and an anhydride-cured epoxy system, A.T.A.R.D. Laboratories SI-ZG-5A, were characterized for application in the VARTM process [Grimsley et al., 2002]. Again, process

simulations were carried out using COMPRO to examine heat transfer, cure kinetics and viscosity for different panel thicknesses and cure cycles. The results of these simulations indicated that the two resins, each cured by a different chemical reaction, had significantly different curing behaviors and flow characteristics.

D.3 Cure Kinetics Modeling:

While the current MFC manufacturing procedure is reliable and produces actuators with consistent electromechanical properties, it is time consuming with both value-added steps as well as time spent in the hot-press. If the MFC were to be produced commercially, one would want to minimize this cycle time. Thus the main objective of modeling the epoxy cure kinetics is to ensure that the current time-temperature profiles produce a fully cured actuator in the shortest amount of time possible. This section will first develop a cure kinetics model, and then use experimental data to obtain the necessary curve-fitting parameters. The model is then used to evaluate the current pre-cure and final cure steps and then time saving alternative final cure cycles are examined analytically.

D.3.1 Analytical Model:

The models and experiments discussed in this section are developed following the methodology proposed by Loos and Springer [1983], and used extensively by Grimsley et al. [2001] and Grimsley et al. [2002]. The degree of cure of an epoxy system, α, is defined as

$$\alpha = \frac{H(t)}{H_R} \tag{D.1}$$

where $H(t)$ is the heat evolved from the beginning of the reaction (mixing the resin and hardener) to some intermediate point in time, t, and H_R is the ultimate or total heat of reaction during cure. Clearly, at the beginning of the reaction, α is equal to zero and

increases asymptotically towards unity as the resin approaches the fully cured state. If Equation D.1 is solved for *H(t)* and differentiated with respect to time, the rate of heat generation is seen to be proportional to the rate of the cure reaction:

$$\frac{d\,H(t)}{dt} = \frac{d\alpha}{dt} H_R \tag{D.2}$$

where $d\alpha/dt$ is called the rate of cure. For thermosetting resins, the rate of cure depends on the temperature and the degree of cure, and various resin systems exhibit different types of cure rate behavior. Thus, the rate of cure for a given epoxy is expressed as

$$\frac{d\alpha}{dt} = f(T,\alpha) \tag{D.3}$$

If the diffusion of chemical species is neglected, then Equation D.3 can be integrated to determine the degree of cure at any point in time:

$$\alpha = \int_0^t \left(\frac{d\alpha}{dt} \right) dt \tag{D.4}$$

D.3.2 Differential Scanning Calorimeter Experiments

The functional relationship in Equation D.3 and the degree of cure of the LOCTITE DURABOND E-120HP used for the MFC are now determined experimentally using a differential scanning calorimeter (DSC), and then an empirical model is developed to represent the collected data. The first step in all of the experimental procedures was to mix a batch of the resin and hardener in the ratio specified by the manufacturer, place a small sample into an aluminum pan and then weigh the epoxy. The next step was to determine H_R, which is simply the total heat given off by the epoxy as it completely

cures. This measurement was made by performing dynamic scans on epoxy samples using a Shimadzu DSC-50 differential scanning calorimeter at NASA Langley. During a dynamic scan, the DSC increases the temperature of the epoxy at a specified rate and measures the amount of generated heat as a function of time and temperature. For LOCTITE DURABOND E-120HP, two dynamic scans were performed, one at 1.1°C per minute and the other at 5.0 °C per minute; the latter of which is seen in Figure D.1.

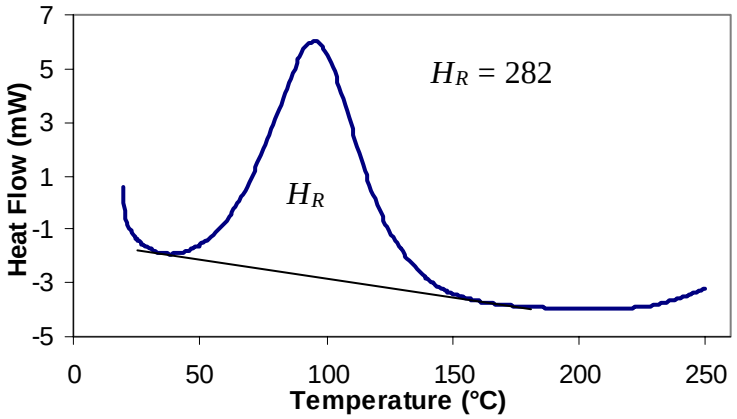

Figure D.1: Dynamic Scan of LOCTITE DURABOND E-120HP Epoxy Resin

H_R was determined by measuring the area under the exothermal peak of the dynamic scan, as illustrated in Figure D.1. While measuring the exact area is somewhat arbitrary, the DSC software performed this calculation automatically. Since the total heat generated by a certain epoxy during its cure does not depend on the heating rate, the H_R values measured for the two scans were similar, thus the average value of 282 J/g was used for subsequent analysis.

Next, isothermal scans were conducted on the epoxy to establish how the curing progresses at a certain temperature. Isothermal scans involve heating the DSC to the desired temperature, inserting the sample and holding at that temperature for a specified amount of time. Again, the heat generated by the reaction is measured along with the time and temperature. After the isothermal hold is complete, the sample was

removed from the test chamber, which essentially stopped the curing reaction. After reconfiguring the lab software, the sample was reinserted into the DSC and another dynamic scan was performed at the heating rate of 5.0 °C per minute to measure the residual heat of reaction. Ideally, there will be little or no residual heat when compared to H_R, as a large amount indicates that the epoxy did not cure sufficiently for the particular isothermal hold time.

For the resin system of interest to the MFC, five such isothermal scans were performed, each followed by a dynamic scan to measure the residual heat. A typical isothermal scan is seen in Figure D.2, while the parameters for these five tests are presented in Table D.1.

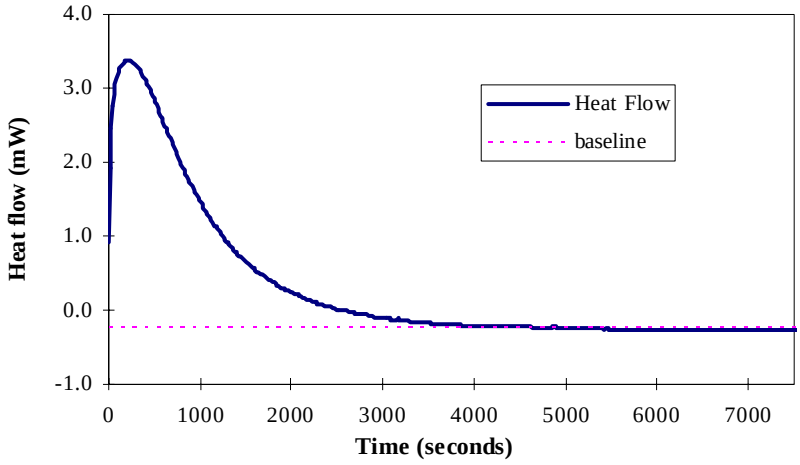

Figure D.2: Isothermal Scan of LOCTITE DURABOND E-120HP Epoxy at 80 °C

Table D.1: Isothermal Scan Parameters for LOCTITE DURABOND E-120HP

Temperature, °C	Sample Mass, mg	Hold time, hours	Residual Heat, J/g
50	18.1	14	72
60	12.7	8	22.5
80	15.1	3	15
100	12.2	3	0
120	18.7	2	0

The resulting data consists of three columns, namely time, temperature and heat flow ($\dot{q}_{in}$). The evolved heat from the reaction, *H(t)*, is the area under the heat flow curve and above the baseline ($\dot{q}_{baseline}$). The baseline value is calculated such that the residual heat plus the heat generated during the isothermal hold is equal to H_R. With this information in hand, the cure rate was calculated at each point in time as:

$$\frac{d\alpha}{dt} = \frac{\left(\dot{q}_{baseline} - \dot{q}_{in}\right)/ m_{sample}}{H_R /\left(1-\alpha_0\right)} \tag{D.5}$$

where the initial degree of cure, α_0, is assumed to be 0.01. Next, the degree of cure of the epoxy at each point in time is found by numerically integrating this expression according to Equation D.4. The resulting experimental curves for cure rate and degree of cure as a function of time are plotted in Figure D.3 for the 80°C isothermal scan.

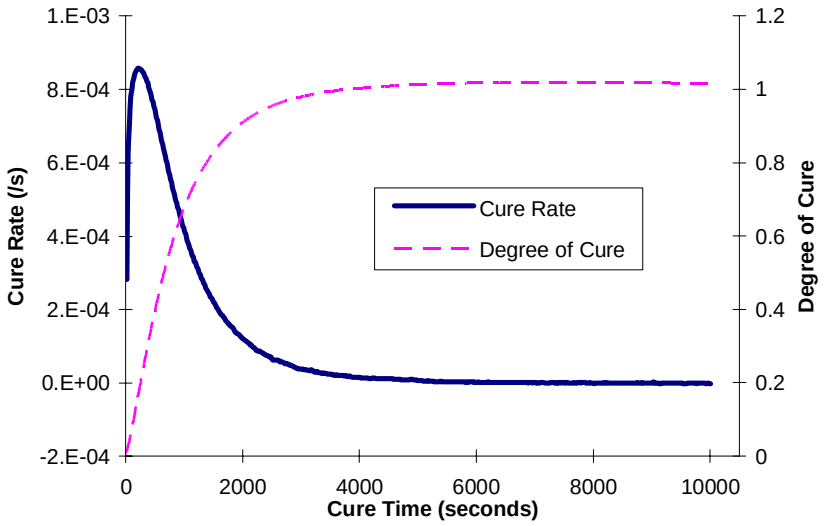

Figure D.3: Cure Rate and Degree of Cure versus Time at 80°C

D.3.3 Empirical Model

Each of the isothermal scans produces a plot similar to that seen in Figure D.3. However, rather than performing an experiment for every cure temperature of interest,

an empirical equation is proposed that relates the cure rate to the cure temperature and degree of cure, as in Equation D.3. The form of this equation varies from one resin system to the next, but a plot of cure rate versus degree of cure is used to indicate which type of equation to use. Figure D.4 shows such a plot for the 80°C isothermal cure.

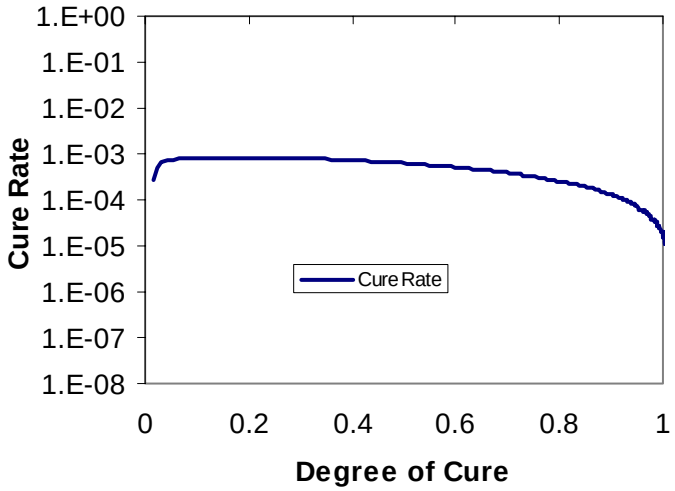

Figure D.4: Cure Rate versus Degree of Cure at 80°C

From the upside-down "U" shape see in Figure D.4, it is reasonable to conclude that this resin is autocatalytic, thus the governing expression for the cure rate is given as

$$\frac{d\alpha}{dt} = K\alpha^m(1-\alpha)^n \tag{D.6}$$

where m and n are kinetic exponents and K is a temperature-dependent rate constant:

$$K = Ae^{\frac{-E}{RT}} \tag{D.7}$$

Here, A is an Arrhenius pre-exponential factor, E is the Arrhenius activation energy, R is the universal gas constant and T is the absolute temperature in Kelvin. The constants

A, *E*, *m* and *n* are properties that correspond to a particular resin system and were determined empirically from the isothermal data for LOCTITE DURABOND E-120HP. While a nonlinear curve-fitting program can be used to iteratively solve Equation D.6 for the unknown parameters, it was much simpler to first determine *E* and then adjust the remaining values by hand to develop a reasonable curve fit.

E is determined from Figure D.5, which shows a plot of the natural logarithm of the cure rate as a function of the inverse of the absolute temperature. For each isothermal cure temperature, there are three points corresponding to degrees of cure 0.1, 0.2 and 0.3. The activation energy *E* is obtained by multiplying the slope of the linear curve fit to these data points by the negative of the universal gas constant, *–R*.

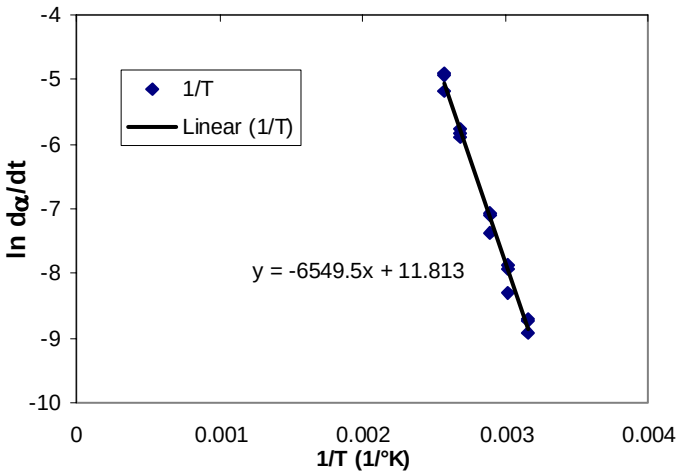

Figure D.5: $\ln\left(\frac{d\alpha}{dt}\right) vs \frac{1}{T}$ for LOCTITE DURABOND E-120HP

The remaining constants *m*, *n*, and A_2 were adjusted manually until the cure rate as a function of degree of cure from Equation D.6 closely matched the corresponding experimental data at each of the five isothermal cure temperatures. This procedure was relatively simple, as the exact value of these parameters does not vary greatly from one resin to the next. Either experience or a careful examination of Equation D.6 shows that,

in general, A determines the vertical position of the curves, m determines the slope at low values of α, and n controls the drop-off at high values of α. Table D.2 provides the determined values for the various constants used in this model.

Table D.2: Cure Kinetics Constants for of DURABOND E-120HP

Property	Value
H_R	282 J/g
E	54453 J/g mole
A	300,000 s^{-1}
m	0.275
n	1.15

The accuracy of the empirical model was assessed by plotting Equation D.6 using the parameters from Table D.2 for the five isothermal hold temperatures (average value of each temperature set obtained from the experimental data). These five curves are shown in Figure D.6, along with the experimental dada which they represent. The empirical model is seen to closely match the data over the entire range of α for each isothermal hold temperature.

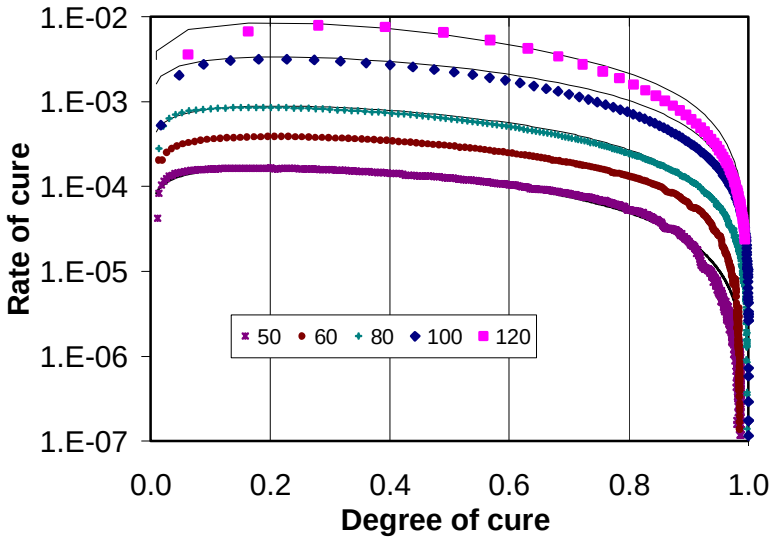

Figure D.6: Comparison of Experimental Data and Cure Kinetics Model - Cure Rate versus Degree of Cure

A plot of the degree of cure as a function of time was produced by numerically integrating Equation D.6 as specified in Equation D.4. Figure D.7 compares these results to the experimental data and finds the two to match closely.

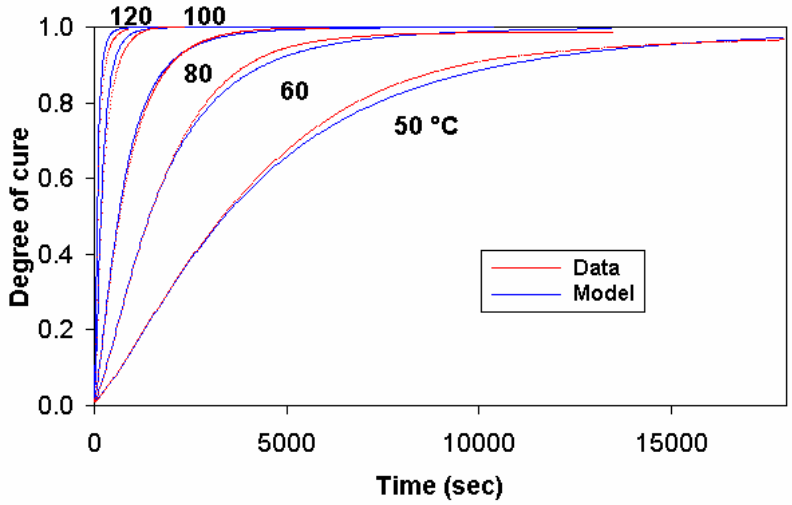

Figure D.7: Degree of Cure as a Function of Time

Since the empirical model has been found to accurately predict the degree of cure at various temperatures, it will be used in the following section to evaluate the suitability of the current MFC cure cycles. Furthermore, the cure kinetics model was applied to other isothermal temperatures to assess how alternate cycles could shorten MFC manufacturing times.

D.4 Analysis of Current Cure Cycles

The cure kinetics model developed above is now used to analyze the current cure cycles used in MFC manufacturing.

D.4.1 Pre-Cure of the Epoxy

As discussed in the manufacturing sections above, the pre-cure is currently done for 15 minutes at 50°C, which, using the model developed earlier, results in α equal to 0.134. However if the temperature of the pre-cure was to be increased, the hold time could be

shortened. Using this cure kinetics model, Table D.3 was constructed showing the hold times that would result in an equivalently pre-cured epoxy.

Table D.3: Hold Times at Elevated Temperature Required to Cure DURABOND E-120HP to a Degree of Cure of 0.134

Pre-Cure to $\alpha = 0.134$	
Temperature, °C	Cure Time, min.
50	16
60	6.5
80	2.75

Of course, if higher temperatures were used, the time could be shortened further, however, shorter cure times would have to be closely monitored to prevent over-curing. It is critical not to over-cure the epoxy at this stage for several reasons. First, the epoxy should only be sticky enough to adhere the fibers to the bottom electrode sheet, but not too tacky to prevent removal of the blue carrier film. Also, the epoxy must be uncured enough to allow it to fully co-cure with the second application of epoxy. Lastly, if the epoxy becomes too stiff, voids will be unable to escape under the vacuum pressure applied by the hot-press, thus resulting in short circuits when the PZT material is later poled.

D.4.2 Final Cure of the Epoxy:

In theory, an epoxy is said to be fully cured when α is equal to one. However, in practice, α only approaches unity asymptotically, thus never reaching a value of unity exactly. Typically, a decision must be made as to what value of α constitutes "fully cured." Any value around 0.95 to 0.99 is normally considered "sufficiently cured." The final cure cycle currently used involved a two hour hold at 120°C. Based on calculations using the cure kinetics model, this cures the epoxy extremely close to α equal to one (0.9999998). However, at this temperature, the epoxy could be cured to α

equal to 0.999 in around 16 minutes. Table D.4 shows the times required to reach other higher degrees of cure.

Table D.4: Acceptable Degrees of Cure and Required Hold Time at 120°C

Cure at 120°C	
α	Cure time, min
0.999	16
0.9999	27.5
0.99999	47
0.999999	78
0.9999999	126

Clearly, there is room to significantly reduce the cycle time required to manufacture MFC actuators. However, further experimentation would be required to make such changes. Particularly, exposing the epoxy to longer holds at elevated temperatures yields an increase in strength and glass transition temperature. Initial experimentation has shown the electrical properties, such as capacitance and impedance to also depend somewhat on the cure time. Also, the cure temperature could be increased, and an acceptable level of cure could be attained even faster, as predicted by the cure kinetics model developed in this paper. However, such changes would require stringent time and temperature monitoring to prevent burning the cured epoxy.

D.5 Summary:

In addition, experimental data were used to develop a cure kinetics model for the LOCTITE DURABOND E-120HP epoxy used to assemble the MFC. Using this model, it was shown that there is a potential to reduce cycle-times by altering the hot-press cure cycles for the pre- and final cures. However, additional experiments to determine the effects of such changes on the mechanical and electrical properties would have to be performed first. Experiments of this type are beyond the scope of the current effort, nevertheless, there is potential to improve the current MFC manufacturing procedure.

D.6 References:

1. Grimsley, C. W., Hubert, P., Hou, T. H., Cano, R. J., Loos, A. C. and Pipes, R. C., 2001, "*Matrix Characterization and Development for the Vacuum Assisted Resin Transfer Molding Process*," American Society for Composites Technical Conference, Vol. 16, CD 221.

2. Grimsley, C. W., Hubert, P., Song, X., Cano, R. J., Loos, A. C. and Pipes, R. C., 2002, "*Effects of Amine and Anhydride Curing Agents on the VARTM Matrix Processing Properties*," International SAMPE Symposium, Vol. 47.

3. Loos, A. C. and Springer, G. S., 1983, "Curing of Epoxy Matrix Composites," *Journal of Composite Materials*, Vol. 17, March.

Appendix E

Temperature and Electric Field Dependent Elastic Properties of the Macro Fiber Composite

E.1 Introduction:

Chapter 2 develops a linear model for the short-circuit mechanical behavior of the Macro Fiber Composite (MFC) under isothermal conditions. However, the MFC actuator is designed for use in aerospace structures such as helicopter rotor blades, fighter jet tailfins, morphing wings and telecommunication satellites. Each of these applications could subject the actuators to extremely wide temperature ranges where thermoelastic behavior of the actuator could become significant. Although the intended purpose of the MFC is actuation through applied voltage, this research effort deals only with the constant-field (short-circuit) thermoelastic properties while developing equations for the elastic and thermal expansion (CTE) coefficients of the MFC as a function of temperature. Pyroelectric effects are also assumed small and therefore neglected. The temperature range of interest is from 0° to 250°C, and the analytical results are verified using the ANSYS finite element software. The required temperature-dependent thermoelastic properties of each constituent material were

obtained, and, for the orthotropic layers, the coefficients of thermal expansion were calculated using a variety of micromechanics models obtained from the literature. The alternative rule of mixtures formula was selected as the most accurate based on a comparison with ANSYS finite element models. With the temperature-dependent properties known for each layer, equations for the two coefficients of thermal expansion of the entire actuator were derived using the classical lamination approach from Chapter 2. These results were seen to agree reasonably well with an ANSYS finite element model of the unit cell of the Macro Fiber Composite actuator.

Towards the end of this appendix, the dependence of E_x of the MFC on various nonzero constant electric fields is investigated through a short set of experiments. These tests involved inserting a reference MFC tensile-test specimen into the hydraulically controlled tensile testing machine, and then applying a constant voltage to the interdigitated electrodes. The specimen is then tensile tested within the linear region with a very low frequency sinusoidal load about various mean load levels. The results showed that E_x does not vary a great deal with electric field, thus further experimentation was not performed to assess the field-dependence of the other parameters.

E.2 Background on Thermal Expansion Coefficients of Composite Materials:

Since this appendix deals with the thermoelastic behavior of the MFC under short-circuit boundary conditions, it is important to review the relevant literature utilized in the current investigation. In addition to being a valuable resource for the mechanics of fiber-reinforced composites in general, texts by Hyer [1998] and Jones [1999] have examples that deal with the thermoelastic behavior of composites. Since the MFC is a symmetric, cross-ply laminate, it has two independent coefficients of thermal expansion (CTE), one parallel and one perpendicular to the PZT fibers. Analytical means to predict these values are of particular interest herein.

Wetherhold and Boss [1988] derived a simple expression for the thermal expansion coefficient perpendicular to the plane of a symmetric composite laminate. They proved that the dominant term in this expression did not change with lamination angle orientation. Furthermore, they showed that the dominance of this term leads to simple design boundaries for laminates with unusual out-of-plane expansion properties.

In their paper, Bowles and Tompkins [1989] presented expressions derived by Shapery, Chamberlin, Chamis, and Rosen-Hashin for the two thermal expansion coefficients of a unidirectional lamina. A finite element analysis was also employed, which was predicated upon a state of generalized plain strain existing in the unidirectional composite. The coefficients of thermal expansion were then measured experimentally for various continuous fiber-reinforced composite materials consisting of graphite fibers embedded in epoxy, metal or ceramic matrices. As expected, each of the analytical methods was in close agreement with measured values of the coefficient of thermal expansion parallel to the fibers over a wide range of fiber volume fractions. However, some formulations produced inaccurate results for the thermal expansion coefficient perpendicular to the fibers. The models that accounted for Poisson constraining effects in this transverse direction, namely finite element, Rosen and Hashin, and Shapery, produced more accurate results. Lastly, a sensitivity analysis showed that the largest change in the coefficient of thermal expansion of the lamina in the fiber direction was due to changes in the CTE of the fiber, while the CTE perpendicular to the fibers was most sensitive to changes in the CTE and modulus of the matrix material.

Islam, Sjolind and Pramila [2001] used a finite element analysis to predict the CTEs of unidirectional composites with both perfect bonding and interfacial cracks at the fiber-matrix interface. Accuracy of the FEA method was established by comparing results for the perfect bonding condition with available experimental and analytical values. Then interfacial cracks were introduced between the fiber and the matrix. Several cases were run, each having the crack length extending a different amount around the

circumference of the fiber. It was found that, in particular, the transverse coefficient of thermal expansion was affected a great deal by the presence of such debondings, as was the orientation of principal direction of transverse thermal expansion changes.

In another work dealing with damaged fiber-reinforced composites, Kim, Crasto, and Schoeppner [2000] measured changes in the thermal expansion coefficients (CTE) of cross-ply laminates due to cracks in the transverse plies caused by both thermal cycling and mechanical loading. The results were seen to agree closely with a 2-D variational model as well as an exact 3-D laminate theory. This work showed the ability of traditional laminated plate theory to handle more complex scenarios stemming from variations in material properties that are oftentimes considered constant.

Yoon and Kim [2000] measured and characterized the temperature-dependent coefficients of thermal expansion and elastic properties of unidirectional laminae in the principal material directions from room temperature up to the cure temperature. The characterized properties were used with classical lamination theory to predict the coefficients of thermal expansion for a general laminate as a function of temperature. Experiments were performed on various angle ply laminates over the specified temperature to measure the change in CTEs. The data and model were in good agreement, and, again, the use of classical lamination theory was found to produce accurate results when used represent complex behavior where material properties do not remain constant.

The impact of such changes in material properties was demonstrated in a follow up to the above work [Yoon and Kim, 2001], where the model prescribing the change in CTEs of a general laminate was combined with a model of chemical shrinkage of the epoxy matrix during curing and used to predict the distortion of a curved laminate. The spring-forward angles of an L-section laminate with various angle-ply orientations were measured and found to match the predicted values reasonably well. Furthermore, it

was noted that *both* the change in thermal expansion coefficients and the chemical shrinkage strains contribute to the change in angle of the L-section.

E.3 Thermal Modeling:

In this section, the required temperature-dependent material properties are obtained, and then the behavior of the orthotropic layers is investigated using ANSYS finite element analyses. Then, the temperature-dependent behavior of the MFC is predicted by combining the layer-wise material properties in a manner similar to the classical lamination model from Chapter 2.

E.3.1 Constituent Material Properties:

The first step in the current analysis is to obtain all of the required thermoelastic properties as a function of temperature for each of the five constituent materials, namely Kapton, acrylic, copper, epoxy (all isotropic) and PZT (transversely isotropic). These values were obtained from manufacturers (DuPont GS-96-7 and Morgan Matroc), when available, or from materials handbooks (MatWeb) or other research institutions (NASA, Georgia Tech Mechanical Properties Research Lab, and Yoon and Kim 2000). Each property (elastic moduli and CTE) was represented as an algebraic, temperature-dependent equation (Poisson's ratio was assumed constant with temperature). The figures below show the temperature-dependent behavior of the various constituent materials of the MFC. Figure E.1 shows the CTEs of the constituent materials as a function of temperature. The polymer materials exhibit step-changes in this property at their glass transition temperature, and were represented as such mathematically. However the metallic copper has the linear relationship specified in the figure. Figure E.2 shows the CTE behavior of the transversely isotropic poled PZT fibers, which are poled in the 3-direction. It should be noted that these data are for temperature-stabilized PZT, which means that they have been heated above 250°C at least one time in the past, but after poling. Also of interest is the fact that the transverse CTE for the PZT becomes negative at high temperatures. The regression equations used to

represent these data are color-coded in the figure. Next, Figure E.3 depicts the temperature-dependent moduli for the four isotropic materials. From the literature, they each decrease by a give amount over the temperature range of interest, and the regression equations used for the classical model are also color-coded on the plot.

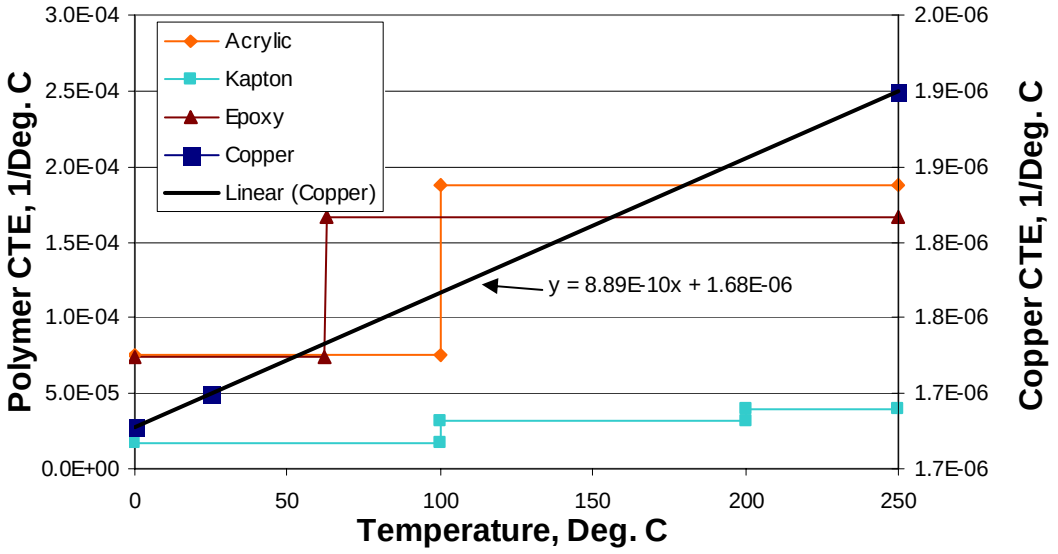

Figure E.1: Temperature-Dependent CTE for Isotropic Materials

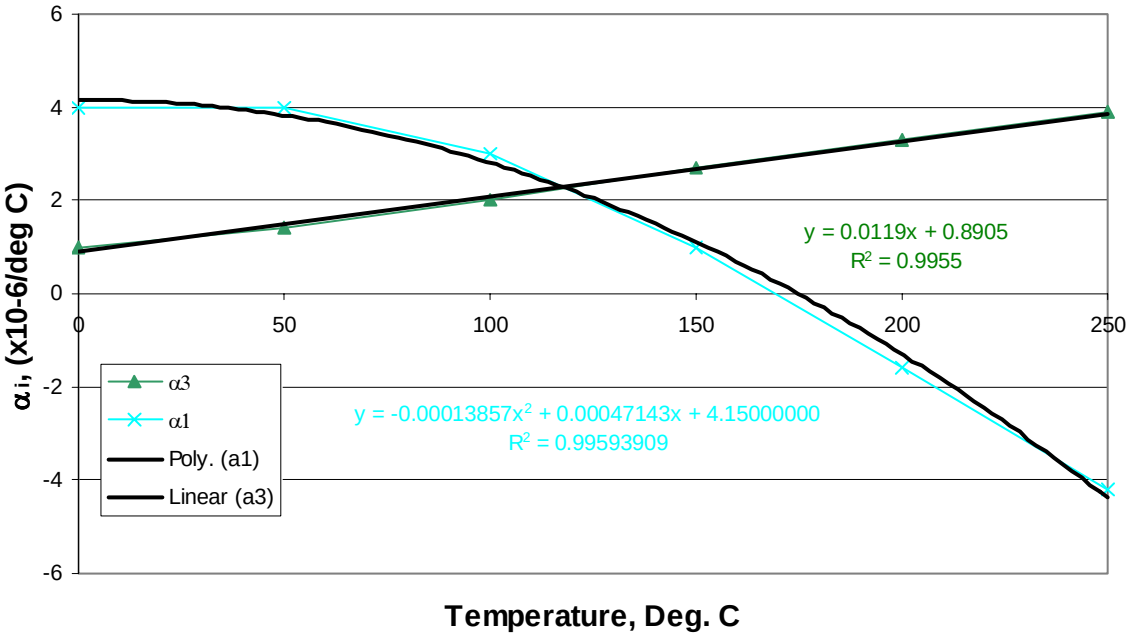

Figure E.2: Temperature-Dependent CTE for Trans. Isotropic PZT (poled in 3-direction)

Lastly, Figure E.4 shows the elastic properties of the PZT material as a function of temperature, again, where the ceramic is poled in the 3-direction.

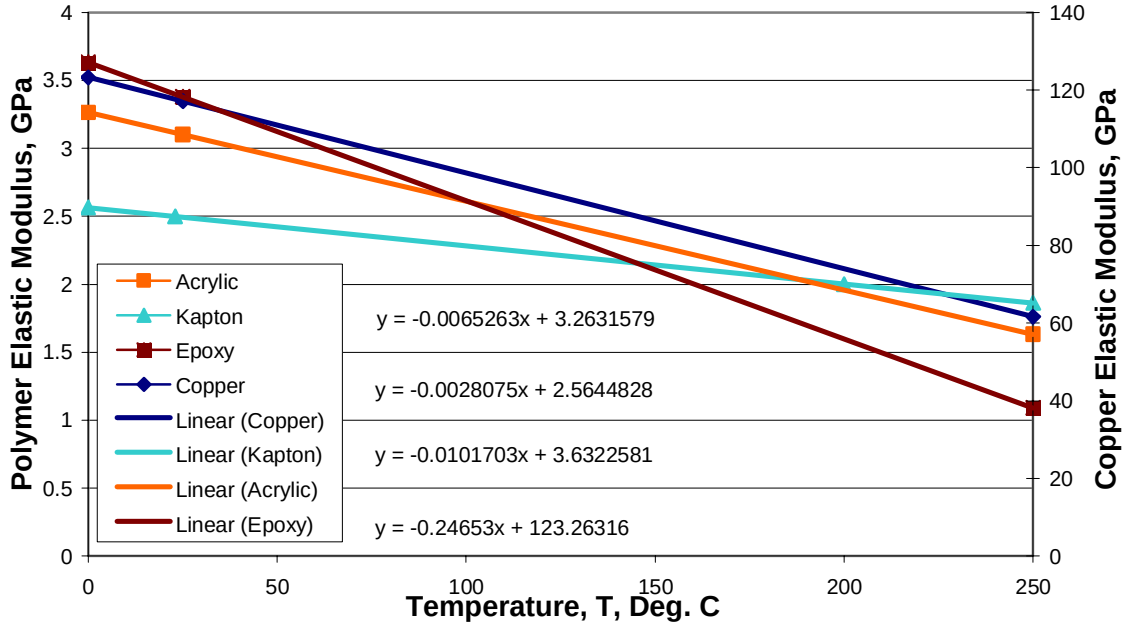

Figure E.3: Temperature-Dependent Moduli for Isotropic Materials

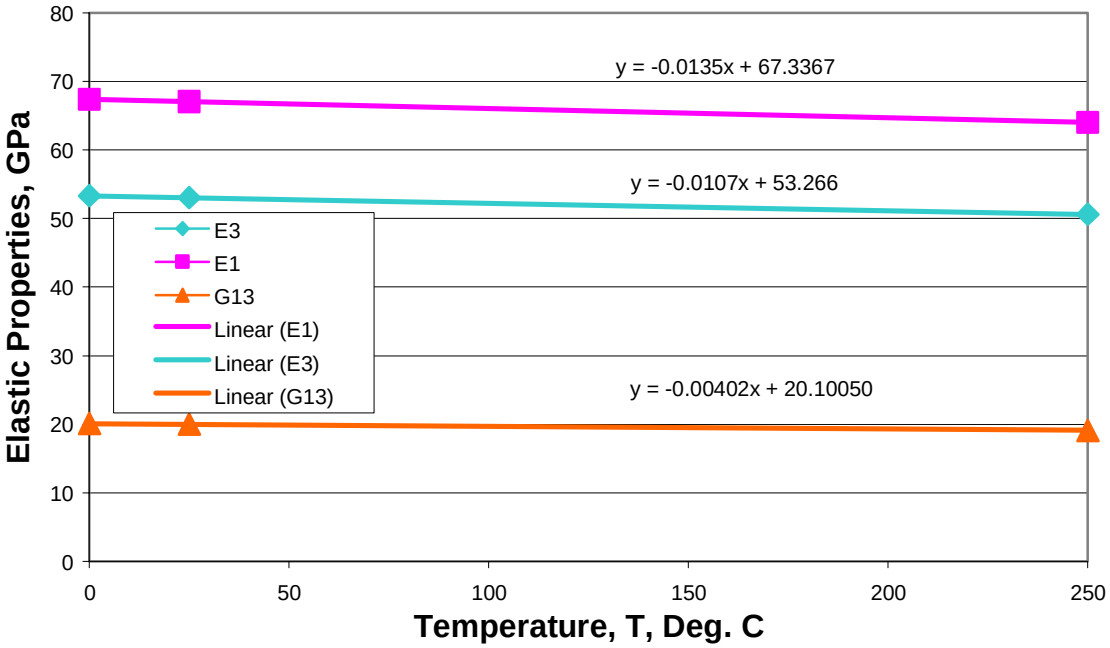

Figure E.4: Temperature-Dependent Moduli for Trans. Isotropic PZT

E.3.2 Orthotropic Layers:

Figure E.5 shows the four basic layers that comprise the MFC actuator and the geometric Cartesian coordinate system used in the forthcoming analysis.

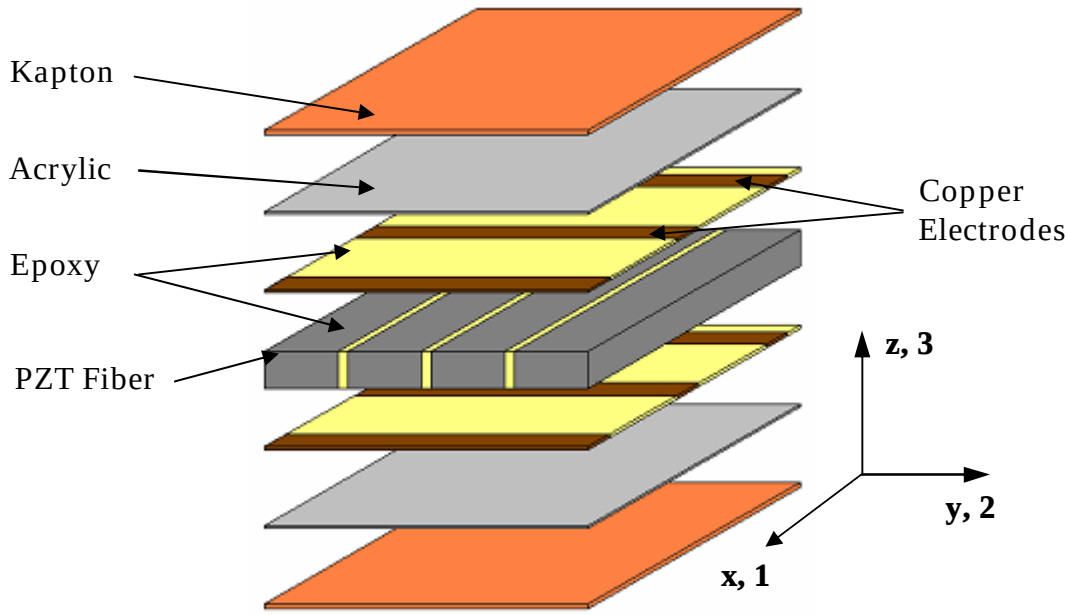

Figure E.5: Layers of the MFC actuator

For the Kapton and acrylic, the isotropic material properties depicted above in Figures E.1 and E.3 and the geometric properties listed in Table E.1 are sufficient to describe the behavior of their respective layers. However, the thermoelastic properties of the orthotropic copper/epoxy and PZT/epoxy laminae must be determined using a micromechanics approach. The fiber-direction modulus, E_1, for these layers, is calculated from the rule-of-mixtures formula

$$E_1 = \mathrm{V}_f E_f^1 + \mathrm{V}_m E_m \tag{E.1}$$

where E_m is the elastic modulus of the matrix and E_f^1 is the elastic modulus of the fiber in the 1-direction. Now the major Poisson's ratio for each orthotropic layer, ν_{12}, is calculated as

Table E.1: MFC Laminae Geometric Properties for Thermal Analysis

Property	Value
Kapton Thickness, mm (in.)	25.40 (0.001)
Acrylic Thickness, mm (in.)	12.70 (0.0005)
Copper Thickness, mm (in.)	17.78 (0.0007)
PZT Thickness, mm (in.)	127.00 (0.005)
PZT Fiber Width, mm (in.)	355.60 (0.014)
PZT Fiber Kerf, mm (in.)	76.20 (0.003)
Copper Fiber Width, mm (in.)	101.60 (0.004)
Copper Fiber Kerf, mm (in.)	431.80 (0.017)
PZT Fiber Volume Fraction	0.824
Copper Fiber Volume Fraction	0.190

$$\nu_{12} = \mathrm{V}_f \nu_f^{12} + \mathrm{V}_m \nu_m \tag{E.2}$$

where ν_f^{12} is the Poisson's ratio of the transversely isotropic PZT fiber relating strains induced in the 2-directions to those applied in the 1-direction of the fiber. The rule-of-mixtures formula gives the CTE of the orthotropic layers in the fiber direction, α_1, as

$$\alpha_1 = \frac{\left(\alpha_f^1 E_f^1 - \alpha_m E_m\right) V_f + \alpha_m E_m}{\left(E_f^1 - E_m\right) V_f + E_m} \tag{E.3}$$

Here, E is the elastic modulus, V represents the volume fraction, subscript f and m denote fiber and matrix properties, respectively and the superscript 1 denotes the fiber direction. The suitability of Equation E.3 is shown in Figure E.6, where the calculated curve is compared with ANSYS finite element results.

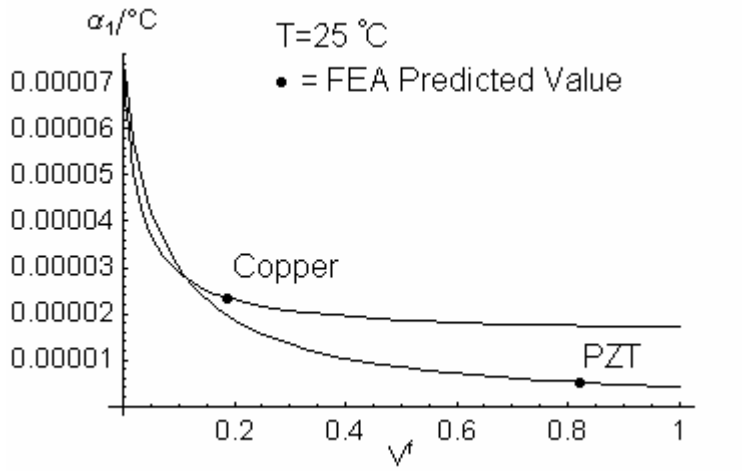

Figure E.6: Rule-of-Mixture Formulation for α_1 of Orthotropic Laminae

The transverse elastic properties are also obtained from rule-of-mixtures formulations, which were found to work well for a single row of evenly spaced rectangular cross-section fibers in Chapters 2 and 3. Hence, the modulus of the lamina transverse to the fibers, E_2, is

$$E_2 = \frac{E_f^2 E_m}{V_m E_f^2 + V_f E_m} \tag{E.4}$$

where E_f^2 is the modulus of the fiber in the 2-direction. Also, the in-plane shear modulus, G_{12}, is

$$G_{12} = \frac{G_f^{12} G_m}{V_m G_f^{12} + V_f G_m} \tag{E.5}$$

where G_f^{12} is the shear modulus in the 1-2 plane of the of the fiber. However, the transverse CTE of an orthotropic layer is more difficult to predict. Therefore, several micromechanics models were applied to the MFC, including the rule of mixtures, alternative rule of mixtures, Chamis, Shapery and modified strip (Hyer, 1999 and

Bowles and Tompkins, 1989). A large number of formulas were considered as some are more accurate at higher or lower fiber volume fractions, and, for the MFC geometry, the copper/epoxy layer has a low V^f, while the PZT/epoxy layer has a high V^f. The results of each equation were compared to an ANSYS finite element model of each orthotropic layer, and the alternative rule of mixtures formula was adopted as it provided the most accurate values. Therefore, for the remainder of the current analysis, the CTE in the transverse direction of an orthotropic lamina, α_2, will be taken as

$$\alpha_2 = \alpha^m + \left(\alpha_2^f - \alpha^m\right)V^f + \left(\frac{E_1^f \nu^m - E^m \nu_1^f}{E_1}\right)\left(\alpha^m - \alpha_1^f\right)\left(1 - V^f\right)V^f \tag{E.6}$$

Here, the notation is the same as before, with ν denoting Poisson's ratio and this model is seen to compare most favorably with the ANSYS results in Figures E.7 and E.8. In the former, the FEA predicts the CTE for the high volume fraction of PZT to be closest to the Alternative Rule of Mixtures or Shapery formulae, while the latter has an identical curve for these two models. In any event, the suitability of Equation E.6 is established.

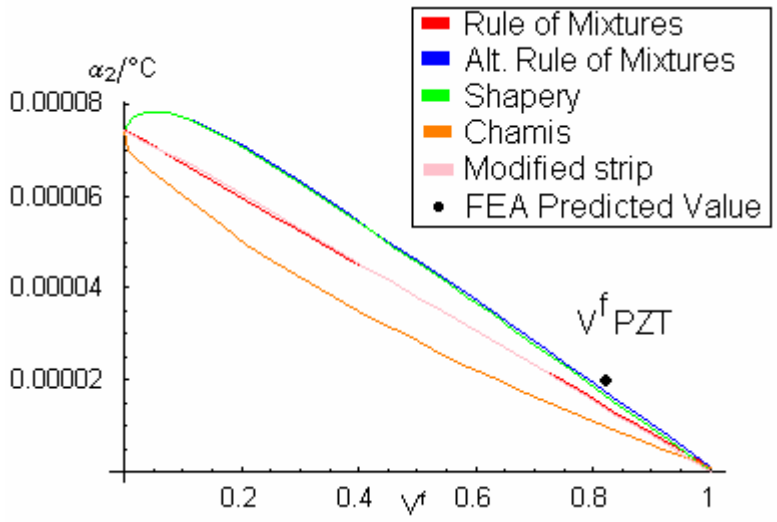

Figure E.7: Models for Transverse CTE for Orthotropic PZT/Epoxy Layer

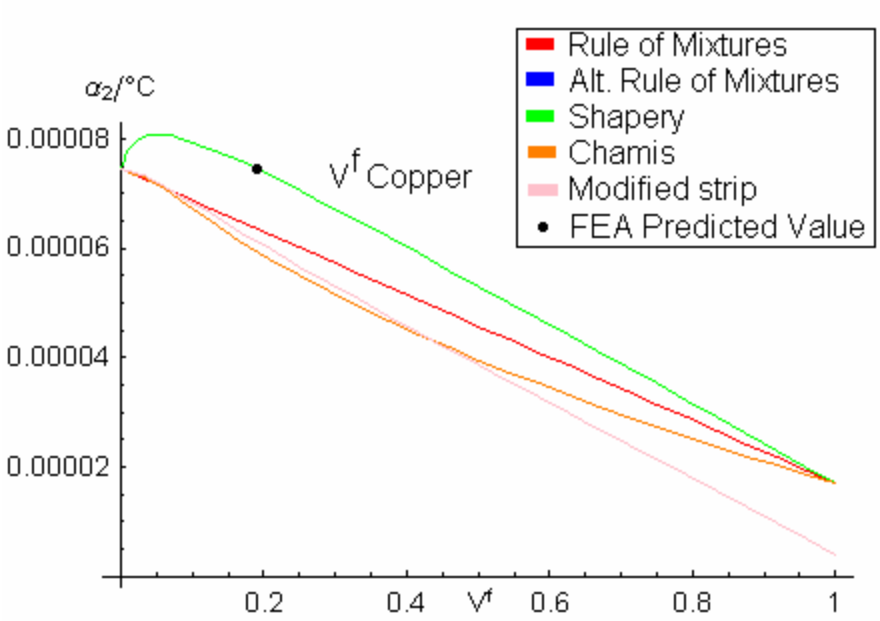

Figure E.8: Models for Transverse CTE for Orthotropic Copper / Epoxy Layer

E.3.3 Classical Lamination Theory:

With all stiffness and thermal expansion properties expressed as a function of temperature, a classical lamination approach is applied to the MFC. From a modeling standpoint, the MFC behaves as a symmetric, cross-ply laminate subjected to only a uniform temperature change, ΔT. The free thermal strains of such a laminate are expressed as

$$\begin{pmatrix} \varepsilon_x^{\circ T} \\ \varepsilon_y^{\circ T} \\ \gamma_{xy}^{\circ T} \end{pmatrix} = \begin{bmatrix} A_{11} & A_{12} & 0 \\ A_{12} & A_{22} & 0 \\ 0 & 0 & A_{66} \end{bmatrix}^{-1} \begin{pmatrix} N_x^T \\ N_y^T \\ N_{xy}^T \end{pmatrix} \tag{E.7}$$

where the thermal force resultants are expressed as

$$\begin{pmatrix} N_x^T \\ N_y^T \end{pmatrix} = \sum_{k=1}^{N} \begin{bmatrix} \overline{Q}_{11} & \overline{Q}_{12} \\ \overline{Q}_{12} & \overline{Q}_{22} \end{bmatrix}_k \begin{pmatrix} \alpha_x \\ \alpha_y \end{pmatrix}_k (z_k - z_{k-1}) \Delta T \tag{E.8}$$

and A_{ij} is the in-plane extensional stiffness matrix for the MFC, Q_{ij} is the transformed reduced stiffness matrix of the k^{th} of N total layers, z represents thickness coordinates and superscript T denotes free thermal quantities. Also, it should be noted that N_{xy}^T does not appear in Equation E.8 because the symmetric cross-ply nature of the MFC eliminates any induced thermal shear strains, i.e. α_{xy} for all layers is zero. Next, for a unit temperature change, the free thermal strains become the coefficients of thermal expansion, by definition, and Equations E.7 and E.8 are combined to give the following formulas for the CTEs of the MFC actuator (Hyer, 1999):

$$\alpha_x^{MFC} = \frac{A_{22}\hat{N}_x^T - A_{12}\hat{N}_y^T}{A_{11}A_{22} - A_{12}^2} \tag{E.9}$$

$$\alpha_y^{MFC} = \frac{A_{11}\hat{N}_y^T - A_{12}\hat{N}_x^T}{A_{11}A_{22} - A_{12}^2} \tag{E.10}$$

where

$$\hat{N}_x^T = \sum_{k=1}^{N} \overline{Q}_{11_k}\alpha_{x_k} + \overline{Q}_{12_k}\alpha_{y_k}\left(z_k - z_{k-1}\right) \tag{E.11}$$

$$\hat{N}_y^T = \sum_{k=1}^{N} \overline{Q}_{12_k}\alpha_{x_k} + \overline{Q}_{22_k}\alpha_{y_k}\left(z_k - z_{k-1}\right) \tag{E.12}$$

Of course, each of the properties required to calculate both $\overline{Q}_{ij}$ and A_{ij} are known as a function of temperature, thus the CTEs of the MFC given by Equations E.11 and E.12 are implicitly dependent on temperature. Due to the lengthy nature and numerous temperature-dependent properties involved in this analysis, the full expressions for these CTEs are omitted; however, the resulting curves generated by *Mathematica* are presented in Figure E.12, along with the corresponding FEA results in the next section.

In Chapter 2, the in-plane extensional stiffness matrix *[A]* was inverted to obtain the effective orthotropic stiffness parameters for the MFC. Since the *[A]* matrix formulated in the current analysis is already a function of temperature, it is straightforward to plot

these apparent properties as a function of temperature. Figure E.9 shows that the longitudinal modulus and major Poisson's ratio are not highly temperature dependent, while the transverse and shear moduli, known to be matrix-dependent properties, do vary a great deal with temperature. Most epoxy systems are not used at operating temperatures above that at which they were cured, but the MFC could still suffer approximately a 30% decrease in these stiffness properties near the cure temperature.

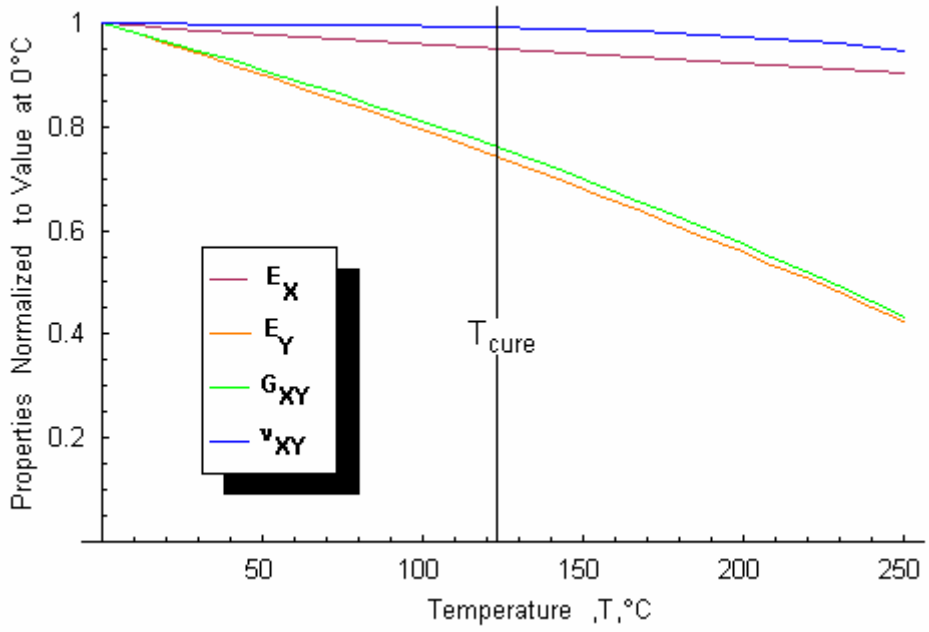

Figure E.9: Mechanical Properties of the MFC as a Function of Temperature

E.4 Finite Element Analysis:

In order to verify the forgoing analysis, i.e. Equations E.9 and E.10, an ANSYS finite element model was constructed using the appropriate temperature-dependent properties. In developing the model, a unit cell of the MFC was isolated, and then the quarter model of this repeating cell was drawn in ANSYS, as shown in Figure E.10. This geometry was meshed with 17,336 ANSYS SOLID185 elements. Since a quarter-model was used, symmetric boundary conditions were enforced along the bottom and hidden X-Z surfaces, and the nodal displacements along the top and exposed X-Z faces

were coupled in their respective normal directions. A unit thermal load (1°C ΔT) was applied at all nodes, and multiple solutions were run at various temperatures, where the material properties were updated accordingly.

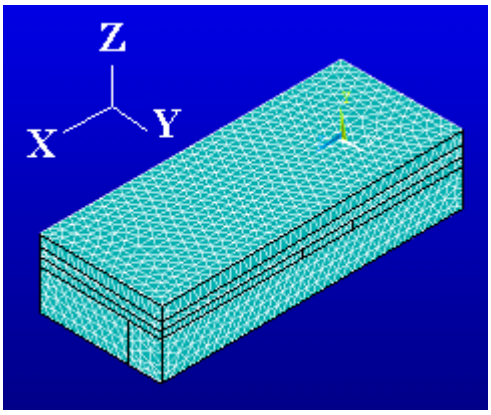

Figure E.10: ANSYS Quarter Unit Cell Model of MFC Actuator

Figure E.11 shows the calculated nodal displacement fields in the *x* and *y*-directions.

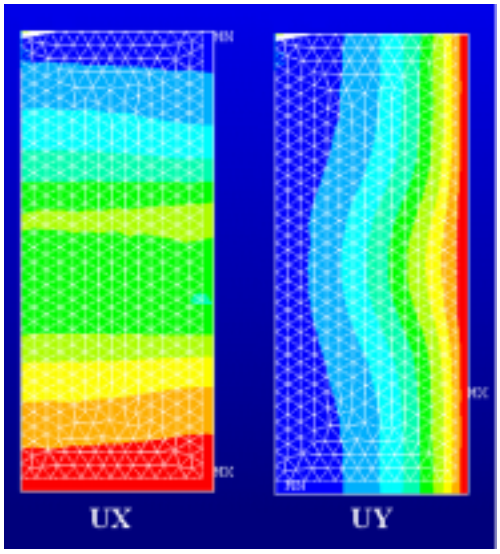

Figure E.11: ANSYS *x* and *z* Nodal Displacement Fields

From a list of the maximum nodal displacements, Δx and Δy, the appropriate CTEs were calculated as

$$\alpha_x^{MFC} = \frac{\Delta x}{x * \Delta T} \tag{E.13}$$

$$\alpha_y^{MFC} = \frac{\Delta y}{y * \Delta T} \tag{E.14}$$

E.5 Thermal Modeling Results and Discussion:

Figure E.12 depicts the coefficients of thermal expansion for the MFC actuator, α_x^{MFC} and α_y^{MFC}, as a function of temperature from 0° to 250°C. The lines represent the classical lamination theory solution, while the discreet points represent the ANSYS finite element solutions. Clearly, the two methods are in reasonably close agreement, particularly below the 120°C cure temperature.

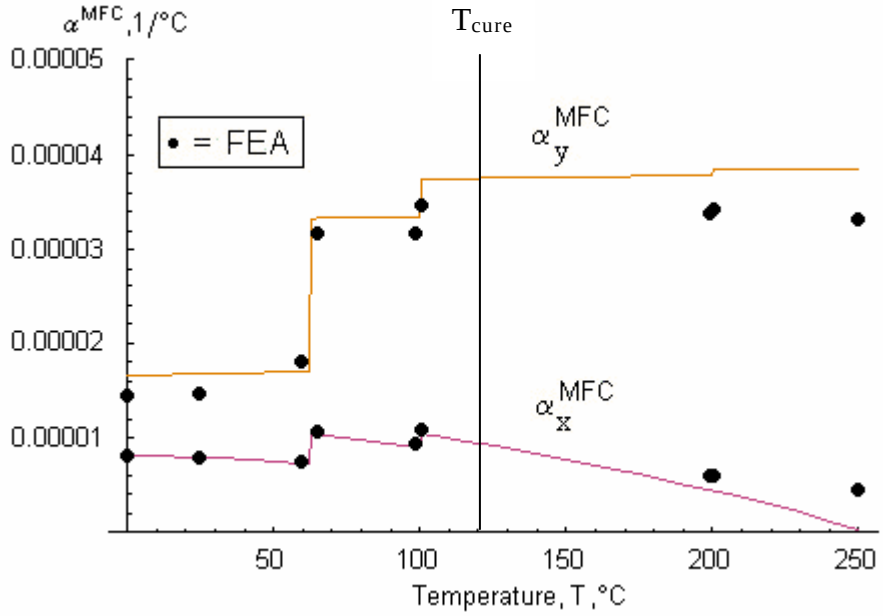

Figure E.12: Coefficients of Thermal Expansion for the MFC Actuator

From this figure, many interesting trends are noted. First, the lower curve, which represents the CTE in the PZT fiber direction, is nearly constant from zero up to the cure temperature, 120°C, and could reasonably be represented as a temperature *independent* property. Since there is a high volume fraction of PZT fibers in the MFC,

α_x^{MFC} is dominated by the CTE of the piezoceramic in that direction. This behavior is evident when one notices how α_x^{MFC} decreases between each set of step changes. The steps "jumps" are evidence of the influence of the epoxy. However, despite the fact that the CTE of the PZT becomes negative at high temperatures, the effects of the other constituent materials maintains a positive α_x^{MFC}. This behavior could be a cause for concern in terms of residual stresses at the interface between the fiber and epoxy matrix. Next, the top curve, which represents the CTE of the MFC transverse to the PZT fibers, does vary significantly over the temperature range of interest. The fact that the large step changes in value closely mimic the behavior of the epoxy is in indication that α_y^{MFC} is a matrix-dominated property. The slight discrepancies between the model and the ANSYS results stem from the way that the orthotropic elastic properties in the *y*-direction are calculated. E_y is notoriously difficult to predict, so for the model to be match the FEA data reasonably well indicates an adequate model for this initial temperature-dependent property characterization.

E.6 Electric Field-Dependent Stiffness:

In Chapter 3, the orthotropic mechanical properties of the MFC were measured under short-circuit electrical boundary conditions which provided a constant electric field equal to zero. However, there was some question as to how these measured / predicted stiffnesses vary with non-zero electric fields. If these properties change in a significant manner with electric field, then additional experimentation and modeling would be required to properly characterize the piezomechanical behavior of the MFC actuator. In contrast, if this dependence is on the order of less than around ten percent, then such effects for this initial characterization effort can be disregarded. An experimental approach was applied to investigate this field-dependent behavior.

E.6.1 Experimental Procedure:

Since this field-dependent property section was a preliminary investigation rather than a comprehensive characterization effort, only one specimen was tested at NASA

Langley. The reference geometry tensile test specimen was loaded into the hydraulic grips of the hydraulically controlled tensile testing machine, as seen in Figure E.13.

Figure E.13: MFC Specimen Loaded into Hydraulic Grips of Testing Machine

The power leads were connected to the HP high voltage amplifier and the strains were measured on the front and back of the specimen in order to eliminate bending strains from the collected data. Biaxial strain gages were used to measure both *x* and *y*-direction strains, which were measured with digital readout strain gage boxes. However, only the *x*-direction data was subsequently analyzed. All strain, load, and voltage data was collected on a PC, which also controlled the parameters of the experiment.

With the specimen properly connected to the testing machine, amplifier and strain gage boxes, the specimen was loaded up to a predetermined mean load level in the linear

elastic region, as prescribed in Table E.2, and then a constant electric field applied by the high voltage amplifier. Under this constant applied electric field, the specimen was then subjected to five cycles of a ±10 pound sinusoidal load of on top of the mean load level at a frequency of 0.1 Hz. After the mechanical loading was complete, the voltage was changed to the next voltage step, as dictated by Table E.3, and the mechanical cycling was repeated. This incremental process was repeated at the various constant-voltage steps were complete.

Table E.2: Elastic Load Levels Applied to the MFC to Measure E_x

Mean Load Level, lbs (N)	Harmonic Load Amplitude, lbs (N)	Maximum Load, lbs (N)	Minimum Load, lbs (N)
20 (89)	10 (44.5)	30 (133.5)	10 (44.5)
30 (133.5)	10 (44.5)	40 (177.9)	20 (89)
40 (177.9)	10 (44.5)	50 (222.4)	30 (133.5)
50 (222.4)	10 (44.5)	60 (266.9)	40 (177.9)

Table E.3: Constant Voltages Applied to the MFC During Load Cycling

Voltage Step	Applied Electrode Voltage, V
1	0
2	250
3	500
4	750
5	1000
6	1250
7	1500
8	1250
9	1000
10	750
11	500
12	250
13	0
14	-250
15	-500
16	-250
17	0

At this time, the mean load was increased to the next predetermined level, and the electrical loads reapplied as described above. This testing procedure was repeated at all of the specified mean load levels.

E.6.2 Experimental Results and Discussion:

The experimental procedure described above produces a stress-strain curve for *x*-direction behavior at each of the voltage steps. A linear regression analysis was performed on the data from each of these linear stress-strain curves to determine the effective E_x of the MFC at a particular constant applied electrode voltage. Figure E.14 shows the relationship between measured effective PZT fiber-direction modulus and constant applied electrode voltage.

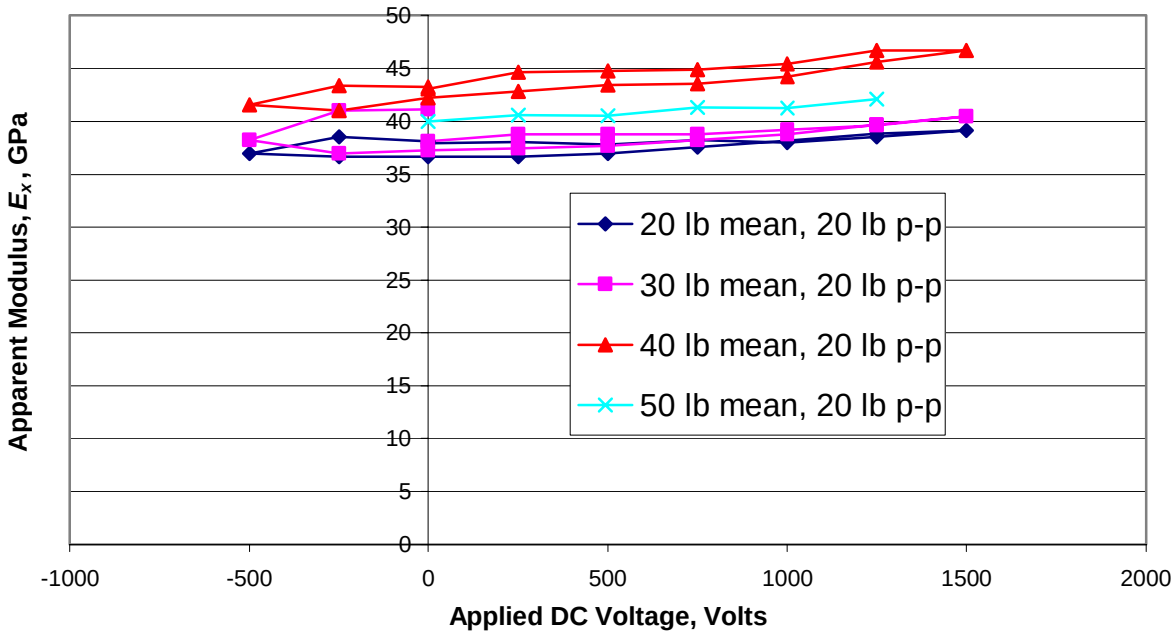

Figure E.14: Effective *x*-direction MFC Modulus at Various Constant Applied Voltages

From this figure, the hysteresis loops are nearly horizontal, which indicates only a *small* dependence of E_x on applied voltage over a wide range of applicable voltages for the MFC. However, there does appear to be a small linear increase in apparent stiffness as

from the lowest voltages to the higher levels. However, the slope of the upper and lower sections of the hysteresis loop at each load level is nearly the same. In order to check how much variation in stiffness is present, the percent change over the entire voltage range is calculated for each load level, and the results are tabulated in Table E.4.

Table E.4: Percent Change in E_x Over Voltage Range

Mean Load Level, lbs (N)	Percent Change Between Max. and Min. Stiffnesses
20 (89)	6.35%
30 (133.5)	10.14%
40 (177.9)	12.20%
50 (222.4)	4.95%

From this table, it is clear that over a very wide range of applied voltages for a wide range of mean load levels, the changes in apparent stiffness are small. In fact, the changes in stiffness due to nonlinear mechanical behavior and the changes in d_{ij} under high electric fields are one or two orders of magnitude larger than the changes detected in E_x over similar voltage regimes. Therefore, for this initial characterization effort, the effects of field-dependent stiffness properties will be disregarded.

E.7 Summary:

Appendix E presented the coefficients of thermal expansion for the MFC actuator as a function of temperature, based on finite element and classical lamination analyses. It was found that while α_x^{MFC} is nearly constant between 0° and 120°C, α_y^{MFC} does vary significantly, primarily due to the thermoelastic behavior of the epoxy matrix. As a result, the variation of thermoelastic properties with temperature should be carefully modeled, particularly when transverse behavior of the MFC is deemed critical. In addition, the effect of nonzero electric field on the apparent PZT fiber-direction modulus of the MFC was experimentally investigated. Since the changes in this

stiffness parameter were small with respect to large variations in voltage, such nonlinear material behavior effects have been ignored.

E.8 References:

1. Bowles, D. E. and Tompkins, S. S., 1989, "Prediction of Coefficients of Thermal Expansion for Unidirectional Composites," *Journal of Composite Materials*, Vol. 23, pp. 370-388.

2. DuPont Films, "High Performance Films: Kapton General Specifications" Bulletin GS-96-7, http://www.dupont.com/corp/markets/aerospace/products/kapton.html.

3. Georgia Institute of Technology, Mechanical Properties Research Lab, http://216.239.51.100/search?q=cache:SaBsbPNY_GgC:www.me.gatech.edu/MPRL/MPRLRPT.00.PDF+PZT+modulus+%22temperature+dependent%22+&hl=en&ie=UTF8.

4. Hyer, M.W., *Stress Analysis of Fiber-Reinforced Composite Materials*, WCB/McGraw Hill, New York, 1998.

5. Islam, MD. R., Sjolind, S. G., and Pramila, A., 2001, "Finite Element Analysis of Linear Thermal Expansion Coefficients of Unidirectional Cracked Composites," *Journal of Composite Materials*, Vol. 35, pp. 1762-1776.

6. Jones, R. M., *Mechanics of Composite Materials, Second Edition*, Taylor & Francis, 1999.

7. Kim, R. Y., Crasto, A. S., and Schoeppner, G. A., 2000, "Dimensional Stability of Composite in a Space Thermal Environment," *Composites Science and Technology*, Vol. 60, pp. 2601-2608.

8. Morgan Electroceramics, http://www.morganelectroceramics.com/piezoguide11.html.

9. NASA, http://nepp.nasa.gov/DocUploads/A646EF4E-78D7-4B0A-88E89C0810D7FFC0/epoxyeval.pdf.

10. Wetherhold, R. C. and Boss, C. S., 1988, "Transverse Thermals Expansion Coefficients for Composite Laminates," *Journal of Composite Materials*, Vol. 22, pp. 812-817.

11. Williams, R. B., Inman, D. J. and Wilkie, W. K., “Modeling of Temperature Effects in Macro Fiber Composite Actuators,” USNCAM14 Conference, June 24th – 28th, 2002, Donaldson Brown Hotel and Conference Center, Blacksburg, VA.

12. Williams, R. B., Inman, D. J. and Wilkie, W. K., ”Nonlinear Mechanical Behavior of Macro Fiber Composite Actuators,” *Proceedings of the Sixth International Conference on Sandwich Structures*, March 31-April 2, 2003, Marriott Marina Hotel, Ft. Lauderdale, FL.

13. Yoon, K. J. and Kim, J. S., 2000, “Prediction of Thermal Expansion Properties of Carbon/Epoxy Laminates for Temperature Variation,” *Journal of Composite Materials*, Vol. 34, No. 2, pp. 90-100.

14. Yoon, K. J. and Kim, J. S., 2001, “Effect of Thermal Deformation and Chemical Shrinkage on the Process Induced Distortion of Carbon/Epoxy Curved Laminates,” *Journal of Composite Materials*, Vol. 35, No. 3, pp. 253-263.

Appendix F

Mathematica Code for Sensitivity Analysis of Classical Lamination Model of the Macro Fiber Composite

F.1 Introduction:

In Chapter 4, the classical lamination model from Chapter 2 is modified to predict the sensitivity of the predicted orthotropic properties of the MFC to variations in geometric parameters and uncertainty in material properties. In order to perform these calculations and generate the necessary plots and subsequent data analysis, a *Mathematica* computer code was written. This appendix presents this code, which was developed in *Mathematica* Version 4.0.

F.2 *Mathematica* Code:

MFC Property Calculations 15x2x7.5 mil, 5 mil Cu Sensitivity Analysis

```
<< Graphics`Colors`
<< Graphics`Legend`
Off[General::spell1]
```

■ Calculate Elastic Constants for Each Orthotropic Layer

■ **Properties calculated using rule of mixtures.**

PZT Fiber Layer

$$E1PZT = VfiberPZT * E11EPZT + VmatrixPZT * Eepoxy;$$

$$E2PZT = \frac{1}{\frac{VfiberPZT}{E22EPZT} + \frac{1-VfiberPZT}{Eepoxy}};$$

$$G12PZT = \frac{\left(\frac{Eepoxy}{2*(1+\nu epoxy)} * G12fiber\right)}{\left((1 - VfiberPZT) * G12fiber + VfiberPZT * \frac{Eepoxy}{2*(1+\nu epoxy)}\right)};$$

$$\nu 12PZT = VfiberPZT * \nu fiber + VmatrixPZT * \nu epoxy;$$

Copper-Epoxy Electrode Layer

$$E1electrode = Vfiberelectrode * Ecopper + Vmatrixelectrode * Eepoxy;$$

$$E2electrode = \frac{1}{\frac{Vfiberelectrode}{Ecopper} + \frac{1-Vfiberelectrode}{Eepoxy}};$$

$$G12electrode = \frac{\left(\frac{Eepoxy}{2*(1+\nu epoxy)} * \frac{Ecopper}{2*(1+\nu copper)}\right)}{\left((1 - Vfiberelectrode) * \frac{Ecopper}{2*(1+\nu copper)} + Vfiberelectrode * \frac{Eepoxy}{2*(1+\nu epoxy)}\right)};$$

$$\nu 12electrode = Vfiberelectrode * \nu copper + Vmatrixelectrode * \nu epoxy;$$

■ Input Laminate Parameters

■ **Define number of layers and number of different material types.**

```
Nlayers = 8;
Nsets = 4;
layerset[1] = 1;
```

■ **Define the thicknesses of the layers (symmetric lay-up). PZT layer is treated as two layers divided in half by the laminate midplane. Layer numer starts at the top of the laminate (1=Kapton, 2=Acrylic, 3=Copper/Epoxy, 4=PZT/Epoxy).**

```
thick[1] = tkapton;
thick[2] = tacrylic;
thick[3] = tcopper;
thick[4] = tfiber/2;
thick[5] = thick[4];
thick[6] = thick[3];
thick[7] = thick[2];
thick[8] = thick[1];
totalthickness = Sum[thick[i] (*m*), {i, 1, Nlayers}];
```

- **Define the z values for the top and bottom of each layer**

```
Clear[z]
z = Table[0, {i, 1, Nlayers + 1}];
z[[Nlayers + 1]] = totalthickness/2;
Do[z[[i]] = Chop[z[[i + 1]] - thick[i]], {i, Nlayers, 1, -1}]
(*z*)
```

- **Define the elastic properties and fiber-angle orientation of the layers. All calculations are made as if all layers are orthotropic, however, isotropic layers are defined with $E_1 = E_2$.**

Kapton Layer (Isotropic)

```
E1[1] = Ekapton;
E2[1] = Ekapton;
G12[1] = Ekapton/(2*(1 + νkapton));
ν12[1] = νkapton;
```

Acrylic Layer (Isotropic)

```
E1[2] = Eacrylic;
E2[2] = Eacrylic;
G12[2] = Eacrylic/(2*(1 + νacrylic));
ν12[2] = νacrylic;
```

Copper-Epoxy Layer (Orthotropic, 90°)

```
E1[3] = E1electrode;
E2[3] = E2electrode;
G12[3] = G12electrode;
ν12[3] = ν12electrode;
θ[3] = 90;
θ[6] = 90;
```

PZT-Epoxy Layer (Orthotropic, 0°)

```
E1[4] = E1PZT;
E2[4] = E2PZT;
G12[4] = G12PZT;
ν12[4] = ν12PZT;
```

■ Calculating Laminae Matrices

■ Compliance Matrix, S

```
Sij = Array[S, {3, 3, Nsets}];
Do[S[1, 1, i] = 1/E1[i];
 S[1, 2, i] = -ν12[i]/E1[i];
 S[1, 3, i] = 0;
 S[2, 1, i] = S[1, 2, i];
 S[2, 2, i] = 1/E2[i];
 S[2, 3, i] = 0;
 S[3, 1, i] = 0;
 S[3, 2, i] = 0;
 S[3, 3, i] = 1/G12[i], {i, 1, Nsets}]
Do[
 compliance[i] =
  Partition[Extract[Sij, {{1, 1, i}, {1, 2, i}, {1, 3, i}, {2, 1, i},
     {2, 2, i}, {2, 3, i}, {3, 1, i}, {3, 2, i}, {3, 3, i}}], 3], {i, 1, Nsets}]
MatrixForm[compliance[1]];
MatrixForm[compliance[2]];
MatrixForm[compliance[3]];
MatrixForm[compliance[4]];
```

■ Reduced Stiffness Matrix

```
Do[Q[i] = Inverse[compliance[i]], {i, 1, Nsets}];
MatrixForm[Q[1]];
MatrixForm[Q[2]];
MatrixForm[Q[3]];
MatrixForm[Q[4]];
```

■ **Transformation Matrices for Each Layer**

```
T[1] = {{1, 0, 0}, {0, 1, 0}, {0, 0, 1}};
T[2] = {{1, 0, 0}, {0, 1, 0}, {0, 0, 1}};
T[3] = {{0, 1, 0}, {1, 0, 0}, {0, 0, -1}};
T[4] = {{1, 0, 0}, {0, 1, 0}, {0, 0, 1}};
T[5] = T[4];
T[6] = T[3];
T[7] = T[2];
T[8] = T[1];
```

■ **Inverse Transformation Matrices for Each Layer**

```
Do[Tinv[i] = Inverse[T[i]], {i, 1, 8}]
```

■ **In-plane Laminate Extensional Stiffness Matrix, [A]**

```
Clear[A]
extenstiff = Array[A, {3, 3}];
For[i = 1, i ≤ 3, A[i, 1] = Sum[Extract[qbar[k], {i, 1}] * thick[k]; i++, {k, 1, Nlayers}]]
Clear[i]
For[i = 1, i ≤ 3, A[i, 2] = Sum[Extract[qbar[k], {i, 2}] * thick[k]; i++, {k, 1, Nlayers}]]
Clear[i]
For[i = 1, i ≤ 3, A[i, 3] = Sum[Extract[qbar[k], {i, 3}] * thick[k]; i++, {k, 1, Nlayers}]]
Clear[i]
(*Simplify[MatrixForm[extenstiff]]*)
(*MatrixForm[extenstiff]*)
```

■ Inversion of the [A] Matrix and Calculation of Laminate Engineering Properties

```
ainv = Inverse[extenstiff];
Ex = 1 / (ainv[[1, 1]] * totalthickness);
Gxy = 1 / (ainv[[3, 3]] * totalthickness);
Ey = 1 / (ainv[[2, 2]] * totalthickness);
νxy = -ainv[[2, 1]] / ainv[[1, 1]];
```

■ Define Reference MFC Properties

```
ExMFCnominal =
  Ex /. {Ekapton → 2.5, νkapton -> 0.34, Eacrylic -> 2.7, νacrylic -> 0.35,
    Ecopper -> 117.2, νcopper -> 0.31, Eepoxy -> 3.378, νepoxy -> 0.27,
    E11EPZT -> 53, E22EPZT -> 61, νfiber -> 0.384, G12fiber -> 21,
    Vfiberelectrode → 0.238095, Vmatrixelectrode → .761905,
    VfiberPZT → .882353, VMatrixPZT -> .117647};
GxyMFCnominal =
  Gxy /. {Ekapton → 2.5, νkapton -> 0.34, Eacrylic -> 2.7, νacrylic -> 0.35,
    Ecopper -> 117.2, νcopper -> 0.31, Eepoxy -> 3.378, νepoxy -> 0.27,
    E11EPZT -> 53, E22EPZT -> 61, νfiber -> 0.384, G12fiber -> 21,
    Vfiberelectrode → 0.238095, Vmatrixelectrode → .761905,
    VfiberPZT → .882353, VMatrixPZT -> .117647};
EyMFCnominal =
  Ey /. {Ekapton → 2.5, νkapton -> 0.34, Eacrylic -> 2.7, νacrylic -> 0.35,
    Ecopper -> 117.2, νcopper -> 0.31, Eepoxy -> 3.378, νepoxy -> 0.27,
    E11EPZT -> 53, E22EPZT -> 61, νfiber -> 0.384, G12fiber -> 21,
    Vfiberelectrode → 0.238095, Vmatrixelectrode → .761905,
    VfiberPZT → .882353, VMatrixPZT -> .117647};
νxyMFCnominal =
  νxy /. {Ekapton → 2.5, νkapton -> 0.34, Eacrylic -> 2.7, νacrylic -> 0.35,
    Ecopper -> 117.2, νcopper -> 0.31, Eepoxy -> 3.378, νepoxy -> 0.27,
    E11EPZT -> 53, E22EPZT -> 61, νfiber -> 0.384, G12fiber -> 21,
    Vfiberelectrode → 0.238095, Vmatrixelectrode → .761905,
    VfiberPZT → .882353, VMatrixPZT -> .117647};
```

■ Calculate Volume Fractions

PZT-Epoxy Layer

```
unitlengthfiber = wfiber + fiberspacing;
unitareafiber = unitlengthfiber * tfiber;
VfiberPZT = tfiber * wfiber / unitareafiber;
VmatrixPZT = tfiber * fiberspacing / unitareafiber;
```

Copper-Epoxy Electrode Layer

```
unitlengthelectrode = electrodespacing;
unitareaelectrode = unitlengthelectrode * tcopper;

Vfiberelectrode = tcopper * wcopper / unitareaelectrode;
Vmatrixelectrode = (tcopper * (electrodespacing - wcopper)) /
   unitareaelectrode;
```

■ Kapton Material Property Variation

Modulus of Kapton

```
ExMFC[Ekapton_] =
  Ex /. {νkapton -> 0.34, Eacrylic -> 2.7, νacrylic -> 0.35, Ecopper -> 117.2,
    νcopper -> 0.31, Eepoxy -> 3.378, νepoxy -> 0.27, E11EPZT -> 53,
    E22EPZT -> 61, νfiber -> 0.384, G12fiber -> 21};
EyMFC[Ekapton_] =
  Ey /. {νkapton -> 0.34, Eacrylic -> 2.7, νacrylic -> 0.35, Ecopper -> 117.2,
    νcopper -> 0.31, Eepoxy -> 3.378, νepoxy -> 0.27, E11EPZT -> 53,
    E22EPZT -> 61, νfiber -> 0.384, G12fiber -> 21};
GxyMFC[Ekapton_] =
  Gxy /. {νkapton -> 0.34, Eacrylic -> 2.7, νacrylic -> 0.35, Ecopper -> 117.2,
    νcopper -> 0.31, Eepoxy -> 3.378, νepoxy -> 0.27, E11EPZT -> 53,
    E22EPZT -> 61, νfiber -> 0.384, G12fiber -> 21};
νxyMFC[Ekapton_] =
  νxy /. {νkapton -> 0.34, Eacrylic -> 2.7, νacrylic -> 0.35, Ecopper -> 117.2,
    νcopper -> 0.31, Eepoxy -> 3.378, νepoxy -> 0.27, E11EPZT -> 53,
    E22EPZT -> 61, νfiber -> 0.384, G12fiber -> 21};
```

```
Simplify[ExMFC[Ekapton]];
Simplify[EyMFC[Ekapton]];
Simplify[GxyMFC[Ekapton]];
Simplify[νxyMFC[Ekapton]];
Extable = Table[{Ekapton / 2.5, ExMFC[Ekapton] / ExMFCnominal},
   {Ekapton, .5 * 2.5, 1.5 * 2.5, (1.5 * 2.5 - .5 * 2.5) / 100}];
Eytable = Table[{Ekapton / 2.5, EyMFC[Ekapton] / EyMFCnominal},
   {Ekapton, .5 * 2.5, 1.5 * 2.5, (1.5 * 2.5 - .5 * 2.5) / 100}];
Gxytable = Table[{Ekapton / 2.5, GxyMFC[Ekapton] / GxyMFCnominal},
   {Ekapton, .5 * 2.5, 1.5 * 2.5, (1.5 * 2.5 - .5 * 2.5) / 100}];
νxytable = Table[{Ekapton / 2.5, νxyMFC[Ekapton] / νxyMFCnominal},
   {Ekapton, .5 * 2.5, 1.5 * 2.5, (1.5 * 2.5 - .5 * 2.5) / 100}];
plot1 = ListPlot[Extable, PlotJoined → True, PlotRange → {.98, 1.02},
  TextStyle → {FontFamily → "Times", FontSize → 12},
  PlotLabel → "kapton modulus varies", AxesOrigin → {.5, 1},
  PlotStyle -> {Red, Dashing[{}]}, DisplayFunction → Identity]
plot2 = ListPlot[Eytable, PlotJoined → True,
  PlotStyle -> {DodgerBlue, Dashing[{.015}]}, DisplayFunction → Identity]
plot3 = ListPlot[Gxytable, PlotJoined → True,
  PlotStyle -> {Green, Dashing[{.03}]}, DisplayFunction → Identity]
plot4 = ListPlot[νxytable, PlotJoined → True,
  PlotStyle -> {Carrot, Dashing[{.005, .025, .025, .025}]},
  DisplayFunction → Identity]
Show[plot1, plot2, plot3, plot4, DisplayFunction → $DisplayFunction]
- Graphics -

- Graphics -

- Graphics -

- Graphics -

- Graphics -
slopeExcalc = Array[slopeEx, 12];
slopeEycalc = Array[slopeEy, 12];
slopeGxycalc = Array[slopeGxy, 12];
slopevxycalc = Array[slopevxy, 12];

slopeEx[1] = (Extable[[52, 2]] - Extable[[50, 2]]) / (Extable[[52, 1]] - Extable[[50, 1]]);
slopeEy[1] = (Eytable[[52, 2]] - Eytable[[50, 2]]) / (Eytable[[52, 1]] - Eytable[[50, 1]]);
slopeGxy[1] = (Gxytable[[52, 2]] - Gxytable[[50, 2]]) / (Gxytable[[52, 1]] - Gxytable[[50, 1]]);
slopevxy[1] = (νxytable[[52, 2]] - νxytable[[50, 2]]) / (νxytable[[52, 1]] - νxytable[[50, 1]]);
```

Poisson's ratio of Kapton

```
ExMFC[νkapton_] =
  Ex /. {Ekapton → 2.5, Eacrylic -> 2.7, νacrylic -> 0.35, Ecopper -> 117.2,
    νcopper -> 0.31, Eepoxy -> 3.378, νepoxy -> 0.27, E11EPZT -> 53,
    E22EPZT -> 61, νfiber -> 0.384, G12fiber -> 21};
EyMFC[νkapton_] =
  Ey /. {Ekapton → 2.5, Eacrylic -> 2.7, νacrylic -> 0.35, Ecopper -> 117.2,
    νcopper -> 0.31, Eepoxy -> 3.378, νepoxy -> 0.27, E11EPZT -> 53,
    E22EPZT -> 61, νfiber -> 0.384, G12fiber -> 21};
GxyMFC[νkapton_] =
  Gxy /. {Ekapton → 2.5, Eacrylic -> 2.7, νacrylic -> 0.35, Ecopper -> 117.2,
    νcopper -> 0.31, Eepoxy -> 3.378, νepoxy -> 0.27, E11EPZT -> 53,
    E22EPZT -> 61, νfiber -> 0.384, G12fiber -> 21};
νxyMFC[νkapton_] =
  νxy /. {Ekapton → 2.5, Eacrylic -> 2.7, νacrylic -> 0.35, Ecopper -> 117.2,
    νcopper -> 0.31, Eepoxy -> 3.378, νepoxy -> 0.27, E11EPZT -> 53,
    E22EPZT -> 61, νfiber -> 0.384, G12fiber -> 21};
Simplify[ExMFC[νkapton]];
Simplify[EyMFC[νkapton]];
Simplify[GxyMFC[νkapton]];
Simplify[νxyMFC[νkapton]];
Extable = Table[{νkapton / .34, ExMFC[νkapton] / ExMFCnominal},
   {νkapton, .5 * .34, 1.5 * .34, (1.5 * .34 - .5 * .34) / 100}];
Eytable = Table[{νkapton / .34, EyMFC[νkapton] / EyMFCnominal},
   {νkapton, .5 * .34, 1.5 * .34, (1.5 * .34 - .5 * .34) / 100}];
Gxytable = Table[{νkapton / .34, GxyMFC[νkapton] / GxyMFCnominal},
   {νkapton, .5 * .34, 1.5 * .34, (1.5 * .34 - .5 * .34) / 100}];
νxytable = Table[{νkapton / .34, νxyMFC[νkapton] / νxyMFCnominal},
   {νkapton, .5 * .34, 1.5 * .34, (1.5 * .34 - .5 * .34) / 100}];
plot1 = ListPlot[Extable, PlotJoined → True, PlotRange → {.98, 1.02},
  TextStyle → {FontFamily → "Times", FontSize → 12},
  PlotLabel → "kapton ν varies", AxesOrigin → {.5, 1},
  PlotStyle -> {Red, Dashing[{}]}, DisplayFunction → Identity]
plot2 = ListPlot[Eytable, PlotJoined → True,
  PlotStyle -> {DodgerBlue, Dashing[{.015}]}, DisplayFunction → Identity]
plot3 = ListPlot[Gxytable, PlotJoined → True,
  PlotStyle -> {Green, Dashing[{.03}]}, DisplayFunction → Identity]
plot4 = ListPlot[νxytable, PlotJoined → True,
  PlotStyle -> {Carrot, Dashing[{.005, .025, .025, .025}]},
  DisplayFunction → Identity]
Show[plot1, plot2, plot3, plot4, DisplayFunction → $DisplayFunction]
```

- Graphics -

- Graphics -

- Graphics -

- Graphics -

- Graphics -

$$\text{slopeEx}[2] = \frac{\text{Extable}[[52, 2]] - \text{Extable}[[50, 2]]}{\text{Extable}[[52, 1]] - \text{Extable}[[50, 1]]};$$

$$\text{slopeEy}[2] = \frac{\text{Eytable}[[52, 2]] - \text{Eytable}[[50, 2]]}{\text{Eytable}[[52, 1]] - \text{Eytable}[[50, 1]]};$$

$$\text{slopeGxy}[2] = \frac{\text{Gxytable}[[52, 2]] - \text{Gxytable}[[50, 2]]}{\text{Gxytable}[[52, 1]] - \text{Gxytable}[[50, 1]]};$$

$$\text{slopevxy}[2] = \frac{\nu\text{xytable}[[52, 2]] - \nu\text{xytable}[[50, 2]]}{\nu\text{xytable}[[52, 1]] - \nu\text{xytable}[[50, 1]]};$$

■ Acrylic Material Property Variation

Modulus of Acrylic

```
ExMFC[Eacrylic_] =
  Ex /. {Ekapton → 2.5, νkapton -> 0.34, νacrylic -> 0.35, Ecopper -> 117.2,
    νcopper -> 0.31, Eepoxy -> 3.378, νepoxy -> 0.27, E11EPZT -> 53,
    E22EPZT -> 61, νfiber -> 0.384, G12fiber -> 21};
EyMFC[Eacrylic_] =
  Ey /. {Ekapton → 2.5, νkapton -> 0.34, νacrylic -> 0.35, Ecopper -> 117.2,
    νcopper -> 0.31, Eepoxy -> 3.378, νepoxy -> 0.27, E11EPZT -> 53,
    E22EPZT -> 61, νfiber -> 0.384, G12fiber -> 21};
GxyMFC[Eacrylic_] =
  Gxy /. {Ekapton → 2.5, νkapton -> 0.34, νacrylic -> 0.35, Ecopper -> 117.2,
    νcopper -> 0.31, Eepoxy -> 3.378, νepoxy -> 0.27, E11EPZT -> 53,
    E22EPZT -> 61, νfiber -> 0.384, G12fiber -> 21};
νxyMFC[Eacrylic_] =
  νxy /. {Ekapton → 2.5, νkapton -> 0.34, νacrylic -> 0.35, Ecopper -> 117.2,
    νcopper -> 0.31, Eepoxy -> 3.378, νepoxy -> 0.27, E11EPZT -> 53,
    E22EPZT -> 61, νfiber -> 0.384, G12fiber -> 21};
Simplify[ExMFC[Eacrylic]];
Simplify[EyMFC[Eacrylic]];
Simplify[GxyMFC[Eacrylic]];
Simplify[νxyMFC[Eacrylic]];
```

```
Extable = Table[{Eacrylic / 2.7, ExMFC[Eacrylic] / ExMFCnominal},
   {Eacrylic, .5*2.7, 1.5*2.7, (1.5*2.7 - .5*2.7) / 100}];
Eytable = Table[{Eacrylic / 2.7, EyMFC[Eacrylic] / EyMFCnominal},
   {Eacrylic, .5*2.7, 1.5*2.7, (1.5*2.7 - .5*2.7) / 100}];
Gxytable = Table[{Eacrylic / 2.7, GxyMFC[Eacrylic] / GxyMFCnominal},
   {Eacrylic, .5*2.7, 1.5*2.7, (1.5*2.7 - .5*2.7) / 100}];
νxytable = Table[{Eacrylic / 2.7, νxyMFC[Eacrylic] / νxyMFCnominal},
   {Eacrylic, .5*2.7, 1.5*2.7, (1.5*2.7 - .5*2.7) / 100}];
plot1 = ListPlot[Extable, PlotJoined → True, PlotRange → {.99, 1.01},
  TextStyle → {FontFamily → "Times", FontSize → 12},
  PlotLabel → "acrylic modulus varies", AxesOrigin → {.5, 1},
  PlotStyle -> {Red, Dashing[{}]}, DisplayFunction → Identity]
plot2 = ListPlot[Eytable, PlotJoined → True,
  PlotStyle -> {DodgerBlue, Dashing[{.015}]}, DisplayFunction → Identity]
plot3 = ListPlot[Gxytable, PlotJoined → True,
  PlotStyle -> {Green, Dashing[{.03}]}, DisplayFunction → Identity]
plot4 = ListPlot[νxytable, PlotJoined → True,
  PlotStyle -> {Carrot, Dashing[{.005, .025, .025, .025}]},
  DisplayFunction → Identity]
Show[plot1, plot2, plot3, plot4, DisplayFunction → $DisplayFunction]
```

```
- Graphics -
```

```
- Graphics -
```

```
- Graphics -
```

```
- Graphics -
```

```
- Graphics -
```

$$\text{slopeEx}[3] = \frac{\text{Extable}[[52, 2]] - \text{Extable}[[50, 2]]}{\text{Extable}[[52, 1]] - \text{Extable}[[50, 1]]};$$

$$\text{slopeEy}[3] = \frac{\text{Eytable}[[52, 2]] - \text{Eytable}[[50, 2]]}{\text{Eytable}[[52, 1]] - \text{Eytable}[[50, 1]]};$$

$$\text{slopeGxy}[3] = \frac{\text{Gxytable}[[52, 2]] - \text{Gxytable}[[50, 2]]}{\text{Gxytable}[[52, 1]] - \text{Gxytable}[[50, 1]]};$$

$$\text{slopevxy}[3] = \frac{\text{νxytable}[[52, 2]] - \text{νxytable}[[50, 2]]}{\text{νxytable}[[52, 1]] - \text{νxytable}[[50, 1]]};$$

Poisson's Ratio of Acrylic

```
ExMFC[νacrylic_] =
  Ex /. {Ekapton → 2.5, νkapton -> 0.34, Eacrylic → 2.7, Ecopper -> 117.2,
    νcopper -> 0.31, Eepoxy -> 3.378, νepoxy -> 0.27, E11EPZT -> 53,
    E22EPZT -> 61, νfiber -> 0.384, G12fiber -> 21};
EyMFC[νacrylic_] =
  Ey /. {Ekapton → 2.5, νkapton -> 0.34, Eacrylic → 2.7, Ecopper -> 117.2,
    νcopper -> 0.31, Eepoxy -> 3.378, νepoxy -> 0.27, E11EPZT -> 53,
    E22EPZT -> 61, νfiber -> 0.384, G12fiber -> 21};
GxyMFC[νacrylic_] =
  Gxy /. {Ekapton → 2.5, νkapton -> 0.34, Eacrylic → 2.7, Ecopper -> 117.2,
    νcopper -> 0.31, Eepoxy -> 3.378, νepoxy -> 0.27, E11EPZT -> 53,
    E22EPZT -> 61, νfiber -> 0.384, G12fiber -> 21};
νxyMFC[νacrylic_] =
  νxy /. {Ekapton → 2.5, νkapton -> 0.34, Eacrylic → 2.7, Ecopper -> 117.2,
    νcopper -> 0.31, Eepoxy -> 3.378, νepoxy -> 0.27, E11EPZT -> 53,
    E22EPZT -> 61, νfiber -> 0.384, G12fiber -> 21};
Simplify[ExMFC[νacrylic]];
Simplify[EyMFC[νacrylic]];
Simplify[GxyMFC[νacrylic]];
Simplify[νxyMFC[νacrylic]];
Extable = Table[{νacrylic / .35, ExMFC[νacrylic] / ExMFCnominal},
   {νacrylic, .5 * .35, 1.5 * .35, (1.5 * .35 - .5 * .35) / 100}];
Eytable = Table[{νacrylic / .35, EyMFC[νacrylic] / EyMFCnominal},
   {νacrylic, .5 * .35, 1.5 * .35, (1.5 * .35 - .5 * .35) / 100}];
Gxytable = Table[{νacrylic / .35, GxyMFC[νacrylic] / GxyMFCnominal},
   {νacrylic, .5 * .35, 1.5 * .35, (1.5 * .35 - .5 * .35) / 100}];
νxytable = Table[{νacrylic / .35, νxyMFC[νacrylic] / νxyMFCnominal},
   {νacrylic, .5 * .35, 1.5 * .35, (1.5 * .35 - .5 * .35) / 100}];
plot1 = ListPlot[Extable, PlotJoined → True, PlotRange → {.99, 1.01},
  TextStyle → {FontFamily → "Times", FontSize → 12},
  PlotLabel → "Acrylic ν varies", AxesOrigin → {.5, 1},
  PlotStyle -> {Red, Dashing[{}]}, DisplayFunction → Identity]
plot2 = ListPlot[Eytable, PlotJoined → True,
  PlotStyle -> {DodgerBlue, Dashing[{.015}]}, DisplayFunction → Identity]
plot3 = ListPlot[Gxytable, PlotJoined → True,
  PlotStyle -> {Green, Dashing[{.03}]}, DisplayFunction → Identity]
plot4 = ListPlot[νxytable, PlotJoined → True,
  PlotStyle -> {Carrot, Dashing[{.005, .025, .025, .025}]},
  DisplayFunction → Identity]
Show[plot1, plot2, plot3, plot4, DisplayFunction → $DisplayFunction]
```

- Graphics -

- Graphics -

- Graphics -

- Graphics -

- Graphics -

$$\text{slopeEx}[4] = \frac{\text{Extable}[[52, 2]] - \text{Extable}[[50, 2]]}{\text{Extable}[[52, 1]] - \text{Extable}[[50, 1]]};$$

$$\text{slopeEy}[4] = \frac{\text{Eytable}[[52, 2]] - \text{Eytable}[[50, 2]]}{\text{Eytable}[[52, 1]] - \text{Eytable}[[50, 1]]};$$

$$\text{slopeGxy}[4] = \frac{\text{Gxytable}[[52, 2]] - \text{Gxytable}[[50, 2]]}{\text{Gxytable}[[52, 1]] - \text{Gxytable}[[50, 1]]};$$

$$\text{slopevxy}[4] = \frac{\nu\text{xytable}[[52, 2]] - \nu\text{xytable}[[50, 2]]}{\nu\text{xytable}[[52, 1]] - \nu\text{xytable}[[50, 1]]};$$

■ Copper Material Property Variation

Modulus of Copper

```
ExMFC[Ecopper_] =
  Ex /. {Ekapton → 2.5, νkapton -> 0.34, Eacrylic → 2.7, νacrylic -> 0.35,
    νcopper -> 0.31, Eepoxy -> 3.378, νepoxy -> 0.27, E11EPZT -> 53,
    E22EPZT -> 61, νfiber -> 0.384, G12fiber -> 21};
EyMFC[Ecopper_] =
  Ey /. {Ekapton → 2.5, νkapton -> 0.34, Eacrylic → 2.7, νacrylic -> 0.35,
    νcopper -> 0.31, Eepoxy -> 3.378, νepoxy -> 0.27, E11EPZT -> 53,
    E22EPZT -> 61, νfiber -> 0.384, G12fiber -> 21};
GxyMFC[Ecopper_] =
  Gxy /. {Ekapton → 2.5, νkapton -> 0.34, Eacrylic → 2.7, νacrylic -> 0.35,
    νcopper -> 0.31, Eepoxy -> 3.378, νepoxy -> 0.27, E11EPZT -> 53,
    E22EPZT -> 61, νfiber -> 0.384, G12fiber -> 21};
νxyMFC[Ecopper_] =
  νxy /. {Ekapton → 2.5, νkapton -> 0.34, Eacrylic → 2.7, νacrylic -> 0.35,
    νcopper -> 0.31, Eepoxy -> 3.378, νepoxy -> 0.27, E11EPZT -> 53,
    E22EPZT -> 61, νfiber -> 0.384, G12fiber -> 21};
Simplify[ExMFC[Ecopper]];
Simplify[EyMFC[Ecopper]];
Simplify[GxyMFC[Ecopper]];
Simplify[νxyMFC[Ecopper]];
```

```
Extable = Table[{Ecopper / 117.2, ExMFC[Ecopper] / ExMFCnominal},
   {Ecopper, .5 * 117.2, 1.5 * 117.2, (1.5 * 117.2 - .5 * 117.2) / 100}];
Eytable = Table[{Ecopper / 117.2, EyMFC[Ecopper] / EyMFCnominal},
   {Ecopper, .5 * 117.2, 1.5 * 117.2, (1.5 * 117.2 - .5 * 117.2) / 100}];
Gxytable = Table[{Ecopper / 117.2, GxyMFC[Ecopper] / GxyMFCnominal},
   {Ecopper, .5 * 117.2, 1.5 * 117.2, (1.5 * 117.2 - .5 * 117.2) / 100}];
νxytable = Table[{Ecopper / 117.2, νxyMFC[Ecopper] / νxyMFCnominal},
   {Ecopper, .5 * 117.2, 1.5 * 117.2, (1.5 * 117.2 - .5 * 117.2) / 100}];
plot1 = ListPlot[Extable, PlotJoined → True, PlotRange → {.95, 1.05},
  TextStyle → {FontFamily → "Times", FontSize → 12},
  PlotLabel → "Copper modulus varies", AxesOrigin → {.5, 1},
  PlotStyle -> {Red, Dashing[{}]}, DisplayFunction → Identity]
plot2 = ListPlot[Eytable, PlotJoined → True,
  PlotStyle -> {DodgerBlue, Dashing[{.015}]}, DisplayFunction → Identity]
plot3 = ListPlot[Gxytable, PlotJoined → True,
  PlotStyle -> {Green, Dashing[{.03}]}, DisplayFunction → Identity]
plot4 = ListPlot[νxytable, PlotJoined → True,
  PlotStyle -> {Carrot, Dashing[{.005, .025, .025, .025}]},
  DisplayFunction → Identity]
Show[plot1, plot2, plot3, plot4, DisplayFunction → $DisplayFunction]
```

```
- Graphics -
```

```
- Graphics -
```

```
- Graphics -
```

```
- Graphics -
```

```
- Graphics -
```

$$\text{slopeEx}[5] = \frac{\text{Extable}[[52, 2]] - \text{Extable}[[50, 2]]}{\text{Extable}[[52, 1]] - \text{Extable}[[50, 1]]};$$

$$\text{slopeEy}[5] = \frac{\text{Eytable}[[52, 2]] - \text{Eytable}[[50, 2]]}{\text{Eytable}[[52, 1]] - \text{Eytable}[[50, 1]]};$$

$$\text{slopeGxy}[5] = \frac{\text{Gxytable}[[52, 2]] - \text{Gxytable}[[50, 2]]}{\text{Gxytable}[[52, 1]] - \text{Gxytable}[[50, 1]]};$$

$$\text{slopevxy}[5] = \frac{\text{νxytable}[[52, 2]] - \text{νxytable}[[50, 2]]}{\text{νxytable}[[52, 1]] - \text{νxytable}[[50, 1]]};$$

Poisson's Ratio of Copper

```
ExMFC[νcopper_] =
  Ex /. {Ekapton → 2.5, νkapton -> 0.34, Eacrylic → 2.7, νacrylic -> 0.35,
    Ecopper → 117.2, Eepoxy -> 3.378, νepoxy -> 0.27, E11EPZT -> 53,
    E22EPZT -> 61, νfiber -> 0.384, G12fiber -> 21};
EyMFC[νcopper_] =
  Ey /. {Ekapton → 2.5, νkapton -> 0.34, Eacrylic → 2.7, νacrylic -> 0.35,
    Ecopper → 117.2, Eepoxy -> 3.378, νepoxy -> 0.27, E11EPZT -> 53,
    E22EPZT -> 61, νfiber -> 0.384, G12fiber -> 21};
GxyMFC[νcopper_] =
  Gxy /. {Ekapton → 2.5, νkapton -> 0.34, Eacrylic → 2.7, νacrylic -> 0.35,
    Ecopper → 117.2, Eepoxy -> 3.378, νepoxy -> 0.27, E11EPZT -> 53,
    E22EPZT -> 61, νfiber -> 0.384, G12fiber -> 21};
νxyMFC[νcopper_] =
  νxy /. {Ekapton → 2.5, νkapton -> 0.34, Eacrylic → 2.7, νacrylic -> 0.35,
    Ecopper → 117.2, Eepoxy -> 3.378, νepoxy -> 0.27, E11EPZT -> 53,
    E22EPZT -> 61, νfiber -> 0.384, G12fiber -> 21};
Simplify[ExMFC[νcopper]];
Simplify[EyMFC[νcopper]];
Simplify[GxyMFC[νcopper]];
Simplify[νxyMFC[νcopper]];
nomprop = 0.31;
Extable = Table[{νcopper / nomprop, ExMFC[νcopper] / ExMFCnominal},
   {νcopper, .5 * nomprop, 1.5 * nomprop, (1.5 * nomprop - .5 * nomprop) / 100}];
Eytable = Table[{νcopper / nomprop, EyMFC[νcopper] / EyMFCnominal},
   {νcopper, .5 * nomprop, 1.5 * nomprop, (1.5 * nomprop - .5 * nomprop) / 100}];
Gxytable = Table[{νcopper / nomprop, GxyMFC[νcopper] / GxyMFCnominal},
   {νcopper, .5 * nomprop, 1.5 * nomprop, (1.5 * nomprop - .5 * nomprop) / 100}];
νxytable = Table[{νcopper / nomprop, νxyMFC[νcopper] / νxyMFCnominal},
   {νcopper, .5 * nomprop, 1.5 * nomprop, (1.5 * nomprop - .5 * nomprop) / 100}];
plot1 = ListPlot[Extable, PlotJoined → True, PlotRange → {.995, 1.005},
  TextStyle → {FontFamily → "Times", FontSize → 12},
  PlotLabel → "Copper  ν varies", AxesOrigin → {.5, 1},
  PlotStyle -> {Red, Dashing[{}]}, DisplayFunction → Identity]
plot2 = ListPlot[Eytable, PlotJoined → True,
  PlotStyle -> {DodgerBlue, Dashing[{.015}]}, DisplayFunction → Identity]
plot3 = ListPlot[Gxytable, PlotJoined → True,
  PlotStyle -> {Green, Dashing[{.03}]}, DisplayFunction → Identity]
plot4 = ListPlot[νxytable, PlotJoined → True,
  PlotStyle -> {Carrot, Dashing[{.005, .025, .025, .025}]},
  DisplayFunction → Identity]
Show[plot1, plot2, plot3, plot4, DisplayFunction → $DisplayFunction]
```

- Graphics -

- Graphics -

- Graphics -

- Graphics -

- Graphics -

$$\text{slopeEx}[6] = \frac{\text{Extable}[[52, 2]] - \text{Extable}[[50, 2]]}{\text{Extable}[[52, 1]] - \text{Extable}[[50, 1]]};$$

$$\text{slopeEy}[6] = \frac{\text{Eytable}[[52, 2]] - \text{Eytable}[[50, 2]]}{\text{Eytable}[[52, 1]] - \text{Eytable}[[50, 1]]};$$

$$\text{slopeGxy}[6] = \frac{\text{Gxytable}[[52, 2]] - \text{Gxytable}[[50, 2]]}{\text{Gxytable}[[52, 1]] - \text{Gxytable}[[50, 1]]};$$

$$\text{slopevxy}[6] = \frac{\nu\text{xytable}[[52, 2]] - \nu\text{xytable}[[50, 2]]}{\nu\text{xytable}[[52, 1]] - \nu\text{xytable}[[50, 1]]};$$

■ Epoxy Material Property Variation

Modulus of Epoxy

```
ExMFC[Eepoxy_] =
  Ex /. {Ekapton → 2.5, νkapton -> 0.34, Eacrylic → 2.7, νacrylic -> 0.35,
    Ecopper → 117.2, νcopper -> 0.31, νepoxy -> 0.27, E11EPZT -> 53,
    E22EPZT -> 61, νfiber -> 0.384, G12fiber -> 21};
EyMFC[Eepoxy_] =
  Ey /. {Ekapton → 2.5, νkapton -> 0.34, Eacrylic → 2.7, νacrylic -> 0.35,
    Ecopper → 117.2, νcopper -> 0.31, νepoxy -> 0.27, E11EPZT -> 53,
    E22EPZT -> 61, νfiber -> 0.384, G12fiber -> 21};
GxyMFC[Eepoxy_] =
  Gxy /. {Ekapton → 2.5, νkapton -> 0.34, Eacrylic → 2.7, νacrylic -> 0.35,
    Ecopper → 117.2, νcopper -> 0.31, νepoxy -> 0.27, E11EPZT -> 53,
    E22EPZT -> 61, νfiber -> 0.384, G12fiber -> 21};
νxyMFC[Eepoxy_] =
  νxy /. {Ekapton → 2.5, νkapton -> 0.34, Eacrylic → 2.7, νacrylic -> 0.35,
    Ecopper → 117.2, νcopper -> 0.31, νepoxy -> 0.27, E11EPZT -> 53,
    E22EPZT -> 61, νfiber -> 0.384, G12fiber -> 21};
Simplify[ExMFC[Eepoxy]];
Simplify[EyMFC[Eepoxy]];
Simplify[GxyMFC[Eepoxy]];
Simplify[νxyMFC[Eepoxy]];
nomprop = 3.378;
```

```
Extable = Table[{Eepoxy / nomprop, ExMFC[Eepoxy] / ExMFCnominal},
   {Eepoxy, .5 * nomprop, 1.5 * nomprop, (1.5 * nomprop - .5 * nomprop) / 100}];
Eytable = Table[{Eepoxy / nomprop, EyMFC[Eepoxy] / EyMFCnominal},
   {Eepoxy, .5 * nomprop, 1.5 * nomprop, (1.5 * nomprop - .5 * nomprop) / 100}];
Gxytable = Table[{Eepoxy / nomprop, GxyMFC[Eepoxy] / GxyMFCnominal},
   {Eepoxy, .5 * nomprop, 1.5 * nomprop, (1.5 * nomprop - .5 * nomprop) / 100}];
νxytable = Table[{Eepoxy / nomprop, νxyMFC[Eepoxy] / νxyMFCnominal},
   {Eepoxy, .5 * nomprop, 1.5 * nomprop, (1.5 * nomprop - .5 * nomprop) / 100}];
plot1 = ListPlot[Extable, PlotJoined → True, PlotRange → {.6, 1.4},
  TextStyle → {FontFamily → "Times", FontSize → 12},
  PlotLabel → "Epoxy modulus varies", AxesOrigin → {.5, 1},
  PlotStyle -> {Red, Dashing[{}]}, DisplayFunction → Identity]
plot2 = ListPlot[Eytable, PlotJoined → True,
  PlotStyle -> {DodgerBlue, Dashing[{.015}]}, DisplayFunction → Identity]
plot3 = ListPlot[Gxytable, PlotJoined → True,
  PlotStyle -> {Green, Dashing[{.03}]}, DisplayFunction → Identity]
plot4 = ListPlot[νxytable, PlotJoined → True,
  PlotStyle -> {Carrot, Dashing[{.005, .025, .025, .025}]},
  DisplayFunction → Identity]
Show[plot1, plot2, plot3, plot4, DisplayFunction → $DisplayFunction]
```

```
- Graphics -
```

```
- Graphics -
```

```
- Graphics -
```

```
- Graphics -
```

```
- Graphics -
```

$$\text{slopeEx}[7] = \frac{\text{Extable}[[52, 2]] - \text{Extable}[[50, 2]]}{\text{Extable}[[52, 1]] - \text{Extable}[[50, 1]]};$$

$$\text{slopeEy}[7] = \frac{\text{Eytable}[[52, 2]] - \text{Eytable}[[50, 2]]}{\text{Eytable}[[52, 1]] - \text{Eytable}[[50, 1]]};$$

$$\text{slopeGxy}[7] = \frac{\text{Gxytable}[[52, 2]] - \text{Gxytable}[[50, 2]]}{\text{Gxytable}[[52, 1]] - \text{Gxytable}[[50, 1]]};$$

$$\text{slopevxy}[7] = \frac{\text{νxytable}[[52, 2]] - \text{νxytable}[[50, 2]]}{\text{νxytable}[[52, 1]] - \text{νxytable}[[50, 1]]};$$

Poisson's Ratio of Epoxy

```
ExMFC[νepoxy_] =
  Ex /. {Ekapton → 2.5, νkapton -> 0.34, Eacrylic → 2.7, νacrylic -> 0.35,
    Ecopper → 117.2, νcopper -> 0.31, Eepoxy -> 3.378, E11EPZT -> 53,
    E22EPZT -> 61, νfiber -> 0.384, G12fiber -> 21};
EyMFC[νepoxy_] =
 Ey /. {Ekapton → 2.5, νkapton -> 0.34, Eacrylic → 2.7, νacrylic -> 0.35,
   Ecopper → 117.2, νcopper -> 0.31, Eepoxy -> 3.378, E11EPZT -> 53,
   E22EPZT -> 61, νfiber -> 0.384, G12fiber -> 21};
GxyMFC[νepoxy_] =
 Gxy /. {Ekapton → 2.5, νkapton -> 0.34, Eacrylic → 2.7, νacrylic -> 0.35,
   Ecopper → 117.2, νcopper -> 0.31, Eepoxy -> 3.378, E11EPZT -> 53,
   E22EPZT -> 61, νfiber -> 0.384, G12fiber -> 21};
νxyMFC[νepoxy_] =
 νxy /. {Ekapton → 2.5, νkapton -> 0.34, Eacrylic → 2.7, νacrylic -> 0.35,
   Ecopper → 117.2, νcopper -> 0.31, Eepoxy -> 3.378, E11EPZT -> 53,
   E22EPZT -> 61, νfiber -> 0.384, G12fiber -> 21};
Simplify[ExMFC[νepoxy]];
Simplify[EyMFC[νepoxy]];
Simplify[GxyMFC[νepoxy]];
Simplify[νxyMFC[νepoxy]];
nomprop = 0.27;
Extable = Table[{νepoxy / nomprop, ExMFC[νepoxy] / ExMFCnominal},
   {νepoxy, .5 * nomprop, 1.5 * nomprop, (1.5 * nomprop - .5 * nomprop) / 100}];
Eytable = Table[{νepoxy / nomprop, EyMFC[νepoxy] / EyMFCnominal},
  {νepoxy, .5 * nomprop, 1.5 * nomprop, (1.5 * nomprop - .5 * nomprop) / 100}];
Gxytable = Table[{νepoxy / nomprop, GxyMFC[νepoxy] / GxyMFCnominal},
  {νepoxy, .5 * nomprop, 1.5 * nomprop, (1.5 * nomprop - .5 * nomprop) / 100}];
νxytable = Table[{νepoxy / nomprop, νxyMFC[νepoxy] / νxyMFCnominal},
  {νepoxy, .5 * nomprop, 1.5 * nomprop, (1.5 * nomprop - .5 * nomprop) / 100}];
plot1 = ListPlot[Extable, PlotJoined → True, PlotRange → {.92, 1.1},
  TextStyle → {FontFamily → "Times", FontSize → 12},
  PlotLabel → "Epoxy  ν varies", AxesOrigin → {.5, 1},
  PlotStyle -> {Red, Dashing[{}]}, DisplayFunction → Identity]
plot2 = ListPlot[Eytable, PlotJoined → True,
  PlotStyle -> {DodgerBlue, Dashing[{.015}]}, DisplayFunction → Identity]
plot3 = ListPlot[Gxytable, PlotJoined → True,
  PlotStyle -> {Green, Dashing[{.03}]}, DisplayFunction → Identity]
plot4 = ListPlot[νxytable, PlotJoined → True,
  PlotStyle -> {Carrot, Dashing[{.005, .025, .025, .025}]},
  DisplayFunction → Identity]
Show[plot1, plot2, plot3, plot4, DisplayFunction → $DisplayFunction]
```

- Graphics -

- Graphics -

- Graphics -

- Graphics -

- Graphics -

$$\text{slopeEx}[8] = \frac{\text{Extable}[[52, 2]] - \text{Extable}[[50, 2]]}{\text{Extable}[[52, 1]] - \text{Extable}[[50, 1]]};$$

$$\text{slopeEy}[8] = \frac{\text{Eytable}[[52, 2]] - \text{Eytable}[[50, 2]]}{\text{Eytable}[[52, 1]] - \text{Eytable}[[50, 1]]};$$

$$\text{slopeGxy}[8] = \frac{\text{Gxytable}[[52, 2]] - \text{Gxytable}[[50, 2]]}{\text{Gxytable}[[52, 1]] - \text{Gxytable}[[50, 1]]};$$

$$\text{slopevxy}[8] = \frac{\nu\text{xytable}[[52, 2]] - \nu\text{xytable}[[50, 2]]}{\nu\text{xytable}[[52, 1]] - \nu\text{xytable}[[50, 1]]};$$

■ **PZT Material Property Variation**

Poling direction modulus of PZT

```
ExMFC[E11EPZT_] =
  Ex /. {Ekapton → 2.5, νkapton -> 0.34, Eacrylic → 2.7, νacrylic -> 0.35,
    Ecopper → 117.2, νcopper -> 0.31, Eepoxy → 3.378, νepoxy -> 0.27,
    E22EPZT -> 61, νfiber -> 0.384, G12fiber -> 21};
EyMFC[E11EPZT_] =
  Ey /. {Ekapton → 2.5, νkapton -> 0.34, Eacrylic → 2.7, νacrylic -> 0.35,
    Ecopper → 117.2, νcopper -> 0.31, Eepoxy → 3.378, νepoxy -> 0.27,
    E22EPZT -> 61, νfiber -> 0.384, G12fiber -> 21};
GxyMFC[E11EPZT_] =
  Gxy /. {Ekapton → 2.5, νkapton -> 0.34, Eacrylic → 2.7, νacrylic -> 0.35,
    Ecopper → 117.2, νcopper -> 0.31, Eepoxy → 3.378, νepoxy -> 0.27,
    E22EPZT -> 61, νfiber -> 0.384, G12fiber -> 21};
νxyMFC[E11EPZT_] =
  νxy /. {Ekapton → 2.5, νkapton -> 0.34, Eacrylic → 2.7, νacrylic -> 0.35,
    Ecopper → 117.2, νcopper -> 0.31, Eepoxy → 3.378, νepoxy -> 0.27,
    E22EPZT -> 61, νfiber -> 0.384, G12fiber -> 21};
Simplify[ExMFC[E11EPZT]];
Simplify[EyMFC[E11EPZT]];
Simplify[GxyMFC[E11EPZT]];
Simplify[νxyMFC[E11EPZT]];
nomprop = 53;
```

```
Extable = Table[{E11EPZT / nomprop, ExMFC[E11EPZT] / ExMFCnominal},
   {E11EPZT, .5 * nomprop, 1.5 * nomprop, (1.5 * nomprop - .5 * nomprop) / 100}];
Eytable = Table[{E11EPZT / nomprop, EyMFC[E11EPZT] / EyMFCnominal},
   {E11EPZT, .5 * nomprop, 1.5 * nomprop, (1.5 * nomprop - .5 * nomprop) / 100}];
Gxytable = Table[{E11EPZT / nomprop, GxyMFC[E11EPZT] / GxyMFCnominal},
   {E11EPZT, .5 * nomprop, 1.5 * nomprop, (1.5 * nomprop - .5 * nomprop) / 100}];
νxytable = Table[{E11EPZT / nomprop, νxyMFC[E11EPZT] / νxyMFCnominal},
   {E11EPZT, .5 * nomprop, 1.5 * nomprop, (1.5 * nomprop - .5 * nomprop) / 100}];
plot1 = ListPlot[Extable, PlotJoined → True, PlotRange → {.5, 1.5},
  TextStyle → {FontFamily → "Times", FontSize → 12},
  PlotLabel → "PZT poling direction modulus varies", AxesOrigin → {.5, 1},
  PlotStyle -> {Red, Dashing[{}]}, DisplayFunction → Identity]
plot2 = ListPlot[Eytable, PlotJoined → True,
  PlotStyle -> {DodgerBlue, Dashing[{.015}]}, DisplayFunction → Identity]
plot3 = ListPlot[Gxytable, PlotJoined → True,
  PlotStyle -> {Green, Dashing[{.03}]}, DisplayFunction → Identity]
plot4 = ListPlot[νxytable, PlotJoined → True,
  PlotStyle -> {Carrot, Dashing[{.005, .025, .025, .025}]},
  DisplayFunction → Identity]
Show[plot1, plot2, plot3, plot4, DisplayFunction → $DisplayFunction]
```

```
- Graphics -
```

```
- Graphics -
```

```
- Graphics -
```

```
- Graphics -
```

```
- Graphics -
```

$$\text{slopeEx}[9] = \frac{\text{Extable}[[52, 2]] - \text{Extable}[[50, 2]]}{\text{Extable}[[52, 1]] - \text{Extable}[[50, 1]]};$$

$$\text{slopeEy}[9] = \frac{\text{Eytable}[[52, 2]] - \text{Eytable}[[50, 2]]}{\text{Eytable}[[52, 1]] - \text{Eytable}[[50, 1]]};$$

$$\text{slopeGxy}[9] = \frac{\text{Gxytable}[[52, 2]] - \text{Gxytable}[[50, 2]]}{\text{Gxytable}[[52, 1]] - \text{Gxytable}[[50, 1]]};$$

$$\text{slopevxy}[9] = \frac{\text{νxytable}[[52, 2]] - \text{νxytable}[[50, 2]]}{\text{νxytable}[[52, 1]] - \text{νxytable}[[50, 1]]};$$

Transverse direction modulus of PZT

```
ExMFC[E22EPZT_] =
  Ex /. {Ekapton → 2.5, νkapton -> 0.34, Eacrylic → 2.7, νacrylic -> 0.35,
    Ecopper → 117.2, νcopper -> 0.31, Eepoxy → 3.378, νepoxy -> 0.27,
    E11EPZT -> 53, νfiber -> 0.384, G12fiber -> 21};
EyMFC[E22EPZT_] =
  Ey /. {Ekapton → 2.5, νkapton -> 0.34, Eacrylic → 2.7, νacrylic -> 0.35,
    Ecopper → 117.2, νcopper -> 0.31, Eepoxy → 3.378, νepoxy -> 0.27,
    E11EPZT -> 53, νfiber -> 0.384, G12fiber -> 21};
GxyMFC[E22EPZT_] =
  Gxy /. {Ekapton → 2.5, νkapton -> 0.34, Eacrylic → 2.7, νacrylic -> 0.35,
    Ecopper → 117.2, νcopper -> 0.31, Eepoxy → 3.378, νepoxy -> 0.27,
    E11EPZT -> 53, νfiber -> 0.384, G12fiber -> 21};
νxyMFC[E22EPZT_] =
  νxy /. {Ekapton → 2.5, νkapton -> 0.34, Eacrylic → 2.7, νacrylic -> 0.35,
    Ecopper → 117.2, νcopper -> 0.31, Eepoxy → 3.378, νepoxy -> 0.27,
    E11EPZT -> 53, νfiber -> 0.384, G12fiber -> 21};
Simplify[ExMFC[E22EPZT]];
Simplify[EyMFC[E22EPZT]];
Simplify[GxyMFC[E22EPZT]];
Simplify[νxyMFC[E22EPZT]];
nomprop = 61;
Extable = Table[{E22EPZT / nomprop, ExMFC[E22EPZT] / ExMFCnominal},
   {E22EPZT, .5 * nomprop, 1.5 * nomprop, (1.5 * nomprop - .5 * nomprop) / 100}];
Eytable = Table[{E22EPZT / nomprop, EyMFC[E22EPZT] / EyMFCnominal},
   {E22EPZT, .5 * nomprop, 1.5 * nomprop, (1.5 * nomprop - .5 * nomprop) / 100}];
Gxytable = Table[{E22EPZT / nomprop, GxyMFC[E22EPZT] / GxyMFCnominal},
   {E22EPZT, .5 * nomprop, 1.5 * nomprop, (1.5 * nomprop - .5 * nomprop) / 100}];
νxytable = Table[{E22EPZT / nomprop, νxyMFC[E22EPZT] / νxyMFCnominal},
   {E22EPZT, .5 * nomprop, 1.5 * nomprop, (1.5 * nomprop - .5 * nomprop) / 100}];
plot1 = ListPlot[Extable, PlotJoined → True, PlotRange → {.8, 1.1},
  TextStyle → {FontFamily → "Times", FontSize → 12},
  PlotLabel → "PZT transverse modulus varies", AxesOrigin → {.5, 1},
  PlotStyle -> {Red, Dashing[{}]}, DisplayFunction → Identity]
plot2 = ListPlot[Eytable, PlotJoined → True,
  PlotStyle -> {DodgerBlue, Dashing[{.015}]}, DisplayFunction → Identity]
plot3 = ListPlot[Gxytable, PlotJoined → True,
  PlotStyle -> {Green, Dashing[{.03}]}, DisplayFunction → Identity]
plot4 = ListPlot[νxytable, PlotJoined → True,
  PlotStyle -> {Carrot, Dashing[{.005, .025, .025, .025}]},
  DisplayFunction → Identity]
Show[plot1, plot2, plot3, plot4, DisplayFunction → $DisplayFunction]
```

- Graphics -

- Graphics -

- Graphics -

- Graphics -

- Graphics -

$$\text{slopeEx}[10] = \frac{\text{Extable}[[52, 2]] - \text{Extable}[[50, 2]]}{\text{Extable}[[52, 1]] - \text{Extable}[[50, 1]]};$$

$$\text{slopeEy}[10] = \frac{\text{Eytable}[[52, 2]] - \text{Eytable}[[50, 2]]}{\text{Eytable}[[52, 1]] - \text{Eytable}[[50, 1]]};$$

$$\text{slopeGxy}[10] = \frac{\text{Gxytable}[[52, 2]] - \text{Gxytable}[[50, 2]]}{\text{Gxytable}[[52, 1]] - \text{Gxytable}[[50, 1]]};$$

$$\text{slopevxy}[10] = \frac{\nu\text{xytable}[[52, 2]] - \nu\text{xytable}[[50, 2]]}{\nu\text{xytable}[[52, 1]] - \nu\text{xytable}[[50, 1]]};$$

In-plane Poisson's Ratio of PZT

```
ExMFC[νfiber_] =
  Ex /. {Ekapton → 2.5, νkapton -> 0.34, Eacrylic → 2.7, νacrylic -> 0.35,
    Ecopper → 117.2, νcopper -> 0.31, Eepoxy → 3.378, νepoxy -> 0.27,
    E11EPZT -> 53, E22EPZT -> 61, G12fiber -> 21};
EyMFC[νfiber_] =
  Ey /. {Ekapton → 2.5, νkapton -> 0.34, Eacrylic → 2.7, νacrylic -> 0.35,
    Ecopper → 117.2, νcopper -> 0.31, Eepoxy → 3.378, νepoxy -> 0.27,
    E11EPZT -> 53, E22EPZT -> 61, G12fiber -> 21};
GxyMFC[νfiber_] =
  Gxy /. {Ekapton → 2.5, νkapton -> 0.34, Eacrylic → 2.7, νacrylic -> 0.35,
    Ecopper → 117.2, νcopper -> 0.31, Eepoxy → 3.378, νepoxy -> 0.27,
    E11EPZT -> 53, E22EPZT -> 61, G12fiber -> 21};
νxyMFC[νfiber_] =
  νxy /. {Ekapton → 2.5, νkapton -> 0.34, Eacrylic → 2.7, νacrylic -> 0.35,
    Ecopper → 117.2, νcopper -> 0.31, Eepoxy → 3.378, νepoxy -> 0.27,
    E11EPZT -> 53, E22EPZT -> 61, G12fiber -> 21};
Simplify[ExMFC[νfiber]];
Simplify[EyMFC[νfiber]];
Simplify[GxyMFC[νfiber]];
Simplify[νxyMFC[νfiber]];
nomprop = 0.384;
```

```
Extable = Table[{νfiber / nomprop, ExMFC[νfiber] / ExMFCnominal},
   {νfiber, .5 * nomprop, 1.5 * nomprop, (1.5 * nomprop - .5 * nomprop) / 100}];
Eytable = Table[{νfiber / nomprop, EyMFC[νfiber] / EyMFCnominal},
   {νfiber, .5 * nomprop, 1.5 * nomprop, (1.5 * nomprop - .5 * nomprop) / 100}];
Gxytable = Table[{νfiber / nomprop, GxyMFC[νfiber] / GxyMFCnominal},
   {νfiber, .5 * nomprop, 1.5 * nomprop, (1.5 * nomprop - .5 * nomprop) / 100}];
νxytable = Table[{νfiber / nomprop, νxyMFC[νfiber] / νxyMFCnominal},
   {νfiber, .5 * nomprop, 1.5 * nomprop, (1.5 * nomprop - .5 * nomprop) / 100}];
plot1 = ListPlot[Extable, PlotJoined → True, PlotRange → {.55, 1.5},
  TextStyle → {FontFamily → "Times", FontSize → 12},
  PlotLabel → "PZT in-plane  ν varies", AxesOrigin → {.5, 1},
  PlotStyle -> {Red, Dashing[{}]}, DisplayFunction → Identity]
plot2 = ListPlot[Eytable, PlotJoined → True,
  PlotStyle -> {DodgerBlue, Dashing[{.015}]}, DisplayFunction → Identity]
plot3 = ListPlot[Gxytable, PlotJoined → True,
  PlotStyle -> {Green, Dashing[{.03}]}, DisplayFunction → Identity]
plot4 = ListPlot[νxytable, PlotJoined → True,
  PlotStyle -> {Carrot, Dashing[{.005, .025, .025, .025}]},
  DisplayFunction → Identity]
Show[plot1, plot2, plot3, plot4, DisplayFunction → $DisplayFunction]
```

```
- Graphics -
```

```
- Graphics -
```

```
- Graphics -
```

```
- Graphics -
```

```
- Graphics -
```

$$\text{slopeEx}[11] = \frac{\text{Extable}[[52, 2]] - \text{Extable}[[50, 2]]}{\text{Extable}[[52, 1]] - \text{Extable}[[50, 1]]};$$

$$\text{slopeEy}[11] = \frac{\text{Eytable}[[52, 2]] - \text{Eytable}[[50, 2]]}{\text{Eytable}[[52, 1]] - \text{Eytable}[[50, 1]]};$$

$$\text{slopeGxy}[11] = \frac{\text{Gxytable}[[52, 2]] - \text{Gxytable}[[50, 2]]}{\text{Gxytable}[[52, 1]] - \text{Gxytable}[[50, 1]]};$$

$$\text{slopevxy}[11] = \frac{\nu\text{xytable}[[52, 2]] - \nu\text{xytable}[[50, 2]]}{\nu\text{xytable}[[52, 1]] - \nu\text{xytable}[[50, 1]]};$$

In-plane shear modulus of PZT

```
ExMFC[G12fiber_] =
  Ex /. {Ekapton → 2.5, νkapton -> 0.34, Eacrylic → 2.7, νacrylic -> 0.35,
    Ecopper → 117.2, νcopper -> 0.31, Eepoxy → 3.378, νepoxy -> 0.27,
    E11EPZT -> 53, E22EPZT -> 61, νfiber -> 0.384};
EyMFC[G12fiber_] =
  Ey /. {Ekapton → 2.5, νkapton -> 0.34, Eacrylic → 2.7, νacrylic -> 0.35,
    Ecopper → 117.2, νcopper -> 0.31, Eepoxy → 3.378, νepoxy -> 0.27,
    E11EPZT -> 53, E22EPZT -> 61, νfiber -> 0.384};
GxyMFC[G12fiber_] =
  Gxy /. {Ekapton → 2.5, νkapton -> 0.34, Eacrylic → 2.7, νacrylic -> 0.35,
    Ecopper → 117.2, νcopper -> 0.31, Eepoxy → 3.378, νepoxy -> 0.27,
    E11EPZT -> 53, E22EPZT -> 61, νfiber -> 0.384};
νxyMFC[G12fiber_] =
  νxy /. {Ekapton → 2.5, νkapton -> 0.34, Eacrylic → 2.7, νacrylic -> 0.35,
    Ecopper → 117.2, νcopper -> 0.31, Eepoxy → 3.378, νepoxy -> 0.27,
    E11EPZT -> 53, E22EPZT -> 61, νfiber -> 0.384};
Simplify[ExMFC[G12fiber]];
Simplify[EyMFC[G12fiber]];
Simplify[GxyMFC[G12fiber]];
Simplify[νxyMFC[G12fiber]];
nomprop = 21;
Extable = Table[{G12fiber / nomprop, ExMFC[G12fiber] / ExMFCnominal},
   {G12fiber, .5 * nomprop, 1.5 * nomprop, (1.5 * nomprop - .5 * nomprop) / 100}];
Eytable = Table[{G12fiber / nomprop, EyMFC[G12fiber] / EyMFCnominal},
   {G12fiber, .5 * nomprop, 1.5 * nomprop, (1.5 * nomprop - .5 * nomprop) / 100}];
Gxytable = Table[{G12fiber / nomprop, GxyMFC[G12fiber] / GxyMFCnominal},
   {G12fiber, .5 * nomprop, 1.5 * nomprop, (1.5 * nomprop - .5 * nomprop) / 100}];
νxytable = Table[{G12fiber / nomprop, νxyMFC[G12fiber] / νxyMFCnominal},
   {G12fiber, .5 * nomprop, 1.5 * nomprop, (1.5 * nomprop - .5 * nomprop) / 100}];
plot1 = ListPlot[Extable, PlotJoined → True, PlotRange → {.7, 1.2},
  TextStyle → {FontFamily → "Times", FontSize → 12},
  PlotLabel → "PZT in-plane shear modulus varies", AxesOrigin → {.5, 1},
  PlotStyle -> {Red, Dashing[{}]}, DisplayFunction → Identity]
plot2 = ListPlot[Eytable, PlotJoined → True,
  PlotStyle -> {DodgerBlue, Dashing[{.015}]}, DisplayFunction → Identity]
plot3 = ListPlot[Gxytable, PlotJoined → True,
  PlotStyle -> {Green, Dashing[{.03}]}, DisplayFunction → Identity]
plot4 = ListPlot[νxytable, PlotJoined → True,
  PlotStyle -> {Carrot, Dashing[{.005, .025, .025, .025}]},
  DisplayFunction → Identity]
Show[plot1, plot2, plot3, plot4, DisplayFunction → $DisplayFunction]
```

- Graphics -

- Graphics -

- Graphics -

- Graphics -

- Graphics -

$$\text{slopeEx}[12] = \frac{\text{Extable}[[52, 2]] - \text{Extable}[[50, 2]]}{\text{Extable}[[52, 1]] - \text{Extable}[[50, 1]]};$$

$$\text{slopeEy}[12] = \frac{\text{Eytable}[[52, 2]] - \text{Eytable}[[50, 2]]}{\text{Eytable}[[52, 1]] - \text{Eytable}[[50, 1]]};$$

$$\text{slopeGxy}[12] = \frac{\text{Gxytable}[[52, 2]] - \text{Gxytable}[[50, 2]]}{\text{Gxytable}[[52, 1]] - \text{Gxytable}[[50, 1]]};$$

$$\text{slopevxy}[12] = \frac{\nu\text{xytable}[[52, 2]] - \nu\text{xytable}[[50, 2]]}{\nu\text{xytable}[[52, 1]] - \nu\text{xytable}[[50, 1]]};$$

slopeExcalc
slopeEycalc
slopeGxycalc
slopevxycalc

{0.0134874, 0.000391283, 0.00729027, 0.000279302, 0.00962406, -0.000601029,
 0.0244814, 0.000223464, 0.944492, 0.00062517, 0.0202517, 0.}

{0.0254923, 0.00352973, 0.0138239, 0.00210358, 0.192545, 0.000518845,
 0.545533, 0.00114178, 0.00359104, 0.21903, -0.00324582, 0.}

{0.0297234, -0.00754182, 0.0159318, -0.00413049, 0.000355122,
 -0.0000840281, 0.659099, -0.140122, 0., 0., 0., 0.294911}

{0.0032569, 0.0305777, 0.00224838, 0.017282, -0.182937,
 0.00604777, 0.135093, 0.0981153, -0.0105627, 0.0529133, 0.86677, 0.}

■ Now look at sensitivities due to variations in volume fractions of PZT and Copper layers for reference material properties:

First we will vary the fiber volume fraction of the PZT fiber layer.

```
Clear[VfiberPZT, VmatrixPZT, Vfiberelectrode, Vmatrixelectrode]
VmatrixPZT = 1 - VfiberPZT;
Vfiberelectrode = wcopper / (wcopper + (electrodespacing - wcopper));
Vmatrixelectrode = 1 - Vfiberelectrode;
ExMFC[VfiberPZT_] =
  Ex /. {Ekapton → 2.5, νkapton -> 0.34, Eacrylic → 2.7, νacrylic -> 0.35,
    Ecopper → 117.2, νcopper -> 0.31, Eepoxy → 3.378, νepoxy -> 0.27,
    E11EPZT -> 53, E22EPZT -> 61, νfiber -> 0.384, G12fiber -> 21};
EyMFC[VfiberPZT_] =
  Ey /. {Ekapton → 2.5, νkapton -> 0.34, Eacrylic → 2.7, νacrylic -> 0.35,
    Ecopper → 117.2, νcopper -> 0.31, Eepoxy → 3.378, νepoxy -> 0.27,
    E11EPZT -> 53, E22EPZT -> 61, νfiber -> 0.384, G12fiber -> 21};
GxyMFC[VfiberPZT_] =
  Gxy /. {Ekapton → 2.5, νkapton -> 0.34, Eacrylic → 2.7, νacrylic -> 0.35,
    Ecopper → 117.2, νcopper -> 0.31, Eepoxy → 3.378, νepoxy -> 0.27,
    E11EPZT -> 53, E22EPZT -> 61, νfiber -> 0.384, G12fiber -> 21};
νxyMFC[VfiberPZT_] =
  νxy /. {Ekapton → 2.5, νkapton -> 0.34, Eacrylic → 2.7, νacrylic -> 0.35,
    Ecopper → 117.2, νcopper -> 0.31, Eepoxy → 3.378, νepoxy -> 0.27,
    E11EPZT -> 53, E22EPZT -> 61, νfiber -> 0.384, G12fiber -> 21};
Simplify[ExMFC[VfiberPZT]];
Simplify[EyMFC[VfiberPZT]];
Simplify[GxyMFC[VfiberPZT]];
Simplify[νxyMFC[VfiberPZT]];
Plot[{ExMFC[VfiberPZT] / ExMFCnominal, EyMFC[VfiberPZT] / EyMFCnominal,
  GxyMFC[VfiberPZT] / GxyMFCnominal, νxyMFC[VfiberPZT] / νxyMFCnominal},
 {VfiberPZT, 0, 1},
 PlotStyle -> {{Red, Dashing[{}]}, {DodgerBlue, Dashing[{.015}]},
   {Green, Dashing[{.03}]}, {Carrot, Dashing[{.005, .025, .025, .025}]}},
 TextStyle → {FontFamily → "Times", FontSize → 12},
 PlotLabel → "volume fraction of PZT varies",
 PlotLegend → {"E_x^MFC/ref. E_x^MFC", "E_y^MFC/ref. E_y^MFC", "G_xy^MFC/ref. G_xy^MFC",
   "ν_xy^MFC/ref. ν_xy^MFC"}, LegendPosition → {-.6, .1}, LegendSize → {1.2, .4}]
```

- Graphics -

Next, we will vary the fiber volume fraction of the copper electrode layer.

```
Clear[VfiberPZT, VmatrixPZT, Vfiberelectrode, Vmatrixelectrode]
VfiberPZT = wfiber / (wfiber + fiberspacing);
VmatrixPZT = 1 - VfiberPZT;
Vmatrixelectrode = 1 - Vfiberelectrode;
ExMFC[Vfiberelectrode_] =
  Ex /. {Ekapton → 2.5, νkapton -> 0.34, Eacrylic → 2.7, νacrylic -> 0.35,
    Ecopper → 117.2, νcopper -> 0.31, Eepoxy → 3.378, νepoxy -> 0.27,
    E11EPZT -> 53, E22EPZT -> 61, νfiber -> 0.384, G12fiber -> 21};
EyMFC[Vfiberelectrode_] =
  Ey /. {Ekapton → 2.5, νkapton -> 0.34, Eacrylic → 2.7, νacrylic -> 0.35,
    Ecopper → 117.2, νcopper -> 0.31, Eepoxy → 3.378, νepoxy -> 0.27,
    E11EPZT -> 53, E22EPZT -> 61, νfiber -> 0.384, G12fiber -> 21};
GxyMFC[Vfiberelectrode_] =
  Gxy /. {Ekapton → 2.5, νkapton -> 0.34, Eacrylic → 2.7, νacrylic -> 0.35,
    Ecopper → 117.2, νcopper -> 0.31, Eepoxy → 3.378, νepoxy -> 0.27,
    E11EPZT -> 53, E22EPZT -> 61, νfiber -> 0.384, G12fiber -> 21};
νxyMFC[Vfiberelectrode_] =
  νxy /. {Ekapton → 2.5, νkapton -> 0.34, Eacrylic → 2.7, νacrylic -> 0.35,
    Ecopper → 117.2, νcopper -> 0.31, Eepoxy → 3.378, νepoxy -> 0.27,
    E11EPZT -> 53, E22EPZT -> 61, νfiber -> 0.384, G12fiber -> 21};
Simplify[ExMFC[Vfiberelectrode]];
Simplify[EyMFC[Vfiberelectrode]];
Simplify[GxyMFC[Vfiberelectrode]];
Simplify[νxyMFC[Vfiberelectrode]];
Plot[{ExMFC[Vfiberelectrode] / ExMFCnominal,
  EyMFC[Vfiberelectrode] / EyMFCnominal,
  GxyMFC[Vfiberelectrode] / GxyMFCnominal,
  νxyMFC[Vfiberelectrode] / νxyMFCnominal}, {Vfiberelectrode, 0, 1},
 PlotStyle -> {{Red, Dashing[{}]}, {DodgerBlue, Dashing[{.015}]},
   {Green, Dashing[{.03}]}, {Carrot, Dashing[{.005, .025, .025, .025}]}},
 TextStyle → {FontFamily → "Times", FontSize → 12},
 PlotLabel → "volume fraction of copper varies",
 PlotLegend → {"E_x^MFC/ref. E_x^MFC", "E_y^MFC/ref. E_y^MFC", "G_xy^MFC/ref. G_xy^MFC",
   "ν_xy^MFC/ref. ν_xy^MFC"}, LegendPosition → {-.7, .1}, LegendSize → {1.2, .4}]
```

- Graphics -

■ Now look at sensitivities due to variations in layer thicknesses for reference fiber geometry and material properties:

First we will vary the thickness of the Kapton layer.

```
Clear[tkapton, tacrylic, tcopper, tfiber]
VfiberPZT = .882353;
VmatrixPZT = 1 - VfiberPZT;
Vfiberelectrode = 0.238095;
Vmatrixelectrode = 1 - Vfiberelectrode;
ExMFC[tkapton_] =
  Ex /. {Ekapton → 2.5, νkapton -> 0.34, Eacrylic → 2.7, νacrylic -> 0.35,
    Ecopper → 117.2, νcopper -> 0.31, Eepoxy → 3.378, νepoxy -> 0.27,
    E11EPZT -> 53, E22EPZT -> 61, νfiber -> 0.384, G12fiber -> 21,
    tacrylic -> 1.27 * 10^-5, tcopper -> 1.778 * 10^-5, tfiber -> 1.905 * 10^-4};
EyMFC[tkapton_] =
  Ey /. {Ekapton → 2.5, νkapton -> 0.34, Eacrylic → 2.7, νacrylic -> 0.35,
    Ecopper → 117.2, νcopper -> 0.31, Eepoxy → 3.378, νepoxy -> 0.27,
    E11EPZT -> 53, E22EPZT -> 61, νfiber -> 0.384, G12fiber -> 21,
    tacrylic -> 1.27 * 10^-5, tcopper -> 1.778 * 10^-5, tfiber -> 1.905 * 10^-4};
GxyMFC[tkapton_] =
  Gxy /. {Ekapton → 2.5, νkapton -> 0.34, Eacrylic → 2.7, νacrylic -> 0.35,
    Ecopper → 117.2, νcopper -> 0.31, Eepoxy → 3.378, νepoxy -> 0.27,
    E11EPZT -> 53, E22EPZT -> 61, νfiber -> 0.384, G12fiber -> 21,
    tacrylic -> 1.27 * 10^-5, tcopper -> 1.778 * 10^-5, tfiber -> 1.905 * 10^-4};
νxyMFC[tkapton_] =
  νxy /. {Ekapton → 2.5, νkapton -> 0.34, Eacrylic → 2.7, νacrylic -> 0.35,
    Ecopper → 117.2, νcopper -> 0.31, Eepoxy → 3.378, νepoxy -> 0.27,
    E11EPZT -> 53, E22EPZT -> 61, νfiber -> 0.384, G12fiber -> 21,
    tacrylic -> 1.27 * 10^-5, tcopper -> 1.778 * 10^-5, tfiber -> 1.905 * 10^-4};
Simplify[ExMFC[tkapton]];
Simplify[EyMFC[tkapton]];
Simplify[GxyMFC[tkapton]];
Simplify[νxyMFC[tkapton]];
nomprop = 2.54 * 10^-5;
```

```
Extable = Table[{tkapton / nomprop, ExMFC[tkapton] / ExMFCnominal},
   {tkapton, .5 * nomprop, 1.5 * nomprop, (1.5 * nomprop - .5 * nomprop) / 100}];
Eytable = Table[{tkapton / nomprop, EyMFC[tkapton] / EyMFCnominal},
   {tkapton, .5 * nomprop, 1.5 * nomprop, (1.5 * nomprop - .5 * nomprop) / 100}];
Gxytable = Table[{tkapton / nomprop, GxyMFC[tkapton] / GxyMFCnominal},
   {tkapton, .5 * nomprop, 1.5 * nomprop, (1.5 * nomprop - .5 * nomprop) / 100}];
νxytable = Table[{tkapton / nomprop, νxyMFC[tkapton] / νxyMFCnominal},
   {tkapton, .5 * nomprop, 1.5 * nomprop, (1.5 * nomprop - .5 * nomprop) / 100}];
plot1 = ListPlot[Extable, PlotJoined → True,
  TextStyle → {FontFamily → "Times", FontSize → 12},
  PlotLabel → "Kapton thickness varies", AxesOrigin → {.5, 1},
  PlotStyle -> {Red, Dashing[{}]}, DisplayFunction → Identity]
plot2 = ListPlot[Eytable, PlotJoined → True,
  PlotStyle -> {DodgerBlue, Dashing[{.015}]}, DisplayFunction → Identity]
plot3 = ListPlot[Gxytable, PlotJoined → True, PlotStyle -> {Green, Dashing[{.03}]},
  DisplayFunction → Identity]
plot4 = ListPlot[νxytable, PlotJoined → True,
  PlotStyle -> {Carrot, Dashing[{.005, .025, .025, .025}]},
  DisplayFunction → Identity]
Show[plot1, plot2, plot3, plot4, DisplayFunction → $DisplayFunction]
```

- Graphics -

- Graphics -

- Graphics -

- Graphics -

- Graphics -

Second, we will vary the thickness of the acrylic layer.

```
ExMFC[tacrylic_] =
  Ex /. {Ekapton → 2.5, νkapton -> 0.34, Eacrylic → 2.7, νacrylic -> 0.35, Ecopper → 117.2,
    νcopper -> 0.31, Eepoxy → 3.378, νepoxy -> 0.27, E11EPZT -> 53, E22EPZT -> 61,
    νfiber -> 0.384, G12fiber -> 21, tkapton -> 2.54 * 10^-5, tcopper -> 1.778 * 10^-5,
    tfiber -> 1.905 * 10^-4};
EyMFC[tacrylic_] =
  Ey /. {Ekapton → 2.5, νkapton -> 0.34, Eacrylic → 2.7, νacrylic -> 0.35, Ecopper → 117.2,
    νcopper -> 0.31, Eepoxy → 3.378, νepoxy -> 0.27, E11EPZT -> 53, E22EPZT -> 61,
    νfiber -> 0.384, G12fiber -> 21, tkapton -> 2.54 * 10^-5, tcopper -> 1.778 * 10^-5,
    tfiber -> 1.905 * 10^-4};
```

```
GxyMFC[tacrylic_] =
  Gxy /. {Ekapton → 2.5, νkapton -> 0.34, Eacrylic → 2.7, νacrylic -> 0.35,
    Ecopper → 117.2, νcopper -> 0.31, Eepoxy → 3.378, νepoxy -> 0.27, E11EPZT -> 53,
    E22EPZT -> 61, νfiber -> 0.384, G12fiber -> 21, tkapton -> 2.54 * 10^-5,
    tcopper -> 1.778 * 10^-5, tfiber -> 1.905 * 10^-4};
νxyMFC[tacrylic_] =
 νxy /. {Ekapton → 2.5, νkapton -> 0.34, Eacrylic → 2.7, νacrylic -> 0.35, Ecopper → 117.2,
   νcopper -> 0.31, Eepoxy → 3.378, νepoxy -> 0.27, E11EPZT -> 53, E22EPZT -> 61,
   νfiber -> 0.384, G12fiber -> 21, tkapton -> 2.54 * 10^-5, tcopper -> 1.778 * 10^-5,
   tfiber -> 1.905 * 10^-4};
Simplify[ExMFC[tacrylic]];
Simplify[EyMFC[tacrylic]];
Simplify[GxyMFC[tacrylic]];
Simplify[νxyMFC[tacrylic]];
nomprop = 1.27 * 10^-5;
Extable = Table[{tacrylic / nomprop, ExMFC[tacrylic] / ExMFCnominal},
   {tacrylic, .5 * nomprop, 1.5 * nomprop, (1.5 * nomprop - .5 * nomprop) / 100}];
Eytable = Table[{tacrylic / nomprop, EyMFC[tacrylic] / EyMFCnominal},
  {tacrylic, .5 * nomprop, 1.5 * nomprop, (1.5 * nomprop - .5 * nomprop) / 100}];
Gxytable = Table[{tacrylic / nomprop, GxyMFC[tacrylic] / GxyMFCnominal},
  {tacrylic, .5 * nomprop, 1.5 * nomprop, (1.5 * nomprop - .5 * nomprop) / 100}];
νxytable = Table[{tacrylic / nomprop, νxyMFC[tacrylic] / νxyMFCnominal},
  {tacrylic, .5 * nomprop, 1.5 * nomprop, (1.5 * nomprop - .5 * nomprop) / 100}];
plot1 = ListPlot[Extable, PlotJoined → True,
  TextStyle → {FontFamily → "Times", FontSize → 12}, PlotLabel → "Acrylic thickness varies",
  AxesOrigin → {.5, 1}, PlotStyle -> {Red, Dashing[{}]}, DisplayFunction → Identity]
plot2 = ListPlot[Eytable, PlotJoined → True, PlotStyle -> {DodgerBlue, Dashing[{.015}]},
  DisplayFunction → Identity]
plot3 = ListPlot[Gxytable, PlotJoined → True, PlotStyle -> {Green, Dashing[{.03}]},
  DisplayFunction → Identity]
plot4 = ListPlot[νxytable, PlotJoined → True,
  PlotStyle -> {Carrot, Dashing[{.005, .025, .025, .025}]}, DisplayFunction → Identity]
Show[plot1, plot2, plot3, plot4, DisplayFunction → $DisplayFunction]
```

- Graphics -

- Graphics -

- Graphics -

- Graphics -

- Graphics -

Third, we will vary the thickness of the copper layer.

```
ExMFC[tcopper_] =
  Ex /. {Ekapton → 2.5, νkapton -> 0.34, Eacrylic → 2.7, νacrylic -> 0.35, Ecopper → 117.2,
    νcopper -> 0.31, Eepoxy → 3.378, νepoxy -> 0.27, E11EPZT -> 53, E22EPZT -> 61,
    νfiber -> 0.384, G12fiber -> 21, tacrylic -> 1.27 * 10^-5, tkapton -> 2.54 * 10^-5,
    tfiber -> 1.905 * 10^-4};
EyMFC[tcopper_] =
  Ey /. {Ekapton → 2.5, νkapton -> 0.34, Eacrylic → 2.7, νacrylic -> 0.35, Ecopper → 117.2,
    νcopper -> 0.31, Eepoxy → 3.378, νepoxy -> 0.27, E11EPZT -> 53, E22EPZT -> 61,
    νfiber -> 0.384, G12fiber -> 21, tacrylic -> 1.27 * 10^-5, tkapton -> 2.54 * 10^-5,
    tfiber -> 1.905 * 10^-4};
GxyMFC[tcopper_] =
  Gxy /. {Ekapton → 2.5, νkapton -> 0.34, Eacrylic → 2.7, νacrylic -> 0.35,
    Ecopper → 117.2, νcopper -> 0.31, Eepoxy → 3.378, νepoxy -> 0.27, E11EPZT -> 53,
    E22EPZT -> 61, νfiber -> 0.384, G12fiber -> 21, tacrylic -> 1.27 * 10^-5,
    tkapton -> 2.54 * 10^-5, tfiber -> 1.905 * 10^-4};
νxyMFC[tcopper_] =
  νxy /. {Ekapton → 2.5, νkapton -> 0.34, Eacrylic → 2.7, νacrylic -> 0.35,
    Ecopper → 117.2, νcopper -> 0.31, Eepoxy → 3.378, νepoxy -> 0.27, E11EPZT -> 53,
    E22EPZT -> 61, νfiber -> 0.384, G12fiber -> 21, tacrylic -> 1.27 * 10^-5,
    tkapton -> 2.54 * 10^-5, tfiber -> 1.905 * 10^-4};
Simplify[ExMFC[tcopper]];
Simplify[EyMFC[tcopper]];
Simplify[GxyMFC[tcopper]];
Simplify[νxyMFC[tcopper]];
nomprop = 1.778 * 10^-5;
Extable = Table[{tcopper / nomprop, ExMFC[tcopper] / ExMFCnominal},
   {tcopper, .5 * nomprop, 1.5 * nomprop, (1.5 * nomprop - .5 * nomprop) / 100}];
Eytable = Table[{tcopper / nomprop, EyMFC[tcopper] / EyMFCnominal},
   {tcopper, .5 * nomprop, 1.5 * nomprop, (1.5 * nomprop - .5 * nomprop) / 100}];
Gxytable = Table[{tcopper / nomprop, GxyMFC[tcopper] / GxyMFCnominal},
   {tcopper, .5 * nomprop, 1.5 * nomprop, (1.5 * nomprop - .5 * nomprop) / 100}];
νxytable = Table[{tcopper / nomprop, νxyMFC[tcopper] / νxyMFCnominal},
   {tcopper, .5 * nomprop, 1.5 * nomprop, (1.5 * nomprop - .5 * nomprop) / 100}];

plot1 = ListPlot[Extable, PlotJoined → True,
  TextStyle → {FontFamily → "Times", FontSize → 12}, PlotLabel → "Copper thickness varies",
  AxesOrigin → {.5, 1}, PlotStyle -> {Red, Dashing[{}]}, DisplayFunction → Identity]
```

```
plot2 = ListPlot[Eytable, PlotJoined → True, PlotStyle -> {DodgerBlue, Dashing[{.015}]},
  DisplayFunction → Identity]
plot3 = ListPlot[Gxytable, PlotJoined → True, PlotStyle -> {Green, Dashing[{.03}]},
  DisplayFunction → Identity]
plot4 = ListPlot[νxytable, PlotJoined → True,
  PlotStyle -> {Carrot, Dashing[{.005, .025, .025, .025}]}, DisplayFunction → Identity]
Show[plot1, plot2, plot3, plot4, DisplayFunction → $DisplayFunction]
```

```
- Graphics -
```

```
- Graphics -
```

```
- Graphics -
```

```
- Graphics -
```

```
- Graphics -
```

Lastly, we will vary the thickness of the PZT layer.

```
ExMFC[tfiber_] =
  Ex /. {Ekapton → 2.5, νkapton -> 0.34, Eacrylic → 2.7, νacrylic -> 0.35, Ecopper → 117.2,
    νcopper -> 0.31, Eepoxy → 3.378, νepoxy -> 0.27, E11EPZT -> 53, E22EPZT -> 61,
    νfiber -> 0.384, G12fiber -> 21, tacrylic -> 1.27 * 10^-5, tcopper -> 1.778 * 10^-5,
    tkapton -> 2.54 * 10^-5};
EyMFC[tfiber_] =
  Ey /. {Ekapton → 2.5, νkapton -> 0.34, Eacrylic → 2.7, νacrylic -> 0.35, Ecopper → 117.2,
    νcopper -> 0.31, Eepoxy → 3.378, νepoxy -> 0.27, E11EPZT -> 53, E22EPZT -> 61,
    νfiber -> 0.384, G12fiber -> 21, tacrylic -> 1.27 * 10^-5, tcopper -> 1.778 * 10^-5,
    tkapton -> 2.54 * 10^-5};
GxyMFC[tfiber_] =
  Gxy /. {Ekapton → 2.5, νkapton -> 0.34, Eacrylic → 2.7, νacrylic -> 0.35,
    Ecopper → 117.2, νcopper -> 0.31, Eepoxy → 3.378, νepoxy -> 0.27, E11EPZT -> 53,
    E22EPZT -> 61, νfiber -> 0.384, G12fiber -> 21, tacrylic -> 1.27 * 10^-5,
    tcopper -> 1.778 * 10^-5, tkapton -> 2.54 * 10^-5};
νxyMFC[tfiber_] =
  νxy /. {Ekapton → 2.5, νkapton -> 0.34, Eacrylic → 2.7, νacrylic -> 0.35,
    Ecopper → 117.2, νcopper -> 0.31, Eepoxy → 3.378, νepoxy -> 0.27, E11EPZT -> 53,
    E22EPZT -> 61, νfiber -> 0.384, G12fiber -> 21, tacrylic -> 1.27 * 10^-5,
    tcopper -> 1.778 * 10^-5, tkapton -> 2.54 * 10^-5};
Simplify[ExMFC[tfiber]];
Simplify[EyMFC[tfiber]];
Simplify[GxyMFC[tfiber]];
Simplify[νxyMFC[tfiber]];
nomprop = 1.905 * 10^-4;
```

```
Extable = Table[{tfiber / nomprop, ExMFC[tfiber] / ExMFCnominal},
   {tfiber, .5 * nomprop, 1.5 * nomprop, (1.5 * nomprop - .5 * nomprop) / 100}];
Eytable = Table[{tfiber / nomprop, EyMFC[tfiber] / EyMFCnominal},
  {tfiber, .5 * nomprop, 1.5 * nomprop, (1.5 * nomprop - .5 * nomprop) / 100}];
Gxytable = Table[{tfiber / nomprop, GxyMFC[tfiber] / GxyMFCnominal},
  {tfiber, .5 * nomprop, 1.5 * nomprop, (1.5 * nomprop - .5 * nomprop) / 100}];
νxytable = Table[{tfiber / nomprop, νxyMFC[tfiber] / νxyMFCnominal},
   {tfiber, .5 * nomprop, 1.5 * nomprop, (1.5 * nomprop - .5 * nomprop) / 100}];
plot1 = ListPlot[Extable, PlotJoined → True,
  TextStyle → {FontFamily → "Times", FontSize → 12}, PlotLabel → "PZT thickness varies",
  AxesOrigin → {.5, 1}, PlotStyle -> {Red, Dashing[{}]}, DisplayFunction → Identity]
plot2 = ListPlot[Eytable, PlotJoined → True, PlotStyle -> {DodgerBlue, Dashing[{.015}]},
  DisplayFunction → Identity]
plot3 = ListPlot[Gxytable, PlotJoined → True, PlotStyle -> {Green, Dashing[{.03}]},
  DisplayFunction → Identity]
plot4 = ListPlot[νxytable, PlotJoined → True,
  PlotStyle -> {Carrot, Dashing[{.005, .025, .025, .025}]}, DisplayFunction → Identity]
Show[plot1, plot2, plot3, plot4, DisplayFunction → $DisplayFunction]
```

- Graphics -

- Graphics -

- Graphics -

- Graphics -

- Graphics -

F.3 Summary:

Appendix F gives the entire *Mathematica* code used to perform the sensitivity analysis of the classical lamination model to variations in constituent material properties, as well as various PZT and copper fiber volume fractions and layer thicknesses. While the output graphics have been suppressed to shorten this appendix, the plots do appear as required in Chapter 4.

Appendix G

Tabulated Strain Output and Effective Piezoelectric Strain Coefficients for Nonzero Constant Stresses

G.1 Introduction:

In Chapter 6, plots of the peak to peak actuation strain and effective d_{33} and d_{31} strain coefficients were presented for the case of nonzero constant mechanical stresses. Trends in these plots were also discussed at that point. Due to the large amount of data, the tabulated results are presented in this appendix.

G.2 Nonzero Constant Stress Actuation Results:

Below, Tables G.1 through G.11 present the peak to peak actuation strains and effective d_{33} and d_{31} strain coefficients are presented for each nonzero constant load case, as well as each peak to peak voltage cycle and DC biasing voltage condition. The tabulated results represent the average of five reference MFC test specimens tested as discussed in Chapters 5 and 6. The sample standard deviations of all quantities are also given.

Table G.1: Peak to Peak Actuation Strain and Piezoelectric Strain Parameters for 1lb Constant Load (Stress)

DC Offset Voltage, V	Peak to Peak Voltage, V	Peak to Peak 3-Dir. Strain, με	Std. Dev.	Effective d_{33}, m/V	Std. Dev.	Peak to Peak 1-Dir. Strain, με	Std. Dev.	Effective d_{31}, m/V	Std. Dev.
0	250	122.2	12.9	2.61E-10	2.77E-11	61.1	7.2	1.30E-10	1.53E-11
0	500	290.7	17.4	3.10E-10	1.86E-11	134.8	13.6	1.44E-10	1.44E-11
0	750	496.2	20.2	3.53E-10	1.44E-11	225.8	15.2	1.60E-10	1.07E-11
0	1000	740.4	29.9	3.95E-10	1.60E-11	331.5	25.3	1.77E-10	1.35E-11
0	1250	999.8	35.8	4.27E-10	1.53E-11	436.0	35.4	1.86E-10	1.51E-11
250	250	113.8	10.5	2.42E-10	2.27E-11	59.2	10.9	1.26E-10	2.34E-11
250	500	274.7	18.3	2.93E-10	1.96E-11	131.1	10.5	1.40E-10	1.13E-11
250	750	473.9	20.2	3.37E-10	1.44E-11	223.9	14.6	1.59E-10	1.04E-11
250	1000	702.1	36.3	3.75E-10	1.94E-11	327.4	26.5	1.75E-10	1.41E-11
250	1250	951.7	51.5	4.06E-10	2.20E-11	440.7	36.6	1.88E-10	1.56E-11
250	1500	1223.6	65.8	4.35E-10	2.34E-11	561.2	46.9	2.00E-10	1.67E-11
250	1750	1501.8	80.7	4.58E-10	2.46E-11	682.0	58.8	2.08E-10	1.79E-11
500	250	114.3	10.4	2.44E-10	2.24E-11	58.9	6.9	1.26E-10	1.48E-11
500	500	273.3	18.9	2.91E-10	2.01E-11	136.4	10.0	1.45E-10	1.06E-11
500	750	463.4	27.5	3.29E-10	1.95E-11	225.1	13.9	1.60E-10	9.86E-12
500	1000	672.9	37.8	3.59E-10	2.02E-11	328.8	25.2	1.75E-10	1.34E-11
500	1250	901.1	50.3	3.85E-10	2.14E-11	436.3	36.7	1.86E-10	1.57E-11
500	1500	1145.6	60.5	4.07E-10	2.15E-11	551.2	43.0	1.96E-10	1.52E-11
500	1750	1401.7	79.5	4.27E-10	2.42E-11	666.4	58.0	2.03E-10	1.77E-11
500	2000	1674.3	95.1	4.46E-10	2.53E-11	791.2	70.9	2.11E-10	1.89E-11
500	2250	1957.2	107	4.64E-10	2.54E-11	914.6	81.3	2.17E-10	1.93E-11

Table G.2: Peak to Peak Actuation Strain and Piezoelectric Strain Parameters for 10lb Constant Load (Stress)

DC Offset Voltage, V	Peak to Peak Voltage, V	Peak to Peak 3-Dir. Strain, με	Std. Dev.	Effective d_{33}, m/V	Std. Dev.	Peak to Peak 1-Dir. Strain, με	Std. Dev.	Effective d_{31}, m/V	Std. Dev.
0	250	121.7597	7.414617	2.6E-10	1.6E-11	59.55382	5.696336	1.27E-10	1.21E-11
0	500	286.3552	17.13568	3.05E-10	1.84E-11	134.1807	12.43271	1.43E-10	1.33E-11
0	750	493.6857	22.69086	3.51E-10	1.61E-11	224.6528	17.59548	1.6E-10	1.25E-11
0	1000	722.9041	36.34318	3.86E-10	1.95E-11	325.9682	31.8819	1.74E-10	1.71E-11
0	1250	978.6095	48.2991	4.18E-10	2.06E-11	435.609	39.06773	1.86E-10	1.67E-11
250	250	111.0843	6.841265	2.36E-10	1.44E-11	55.59252	6.840249	1.18E-10	1.43E-11
250	500	270.8792	11.52104	2.89E-10	1.23E-11	127.3995	10.34504	1.36E-10	1.1E-11
250	750	468.1722	23.38309	3.33E-10	1.67E-11	221.1951	16.5018	1.57E-10	1.17E-11
250	1000	687.8902	36.35404	3.67E-10	1.94E-11	323.3833	29.71465	1.73E-10	1.58E-11
250	1250	930.2347	53.70469	3.97E-10	2.29E-11	432.8226	43.4904	1.85E-10	1.85E-11
250	1500	1179.797	70.54614	4.2E-10	2.5E-11	545.9212	60.2584	1.94E-10	2.14E-11
250	1750	1448.427	86.11989	4.42E-10	2.62E-11	663.7196	71.3247	2.02E-10	2.17E-11
500	250	115.8849	5.327298	2.47E-10	1.14E-11	59.65452	2.884409	1.27E-10	6.21E-12
500	500	267.5893	14.8121	2.85E-10	1.57E-11	132.8715	13.20525	1.42E-10	1.4E-11
500	750	448.1643	22.04775	3.19E-10	1.57E-11	218.0059	20.41673	1.55E-10	1.45E-11
500	1000	649.9893	33.85319	3.47E-10	1.8E-11	313.95	32.08332	1.67E-10	1.71E-11
500	1250	871.8222	47.53041	3.72E-10	2.02E-11	420.6366	42.04547	1.8E-10	1.79E-11
500	1500	1103.055	58.72179	3.92E-10	2.08E-11	530.7809	54.37729	1.89E-10	1.93E-11
500	1750	1343.687	74.52956	4.1E-10	2.27E-11	643.4767	68.18788	1.96E-10	2.07E-11
500	2000	1600.635	91.81546	4.27E-10	2.45E-11	760.7043	82.99995	2.03E-10	2.22E-11
500	2250	1866.411	106.2748	4.42E-10	2.52E-11	881.2555	93.11897	2.09E-10	2.21E-11

Table G.3: Peak to Peak Actuation Strain and Piezoelectric Strain Parameters for 20lb Constant Load (Stress)

DC Offset Voltage, V	Peak to Peak Voltage, V	Peak to Peak 3-Dir. Strain, με	Std. Dev.	Effective d_{33}, m/V	Std. Dev.	Peak to Peak 1-Dir. Strain, με	Std. Dev.	Effective d_{31}, m/V	Std. Dev.
0	250	118.9398	8.022352	2.54E-10	1.7E-11	58.44599	3.145595	1.25E-10	6.65E-12
0	500	286.2544	17.62627	3.05E-10	1.88E-11	136.4971	11.12479	1.46E-10	1.18E-11
0	750	485.931	26.51394	3.45E-10	1.88E-11	227.7749	20.73088	1.62E-10	1.47E-11
0	1000	710.4495	34.5892	3.79E-10	1.85E-11	325.5653	29.22467	1.74E-10	1.56E-11
0	1250	953.029	43.13129	4.07E-10	1.84E-11	430.9091	39.49271	1.84E-10	1.69E-11
250	250	111.0843	7.024155	2.37E-10	1.49E-11	58.00958	4.220728	1.24E-10	8.97E-12
250	500	270.6442	11.72901	2.89E-10	1.24E-11	129.8502	12.27535	1.38E-10	1.3E-11
250	750	458.0005	26.26829	3.26E-10	1.86E-11	217.6031	21.47408	1.55E-10	1.52E-11
250	1000	670.9036	36.61806	3.58E-10	1.96E-11	319.4555	32.00503	1.7E-10	1.71E-11
250	1250	898.7793	45.86775	3.84E-10	1.97E-11	425.1686	41.04894	1.81E-10	1.75E-11
250	1500	1144.145	56.41624	4.07E-10	2.01E-11	538.905	50.83118	1.92E-10	1.81E-11
250	1750	1392.029	66.24796	4.24E-10	2.01E-11	652.0371	61.32963	1.99E-10	1.87E-11
500	250	112.7964	5.604843	2.41E-10	1.21E-11	61.13162	4.243696	1.3E-10	9.13E-12
500	500	262.1509	13.43095	2.8E-10	1.43E-11	130.0851	12.05323	1.39E-10	1.29E-11
500	750	438.5297	26.0445	3.12E-10	1.84E-11	216.126	21.98429	1.54E-10	1.56E-11
500	1000	634.1776	30.51295	3.38E-10	1.63E-11	312.5065	27.80631	1.67E-10	1.48E-11
500	1250	839.0576	41.28135	3.58E-10	1.76E-11	411.7405	38.17032	1.76E-10	1.63E-11
500	1500	1062.267	51.37026	3.78E-10	1.82E-11	518.3264	51.15805	1.84E-10	1.81E-11
500	1750	1290.78	64.13291	3.93E-10	1.94E-11	625.2815	67.52228	1.91E-10	2.05E-11
500	2000	1532.823	72.07403	4.09E-10	1.93E-11	738.8836	76.32211	1.97E-10	2.04E-11
500	2250	1779.665	82.17885	4.22E-10	1.95E-11	854.1642	88.01795	2.02E-10	2.09E-11

Table G.4: Peak to Peak Actuation Strain and Piezoelectric Strain Parameters for 30lb Constant Load (Stress)

DC Offset Voltage, V	Peak to Peak Voltage, V	Peak to Peak 3-Dir. Strain, με	Std. Dev.	Effective d_{33}, m/V	Std. Dev.	Peak to Peak 1-Dir. Strain, με	Std. Dev.	Effective d_{31}, m/V	Std. Dev.
0	250	123.1025	6.217999	2.63E-10	1.37E-11	61.8366	4.596196	1.32E-10	9.9E-12
0	500	280.3796	13.68663	2.99E-10	1.47E-11	133.4086	11.30256	1.42E-10	1.21E-11
0	750	474.2485	23.21627	3.37E-10	1.64E-11	222.5044	17.43986	1.58E-10	1.23E-11
0	1000	689.6695	28.66079	3.68E-10	1.53E-11	318.5492	28.6438	1.7E-10	1.53E-11
0	1250	915.9001	35.06468	3.91E-10	1.49E-11	435.3069	60.08399	1.86E-10	2.56E-11
250	250	110.5808	6.113866	2.36E-10	1.34E-11	55.22324	5.022956	1.18E-10	1.09E-11
250	500	265.038	7.975177	2.83E-10	8.56E-12	128.2388	6.797472	1.37E-10	7.25E-12
250	750	447.2579	20.31097	3.18E-10	1.43E-11	214.5482	17.21541	1.53E-10	1.22E-11
250	1000	650.6607	31.20116	3.47E-10	1.67E-11	314.0171	30.42365	1.67E-10	1.62E-11
250	1250	868.8009	34.69622	3.71E-10	1.48E-11	416.6417	34.7375	1.78E-10	1.48E-11
250	1500	1093.252	47.12266	3.89E-10	1.69E-11	523.0933	51.97983	1.86E-10	1.85E-11
250	1750	1325.66	47.75071	4.04E-10	1.44E-11	632.9356	59.05299	1.93E-10	1.8E-11
500	250	110.8493	7.298752	2.36E-10	1.6E-11	57.43888	5.10556	1.23E-10	1.13E-11
500	500	256.679	11.34919	2.74E-10	1.22E-11	129.0445	12.18712	1.38E-10	1.31E-11
500	750	426.0415	17.21213	3.03E-10	1.23E-11	211.8961	17.72232	1.51E-10	1.25E-11
500	1000	608.0264	26.14333	3.24E-10	1.39E-11	299.2126	27.44611	1.6E-10	1.46E-11
500	1250	804.1109	34.42754	3.43E-10	1.47E-11	395.2574	37.31832	1.69E-10	1.59E-11
500	1500	1009.897	40.17034	3.59E-10	1.42E-11	497.1435	45.3432	1.77E-10	1.61E-11
500	1750	1227.903	44.2073	3.74E-10	1.34E-11	605.6428	59.42562	1.85E-10	1.81E-11
500	2000	1450.945	51.95728	3.87E-10	1.39E-11	709.5767	69.44568	1.89E-10	1.85E-11
500	2250	1674.758	57.22185	3.97E-10	1.36E-11	815.9276	77.90148	1.93E-10	1.85E-11

Table G.5: Peak to Peak Actuation Strain and Piezoelectric Strain Parameters for 40lb Constant Load (Stress)

DC Offset Voltage, V	Peak to Peak Voltage, V	Peak to Peak 3-Dir. Strain, με	Std. Dev.	Effective d_{33}, m/V	Std. Dev.	Peak to Peak 1-Dir. Strain, με	Std. Dev.	Effective d_{31}, m/V	Std. Dev.
0	250	118.1006	6.132471	2.52E-10	1.32E-11	58.27816	6.595957	1.25E-10	1.41E-11
0	500	269.7714	13.94203	2.88E-10	1.48E-11	126.7617	10.28591	1.35E-10	1.09E-11
0	750	457.9669	20.73584	3.26E-10	1.47E-11	216.3945	19.68215	1.54E-10	1.4E-11
0	1000	661.7726	26.4047	3.53E-10	1.41E-11	311.4322	27.00603	1.66E-10	1.44E-11
0	1250	859.8712	23.94304	3.67E-10	1.02E-11	402.6765	32.43603	1.72E-10	1.38E-11
250	250	109.6408	6.71657	2.34E-10	1.42E-11	54.08186	5.528164	1.15E-10	1.18E-11
250	500	257.0147	6.313324	2.74E-10	6.95E-12	124.5796	5.438238	1.33E-10	5.85E-12
250	750	427.9885	16.98849	3.04E-10	1.21E-11	205.5513	15.12045	1.46E-10	1.08E-11
250	1000	620.8502	22.92339	3.31E-10	1.22E-11	302.7711	24.51854	1.61E-10	1.31E-11
250	1250	821.5339	25.54097	3.51E-10	1.09E-11	398.3795	35.17439	1.7E-10	1.5E-11
250	1500	1035.108	33.27837	3.68E-10	1.18E-11	500.8026	43.05367	1.78E-10	1.53E-11
250	1750	1239.082	27.33252	3.78E-10	8.35E-12	601.3123	49.02559	1.83E-10	1.49E-11
500	250	109.473	4.151411	2.34E-10	8.79E-12	55.92824	3.859481	1.2E-10	8.17E-12
500	500	247.2122	13.32778	2.63E-10	1.42E-11	123.2032	8.123913	1.31E-10	8.64E-12
500	750	409.5919	12.98731	2.91E-10	9.13E-12	202.0264	13.72367	1.44E-10	9.74E-12
500	1000	580.2972	21.82766	3.09E-10	1.17E-11	290.1822	24.74188	1.55E-10	1.32E-11
500	1250	764.2964	23.72316	3.26E-10	1.01E-11	382.165	28.88746	1.63E-10	1.23E-11
500	1500	952.794	23.47124	3.39E-10	8.32E-12	473.6778	37.95213	1.68E-10	1.35E-11
500	1750	1154.451	26.21238	3.52E-10	8E-12	573.1132	42.78567	1.75E-10	1.3E-11
500	2000	1359.096	29.78338	3.63E-10	7.97E-12	670.2323	54.73887	1.79E-10	1.46E-11
500	2250	1556.456	29.64582	3.69E-10	7.06E-12	767.7541	65.70695	1.82E-10	1.56E-11

Table G.6: Peak to Peak Actuation Strain and Piezoelectric Strain Parameters for 50lb Constant Load (Stress)

DC Offset Voltage, V	Peak to Peak Voltage, V	Peak to Peak 3-Dir. Strain, με	Std. Dev.	Effective d_{33}, m/V	Std. Dev.	Peak to Peak 1-Dir. Strain, με	Std. Dev.	Effective d_{31}, m/V	Std. Dev.
0	250	121.1554	8.581335	2.59E-10	1.84E-11	62.34015	10.28467	1.33E-10	2.21E-11
0	500	265.8773	9.845497	2.84E-10	1.05E-11	128.7759	10.45772	1.37E-10	1.11E-11
0	750	443.1959	16.86204	3.15E-10	1.21E-11	212.7689	18.71327	1.51E-10	1.33E-11
0	1000	636.2926	17.96621	3.39E-10	9.59E-12	304.5167	24.12557	1.62E-10	1.29E-11
0	1250	814.249	18.47632	3.47E-10	7.96E-12	388.6105	30.45628	1.66E-10	1.3E-11
250	250	108.8351	8.220922	2.32E-10	1.76E-11	54.18255	8.232786	1.15E-10	1.76E-11
250	500	252.852	11.02505	2.69E-10	1.19E-11	124.9489	10.23663	1.33E-10	1.1E-11
250	750	415.2318	13.20242	2.95E-10	9.51E-12	201.355	13.20953	1.43E-10	9.44E-12
250	1000	593.1882	15.68084	3.16E-10	8.46E-12	288.7387	23.37465	1.54E-10	1.25E-11
250	1250	787.2921	12.85061	3.36E-10	5.6E-12	386.0927	27.21589	1.65E-10	1.16E-11
250	1500	977.3339	24.97685	3.48E-10	9.03E-12	480.8283	37.80033	1.71E-10	1.35E-11
250	1750	1163.716	26.89843	3.55E-10	8.28E-12	575.2281	45.41608	1.75E-10	1.38E-11
500	250	108.6002	7.13519	2.32E-10	1.51E-11	54.68613	3.351564	1.17E-10	7.1E-12
500	500	247.8835	7.839278	2.64E-10	8.5E-12	122.7668	6.681039	1.31E-10	7.13E-12
500	750	396.9024	15.1689	2.82E-10	1.08E-11	196.6552	16.7472	1.4E-10	1.19E-11
500	1000	564.1835	12.09544	3.01E-10	6.64E-12	281.8567	20.27861	1.5E-10	1.09E-11
500	1250	746.3028	19.72504	3.19E-10	8.54E-12	373.8395	26.86479	1.6E-10	1.14E-11
500	1500	928.3883	20.49134	3.3E-10	7.32E-12	466.7623	37.16039	1.66E-10	1.32E-11
500	1750	1117.154	25.02843	3.4E-10	7.64E-12	562.7064	50.60526	1.71E-10	1.54E-11
500	2000	1315.622	25.99995	3.51E-10	7.02E-12	660.9332	56.06459	1.76E-10	1.49E-11
500	2250	1498.917	27.94185	3.55E-10	6.64E-12	758.4216	63.07963	1.8E-10	1.49E-11

Table G.7: Peak to Peak Actuation Strain and Piezoelectric Strain Parameters for 52lb Constant Load (Stress)

DC Offset Voltage, V	Peak to Peak Voltage, V	Peak to Peak 3-Dir. Strain, με	Std. Dev.	Effective d_{33}, m/V	Std. Dev.	Peak to Peak 1-Dir. Strain, με	Std. Dev.	Effective d_{31}, m/V	Std. Dev.
0	250	119.9805	7.8912	2.6E-10	1.7E-11	60.09095	8.39259	1.3E-10	1.8E-11
0	500	272.8263	13.5205	2.9E-10	1.4E-11	131.5287	13.9168	1.4E-10	1.5E-11
0	750	450.3464	15.6809	3.2E-10	1.1E-11	218.1402	15.1855	1.6E-10	1.1E-11
0	1000	636.0576	17.9678	3.4E-10	9.6E-12	301.4283	23.7587	1.6E-10	1.3E-11
0	1250	822.3395	10.2516	3.5E-10	4.4E-12	393.3439	29.7445	1.7E-10	1.3E-11
250	250	111.3865	7.86985	2.4E-10	1.7E-11	57.06962	9.20128	1.2E-10	2E-11
250	500	256.6118	7.36005	2.7E-10	7.9E-12	126.896	6.89113	1.4E-10	7.3E-12
250	750	419.3945	14.4794	3E-10	1.1E-11	203.3692	17.3285	1.4E-10	1.2E-11
250	1000	603.2929	16.6805	3.2E-10	9E-12	297.9369	23.8282	1.6E-10	1.3E-11
250	1250	789.9442	18.9068	3.4E-10	8.1E-12	388.2412	34.5491	1.7E-10	1.5E-11
250	1500	981.1272	17.8134	3.5E-10	6.3E-12	485.4274	44.4502	1.7E-10	1.6E-11
250	1750	1171.371	14.6395	3.6E-10	4.4E-12	578.7866	52.5198	1.8E-10	1.6E-11
500	250	109.5401	5.17435	2.3E-10	1.1E-11	57.3046	8.29601	1.2E-10	1.8E-11
500	500	247.9507	11.4024	2.6E-10	1.2E-11	125.7546	8.2746	1.3E-10	8.8E-12
500	750	401.6021	14.7865	2.9E-10	1.1E-11	201.3214	16.7367	1.4E-10	1.2E-11
500	1000	564.6199	22.6399	3E-10	1.2E-11	283.8038	29.0266	1.5E-10	1.6E-11
500	1250	738.2122	22.9972	3.2E-10	9.8E-12	370.7175	33.9388	1.6E-10	1.4E-11
500	1500	918.1157	30.3299	3.3E-10	1.1E-11	463.3717	44.306	1.6E-10	1.6E-11
500	1750	1105.237	25.7034	3.4E-10	7.7E-12	563.2435	53.4198	1.7E-10	1.6E-11
500	2000	1295.312	25.6118	3.5E-10	6.8E-12	657.8112	56.8993	1.8E-10	1.5E-11
500	2250	1475.417	23.7022	3.5E-10	5.5E-12	751.1032	62.7745	1.8E-10	1.5E-11

Table G.8: Peak to Peak Actuation Strain and Piezoelectric Strain Parameters for 54lb Constant Load (Stress)

DC Offset Voltage, V	Peak to Peak Voltage, V	Peak to Peak 3-Dir. Strain, με	Std. Dev.	Effective d_{33}, m/V	Std. Dev.	Peak to Peak 1-Dir. Strain, με	Std. Dev.	Effective d_{31}, m/V	Std. Dev.
0	250	119.074	5.500352	2.54E-10	1.2E-11	60.89663	4.490468	1.3E-10	9.69E-12
0	500	267.0187	12.09774	2.85E-10	1.3E-11	128.1381	9.885887	1.37E-10	1.06E-11
0	750	436.6833	17.31012	3.1E-10	1.23E-11	210.419	17.37351	1.5E-10	1.24E-11
0	1000	623.4687	16.74803	3.32E-10	8.84E-12	301.0926	26.41344	1.61E-10	1.41E-11
0	1250	807.0314	10.96511	3.44E-10	4.7E-12	391.6654	31.64833	1.67E-10	1.35E-11
250	250	110.0437	7.592944	2.34E-10	1.59E-11	56.43178	2.271895	1.2E-10	4.82E-12
250	500	253.1205	11.17376	2.7E-10	1.18E-11	124.9825	7.538962	1.33E-10	8.02E-12
250	750	416.2054	15.50279	2.96E-10	1.09E-11	206.3234	14.10923	1.47E-10	1E-11
250	1000	587.5484	25.59548	3.13E-10	1.35E-11	290.82	29.86408	1.55E-10	1.59E-11
250	1250	777.3216	19.70276	3.32E-10	8.38E-12	388.0398	35.63827	1.66E-10	1.52E-11
250	1500	960.6829	28.49515	3.42E-10	1.01E-11	478.7469	40.7827	1.7E-10	1.45E-11
250	1750	1140.217	29.50109	3.48E-10	9E-12	572.0389	51.31917	1.74E-10	1.56E-11
500	250	106.8209	7.132793	2.28E-10	1.51E-11	56.19678	3.727667	1.2E-10	7.95E-12
500	500	242.2101	12.99094	2.58E-10	1.38E-11	122.364	9.389951	1.31E-10	1E-11
500	750	389.819	18.42882	2.77E-10	1.31E-11	198.5351	20.0319	1.41E-10	1.43E-11
500	1000	549.6475	24.87341	2.93E-10	1.32E-11	278.8354	26.56421	1.49E-10	1.42E-11
500	1250	718.4729	31.45879	3.07E-10	1.33E-11	365.9505	33.45674	1.56E-10	1.42E-11
500	1500	895.6236	41.61119	3.19E-10	1.47E-11	459.9811	41.09535	1.64E-10	1.46E-11
500	1750	1079.052	41.82891	3.29E-10	1.27E-11	557.1001	51.52831	1.7E-10	1.57E-11
500	2000	1263.454	46.66052	3.37E-10	1.23E-11	651.03	62.09071	1.74E-10	1.66E-11
500	2250	1440.068	45.15033	3.41E-10	1.06E-11	743.9192	66.34575	1.76E-10	1.57E-11

Table G.9: Peak to Peak Actuation Strain and Piezoelectric Strain Parameters for 56lb Constant Load (Stress)

DC Offset Voltage, V	Peak to Peak Voltage, V	Peak to Peak 3-Dir. Strain, με	Std. Dev.	Effective d_{33}, m/V	Std. Dev.	Peak to Peak 1-Dir. Strain, με	Std. Dev.	Effective d_{31}, m/V	Std. Dev.
0	250	117.2278	7.413623	2.5E-10	1.55E-11	60.69521	5.639422	1.3E-10	1.21E-11
0	500	261.0768	14.0768	2.78E-10	1.5E-11	130.9915	9.838748	1.4E-10	1.05E-11
0	750	430.3049	28.42655	3.06E-10	2.02E-11	210.6204	18.90193	1.5E-10	1.35E-11
0	1000	609.772	22.99858	3.25E-10	1.21E-11	302.0325	25.34968	1.61E-10	1.36E-11
0	1250	782.7601	27.85065	3.34E-10	1.19E-11	384.7499	30.33998	1.64E-10	1.29E-11
250	250	107.4253	4.932336	2.29E-10	1.04E-11	56.46535	4.316439	1.2E-10	9.16E-12
250	500	251.1063	11.69737	2.68E-10	1.24E-11	125.9896	9.13259	1.34E-10	9.67E-12
250	750	406.067	23.03283	2.89E-10	1.63E-11	201.7579	16.1779	1.43E-10	1.15E-11
250	1000	576.3023	30.07873	3.07E-10	1.6E-11	291.525	24.18155	1.56E-10	1.29E-11
250	1250	754.8967	35.94076	3.22E-10	1.53E-11	379.5465	35.87071	1.62E-10	1.53E-11
250	1500	942.3872	32.19558	3.35E-10	1.14E-11	474.7856	44.59502	1.69E-10	1.59E-11
250	1750	1116.315	39.96188	3.4E-10	1.22E-11	567.4062	53.82374	1.73E-10	1.64E-11
500	250	106.3845	9.264875	2.27E-10	1.98E-11	56.23035	5.849585	1.2E-10	1.25E-11
500	500	237.4768	11.52411	2.53E-10	1.22E-11	121.189	13.28046	1.29E-10	1.42E-11
500	750	381.93	22.7101	2.71E-10	1.6E-11	193.3317	15.43069	1.37E-10	1.1E-11
500	1000	543.3699	34.29572	2.9E-10	1.82E-11	276.5526	26.89052	1.47E-10	1.43E-11
500	1250	706.9918	36.31863	3.02E-10	1.55E-11	362.4592	36.14286	1.55E-10	1.54E-11
500	1500	879.4428	40.98225	3.13E-10	1.45E-11	452.6292	41.67521	1.61E-10	1.48E-11
500	1750	1060.924	45.23566	3.23E-10	1.37E-11	548.3383	52.46522	1.67E-10	1.6E-11
500	2000	1241.701	47.78898	3.31E-10	1.27E-11	643.3088	63.78066	1.72E-10	1.7E-11
500	2250	1415.595	47.82146	3.36E-10	1.12E-11	735.1909	75.03989	1.74E-10	1.77E-11

Table G.10: Peak to Peak Actuation Strain and Piezoelectric Strain Parameters for 58lb Constant Load (Stress)

DC Offset Voltage, V	Peak to Peak Voltage, V	Peak to Peak 3-Dir. Strain, με	Std. Dev.	Effective d_{33}, m/V	Std. Dev.	Peak to Peak 1-Dir. Strain, με	Std. Dev.	Effective d_{31}, m/V	Std. Dev.
0	250	112.9642	4.94375	2.4E-10	1E-11	57.94244	5.93018	1.2E-10	1.3E-11
0	500	260.5731	17.1376	2.8E-10	1.8E-11	130.723	8.52862	1.4E-10	9.1E-12
0	750	420.0995	21.8089	3E-10	1.6E-11	212.7689	23.5411	1.5E-10	1.7E-11
0	1000	594.5311	27.1451	3.2E-10	1.4E-11	294.8485	25.6167	1.6E-10	1.4E-11
0	1250	768.2577	23.881	3.3E-10	1E-11	381.0571	32.206	1.6E-10	1.4E-11
250	250	107.2908	4.51559	2.3E-10	9.5E-12	58.11029	7.02013	1.2E-10	1.5E-11
250	500	242.848	9.76531	2.6E-10	1E-11	122.7332	8.1632	1.3E-10	8.7E-12
250	750	397.7752	23.5225	2.8E-10	1.7E-11	198.8708	18.6109	1.4E-10	1.3E-11
250	1000	569.3198	29.139	3E-10	1.5E-11	289.4101	29.8737	1.5E-10	1.6E-11
250	1250	744.5906	30.7895	3.2E-10	1.3E-11	379.0429	33.1998	1.6E-10	1.4E-11
250	1500	924.6955	34.6314	3.3E-10	1.2E-11	470.69	46.6817	1.7E-10	1.7E-11
250	1750	1095.3	43.0795	3.3E-10	1.3E-11	563.9149	52.0888	1.7E-10	1.6E-11
500	250	104.2696	6.6788	2.2E-10	1.4E-11	54.88754	2.87072	1.2E-10	6.1E-12
500	500	234.0525	17.661	2.5E-10	1.9E-11	118.1341	6.83818	1.3E-10	7.2E-12
500	750	381.5943	24.0534	2.7E-10	1.7E-11	198.4344	18.6895	1.4E-10	1.3E-11
500	1000	531.6202	34.7508	2.8E-10	1.8E-11	272.3228	26.5897	1.5E-10	1.4E-11
500	1250	695.6114	36.496	3E-10	1.5E-11	360.6464	35.9365	1.5E-10	1.5E-11
500	1500	867.3574	43.6019	3.1E-10	1.5E-11	451.9913	47.1117	1.6E-10	1.7E-11
500	1750	1038.063	52.5891	3.2E-10	1.6E-11	540.9192	55.4748	1.6E-10	1.7E-11
500	2000	1213.266	52.6727	3.2E-10	1.4E-11	633.372	63.1964	1.7E-10	1.7E-11
500	2250	1380.279	57.15	3.3E-10	1.4E-11	724.3477	68.0734	1.7E-10	1.6E-11

Table G.11: Peak to Peak Actuation Strain and Piezoelectric Strain Parameters for 60lb Constant Load (Stress)

DC Offset Voltage, V	Peak to Peak Voltage, V	Peak to Peak 3-Dir. Strain, με	Std. Dev.	Effective d_{33}, m/V	Std. Dev.	Peak to Peak 1-Dir. Strain, με	Std. Dev.	Effective d_{31}, m/V	Std. Dev.
0	250	112.1921	7.013421	2.39E-10	1.49E-11	58.58028	5.302629	1.25E-10	1.14E-11
0	500	252.4827	25.14231	2.69E-10	2.69E-11	128.8766	9.357942	1.37E-10	9.97E-12
0	750	412.3112	25.30235	2.93E-10	1.78E-11	203.8392	14.99697	1.45E-10	1.06E-11
0	1000	583.8222	31.55708	3.11E-10	1.67E-11	292.5321	23.01328	1.56E-10	1.23E-11
0	1250	748.0148	28.72339	3.19E-10	1.22E-11	373.5374	32.24363	1.59E-10	1.37E-11
250	250	100.3419	7.210231	2.14E-10	1.54E-11	52.13477	3.082723	1.11E-10	6.41E-12
250	500	236.1003	15.32995	2.52E-10	1.63E-11	119.4098	9.628176	1.27E-10	1.02E-11
250	750	391.4304	27.53667	2.78E-10	1.95E-11	198.5015	18.45247	1.41E-10	1.31E-11
250	1000	555.5559	33.58396	2.96E-10	1.78E-11	281.1518	23.7891	1.5E-10	1.27E-11
250	1250	723.8777	41.50908	3.09E-10	1.77E-11	367.4276	31.58068	1.57E-10	1.35E-11
250	1500	902.6734	45.80879	3.21E-10	1.63E-11	463.2038	47.13866	1.65E-10	1.67E-11
250	1750	1072.607	39.46075	3.27E-10	1.2E-11	554.8509	54.78692	1.69E-10	1.67E-11
500	250	103.0946	9.80558	2.2E-10	2.09E-11	55.65966	4.68574	1.19E-10	1E-11
500	500	230.3597	19.06161	2.46E-10	2.03E-11	120.2155	7.612229	1.28E-10	8.06E-12
500	750	372.094	25.4872	2.65E-10	1.84E-11	191.7539	17.81548	1.36E-10	1.26E-11
500	1000	522.7577	35.49967	2.79E-10	1.88E-11	270.5771	23.95434	1.44E-10	1.28E-11
500	1250	682.0826	46.12687	2.91E-10	1.97E-11	356.0137	33.96771	1.52E-10	1.45E-11
500	1500	848.7259	55.09653	3.02E-10	1.96E-11	442.7595	47.68696	1.57E-10	1.69E-11
500	1750	1018.659	55.93219	3.1E-10	1.7E-11	533.8359	52.96684	1.63E-10	1.61E-11
500	2000	1189.935	56.81293	3.17E-10	1.5E-11	625.8522	60.38182	1.67E-10	1.61E-11
500	2250	1351.039	59.32105	3.2E-10	1.4E-11	712.7659	70.5134	1.69E-10	1.67E-11

G.3 Conclusions:

This appendix presents the key measured actuation parameters for the five reference MFC specimens tested in the current research effort. They offer the ability for intelligent structures designers in the future to more accurately predict the response of their system under certain mechanical and electrical loading scenarios.

Appendix H

Tabulated Preisach Parameters f_M and f_{Mm} for Nonzero Constant Mechanical Loads

H.1 Introduction:

In the second half of Chapter 6, the Preisach model is developed for use with the hysteresis behavior of the MFC actuator. This model requires the experimental measurement of first-order reversal curves, as described therein. This Appendix presents the measured values for these curves when measured under a constant, nonzero mechanical load.

H.2 Nonzero Constant Stress Actuation Results:

Below, Tables H.1 through H.11 present the measured values of f_M and f_{Mm} for the MFC actuator. The maximum and minimum values of the shifted, fifth electrical cycle data from each peak to peak actuation voltage (i.e. the loops in Figures 6.32 and 6.33) are determined for each MFC specimen. These values represent f_M and f_{Mm}, and the limiting triangle in the α-β half-plane corresponds to the maximum voltage sequence, namely 2250 volts peak to peak with a 500 VDC biasing voltage. Hence, the point (α_0,

β_0) is equal to (1625, -625) volts. The values from three MFC specimens, namely S/N 404, 415, and 424, are then averaged, and the results and their sample standard deviations are presented in tabular form. The other MFCs that were tested, S/N 486 and 487, exhibited too much drift throughout the electrical cycles to be reliable for their extrema values of strain output, thus their behavior is excluded from this Preisach modeling analysis.

Table H.1: Measured Parameters f_M and f_{Mm} for Preisach Model of MFC Hysteresis, 1 and 3-Direction Actuation for 1lb (0.58 MPa)

		3-Direction				1-Direction			
M	m	f_M, $\mu\varepsilon$	f_{Mm}, $\mu\varepsilon$	f_M - Std. Dev.	f_{Mm} - Std. Dev.	f_M, $\mu\varepsilon$	f_{Mm}, $\mu\varepsilon$	f_M - Std. Dev.	f_{Mm} - Std. Dev.
125	-125	42.5	-75.4	10.6	4.7	36.7	-21.2	3.2	8.8
250	-250	118.7	-165.8	14.0	10.1	73.4	-58.0	7.6	10.8
375	-375	244.8	-243.6	14.4	11.4	106.1	-115.1	9.7	10.6
375	125	362.3	246.5	15.3	6.8	-100.5	-163.7	8.2	17.1
500	-500	398.8	-326.3	14.2	15.5	144.3	-180.9	12.2	20.8
500	0	479.7	207.1	17.0	10.1	-86.7	-215.5	10.8	18.4
625	-625	575.0	-409.5	24.3	18.3	176.2	-253.4	18.4	28.5
625	-125	597.6	132.5	17.8	6.7	-51.2	-271.4	9.0	24.3
625	375	628.0	515.1	18.2	6.3	-237.7	-296.8	24.2	30.6
750	-250	715.8	34.1	22.2	11.4	-7.5	-323.8	7.8	30.4
750	250	737.0	469.7	24.0	2.1	-217.6	-349.1	24.7	29.5
875	-375	831.4	-91.0	28.1	18.5	46.0	-378.1	8.0	35.7
875	125	846.8	394.5	27.8	5.3	-182.1	-400.1	24.2	35.5
1000	-500	948.9	-235.9	32.8	21.9	103.8	-434.8	9.3	38.9
1000	0	955.2	301.4	32.1	7.3	-135.1	-451.4	18.1	38.9
1125	-625	1057	-394.8	40.6	22.3	167.7	-487.2	17.6	44.7
1125	-125	1067	190.6	44.0	12.9	-87.1	-506.7	12.6	47.9
1250	-250	1179	66.1	46.6	14.1	-32.4	-561.3	8.4	45.2
1375	-375	1285	-72.1	55.4	20.7	24.5	-610.6	5.2	52.4
1500	-500	1392	-227.1	62.8	27.8	91.6	-664.3	9.4	58.8
1625	-625	1496	-396.7	70.5	35.3	156.0	-716.8	17.3	59.5

Table H.2: Measured Parameters f_M and f_{Mm} for Preisach Model of MFC Hysteresis, 1 and 3-Direction Actuation for 10lb (5.8 MPa)

		3-Direction				1-Direction			
M	m	f_M, $\mu\varepsilon$	f_{Mm}, $\mu\varepsilon$	f_M - *Std. Dev.*	f_{Mm} - *Std. Dev.*	f_M, $\mu\varepsilon$	f_{Mm}, $\mu\varepsilon$	f_M - *Std. Dev.*	f_{Mm} - *Std. Dev.*
125	-125	58.3	-62.2	10.4	3.8	30.3	-26.7	5.8	0.4
250	-250	126.3	-151.9	14.2	6.0	68.8	-60.3	9.6	9.0
375	-375	253.3	-228.9	14.5	8.2	104.8	-113.8	9.2	13.2
375	125	358.8	249.5	10.1	3.0	-108.4	-162.8	13.2	19.2
500	-500	404.4	-299.2	17.2	18.3	134.1	-181.9	17.8	22.4
500	0	469.8	205.2	10.9	3.2	-86.9	-210.6	10.7	22.9
625	-625	563.9	-388.1	25.9	19.1	170.8	-251.8	22.7	25.9
625	-125	584.3	127.7	19.8	6.9	-50.6	-265.2	10.2	27.8
625	375	625.4	509.2	17.5	11.4	-233.3	-293.4	26.3	30.2
750	-250	697.1	31.1	20.3	9.1	-6.3	-316.0	5.9	32.7
750	250	728.0	467.1	21.9	11.2	-211.7	-339.1	24.7	39.6
875	-375	813.1	-84.5	28.0	14.1	42.0	-370.1	6.2	40.0
875	125	831.0	395.9	21.8	9.1	-181.0	-388.9	22.2	42.0
1000	-500	919.0	-214.6	23.8	21.9	96.0	-420.4	16.5	45.1
1000	0	934.8	306.1	23.6	10.6	-138.4	-436.8	12.7	46.0
1125	-625	1031	-363.6	37.6	31.6	157.1	-474.0	23.7	52.7
1125	-125	1040	196.4	32.9	14.9	-87.4	-488.2	9.2	53.5
1250	-250	1146	78.7	36.0	21.2	-35.7	-539.2	7.1	59.3
1375	-375	1250	-45.3	36.4	33.3	17.8	-591.1	7.1	59.9
1500	-500	1357	-185.1	48.8	43.4	75.5	-641.8	12.5	66.1
1625	-625	1460	-337.4	53.9	50.3	136.2	-695.4	17.8	69.2

Table H.3: Measured Parameters f_M and f_{Mm} for Preisach Model of MFC Hysteresis, 1 and 3-Direction Actuation for 20lb (11.6 MPa)

		3-Direction				1-Direction			
M	m	f_M, $\mu\varepsilon$	f_{Mm}, $\mu\varepsilon$	f_M - Std. Dev.	f_{Mm} - Std. Dev.	f_M, $\mu\varepsilon$	f_{Mm}, $\mu\varepsilon$	f_M - Std. Dev.	f_{Mm} - Std. Dev.
125	-125	58.9	-55.6	11.5	8.2	29.5	-27.0	1.8	3.1
250	-250	129.5	-147.9	14.0	6.0	69.7	-61.8	7.6	6.5
375	-375	252.3	-220.2	13.4	15.7	102.6	-117.5	14.6	10.2
375	125	347.8	238.4	11.0	5.9	-101.5	-159.0	13.5	17.1
500	-500	397.5	-294.3	20.9	12.1	132.3	-182.2	16.2	17.9
500	0	457.5	192.6	15.2	8.5	-82.4	-207.2	12.9	23.7
625	-625	550.0	-382.5	25.3	21.6	170.4	-250.5	18.9	32.3
625	-125	562.7	120.2	18.3	9.1	-50.0	-257.7	12.6	29.6
625	375	599.9	488.8	15.8	9.8	-226.5	-288.2	23.0	27.5
750	-250	669.1	19.5	19.3	13.1	-2.7	-307.5	6.5	32.0
750	250	699.1	443.9	22.6	11.3	-208.7	-334.3	19.3	32.9
875	-375	777.3	-93.0	24.5	12.0	49.2	-358.9	10.5	41.1
875	125	796.0	372.1	24.2	6.8	-173.5	-379.5	18.8	40.7
1000	-500	886.8	-222.4	24.7	17.8	102.0	-414.0	11.8	43.9
1000	0	899.1	280.9	27.6	8.2	-132.4	-432.7	15.3	43.6
1125	-625	988.1	-362.7	27.8	21.2	163.3	-461.6	19.8	47.7
1125	-125	996.2	182.0	30.3	7.0	-83.0	-475.9	14.2	47.1
1250	-250	1099.1	68.0	33.0	18.1	-33.9	-528.3	9.6	56.3
1375	-375	1197.8	-52.3	39.3	24.1	17.9	-574.0	10.9	58.4
1500	-500	1304.0	-185.1	44.4	38.6	72.9	-630.3	16.2	63.9
1625	-625	1401.46	-329.65	53.23216	44.92357	132.06	-681.35	23.88	68.76

Table H.4: Measured Parameters f_M and f_{Mm} for Preisach Model of MFC Hysteresis, 1 and 3-Direction Actuation for 30lb (17.3 MPa)

		3-Direction				1-Direction			
M	m	f_M, $\mu\varepsilon$	f_{Mm}, $\mu\varepsilon$	f_M - *Std. Dev.*	f_{Mm} - *Std. Dev.*	f_M, $\mu\varepsilon$	f_{Mm}, $\mu\varepsilon$	f_M - *Std. Dev.*	f_{Mm} - *Std. Dev.*
125	-125	60.1	-61.6	14.9	7.9	36.7	-26.8	2.5	7.4
250	-250	132.8	-139.4	10.7	6.4	70.0	-57.7	8.8	3.9
375	-375	246.7	-215.2	12.2	10.4	103.1	-112.6	6.3	13.7
375	125	329.9	221.5	10.3	4.8	-95.4	-148.5	12.1	14.5
500	-500	386.1	-289.2	12.1	17.7	131.6	-176.6	16.3	18.4
500	0	433.2	171.6	9.6	1.4	-70.3	-197.1	11.9	19.0
625	-625	531.2	-370.3	21.0	20.2	188.2	-244.5	58.4	27.5
625	-125	533.9	96.9	16.8	5.1	-37.8	-244.9	11.3	25.8
625	375	568.6	459.6	25.5	22.8	-213.7	-271.6	16.7	23.3
750	-250	635.7	1.4	18.8	13.8	8.0	-293.1	6.9	32.3
750	250	661.3	410.8	26.9	23.4	-190.3	-316.0	13.3	28.0
875	-375	740.2	-109.9	20.1	16.5	56.8	-345.0	9.9	37.2
875	125	756.6	338.7	27.5	20.7	-157.3	-362.8	13.9	31.3
1000	-500	836.7	-230.8	22.1	25.8	111.4	-390.3	18.0	42.6
1000	0	849.3	256.6	28.4	23.4	-120.8	-407.0	12.0	37.2
1125	-625	935.7	-363.6	26.1	29.4	169.1	-439.9	22.5	43.8
1125	-125	944.6	158.9	38.1	28.2	-74.2	-452.5	10.4	39.0
1250	-250	1040	52.4	39.9	32.1	-24.1	-500.2	6.4	44.5
1375	-375	1136	-67.6	38.7	45.5	29.0	-551.3	15.6	52.5
1500	-500	1231	-189.3	46.2	50.2	80.8	-596.9	24.0	50.3
1625	-625	1323.25	-321.478	55.65822	60.40359	135.75	-647.17	31.86	54.44

Table H.5: Measured Parameters f_M and f_{Mm} for Preisach Model of MFC Hysteresis, 1 and 3-Direction Actuation for 40lb (23.2 MPa)

		3-Direction				1-Direction			
M	m	f_M, $\mu\varepsilon$	f_{Mm}, $\mu\varepsilon$	f_M - Std. Dev.	f_{Mm} - Std. Dev.	f_M, $\mu\varepsilon$	f_{Mm}, $\mu\varepsilon$	f_M - Std. Dev.	f_{Mm} - Std. Dev.
125	-125	44.7	-71.2	26.6	32.6	37.1	-20.3	18.8	9.7
250	-250	133.2	-129.4	15.2	2.0	63.5	-59.7	2.6	11.9
375	-375	247.1	-203.9	22.8	4.6	96.0	-115.4	8.0	18.1
375	125	304.3	197.5	6.7	14.2	-71.6	-124.5	32.1	27.2
500	-500	375.4	-275.2	27.6	6.6	131.3	-171.8	3.5	30.4
500	0	398.0	144.2	6.7	11.5	-46.0	-168.5	30.5	33.9
625	-625	507.6	-345.0	26.1	6.4	160.1	-233.2	12.8	29.1
625	-125	492.8	71.5	7.8	16.0	-12.4	-212.2	29.6	38.7
625	375	515.7	405.0	27.8	30.0	-156.2	-214.8	70.0	68.3
750	-250	585.5	-24.0	4.8	21.7	34.3	-258.1	29.5	39.9
750	250	600.4	357.4	29.1	31.0	-132.6	-252.4	72.8	73.0
875	-375	681.9	-125.4	12.9	20.1	81.1	-301.5	30.9	53.5
875	125	691.9	287.7	24.0	26.0	-100.6	-297.3	68.9	73.5
1000	-500	776.1	-245.2	24.1	27.7	138.0	-345.6	40.4	66.1
1000	0	777.4	206.3	27.1	29.9	-60.0	-339.0	70.8	77.3
1125	-625	858.4	-371.3	12.3	34.5	202.2	-379.6	42.3	66.2
1125	-125	865.2	112.2	34.8	33.5	-14.0	-382.6	73.5	88.4
1250	-250	951.9	11.5	33.7	32.0	35.7	-420.3	74.3	97.6
1375	-375	1037	-104.7	38.2	35.4	91.2	-463.1	75.0	105.8
1500	-500	1126	-220.6	40.3	30.6	142.9	-502.0	74.9	111.1
1625	-625	1216	-331.5	34.3	13.7	193.3	-544.8	67.8	110.6

Table H.6: Measured Parameters f_M and f_{Mm} for Preisach Model of MFC Hysteresis, 1 and 3-Direction Actuation for 50lb (29 MPa)

		3-Direction				1-Direction			
M	m	f_M, $\mu\varepsilon$	f_{Mm}, $\mu\varepsilon$	f_M - *Std. Dev.*	f_{Mm} - *Std. Dev.*	f_M, $\mu\varepsilon$	f_{Mm}, $\mu\varepsilon$	f_M - *Std. Dev.*	f_{Mm} - *Std. Dev.*
125	-125	51.5	-70.0	6.6	18.5	57.6	-7.7	32.4	20.1
250	-250	125.8	-136.8	14.4	5.2	80.7	-45.8	15.3	3.0
375	-375	220.6	-220.3	36.4	36.9	132.9	-80.4	34.4	29.8
375	125	287.4	176.4	59.9	55.9	-76.4	-131.6	199.2	205.1
500	-500	357.4	-279.3	27.4	6.8	144.1	-157.1	21.7	15.9
500	0	378.3	126.9	62.4	57.5	-46.0	-169.0	204.5	213.8
625	-625	504.3	-318.9	39.0	19.8	165.3	-219.3	4.5	37.4
625	-125	461.5	48.3	65.3	54.3	-5.4	-203.3	201.7	218.5
625	375	437.2	328.4	148.7	150.7	-8.3	-63.0	118.4	118.8
750	-250	544.0	-45.9	72.8	54.1	48.5	-232.5	201.4	228.6
750	250	515.9	269.9	154.4	160.2	20.3	-98.8	122.8	127.8
875	-375	638.3	-149.9	75.6	60.5	111.1	-267.6	199.9	232.9
875	125	593.8	202.8	162.4	168.0	55.0	-134.3	121.0	133.9
1000	-500	714.8	-268.5	99.5	71.8	182.1	-289.5	208.6	256.9
1000	0	683.2	122.6	155.1	156.6	98.7	-176.4	116.4	136.5
1125	-625	804.3	-370.6	97.3	69.3	250.3	-314.7	198.1	256.8
1125	-125	765.5	23.3	167.1	178.2	143.8	-218.1	120.9	145.1
1250	-250	849.5	-74.1	168.0	175.2	194.6	-256.2	117.2	152.1
1375	-375	930.6	-176.1	168.4	178.0	245.7	-291.5	115.0	158.6
1500	-500	1025	-285.9	179.4	190.6	300.6	-332.2	115.7	169.4
1625	-625	1105	-390.1	187.0	208.5	368.0	-361.3	117.8	183.1

Table H.7: Measured Parameters f_M and f_{Mm} for Preisach Model of MFC Hysteresis, 1 and 3-Direction Actuation for 52lb (30.1 MPa)

		3-Direction				1-Direction			
M	m	f_M, $\mu\varepsilon$	f_{Mm}, $\mu\varepsilon$	f_M - *Std. Dev.*	f_{Mm} - *Std. Dev.*	f_M, $\mu\varepsilon$	f_{Mm}, $\mu\varepsilon$	f_M - *Std. Dev.*	f_{Mm} - *Std. Dev.*
125	-125	34.1	-85.0	13.1	6.3	48.9	-10.2	2.3	8.6
250	-250	122.3	-145.2	12.1	5.1	77.3	-49.1	9.7	9.4
375	-375	237.3	-205.8	13.0	5.6	105.8	-105.8	10.1	8.3
375	125	319.0	207.8	25.3	16.2	-56.2	-114.9	11.9	22.3
500	-500	357.3	-271.8	13.3	9.9	130.2	-161.1	8.8	17.5
500	0	405.6	151.1	23.9	18.3	-30.5	-155.5	15.2	20.3
625	-625	486.3	-335.9	15.3	17.3	166.4	-216.1	11.6	22.0
625	-125	491.2	78.2	23.6	10.4	6.3	-190.8	14.0	21.4
625	375	526.1	418.3	53.2	46.9	-136.6	-192.3	29.0	38.9
750	-250	587.7	-7.2	26.8	11.0	50.7	-237.7	17.9	22.6
750	250	609.4	367.3	57.3	51.6	-111.6	-232.5	33.5	40.1
875	-375	680.9	-98.5	36.0	21.3	96.8	-276.2	24.9	28.5
875	125	690.4	297.9	59.4	52.0	-78.0	-270.0	30.2	41.8
1000	-500	773.7	-196.2	33.5	25.2	149.1	-318.3	36.6	28.2
1000	0	773.7	223.0	58.2	44.6	-41.8	-312.5	21.8	47.0
1125	-625	871.6	-293.0	42.1	35.4	199.4	-360.7	46.5	31.6
1125	-125	861.3	135.6	58.3	45.1	0.5	-354.7	21.7	46.5
1250	-250	939.7	41.2	58.0	49.0	49.2	-393.3	22.1	49.6
1375	-375	1026	-62.1	62.2	53.1	103.3	-437.8	28.0	59.4
1500	-500	1110	-170.6	69.9	62.8	157.6	-474.1	31.5	62.0
1625	-625	1195	-270.3	78.5	85.1	210.3	-515.3	47.0	73.4

Table H.8: Measured Parameters f_M and f_{Mm} for Preisach Model of MFC Hysteresis, 1 and 3-Direction Actuation for 54lb (31.2 MPa)

		3-Direction				1-Direction			
M	m	f_M, $\mu\varepsilon$	f_{Mm}, $\mu\varepsilon$	f_M - *Std. Dev.*	f_{Mm} - *Std. Dev.*	f_M, $\mu\varepsilon$	f_{Mm}, $\mu\varepsilon$	f_M - *Std. Dev.*	f_{Mm} - *Std. Dev.*
125	-125	37.0	-80.7	13.7	11.1	47.5	-14.0	7.8	4.8
250	-250	128.2	-133.3	10.1	12.8	69.8	-52.6	8.1	4.7
375	-375	230.3	-195.6	15.9	17.5	104.3	-98.4	6.6	13.5
375	125	362.7	253.9	122.5	131.6	-71.7	-126.8	28.9	28.2
500	-500	348.9	-263.5	15.7	14.8	133.8	-155.9	10.6	18.6
500	0	453.1	202.8	125.4	137.6	-45.0	-166.9	27.9	33.8
625	-625	477.0	-329.0	19.0	30.7	162.6	-221.1	17.8	22.2
625	-125	540.6	132.2	128.5	140.3	-9.6	-209.0	24.6	39.2
625	375	648.9	543.6	292.1	301.8	-157.5	-212.0	43.0	43.5
750	-250	630.7	59.3	142.4	152.2	28.0	-247.0	20.9	47.9
750	250	736.1	498.7	294.9	310.1	-135.9	-252.5	43.5	48.9
875	-375	730.3	-34.6	149.6	158.0	77.3	-295.7	17.0	53.7
875	125	814.6	435.6	303.3	311.4	-101.4	-291.2	36.4	58.5
1000	-500	835.8	-110.2	186.8	212.6	123.9	-337.5	20.5	60.1
1000	0	900.2	364.7	308.5	323.4	-66.1	-332.0	35.0	61.9
1125	-625	948.5	-180.7	240.5	271.4	174.7	-378.3	19.1	67.5
1125	-125	985.5	284.2	311.3	335.4	-22.2	-371.9	34.0	65.1
1250	-250	1076	201.5	324.6	364.3	26.0	-414.4	29.8	67.2
1375	-375	1161	103.5	334.8	370.9	78.0	-457.5	23.8	75.1
1500	-500	1249	7.5	334.5	378.1	126.7	-497.9	20.4	73.5
1625	-625	1331	-92.5	348.5	396.5	184.6	-536.0	33.0	79.9

Table H.9: Measured Parameters f_M and f_{Mm} for Preisach Model of MFC Hysteresis, 1 and 3-Direction Actuation for 56lb (32.5 MPa)

		3-Direction				1-Direction			
M	m	f_M, $\mu\varepsilon$	f_{Mm}, $\mu\varepsilon$	f_M - *Std. Dev.*	f_{Mm} - *Std. Dev.*	f_M, $\mu\varepsilon$	f_{Mm}, $\mu\varepsilon$	f_M - *Std. Dev.*	f_{Mm} - *Std. Dev.*
125	-125	46.4	-67.0	22.8	27.4	43.4	-15.9	8.9	7.8
250	-250	120.4	-133.0	8.7	20.4	70.2	-56.0	5.1	5.3
375	-375	230.9	-183.9	14.1	33.7	100.8	-100.5	13.5	6.9
375	125	321.9	213.4	62.7	69.3	-70.2	-127.6	16.8	21.9
500	-500	342.8	-255.9	11.0	34.9	134.9	-159.0	9.4	21.6
500	0	412.7	165.2	66.3	79.9	-48.0	-169.0	17.1	25.1
625	-625	463.1	-313.5	5.8	40.8	155.1	-218.5	12.3	24.1
625	-125	492.4	97.7	67.6	91.2	-11.9	-205.5	15.2	31.0
625	375	536.4	433.9	100.5	109.3	-157.1	-212.3	20.7	26.0
750	-250	581.5	21.0	72.2	101.1	29.4	-249.6	14.3	34.5
750	250	618.3	386.8	103.7	110.8	-134.0	-250.6	18.9	35.4
875	-375	665.8	-71.1	75.3	111.3	74.6	-287.2	7.5	43.9
875	125	695.8	324.2	97.1	119.7	-102.7	-288.6	19.4	33.4
1000	-500	759.1	-169.4	91.0	125.9	126.4	-330.8	3.2	54.1
1000	0	776.1	250.3	95.9	126.2	-66.2	-328.2	14.8	38.5
1125	-625	848.2	-257.3	94.0	143.8	176.7	-371.8	14.0	55.9
1125	-125	860.8	172.7	105.4	137.1	-24.0	-369.0	10.0	46.4
1250	-250	941.3	81.1	104.0	145.8	24.5	-410.0	5.7	47.7
1375	-375	1022	-16.6	99.7	142.4	74.9	-450.9	13.2	51.7
1500	-500	1094	-126.6	87.2	135.1	132.1	-487.4	26.9	50.5
1625	-625	1175	-228.7	76.0	128.9	181.3	-528.2	40.7	51.6

Table H.10: Measured Parameters f_M and f_{Mm} for Preisach Model of MFC Hysteresis, 1 and 3-Direction Actuation for 58lb (33.6 MPa)

		3-Direction				1-Direction			
M	m	f_M, $\mu\varepsilon$	f_{Mm}, $\mu\varepsilon$	f_M - *Std. Dev.*	f_{Mm} - *Std. Dev.*	f_M, $\mu\varepsilon$	f_{Mm}, $\mu\varepsilon$	f_M - *Std. Dev.*	f_{Mm} - *Std. Dev.*
125	-125	34.8	-77.5	8.0	12.5	44.8	-12.4	2.4	6.0
250	-250	126.2	-128.4	6.3	17.2	70.4	-56.2	12.5	7.7
375	-375	223.9	-186.1	5.8	23.7	111.4	-99.1	18.4	14.1
375	125	317.4	212.2	54.5	59.3	-74.0	-130.4	22.1	30.9
500	-500	337.4	-245.8	5.6	34.1	126.1	-158.1	8.8	21.1
500	0	401.6	162.1	59.6	70.0	-48.7	-170.4	24.6	35.9
625	-625	453.2	-310.6	3.1	32.1	156.9	-214.6	15.8	25.5
625	-125	484.6	98.9	56.9	79.2	-18.6	-208.5	21.7	39.7
625	375	567.2	463.7	139.2	146.9	-169.4	-224.9	46.2	49.6
750	-250	576.0	22.4	58.7	83.3	20.0	-255.0	16.5	46.6
750	250	645.3	417.4	135.8	156.9	-147.5	-262.9	45.4	53.5
875	-375	663.8	-67.6	59.9	94.4	66.4	-300.1	13.9	53.3
875	125	727.3	356.7	134.3	159.1	-116.6	-307.2	40.8	59.7
1000	-500	750.5	-160.1	71.3	107.9	114.8	-338.8	9.8	62.7
1000	0	803.3	288.5	134.4	168.3	-83.9	-342.1	39.0	60.6
1125	-625	845.1	-243.0	85.9	140.4	165.2	-383.9	4.9	69.1
1125	-125	883.9	207.7	139.2	173.6	-40.5	-383.5	34.3	69.9
1250	-250	964.2	117.4	131.5	176.4	8.4	-424.9	22.9	74.5
1375	-375	1039	24.2	133.8	189.9	55.1	-460.7	20.9	79.0
1500	-500	1130	-63.2	148.7	209.0	104.5	-504.4	10.9	83.7
1625	-625	1225	-140.7	157.5	229.9	157.5	-546.2	6.3	89.5

Table H.11: Measured Parameters f_M and f_{Mm} for Preisach Model of MFC Hysteresis, 1 and 3-Direction Actuation for 60lb (34.8 MPa)

		3-Direction				1-Direction			
M	m	f_M, $\mu\varepsilon$	f_{Mm}, $\mu\varepsilon$	f_M - *Std. Dev.*	f_{Mm} - *Std. Dev.*	f_M, $\mu\varepsilon$	f_{Mm}, $\mu\varepsilon$	f_M - *Std. Dev.*	f_{Mm} - *Std. Dev.*
125	-125	46.5	-63.7	23.2	31.0	42.5	-15.7	10.3	3.7
250	-250	119.8	-122.0	1.4	27.2	71.4	-51.5	4.4	3.2
375	-375	222.4	-178.9	4.2	24.5	97.9	-98.9	8.2	6.3
375	125	312.1	213.0	46.6	55.7	-73.5	-125.0	25.1	27.8
500	-500	328.3	-242.0	10.3	29.0	129.2	-153.2	8.0	18.5
500	0	397.8	167.6	51.2	67.7	-49.5	-164.8	25.1	34.3
625	-625	445.1	-295.6	4.6	42.2	154.1	-209.0	13.0	30.6
625	-125	478.5	100.6	53.7	81.7	-15.8	-204.8	22.1	40.0
625	375	554.0	454.7	113.2	124.0	-163.7	-217.1	52.9	53.2
750	-250	566.6	24.6	51.5	90.6	23.7	-248.2	16.6	42.5
750	250	632.2	408.1	107.7	131.4	-141.5	-256.3	52.2	53.7
875	-375	653.6	-53.9	54.3	103.0	64.1	-289.2	14.2	47.2
875	125	706.7	347.4	112.0	137.5	-111.0	-293.4	48.9	66.5
1000	-500	734.0	-147.6	52.9	102.0	114.5	-327.5	5.5	54.8
1000	0	786.4	279.1	108.7	148.6	-76.2	-335.6	46.1	70.9
1125	-625	818.1	-244.4	65.9	114.6	170.6	-368.9	9.2	66.7
1125	-125	861.3	201.8	111.2	158.9	-33.5	-371.5	44.8	76.0
1250	-250	939.8	118.1	104.1	160.1	8.7	-410.2	32.9	79.2
1375	-375	1022	28.1	106.3	166.6	58.6	-451.7	30.9	85.0
1500	-500	1113	-56.2	114.4	180.7	107.7	-495.5	23.1	90.7
1625	-625	1191	-143.29	118.4914	190.4154	154.30	-531.26	14.41	94.05

H.3 Conclusions:

This appendix presents the key measured parameters for the classical Preisach model as applied to a reference MFC actuator subjected to a nonzero constant mechanical load.

Vita

The author, Robert Brett Williams, grew up in Norfolk, Virginia, where he graduated with honors from Maury High School in June 1995. Brett obtained a Bachelor of Science degree in Mechanical Engineering, Magna cum Laude, from Virginia Polytechnic Institute and State University in May 1999. During his undergraduate studies, Brett held various engineering positions in the mechanical and industrial engineering fields. In February 1999, Brett began research for his Master of Science degree in Mechanical Engineering with Dr. Daniel J. Inman at the Center for Intelligent Material Systems and Structures at Virginia Tech. In August 2000, Brett completed this degree with a thesis pertaining to inflatable communications satellites. He then began doctoral research on active composite materials, again with Dr. Inman at Virginia Tech and Dr. Keats Wilkie at NASA Langley. Brett spent Summer 2001 and April 2003 through April 2004 living in Manhattan while completing his dissertation. The completion of this work in March 2004 marks the completion of Brett's Ph.D., Summa cum Laude.

In April 2004, Brett accepted a position at NASA's Jet Propulsion Laboratory in Pasadena, California, continuing his association with America's space agency while simultaneously fulfilling his goal of living in Los Angeles. His future aspirations include obtaining a Professional Engineering license, an MBA degree and pilot's license.

In his free time, Brett enjoys such outdoor activities as golf, tennis, swimming, running, skiing, SCUBA diving and skydiving. Additionally, Brett is an avid movie, comedy, and music fan and likes to shop and travel. World-wide adventures have included spring breaks in Cancun, backpacking around Europe and extreme sport activities in Australia. Additionally, Brett has attended all four tennis Grand Slam tournaments, the Australian Open, French Open, Wimbledon and the United States Open. It is to his good fortune that many of these interests and activities are shared by his loving girlfriend and future wife, Rachel Bachman.